2009-08-13

Numerical Characterizaton of the Inlet Flow in Eleven Radial Flow Turbomachines

Nathan O. Packard
Brigham Young University - Provo

NUMERICAL CHARACTERIZATION OF THE INLET FLOW IN ELEVEN RADIAL FLOW TURBOMACHINES

by

Nathan O. Packard

A thesis submitted to the faculty of

Brigham Young University

in partial fulfillment of the requirements for the degree of

Master of Science

Department of Mechanical Engineering

Brigham Young University

December 2009

BRIGHAM YOUNG UNIVERSITY

GRADUATE COMMITTEE APPROVAL

of a thesis submitted by

Nathan O. Packard

This thesis has been read by each member of the following graduate committee and by majority vote has been found to be satisfactory.

Date	R. Daniel Maynes, Chair
Date	Steve E. Gorrell
Date	Julie C. Vanderhoff

BRIGHAM YOUNG UNIVERSITY

As chair of the candidate's graduate committee, I have read the thesis of Nathan O. Packard in its final form and have found that (1) its format, citations, and bibliographical style are consistent and acceptable and fulfill university and department style requirements; (2) its illustrative materials including figures, tables, and charts are in place; and (3) the final manuscript is satisfactory to the graduate committee and is ready for submission to the university library.

Date

R. Daniel Maynes
Chair, Graduate Committee

Accepted for the Department

Matthew R. Jones
Graduate Coordinator

Accepted for the College

Alan R. Parkinson
Dean, Ira A. Fulton College of Engineering and Technology

ABSTRACT

NUMERICAL CHARACTERIZATION OF THE INLET FLOW IN ELEVEN RADIAL FLOW TURBOMACHINES

Nathan O. Packard

Department of Mechanical Engineering

Master of Science

Statistics based models have been developed previously to predict a priori the performance of new radial flow compressors and pumps and to model test data of previously designed and tested machines. Unfortunately, critical dynamics in the inlet region of the machines were neglected. Consequently, room for improvement in the previous modeling exists. Historical practice has placed a static pressure tap on the shroud just upstream of the impeller leading edge for experimental characterization. The previously developed statistics based models rely on this measured data. However, the location of the tap may be vulnerable to high gradients which would decrease the dependability of the developed models.

Full Computational Fluid Dynamics (CFD) and Multi-Stream Tube (MST) analysis were performed to test the appropriateness of the historically placed static

pressure tap location and to characterize the inlet flow of typical radial flow turbomachines. All designs and test data were provided by ConceptsNREC and have been collected for over 40 years. Eleven machines were chosen for investigation to provide a wide variety of inlet geometric and flow conditions.

The results derived from the Computational Fluid Dynamics and Multi-Stream Tube analysis suggest that the historically placed static pressure tap location is an inappropriate anchor point for model development. Steep gradients in the static pressure indicate that a relatively minor movement of the static pressure tap would significantly alter the experimental results and generate noise in statistical modeling.

While large variations in the pressure field are apparent near the impeller leading edge for all machines considered, the study results show that the flow field is uniform and very predictable when well upstream of the impeller leading edge. Specifically, a point 3 blade height upstream from the impeller leading edge appears to be a sound location to anchor model development. The model is highly dependent upon the flow parameters in the inlet passage. Thus it is important to ensure that the model is anchored at a location where the flow conditions are known to be stable and good. Future anchoring of the model upstream of the impeller leading edge will lead to a more accurate prediction and modeling of the design performance for radial flow turbomachines.

ACKNOWLEDGMENTS

Special thanks are warranted toward ConceptsNREC for their tremendous contribution to this project. They provided access to their database, as well as technical and financial support, which is most appreciated. Special attention is focused toward Dr. Dave Japikse for his insight, direction and tutelage. His knowledge and passion for turbomachinery is extraordinary.

I would like to thank Dr. Daniel Maynes for his guidance and aid, and for playing an integral role in the quality of the work.

Most importantly I would like to thank my wife, Telisha, for her tremendous patience and support. Her constant encouragement and confidence in my abilities provided continuous inspiration to succeed.

TABLE OF CONTENTS

LIST OF TABLES

LIST OF FIGURES

1 Introduction

1.1 Motivation

Effort has been made to model the performance of radial flow turbomachines[1]. Statistical models, designed to a priori predict performance of future builds, have had modest success. However, there are concerns about the statistical accuracy of existing performance prediction models. Recently Pelton proposed an equation for the prediction of a one dimensional performance parameter that describes the effectiveness of an impeller inlet[1]. This equation was created using stepwise linear regression techniques, with data acquired from over 300 lines of data from previously designed and tested turbomachines. The proposed model was derived from a basic database containing nearly 1000 independent variables for each speedline. While Pelton's model represents many of the expected geometric and flow based variables[2], recent events[3] have shown that this model fails in accurately predicting or accounting for some significant flow physics, particularly at the impeller inlet. Attempts at obtaining a greater understanding of the complexity of impeller-diffuser interaction concluded repeatedly that a better understanding of individual turbomachine components, namely the impeller and the inlet passage, must be obtained before efforts to analyze component interaction should take place. Understanding where the majority of the model error is occurring is of utmost

importance. Consequently, understanding what impact the error has on the accuracy of the model's prediction is of enormous worth.

Discussion and analysis of Pelton's model has led to the conclusion that the largest source of error could lie in a few places[3]. Inlet distortion, caused by a large horseshoe vortex at the leading edge stagnation point, or circumferential variation in the flow, which was assumed negligible (and which is undetectable in computational fluid dynamics (CFD)), could be a major culprit. However, experimentally validating these effects would be incredibly time and cost intensive. Another potentially large source of error is the location of the impeller inlet experimental pressure tap. Thirty years of experimental techniques at ConceptsNREC have followed industry practice in using a general rule of placing the shroud pressure tap, which measures the static pressure on the shroud of the impeller leading edge (P_{1t}), at the equivalent of 2-3 blade thicknesses upstream of the impeller blade leading edge. A typical thickness of the leading edge is about 0.012 inches. This distance was thought to be far enough upstream to avoid detecting inlet distortion. However, this assumption has not previously been verified in a systematic manner, neither experimentally or computationally.

In order to validate the appropriateness of the historical shroud tap location, computational fluid dynamics (CFD) can be used to evaluate if this location is appropriate. By observing how the pressure changes throughout the inlet passage one can examine the pressure field in the region of the impeller inlet and then compare CFD values to experimental observations. Further, the streamwise gradient in the static pressure at the measurement location can be evaluated. If the streamwise pressure gradient from at the tap location is minimal, then this source of error can be disregarded.

In contrast, if the pressure gradient at the tap location is large, perhaps this is the source of statistical uncertainty in the prediction models. Understanding where a good reference location exists would then be vital. A greater understanding of the fundamental impeller inlet flow physics will provide vital information which can improve the design of future centrifugal turbomachines.

1.2 Review of State of the Art

1.2.1 Methods

There are three primary methods utilized in industry for numerically analyzing the flow of turbomachines. One-dimension meanline design, multi-streamtube analysis, and CFD each offer specific advantages and disadvantages to the design process with each increasing in complexity. This added complexity results in added information concerning the region of interest.

1) One-dimensional meanline design

There are 3 levels of modeling in meanline design techniques[2]. They increase in complexity and accuracy. Level One approaches employ the basic principles of similitude to achieve a geometrically and fluid dynamically precise scaling from one application to another. Scaling is often employed in industry, as the process is fast and accurate, and can easily be used to design a family of machines. However, the principle is relevant only within the limitations of the scaling laws, and limits the designer's ability to expand beyond previous designs. In Level Two one attempts to use correlations of basic component performance (impeller alone and diffuser alone) to mix and match components for new applications. While Level Two expands the region of designs that

may be developed, it still limits the designer to previously designed machines. Level Three, however, requires one to propose comprehensive models, like Pelton's, and utilize them systematically in the design and development process to find new optimum configurations. Whenever a new type of machine needs to be developed or significant performance adjustments need to be made to previous designs a functional Level Three 1-D model is ideal. Pelton's efforts focused on creating such a functional model, designed to predict the performance of new radial or mixed flow turbomachines. The empirical approach, which industry relies extensively upon, allows for a limited extension of the design space and extends the realm of previous design procedures, doing so with a rapid and computationally basic process.

In spite of the presented advantages, 1-D modeling has its limitations. While the 1-D meanline code can provide initial geometry definition and define the number of stages, wheel speed, etc. of new designs, it fails to supply any 2-D or 3-D information about the flow. Any regard for detailed information about flow separation or vortices, for example, is thrown aside when a 1-D approach is employed. The general effects of these flow phenomena can only be accounted for in additionally specified modeling parameters.

2) Multi Stream Tube (MST) analysis, a quasi-3-dimensional algorithm

MST analysis is an inviscid solver developed by ConceptsNREC and is based on a quasi-three dimensional flow analysis with a streamline curvature method, used to determine the velocity distribution from hub-to-shroud and linearized blade-to-blade calculations[4]. The multi-stream tube calculation is a pure streamline curvature technique that solves a velocity gradient equation along quasi-orthogonals. MST analysis breaks up

the passage into a number of streamlines from hub-to-shroud, often using between 7 and 11 streamlines. The passage is broken up in the streamwise direction by similar segments, known as quasi-orthogonals, the number of which is determined by the user. Figure 1-1 depicts the MST computational domain for a typical impeller passage. Starting on the left of the image, the vertical lines represent the quasi-orthogonals, while the horizontal lines represent the streamlines.

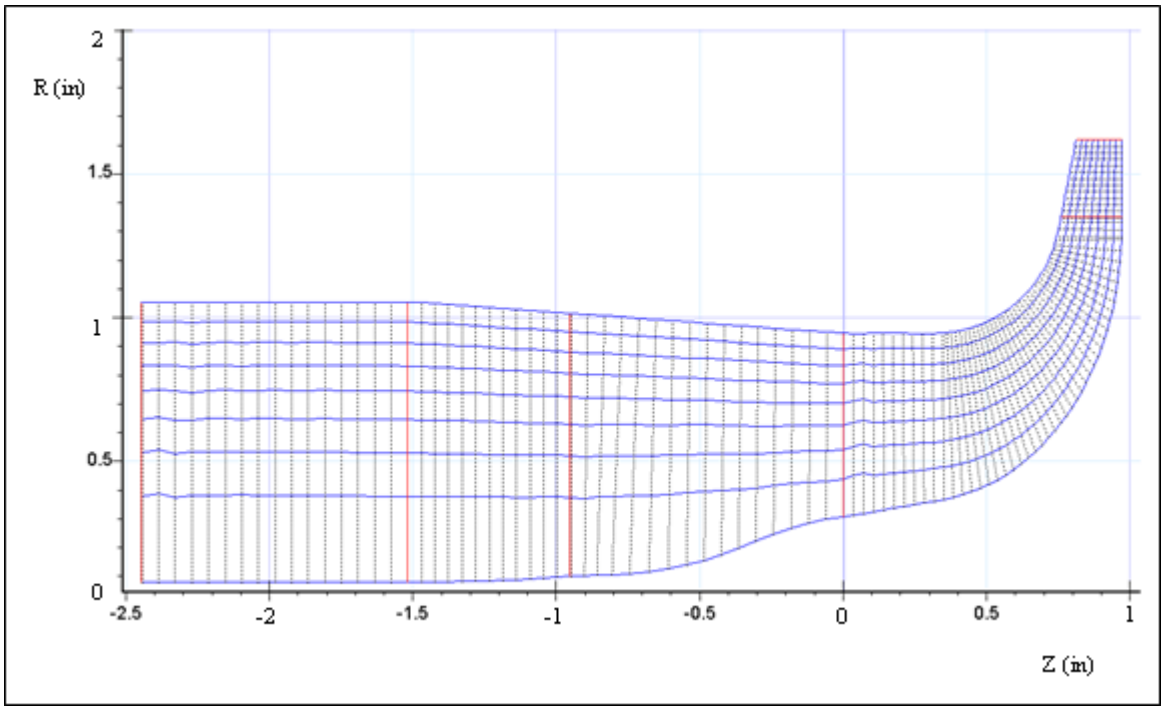

Figure 1-1 A depiction of the streamlines (horizontal lines) and quasi-orthogonals (vertical lines) found in the MST computational domain.

The streamline curvature method employed in MST works as follows[4]:

1) First and second streamwise derivative information is obtained from curve fits of approximate streamline locations.

2) These approximations are refined with subsequent iterations according to various damping and stability criteria.

3) Flow parameters are calculated at all grid locations in the passage.

The method is known to be comparatively stable, fast and unique[4].

The significant advantage of MST is its capability to provide more detailed information than 1-D modeling, while not sacrificing a major quantity of time required. This provides the designer with quasi-3-D flow information, supplementing the information that is available from the 1-D process. Revisiting Fig. 1-1, MST can provide information at any point in the passage, both in the streamwise and spanwise directions. For example, the ratio of the meridional tip velocity to meridional mean velocity at the impeller leading edge (*AK*) cannot be determined from a 1-D analysis, even though it is important to the overall accuracy of the 1-D model. Historically estimates of *AK* were made by experienced intuition[3]. MST can quickly and accurately calculate the velocity ratio, enhancing the accuracy and fidelity of the 1-D model. The major disadvantage in MST is that since the flow information is calculated based on the streamline curvature, care must be made when setting up the MST calculation. In some instances the actual geometry (particularly along the hub) of the design in question must be altered in order to allow for numerical stability to prevail. Further, MST is an inviscid solver, and is unable to discern viscous flow effects beyond traditional boundary layer growth, which can be incorporated into the solver.

3) CFD, computational fluid dynamics

Frequently the 1-D meanline and MST approaches are inadequate in providing the detail that is needed to complete the design process. Using a Reynolds Average Navier Stokes (RANS) turbomachinery flow CFD solver can provide much of this information. With a sufficiently refined grid, a full 3-D solution to the flow state can be obtained,

providing understanding of the flow field and accompanying fluid dynamic parameters. At any point in the computational domain, specific information can be garnered. Viscous effects, including boundary layer growth, vorticity interactions, and flow separation and recirculation are readily detectable. Subsequently this data can be applied back into 1-D analysis codes, enhancing the accuracy of the design process.

While significant advantages are found in the CFD formulation, it is often time consuming and complicated. Although parallel codes can be comparably fast, significant effort is needed for the development of appropriate computational grids. If the grid is dense enough, several days may be required before reliable results can be obtained. Since more information is available than the 1-D and MST procedures, which is the usefulness of CFD, deciphering and extracting the relevant details can also prove cumbersome.

1.2.2 Enhancing 1-D Meanline Modeling

Pelton's objective was to create an accurate and robust Level 3, 1-D model. This model was built upon two theoretical systems proposed by Japikse, the Two-Zone and Two-Elements-In-Series (TEIS) models[2]. Using the Two-Zone and TEIS model approximations together allows the designer to directly model turbomachine performance parameters, like rotor efficiency, in the 1-D procedure, without the complication of MST or CFD computation. The two models combine to provide a basic flow model that is computationally simple, aiding in rapid design and optimization. Further explanation of the Two-Zone and TEIS models is provided.

Two-Zone Model

Simplified flow analysis suggests that centrifugal turbomachine flow may be classified into two regions. The Jet, or primary, region is modeled to consist only of isentropic flow. The Wake, or secondary region, is modeled to contain non-isentropic flow effects[2]. This non-isentropic zone may be comprised of boundary layer fluid near the walls or other viscous regions. As long as it is possible to assign a value to the fraction of the passage area occupied by it, or some equivalent parameter, it is possible to treat the non-isentropic flow separately from the isentropic/primary flow[2]. Figure 1-2 depicts a two-zone model.

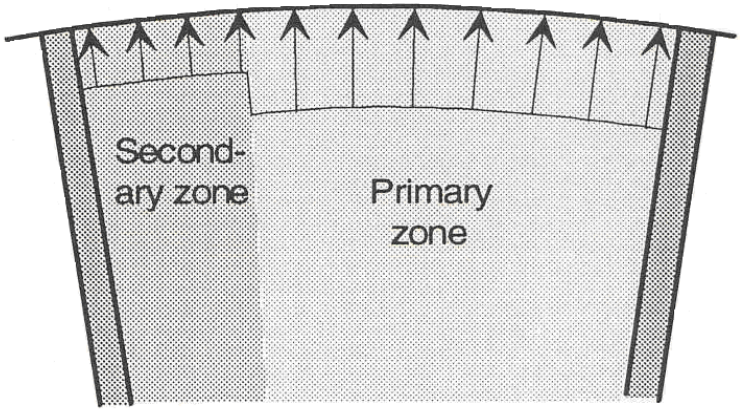

Figure 1-2 A two-zone model[2]. Used by permission.

Three parameters, in addition to those from the TEIS model, are needed to complete the model, allowing for the calculation of the change in fluid properties and kinematic parameters. The first is the ratio of the massflow of the secondary/wake zone flow to the primary/jet zone massflow (χ). This parameter has traditionally been assumed

constant along a speedline, with typical values around 0.15-0.25. While this is not true physically, with χ varying with operating point, it is a modeling parameter. Little is known about how χ changes and one must consequently make the reasonable modeling assumption that it is constant along a speedline[1]. In harmony, Dean showed that the performance prediction was not very sensitive to the specified value of χ [5]. The second parameter is the deviation of the primary zone at the impeller trailing edge (δ_{2p}). Measured in degrees, it is the difference between the impeller exit flow direction and impeller exit blade angle. δ_{2p} varies with massflow and typical values are between (-5) to (-15) degrees. The deviation of the secondary zone at the impeller trailing edge, δ_{2s} is also considered in the model, but in practice has been found to be zero.

The Two-Zone model provides an accurate method for predicting the thermodynamic state change through the radial impeller and subsequently a set of 1-D modeling equations for each zone can be detailed[2]. This set exploits known inlet conditions to generate a very rapid approximation of the impeller output flow thermodynamic conditions. In conjunction with the TEIS model, which provides a simple flow diffusion model of the fluid, the Two-Zone can accurately predict complete outlet conditions.

TEIS Model

The TEIS, or Two-Elements-In-Series, modeling approach is a conceptualized method that incorporates basic principles of turbomachinery[2]. Modeling similarities exist between most impeller and conventional diffuser and nozzle flow fields. In TEIS, blade passages are modeled conceptually as two nozzles or diffusers in series. These elements

are labeled elements “a” and “b”, respectively. Figure 1-3 conceptually represents the TEIS model graphically.

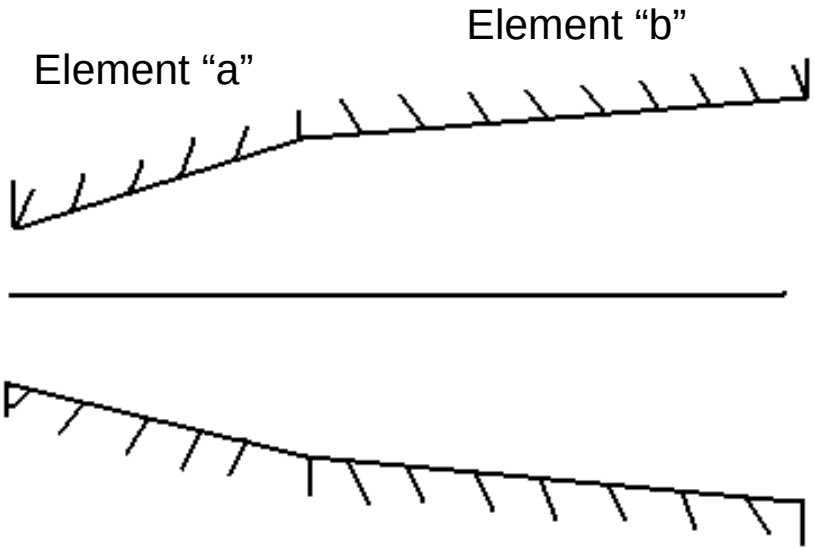

Figure 1-3 A conceptual representation of the TEIS model showing the series arrangement of the two flow elements[2]. Used by permission.

Element “a” is identified as the inlet portion of impeller. It is a variable geometry element which may act as a nozzle or diffuser, with its functionality dependant upon the flow rate. Below a certain flow rate, the inlet acts as a diffuser. Conversely, above this flow rate the inlet element accelerates the flow and acts as a nozzle. A graphic of the element “a” variation is shown in Fig. 1-4.

Element “b” is the passage portion of impeller. For incompressible flow it acts as a fixed geometry diffuser or nozzle. For compressible flow it becomes a variable geometry diffuser due to a change in density. Figure 1-5 illustrates the arrangement of element “b”.

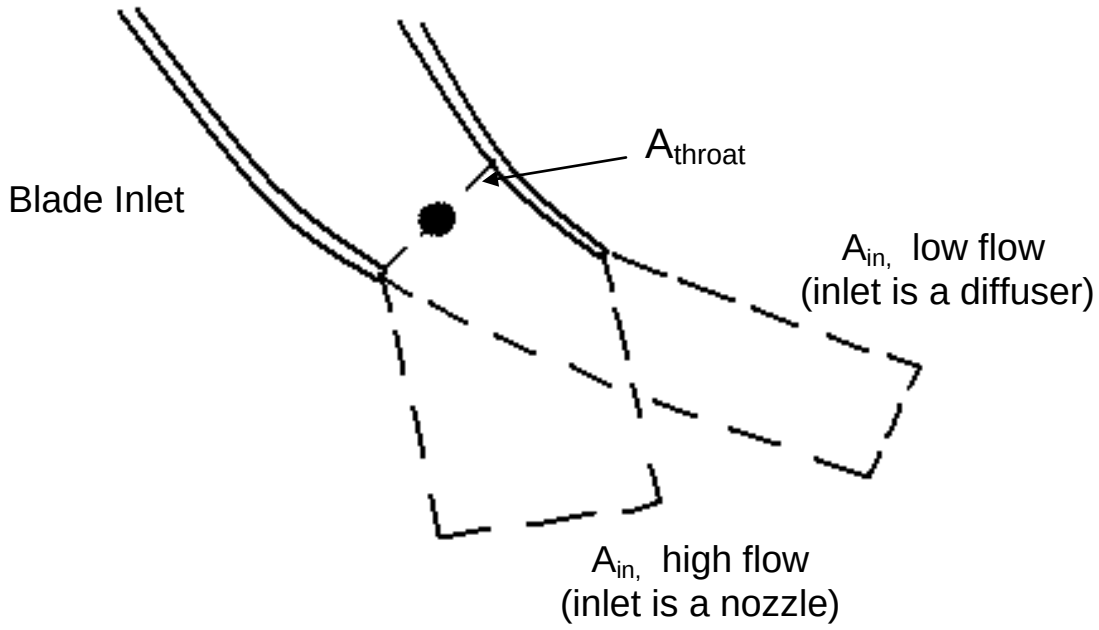

Figure 1-4 The TEIS model inlet portion (element "a") showing the variable geometry characteristic of the model[2]. Used by permission.

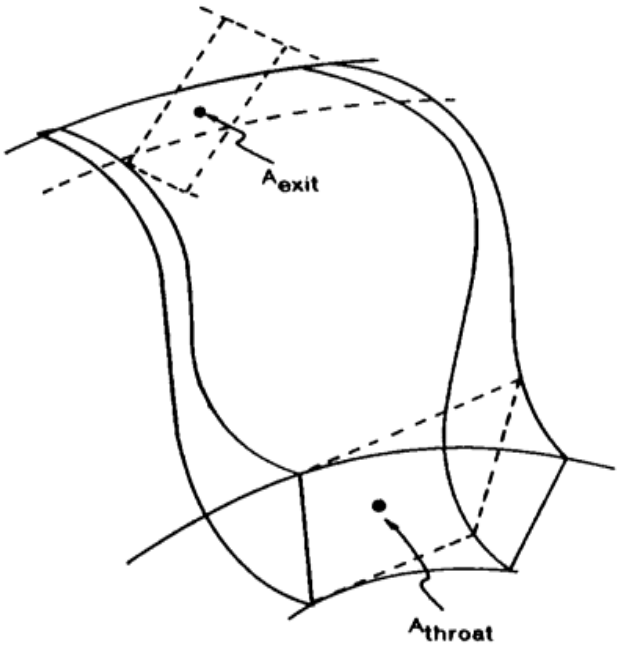

Figure 1-5 The TEIS model passage portion, element "b"[2]. Used by permission.

Each element can be modeled using parameters termed η_a and η_b, the inlet and passage effectiveness's. Each of these effectiveness parameters is functions of the respective element pressure recovery coefficient, C_P, and the element ideal pressure recovery coefficient, $C_{P,i}$. The effectiveness of element "a" is defined as

$$\eta_a = \frac{C_{pa}}{C_{pa,i}} \tag{1-1}$$

For element "a" the pressure recovery terms are calculated as

$$C_p = \frac{\Delta p}{q} \tag{1-2}$$

and

$$C_{pa,i} = 1 - \frac{1}{AR_a^2} = 1 - \left(\frac{\cos \beta_1}{\cos \beta_{1b}} \right) = 1 - \left(\frac{\cos(\beta_{1b} - I_{1t})}{\cos \beta_{1b}} \right) \tag{1-3}$$

where q is the local dynamic head ($^1/_2 \rho W_{1t}{}^2$). This is calculated using the density, ρ, and inlet velocity, relative to the impeller tip, W_{1t}, where Δp is the change in static pressure through the element. AR_a is the area ratio of the inlet to the throat. β_1 is the relative flow angle at the inlet, β_{1b} is the inlet blade angle, and I_{1t} is the inlet tip incidence.

For element "b", η_b is calculated in a similar fashion as

$$\eta_b = \frac{C_{pb}}{C_{pb,i}} \tag{1-4}$$

where

$$C_{pb,i} = 1 - \frac{1}{AR_b^2} = 1 - \left(\frac{A_{th}}{A_{exit}} \right) \tag{1-5}$$

AR_b is the passage area ratio, A_{th} is the throat area, and A_{exit} is the impeller exit area as shown in Fig. 1-5.

In order to complete the TEIS model, the diffusion ratio (DR_2) must be defined

$$DR_2 = \frac{W_{1t}}{W_{2p}} \tag{1-6}$$

where W_{2p} is the relative velocity of the primary flow zone at the impeller exit. To extend the range of the TEIS model, the effects of stall must also be accounted for. When in stall the flow becomes reoriented away from the desired flow direction, known as flow separation, and large viscous shear stresses dominate locally. This generates noise, and consequently the inception of stall and the affect of stall on the machine performance are difficult to accurately predict[2]. However, stall can generally be approximated using knowledge of the diffusion or pressure loss characteristics of an impeller[1]. In the TEIS model, approximating the affects of stall can be done with a constant value of diffusion ratio. Japikse[2] derived the following equation for $DR_2{}^2$ to relate the performance model to the output thermodynamic state, shown below

$$DR_2^2 = \left(\frac{1}{1-\eta_a C_{pa,i}}\right)\left(\frac{1}{1-\eta_b C_{pb,i}}\right) \tag{1-7}$$

Utilizing Equation 1- 7 in combination with Equation 1- 6, the change in the fluid velocity through the rotor can be predicted using η_a and η_b. Furthermore, if η_a and η_b are known, the results can be combined with the two-zone model parameters to get a full knowledge of the impeller output state.

TEIS and Two-Zone models can theoretically provide a quick and accurate 1-D approximation of the flow characteristics of a wide range of turbomachine applications and in theory is capable of prediction beyond the range of previous designs.

1.3 Literature Review

Pelton has completed work on the 1-D empirical modeling of radial flow turbomachinery[1]. His focus upon the TEIS modeling parameter η_a is fairly unique, although the general industry standard is to utilize a meanline modeling approach, often based on the Two-Zone model, involving variables which require user empiricism. Previous to Pelton endeavors were made by Clements and Artt[6] to develop a one-dimensional performance prediction procedure. The two-zone model was utilized to represent the impeller flow, including corrections for backflow and jet-wake static pressure difference. In conjunction, the TEIS model was used to predict the impeller diffusion ratio.

Many in industry use empirical modeling in their 1-D design process. While these models are rarely revealed or discussed, companies or groups generally build these models based on previous design work. The goal is to account for a large number of geometric and flow parameters and reduce them to a more simplified model.

Pelton's prediction models for impeller inlet and passage performance have been developed using multiple regression techniques, focusing on geometric and flow characteristics. However it is observed that some key parameters have been neglected from the model, particularly parameters which would better describe the complexity of the inlet passage.

Japikse has written several books describing general principles of turbomachinery and centrifugal compressor design and performance[2, 7]. He states that the objective of an inlet device is to bring the flow, in a nearly uniform state, to the eye of the impeller. If this is done, improved efficiency and good flow control should result. Nevertheless, inlet

ducts often require a careful quasi-three-dimensional flow field analysis to improve the modeling. In some cases complex inlets cannot readily be analyzed and requires experimental development. Japikse clarifies that very good insight can be obtained by using the one-dimensional calculations utilizing various isentropic relationships. However, the success of the 1-D modeling approach is dependent upon an inlet design which makes every effort to minimize boundary layer growth in order to ensure steady uniform flow entering into the impeller situated immediately downstream of the inlet duct. He asserts that non-uniformity will occur for all inlet configurations except for the straight inlet with a short duct and a good bell mouth for which the boundary layer growth can be reasonable assessed. Other configurations may introduce a level of velocity gradient and distortion which would require a probe survey of the inlet, or else the losses associated with these inlets must be accounted for elsewhere.

It would be ideal to be able to accurately represent inlet flow conditions with a 1-D isentropic approximation. Zemp *et al*[8] use unsteady fluid flow simulations to quantify the forcing function acting on the compressor blades due to inlet flow distortion. The investigation of the effect of idealizing the inlet flow distribution on the forcing function showed an increase of the peak amplitude of the unsteadiness of approximately 30% compared to the actual inlet flow distribution. There is evidence that when inlet distortion is present a large amount of loss, unaccounted for in a simple 1-D approximation, alters the machine performance. Charalambous *et al*[9] use CFD analysis to confirm that the historical approach to compressor design considers uniform inlet flow characteristics. However, the inlet flow is quite often non uniform, and this can result in severe performance degradation. Sonoda[10], like others, confirms through experimental

and numerical investigation that the inlet is a difficult component to analyze, but must be done so to accurately model and predict the performance of centrifugal turbomachines. These studies all show that the inlet geometry affects the performance of the rest of the machine, and consequently deserves attention toward the design and investigation of the flow in that region. While Zemp confirms that inlet distortion makes the 1-D approximation difficult, all cases investigated in the present study can reasonably be assumed to have a uniform, steady inlet flow; all designs utilize a large bell mouth and plenum upstream of the impeller leading edge. Thus a 1-D meanline model is effective in these scenarios.

Despite efforts to classify inlet flow conditions generally, evidence of previous work addressing the static pressure variation in the vicinity of the blade leading edge has not been found. Further, discussion of the appropriateness of the historically placed pressure tap location, as well as the pressure gradient in the vicinity of the leading edge, has yet to occur.

1.4 Scope

A better understanding of the impeller inlet flow physics will lead to increased design capabilities for centrifugal turbomachine designers. Full computational fluid dynamics and multi-streamtube analysis will be executed on 11 previously designed and tested centrifugal turbomachines. These 11 machines are selected to provide a wide variety of geometric sizes and flow conditions, with 9 compressors and 2 pumps. An assortment of inlet passages is investigated. Careful attention will be paid toward the gradient of the static pressure at the experimental tap location and the impeller leading

edge. Information obtained from this investigation will provide a framework where the statistical accuracy of Pelton's η_a model may be improved.

1.5 Contributions

Two primary contributions result from this work:

1) The integrity of Pelton's η_a model is in question. This uncertainty arises from the historic placement for the P_{1t} measurement position. Concern has arisen that the location may make the pressure tap susceptible to detecting impeller inlet distortion, which if it exists would result in a large pressure gradient at the tap location. An assessment of the appropriateness of the historic tap location ensues.

2) A recommendation for an alternative approach in the TEIS modeling development.

1.6 Delimitations

Efforts will be focused exclusively upon how the static pressure at the impeller shroud leading edge may be responsible for error in previous η_a models. While the remaining TEIS and Two-Zone parameters are critical to the accuracy of the 1-D modeling approximations, the focus of this work is to address potential error in the η_a model. Furthermore, this investigation will encompass only twelve representative turbomachine designs. These 11 machines were carefully selected to represent a wide variety of geometries and functions. Most of the inlets generally replicate the straight inlet with a short duct described to produce a near-uniform impeller inlet condition.

1.7 Thesis Overview

Chapter 2 will discuss the procedure employed in the calculation and manipulation of the CFD data. A discussion of grid development and independence and the specified solver settings is presented. Chapter 3 will provide results and analysis of the CFD investigation. Extensive detail will be relayed for one representative machine. Further, representative results will be revealed for the remaining designs and the implications of the results and analysis of all 11 machines will be discussed. Conclusions will be made regarding the appropriateness of the historic P_{1t} tap location, and an alternative approach to the TEIS modeling development will be given. General conclusions and final statements can be found in Chapter 4. Details of other machines can be found in Appendix A.

2 Procedure

2.1 Objective

The objective of this work is to characterize the flow field in the inlet region of several radial flow turbomachines to investigate the appropriateness of historical assumptions regarding the inlet dynamics. The machines chosen are diverse in geometric form and functionality. Of specific interest is the streamwise pressure variation in the inlet region. Specific emphasis is placed on understanding how and why the local static pressure varies in the vicinity of the impeller leading edge with particular attention given to variations near industry's historically placed experimental pressure tap location. This tap location has historically been placed on average about 0.1 inches upstream of the impeller leading edge.

2.2 Overview of Scope

Computational fluid dynamics (CFD) and multi-streamtube (MST) analysis was performed on 11 previously designed and tested centrifugal turbomachines. Only steady, or time-averaged effects were considered. These designs, as well as the experimental results, are supplied by the study sponsor ConceptsNREC. The 11 machines were selected to provide a wide variety of geometric sizes and flow conditions, with 9

compressors and 2 pumps. A wide range of inlet passage types are included in the machines.

Table 2-1 provides a summary of a few important parameters for each machine investigated in this work. These parameters include a designated name of the machine, where CCN and CPN stand for Centrifugal Compressor Number and Centrifugal Pump Number, respectively. Shown in the table for each machine are the shroud and hub radii at the impeller leading edge (R_{1t} and R_{1h}), the radius at the impeller exit, R_2, the operating rotation rate, N, and the mass flow range explored for each speedline.

Table 2-1 Summary of geometric and flow features of the 11 machines investigated.

Machine Name	R1 tip (in)	R1 hub (in)	R2 (in)	N (rpm)	massflow range (lbm/s)
CCN30	0.95	0.31	1.35	120k	0.48 - 0.57
CCN32	0.82	0.43	2.03	76k	0.19 - 0.30
CCN38	0.97	0.32	1.44	110k	0.58 - 0.72
CCN39	0.97	0.32	1.44	110k	0.68 - 0.75
CCN40	1.02	0.50	2.72	58k	0.36 - 0.49
CCN42	1.54	0.39	2.46	53k	1.08 - 1.61
CCN66	1.71	0.60	3.44	39k	4.08 - 6.07
CCN74	1.50	1.50	3.00	39k	0.24 - 0.37
CCN95	1.41	0.49	2.82	34k	0.49 - 0.62
CPN7	1.65	0.79	2.88	3k	79.10-103.37
CPN28	2.69	1.68	3.75	3k	117.98-145.64

Experimental measurements from each design were compared to results from the CFD and MST analysis. For each design the CFD analysis was completed, including the establishment of the solver settings, establishing boundary conditions, grid generation and running the solver to convergence. The CFD results were then compared to the MST results which were initiated by a process similar to the CFD analysis. This process was repeated for mass flow rates at a given impeller rotation rate, designed to match the

experimental operating conditions. Efforts were generally focused away from impeller stall and choke conditions.

Analysis of the data aims to answer the questions from the project objective. With regard to the appropriateness of the historical tap location, contour plots provide an effective visualization of the flow in the region of interest, as well as through the whole inlet passage. Additionally a defined pressure coefficient references the CFD and MST results to the experimentally measured tap static pressure. This coefficient is calculated at all grid locations in the streamwise direction and at several spanwise locations (hub-to-shroud). Determining the appropriateness of the historical pressure tap location is then evaluated using two criteria: 1) how well do the CFD and MST calculations of the tap static pressure match the experimental data? 2) How steep are the streamwise pressure gradients near the experimental tap location?

If results reveal that the experimental tap location is not appropriate, an alternative approach to the TEIS formulation described in Chapter 1 is necessary. Conclusions that anchor the TEIS formulation at a more appropriate location in the passage are made after information from each design is presented and analyzed in Chapter 3.

2.3 Full CFD

2.3.1 CFD Solver

All computations are done using the Spalart-Allmaras (SA) 1-equation turbulence model. It is a Reynolds Averaged Navier Stokes (RANS) model which solves a transport

equation for a viscosity-like variable $\tilde{\nu}$, which may be referred to as the SA variable. The RANS equation is[11]

$$\rho\left(\frac{\partial \overline{U_i}}{\partial t}+\overline{U_j}\frac{\partial \overline{U_i}}{\partial x_j}\right)=-\frac{\partial \overline{P}}{\partial x_i}+\mu\nabla^2\overline{U_i}-\frac{\partial\left(\rho\,\overline{u_i u_j}\right)}{\partial x_j} \qquad \textbf{(2-1)}$$

where the ensemble average of the typical velocity of the flow is $\overline{U}$, $\overline{P}$ is the ensemble average of the pressure, *t* is time and *x* is the space parameter. Further, μ is dynamic viscosity, ∇ is the del operator and $\bar{u}$ is the ensemble average of the turbulent velocity fluctuation, and the product in the third term on the right represents the Reynolds stress. The "i" and "j" subscripts indicate the spatial dimension. Together with the SA model governing equation a system of equations can be formed which one may numerically solve.

A standard representation of the governing equation in the SA model is[12]

$$\begin{aligned}\frac{\partial \tilde{\nu}}{\partial t}+u_j\frac{\partial \tilde{\nu}}{\partial x_j}&=C_{b1}(1-f_{t2})\tilde{S}\,\tilde{\nu}-\left[C_{w1}f_w-\frac{C_{b1}}{\kappa^2}f_{t2}\right]\left(\frac{\tilde{\nu}}{d}\right)^2\\&+\frac{1}{\sigma}\left[\frac{\partial}{\partial x_j}\left((\nu+\tilde{\nu})\frac{\partial \tilde{\nu}}{\partial x_j}\right)+C_{b2}\frac{\partial \tilde{\nu}}{\partial x_i}\frac{\partial \tilde{\nu}}{\partial x_i}\right]\end{aligned} \qquad \textbf{(2-2)}$$

which solves for the viscosity-like variable $\tilde{\nu}$. The molecular kinematic viscosity is ν. Further parameters are defined as

$$\tilde{S}\equiv S+\frac{\tilde{\nu}}{\kappa^2 d^2}f_{v2} \qquad \textbf{(2-3)}$$

where *S* is the strain rate tensor as defined below

$$S=\sqrt{2\Omega_{ij}\Omega_{ij}} \qquad \textbf{(2-4)}$$

and utilizes the rotation tensor

$$\Omega ij = \frac{1}{2}\left(\frac{\partial u_i}{\partial x_j} - \frac{\partial u_j}{\partial x_i}\right) \quad \textbf{(2-5)}$$

The f_{v2} function is defined as

$$f_{v2} = 1 - \frac{\chi}{1 + \chi f_{v1}} \quad \textbf{(2-6)}$$

where the function f_{v1} is

$$f_{v1} = \frac{\chi^3}{\chi^3 + C_{v1}{}^3} \quad \textbf{(2-7)}$$

The parameter χ is

$$\chi = \frac{\tilde{\nu}}{\nu} \quad \textbf{(2-8)}$$

and the constant C_{v1} is

$$C_{v1} = 7.1 \quad \textbf{(2-9)}$$

The parameter d is the distance closest to the surface and κ is a constant set to be

$$\kappa = 0.41 \quad \textbf{(2-10)}$$

The function f_{t2} is defined as

$$f_{t2} = C_{t3} \exp\left(-C_{t4}\chi^2\right) \quad \textbf{(2-11)}$$

with the constants C_{t2} and C_{t4} set as

$$C_{t3} = 1.1 \qquad C_{t4} = 2 \quad \textbf{(2-12)}$$

The function f_w is defined as

$$f_w = g\left[\frac{1 + C_{w3}{}^6}{g^6 + C_{w3}{}^6}\right]^{\frac{1}{6}} \quad \textbf{(2-13)}$$

where

$$g = r + C_{w2}\left(r^6 - r\right) \tag{2-14}$$

Here r is defined as

$$r \equiv \frac{\tilde{\nu}}{\tilde{S}\kappa^2 d^2} \tag{2-15}$$

All other constants are set as

$\sigma = 2/3$ $C_{b1} = 0.1355$ $C_{b2} = 0.622$

$C_{w2} = 0.3$ $C_{w3} = 2$ $C_{w1} = Cb1/\kappa^2 + \left(1 + Cb2\right)/\sigma$

This model is utilized because of its simplicity yet functionality. Advantages of the SA model include:

1) The model is local, in that one point does not depend upon the solution at other points, and is therefore compatible with grids of any structure and Navier-Stokes solvers in two or three dimensions.

2) It yields satisfactory predictions of boundary layers in pressure gradients.

3) It is numerically forgiving, in terms of near-wall resolution and stiffness, and yields fairly rapid convergence to steady state.

Extensive testing has proven the Spalart-Allmaras model to be accurate in a variety of turbomachinery applications. Yang *et al*[13] utilized SA in a three-dimensional hybrid structured-unstructured RANS solver and applied it to a variety of test cases, including a flat plate boundary layer, a 1.5 stage compressor, the unsteady interaction of a wake and turbine cascade and a combination of intake and inlet guide vanes. The validation and application examples have demonstrated that the RANS solver, which utilized the SA model, was accurate for both steady and unsteady state simulations, and it is applicable to the flows in complex turbomachinery geometries. Madden and West[14]

used SA with wall functions and no-slip boundary condition in both the steady and unsteady domains to model the rotor casing treatment as part of a full compressor stage. The model was robust and accurate enough to calculate shock positions, radial efficiency profiles, stator incidence and deviation and time-averaged blade tip static pressures. The SA model accurately modeled the move of the surge trigger from the stator to the rotor when a tip distortion was applied. Lastly, Vassiliev *et al*[15] performed a comparative study using SA, the Standard k-ε, the RNG k-ε, and the Realizable k-ε models. The study concluded that while CFD simulation of flow between structural components remains a challenging task due to very complex geometries, 3D turbulent flow structure with separations, reattachments and vortices, they found that the SA model performed well at predicting various flow results. In predicting the pressure recovery of an axis-symmetric diffuser the SA model accurately agrees with measured results. In all of the studies investigated the SA model adequately performed under a wide variety of conditions and for a wide variety of turbomachinery flows, and is thereby deemed adequate for this intended study.

ConceptsNREC has executed extensive validation efforts to substantiate the use of PushbuttonCFD, the ConceptsNREC software package for CFD and which was used exclusively in this study. Numerical simulation and comparison to experimental data were performed with the SA model on several turbomachine configurations pertinent to this study[16]. This included many well known designs, such as the Eckardt Compressor O, a famous test done in Germany with very detailed measurements. Comparison of the well known test data to the PushbuttonCFD solution is visible in Fig. 2-1.

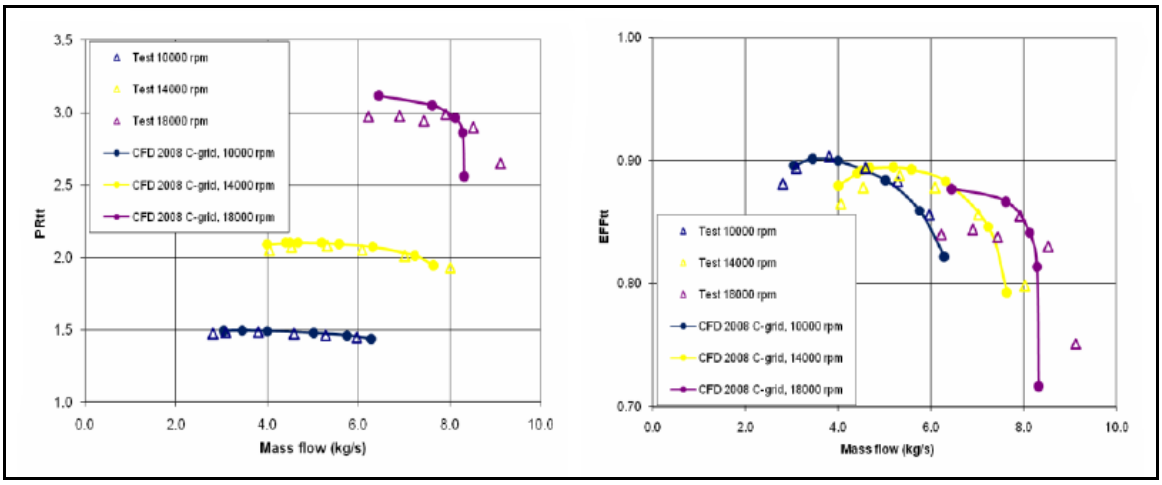

Figure 2-1 Pressure and efficiency maps for the Eckardt Compressor 0, comparing the data derived from experiment and CFD analysis[16]. Used by permission.

Other benchmarking work presented in this study includes the MAN compressor cascade, tested in 1996. CFD and the experimental data show very good agreement for two different incidence angles, as observed in Fig. 2-2.

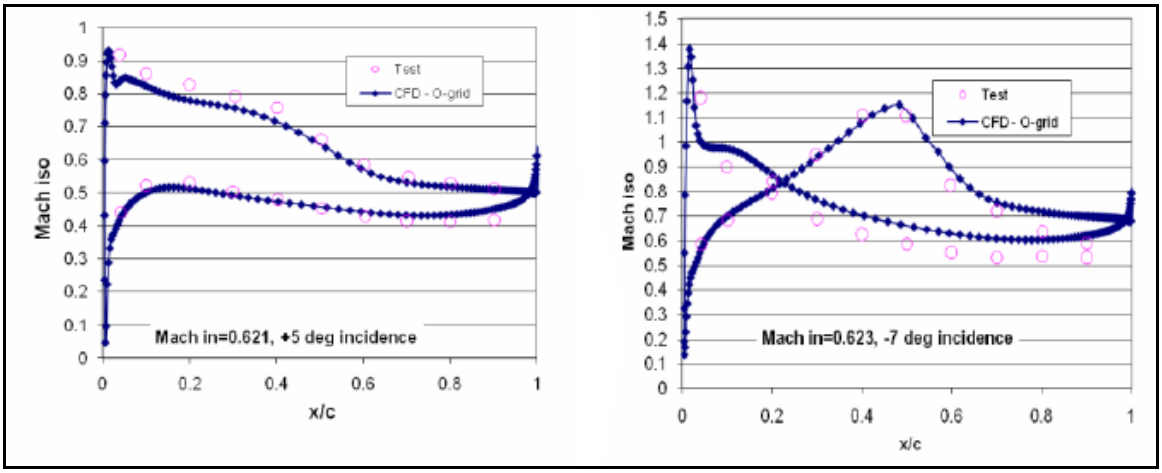

Figure 2-2 Comparison of the test data with the numerical simulation for two varying incidences.

The results presented above are indicative of the agreement found in several other designs. The results presented in this study represent some of the best examples available for general turbomachinery validation and show very good agreement overall[16].

2.3.2 Boundary Conditions

Figure 2-3 presents the locations of the inlet and exit boundary conditions, as well as the shroud and hub walls for a representative machine.

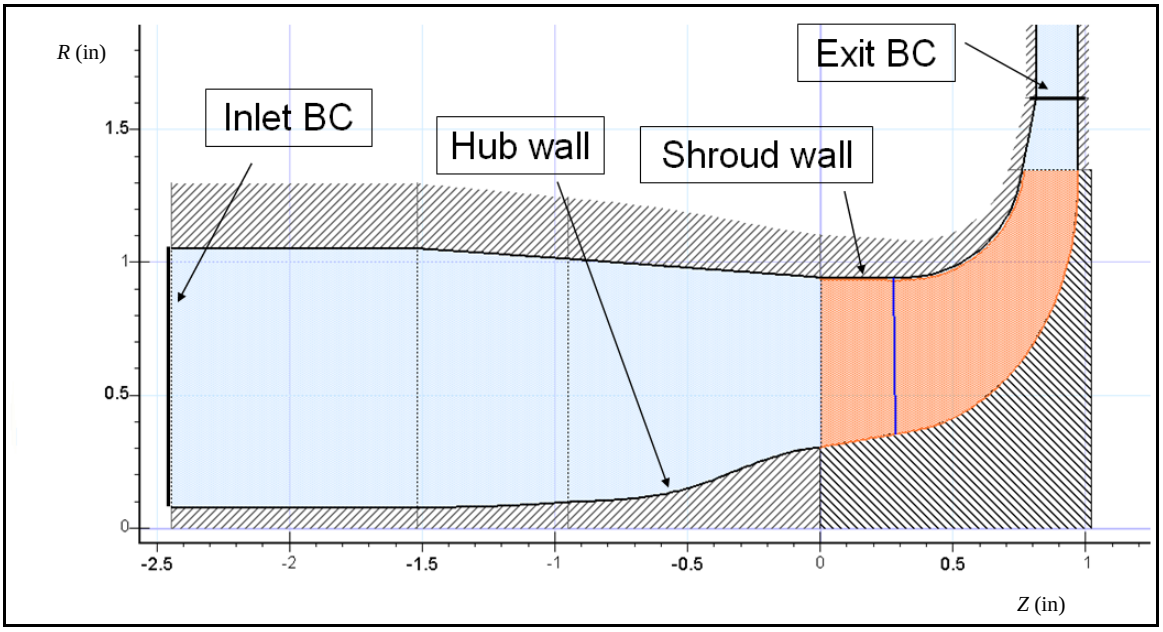

Figure 2-3 A depiction of the boundary conditions and wall locations for a representative machine.

There are two streamwise boundary conditions. One imposed boundary condition is at the inlet and beginning of the computational domain. At this location, the momentum condition is satisfied by specifying the inlet total pressure. The energy condition is satisfied by specifying the inlet total temperature. These values are always set to match the experimentally measured values. The other streamwise boundary is at the

end of a vaneless diffuser directly following the impeller exit. Here the total massflow through the machine is specified to match the experimental values, which is requisite if one wants to compare values between CFD and experimental results. This location is determined to be at the end of some specified geometry domain, and is assumed to be far enough downstream of the impeller for exit mixing to occur (not a location of high gradient). A representative contour plot is shown at the exit of a small vaneless diffuser, as seen in Fig. 2-4. The front surface displays the static pressure variation at the end of a short vaneless space of a representative machine.

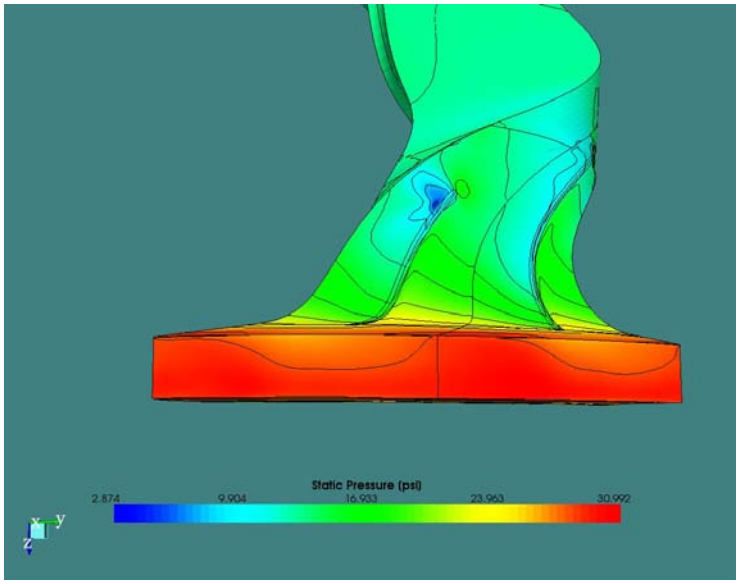

Figure 2-4 Depiction of the near uniform condition at the specified vaneless diffuser exit for a representative machine.

Generally, the exit is therefore assumed to not be in a region of high gradient. However, small exit variations are assumed to have only secondary effects on the inlet passage.

The shroud wall is treated as it exists physically and is specified as no-slip. Since the flow is turbulent, for all scenarios the shroud wall is treated with a log law shear stress model. The hub, however, acts essentially like a line of symmetry, as it would in the experimental setup, except for two exceptions: 1) At the present time, the computational package employed (PushbuttonCFD) will not allow a nonzero radius for the hub wall. Instead the radius is set to about 0.001 inches, from the computational domain inlet up to the beginning of the bullet nose. This represents an average change of about 0.1% and the computational area in this region is only slightly different from the physical area. Because of the minor change in cross-sectional area the hub wall condition can likewise be specified with a log law shear stress model and not have any considerable affect on the flow results[17]. 2) The bullet nose must be slightly modified from its actual geometry. The experimental bullet nose extends upstream of the leading edge of the impeller, ends with a blunt edge which is nearly perpendicular to the flow direction, and ends at a zero radius. Again, the analysis package will not allow a zero radius, and it will not allow such a stagnation point with the geometry perpendicular to the flow direction. Consequently, a small region of the bullet nose is modified. This is done so that while the general shape and slope of the bullet nose is maintained, especially near the end of the bullet nose/impeller leading edge, the entry region is slightly smoothed to allow for numerical stability. Figure 2-5 portrays the modification.

The rotation of the compressor is determined as follows: from impeller leading to trailing edges the hub rotates with the machine. For an open wheel the entire shroud section defaults to stationary, while for a closed wheel the shroud is automatically set to be rotating at the same speed as the machine within the bladed segments[4].

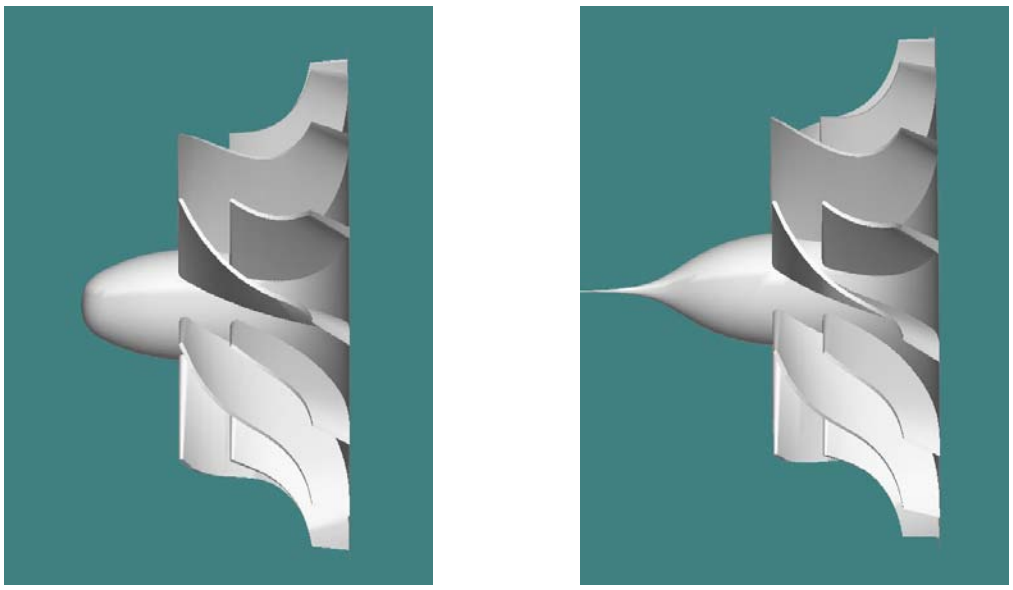

Figure 2-5 A representative modification of the bullet nose in PushbuttonCFD required for numerical stability in the CFD simulations. The physical bullet nose is on the left and the modification for CFD is on the right.

2.3.3 Grid Development

All grid development was accomplished using PushbuttonCFD. Simulations were performed with an O-type grid in the area in the immediate vicinity of the blade[4]. However, standard H-type gridding was employed in the unbladed portions of the geometry, as is shown in Fig. 2-6. The O-grid wraps around bladed elements and often some cells appear similar to the letter 'O', thus the name. H-grid topologies resemble standard structured quadrilateral cells. The locations for the transition from H to O-type grids is determined by PushbuttonCFD and based upon the geometric and flow parameters of the specific machine design, yet the general arrangement of the two grid types is consistent. Figure 2-7 presents a representative grid developed in PushbuttonCFD, with emphasis placed on the locations of the O and H-type grids.

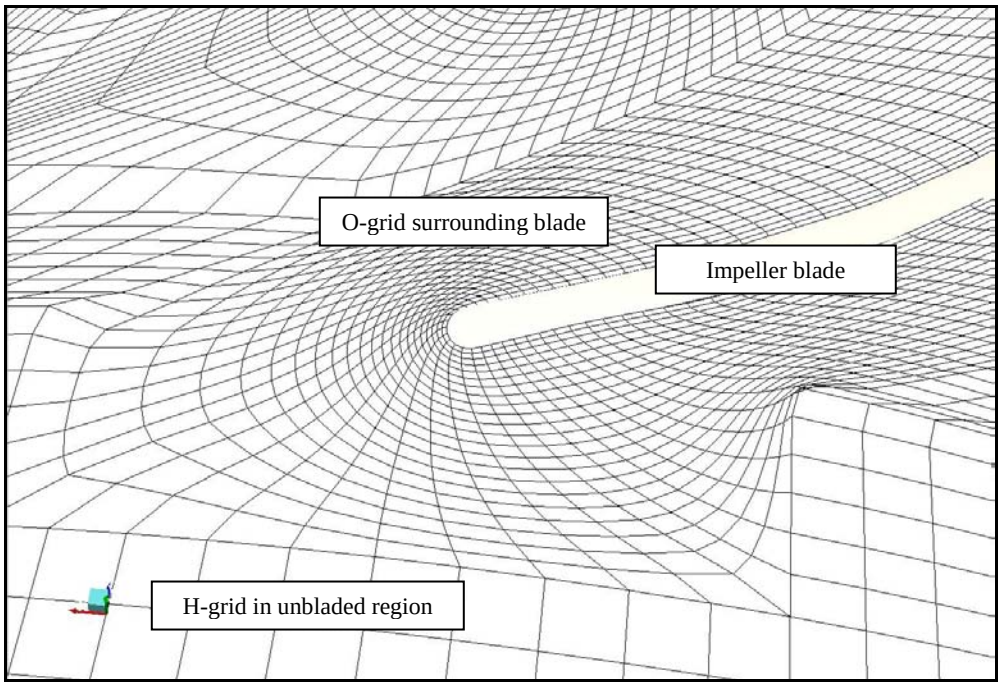

Figure 2-6 Illustration of grid types used in grid generation with O-type grids deployed around bladed elements to preserve the true geometry of the leading edge of the impeller and structured H-type cells deployed in the bulk flow regions.

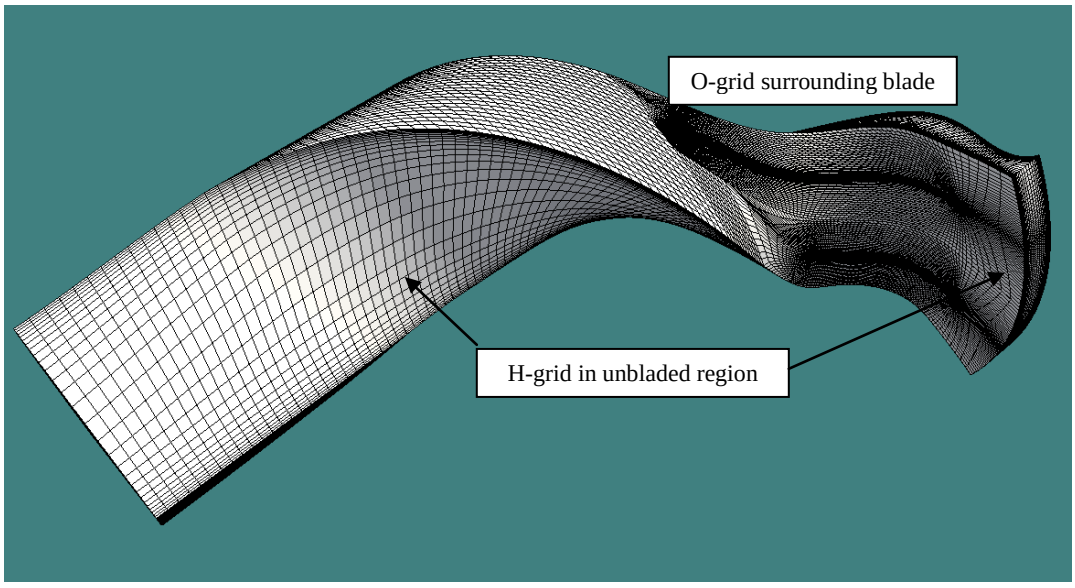

Figure 2-7 Representative depiction of the grid developed in PushbuttonCFD.

CFD solution accuracy is directly related to grid quality, particularly in areas where large gradients exist; such as around the blade leading and trailing edges[4]. The O-grid is designed to better conform to the true blade geometry and to improve the grid quality in the near-blade region. Consequently it provides a clear advantage over the standard H-grid topologies. The capability to utilize O-grids removes the compromise between grid generation and geometry accuracy; the geometry is not changed for the sake of grid generation, as illustrated in Fig. 2-8, where an H-type grid is implemented.

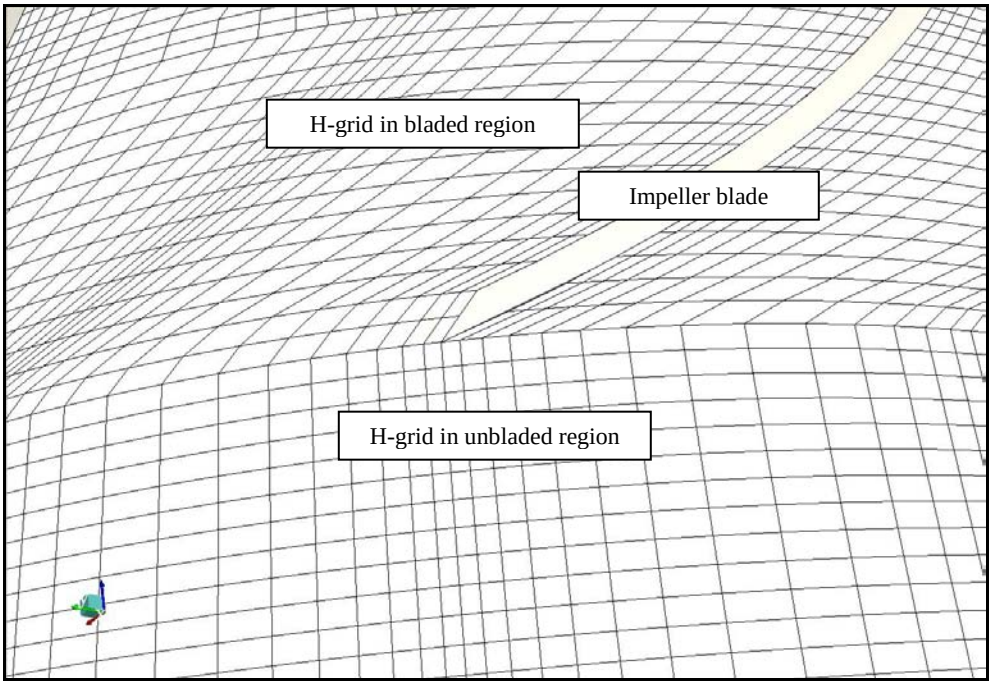

Figure 2-8 Illustration of the compromise in the true geometry of the leading edge of the impeller using the H-type gridding scheme.

2.3.4 Grid Independence

Two critical flow parameters are the average pressure values at the blade leading edge and at the experimental tap location. It is determined that grid independence was attained when both of these two key parameters remained unchanged with successive grid

refinement. Unchanged is agreement within ±0.01 psi, where a typical pressure value is nominally 13.50 psi.

A default grid of approximately 50,000 nodes was created with typical node density of nominally 25 x 17 x 119. These node dimensions represent the spanwise x pitchwise x streamwise directions. The analysis package PushbuttonCFD sets appropriate blade-to-blade and streamwise node values based on a user input hub-to-shroud cell density value. These values are generated based on the flow path and the blade geometry.

Grid refinement was done for each scenario as follows: After convergence was achieved on the default grid, the grid was refined to have approximately twice the number of nodes. The new grid was initialized with information interpolated from the previous grid to save computation time and eliminate initial numerical instability. Grid size continued to be refined, with the node number approximately doubling each time, until the impeller leading edge and tap location pressures ceased to change. At that point the coarsest grid where the solution was independent of grid size and density was employed for the rest of the calculations. Further information regarding the grid density for each machine is provided in Chapter 3.

2.3.5 Convergence

Convergence for each case was achieved when the RMS (root means square) of the residuals of the governing equations cease changing. At this point the computed massflow has leveled off at the specified value. Typically, about 3000-5000 iterations were required to reach convergence.

2.4 MST

2.4.1 MST Solver

MST can be used in a similar fashion to CFD, determining the pressure distribution throughout the computational domain. However, MST is an inviscid solver with an optional boundary layer calculation method. The multi-streamtube analysis is based on a quasi-three dimensional flow analysis with a streamline curvature method, used to determine the velocity distribution from hub-to-shroud and linearized blade-to-blade calculations[4]. It is a pure streamline curvature technique that solves a velocity gradient equation along quasi-orthogonal lines. The method employed in the MST solver was described previously in section 1.2.1. This particular algorithm is part of the software package developed at ConceptsNREC, and extensive testing has shown it to be comparatively stable, fast and unique[4].

2.4.2 Boundary Conditions

The user selects the locations in the passage for starting and ending the MST calculations and in all cases these locations are identical to the CFD computational domain (see Fig. 2-1). Since the solver assumes an inviscid flow, at each streamwise location the total pressure and temperature were specified. The calculation was initialized from rapid loading results[4]. Rapid loading analysis (also called SST or single-streamtube) is based on a single streamline flow analysis through the center of the passage. The calculation is extended out to the corners of the passage by assuming a

linear velocity distribution hub-to-shroud and blade-to-blade. This rapid loading calculation is a simplified form of quasi-3D inviscid flow analysis.

2.4.3 Grid Development

MST analysis breaks up the passage from hub-to-shroud into a number of streamlines, often using between 7 and 11. Additionally, a number of quasi-orthogonal lines are chosen, running vertically through the computational domain. Figure 2-9 depicts the MST computational domain for a typical impeller passage.

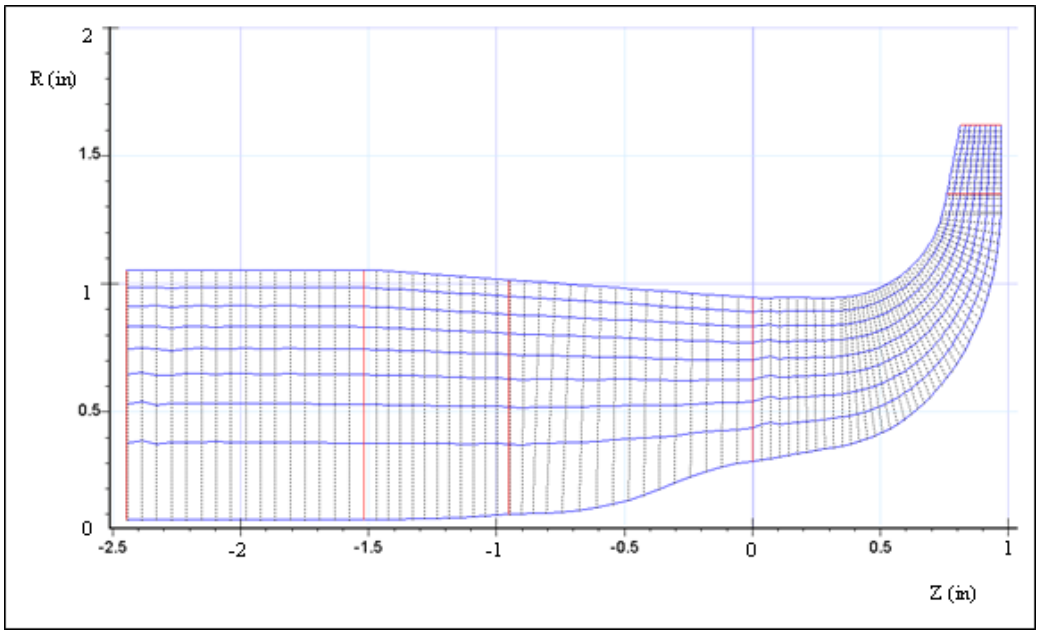

Figure 2-9 A depiction of the streamlines (horizontal lines) and quasi-orthogonals (vertical lines) found in the MST computational domain for a representative machine.

Starting on the left of the image, the vertical running lines represent the quasi-orthogonals, while those running horizontally represent the streamlines. The number of quasi-orthogonal lines and streamlines is user controlled, and like the CFD mesh is

dependent upon the size of the computational domain. A typical design uses about 20 quasi-orthogonal lines in the passage inlet, and about 20 more to model the impeller. Using too few lines fails to adequately represent the flow conditions, while overloading the passage with too many causes numerical instability in the curvature method.

2.4.4 Streamline Analysis

Because of the computation method employed in MST, the bullet nose used in CFD must be "smoothed" further. Smoothing is achieved by stretching out the bullet nose, extending it further downstream of the impeller leading edge. This extension nominally increases the length of the bulletnose by about 20%. It is important to keep the slope and shape of the bullet nose as consistent as possible, especially near the impeller leading edge. A depiction of the bullet nose from CFD along side the further "smoothed" bullet nose can be found in Fig. 2-10.

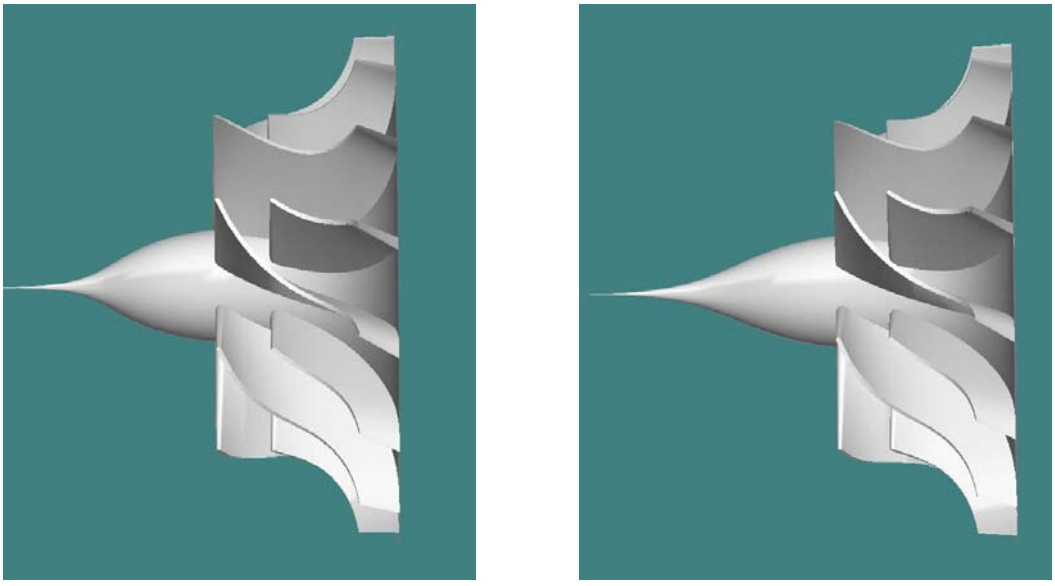

Figure 2-10 A representative modification of the bullet nose in MST required for numerical stability in the MST simulations. The CFD bullet nose is on the left and the MST modification is on the right.

Smoothing is required for MST to be successful. The streamline curvature method utilizes first and second streamwise derivative information. When the bullet nose is too sharp, as seen in the left image, the derivatives become too large and the streamlines cease to be smooth and physically rational, as seen in the top image of Fig. 2-11. These irregular streamlines are modeling a nonphysical streamline shift. In MST, convergence is a function of the maximum streamline shift. If the flow computationally shifts too far, then the modeling of the flow conditions can not be trusted and convergence is not achieved. Smoothing of the bullet nose eliminates this quandary, resulting in a physically sensible and numerically stable approximation, as seen in the bottom image of Fig. 2-11. The change is due to the modest difference in the hub slope.

A sensitivity study reveals that while this hub smoothing will modestly affect the overall shape of the hub streamwise and static pressure distribution, there is negligible influence from about 50% of the span, up to the shroud line. Figure 2-12 depicts the streamwise distribution of the static pressure derived from MST, along the shroud line for each bullet nose configuration.

TEIS modeling relies primarily upon knowledge of the flow along the shroud of the turbomachine. Thus, while a small portion of the flow has been altered by smoothing the hub profile, information pertinent to the modeling objective is not influenced by the modest modification.

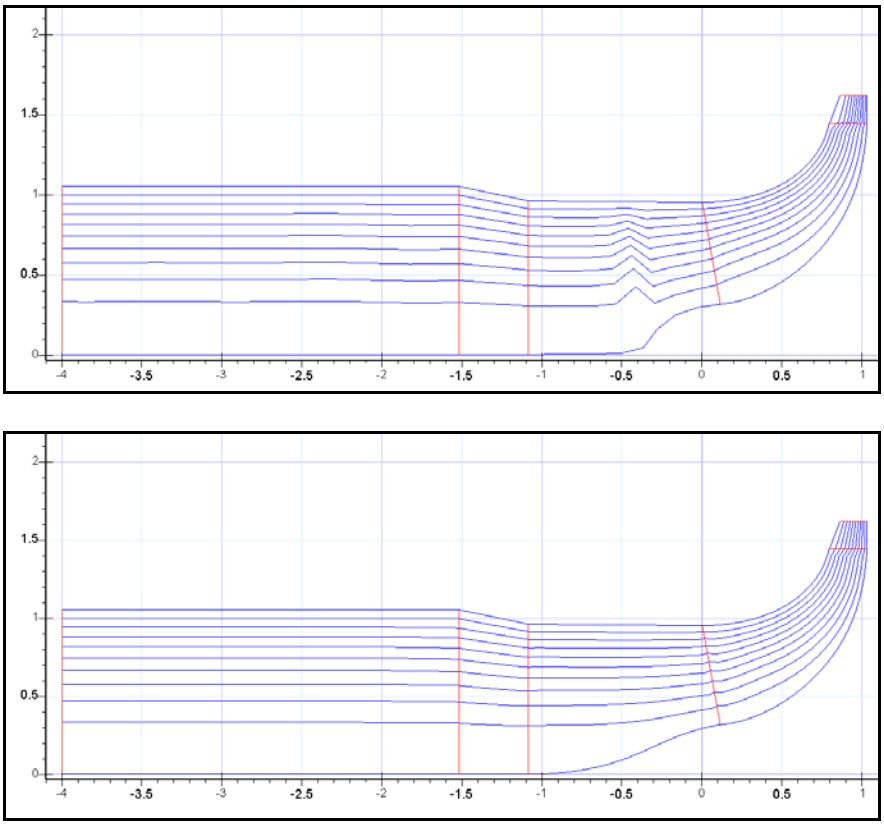

Figure 2-11 Representative streamlines determined with MST resulting from the geometry of the bullet nose used in the CFD analysis (top) and those used in the MST (bottom) calculations.

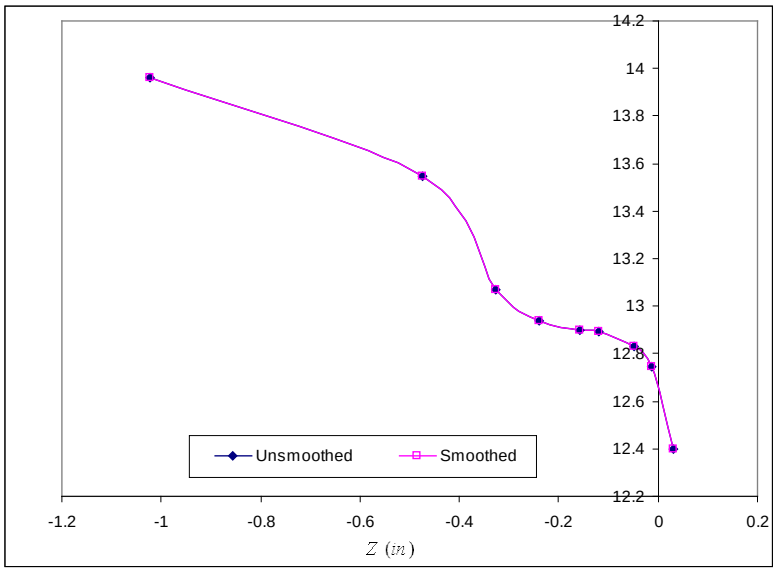

Figure 2-12 A representative streamwise profile of the static pressure along the shroud line for two bullet nose configurations.

2.5 Data Analysis

Once all calculations are complete, the flow field information of interest was extracted from the solution. A blade-to-blade average of the passage static pressure as a function of streamwise position was of particular interest. This pressure was determined at multiple locations upstream, from the inlet of the computational domain to the blade leading edge with special attention given to regions where high gradients may occur.

The spanwise position in the inlet is normalized by the inlet passage height as

$$\hat{H} = \frac{H}{R_H} \tag{2-16}$$

where H is the dimensional radius and R_H is the local inlet passage height, defined as

$$R_H = R_t - R_h \tag{2-17}$$

R_t is the local tip radius, and R_h is the local hub radius. Likewise, for each machine the streamwise position in the impeller inlet is normalized by the inlet blade height as

$$\hat{S} = \frac{S}{B_H} \tag{2-18}$$

where S is the dimensional distance from the leading edge of the blade and B_H is the impeller inlet passage height, defined as

$$B_H = R_{1t} - R_{1h} \tag{2-19}$$

At each streamwise location the pitch-averaged pressure data was recorded along the shroud ($\hat{H}$ = 1), hub ($\hat{H}$ = 0) and at $\hat{H}$ = 0.9, 0.7, 0.5 and 0.25.

2.5.1 Contour Plots

Contour plots of the pressure and velocity can be readily retrieved from the CFD solution, providing a visual assessment of the flow field. Two views are of interest; streamwise, Fig. 2-13, and spanwise, Fig. 2-14. The streamwise view slices the passage at an arbitrary streamwise location and reveals the flow variation from hub-to-shroud, and from blade-to-blade. A streamwise stepping through the passage reveals the 2-D flow conditions through the region of interest. The spanwise view looks down on the passage, providing a blade-to-blade streamwise perspective. At each spanwise location (from hub-to-shroud), the 2-D flow conditions are exposed.

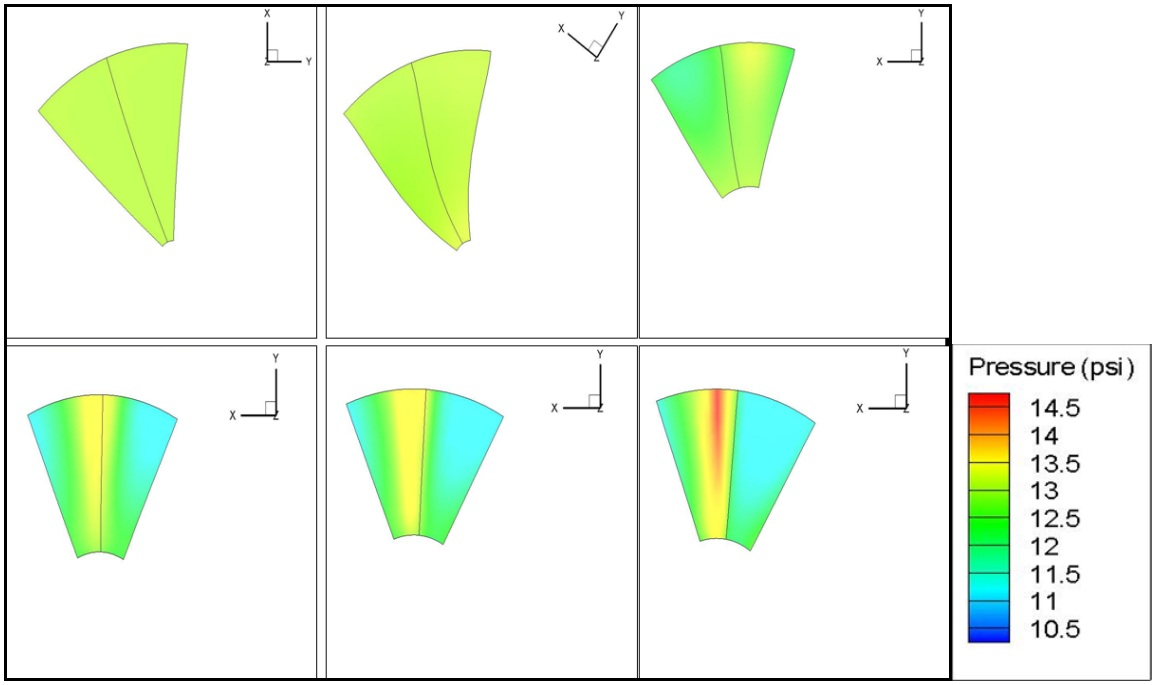

Figure 2-13 A streamwise view of contours of the static pressure in the inlet region for a representative machine. Starting in the upper left and continuing left to right, top to bottom, contours depict the local static pressure at $\hat{S}$ = -6.3, -2.75, -1, -0.5, -0.25, and -0.15.

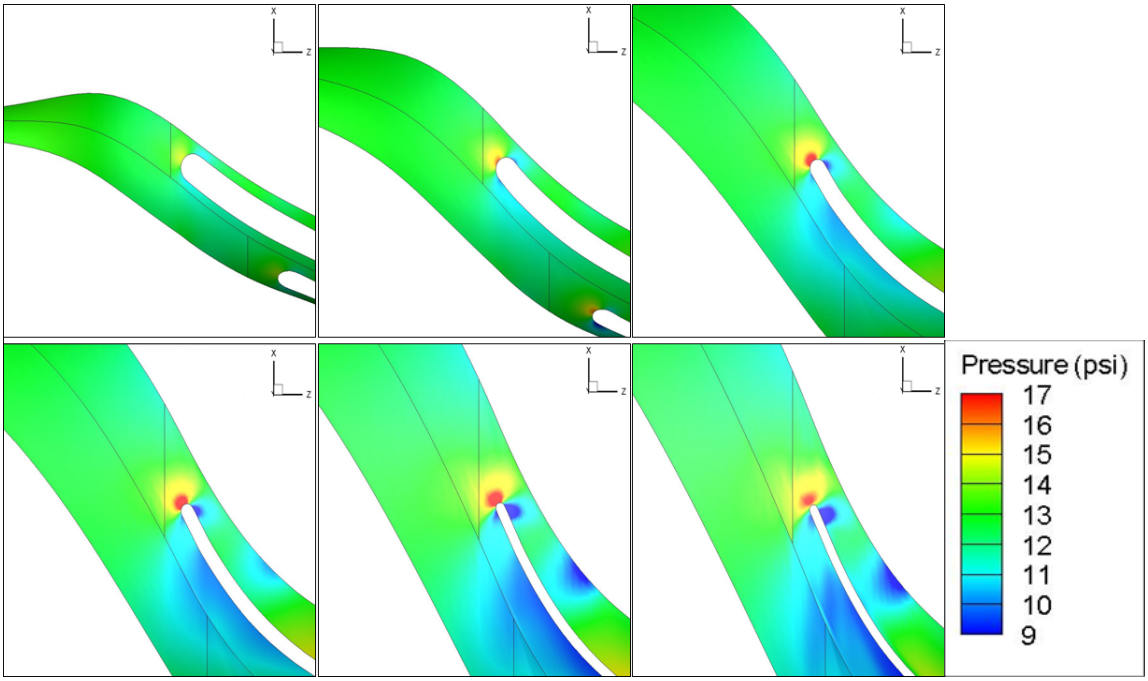

Figure 2-14 A spanwise view of contours of the static pressure in the inlet region for a representative machine. The white bars are the impeller blades. Starting in the upper left and continuing left to right, top to bottom, contours depict the local static pressure at $\hat{H}$ = 0, 0.25, 0.5, 0.7, 0.9, and 1.

2.5.2 Pressure Coefficient

In order to normalize the data, a pressure coefficient was calculated

$$C_P = \frac{P - P_{1t}}{P_0 - P_{1t}} \tag{2-20}$$

P is the pitch averaged static pressure at a given location, P_0 is the stagnation pressure at the upstream inlet, and P_{1t} is the experimentally measured static pressure at the experimental tap location. The experimental static pressure is used as the reference pressure so that a sense of how well the CFD values are comparing to the experimental values is readily apparent.

Shown in Fig. 2-15 is a representative plot of pitch averaged C_P versus $\hat{S}$ with profiles shown from $\hat{H}$ = 0 to $\hat{H}$ = 1.

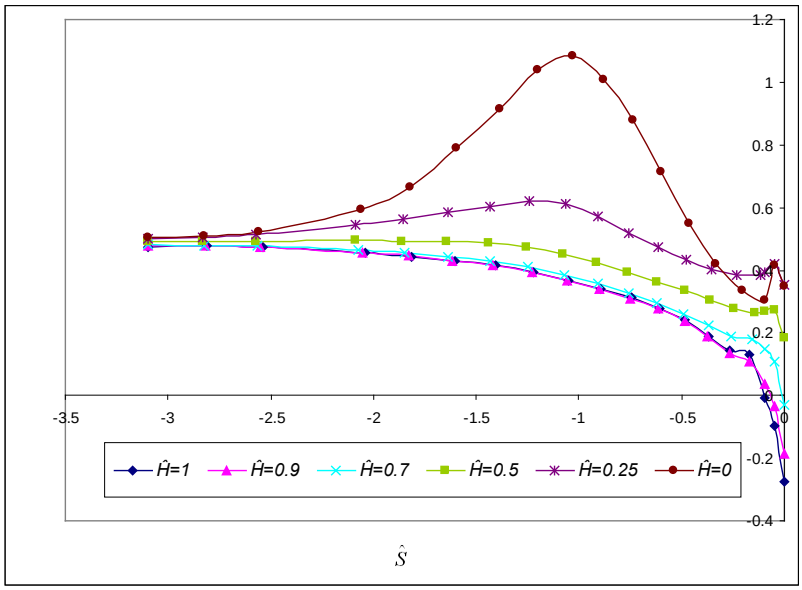

Figure 2-15 A representative Cp profile at a number of $\hat{H}$ locations.

If the predicted pressure derived from the CFD results at the tap location matches the experimental value then CP for the shroud ($\hat{H} = 1$) would equal zero at the third data point from $\hat{S} = 0$. Any deviation illustrates that the CFD analysis did not predict the static pressure at the historical tap location to be the same as the experimentally measured result.

2.5.3 1-D Isentropic Calculation

The flow at any position can be modeled as isentropic, meaning inviscid without any losses. Appropriate comparison with results from the CFD calculation can then provide the amount of deviation from the ideal state. For all scenarios the upstream total pressure, temperature, and mass flow rate (P_0, T_0, and $\dot{m}$) are known and specified in the

CFD and MST analysis. The fundamental definition for mass flow through the passage is[18]

$$\dot{m} = \rho A \overline{V} \tag{2-21}$$

where A is the cross-sectional area, ρ is the fluid density and V is the uniform velocity. Using isentropic equations for an ideal compressible gas results in the following[18]

$$M = \frac{\dot{m}\sqrt{R * T_0}}{P_0 * A\sqrt{\gamma}\left[1 + \frac{\gamma - 1}{2} * M^2\right]^{-\left[\frac{\gamma+1}{2(\gamma-1)}\right]}} \tag{2-22}$$

where M is the Mach number, R is the specific gas constant, A is the local passage area, and γ is the ratio of specific heats. Starting at the computational domain inlet, and progressing through to the impeller leading edge, the Mach number can be computed by iteration for a specified passage area. Subsequently the local static pressure, P_I can be determined from the equation below

$$P_I = P_0\left(1 + \frac{\gamma - 1}{2} M^2\right)^{\frac{\gamma}{\gamma-1}} \tag{2-23}$$

and the pressure coefficient, C_P, can then be determined.

2.5.4 CFD Passage Mass Averaged Pressure

The mass averaged static pressure at each streamwise location represents the average pressure state in the flow passing through the inlet region. This pressure can be computed in the classical manner as[7]

$$P_M = \frac{\int_A P \rho u dA}{\int_A \rho u dA} \tag{2-24}$$

where P is the local static pressure and ρ and u are the local density and velocity, respectively. Figure 2-16 depicts the variation in C_P with $\hat{S}$ for C_P values derived from CFD, the 1-D isentropic assumption, and the mass averaged pressure for a representative machine. The CFD values correspond to the shroud line ($\hat{H} = 1$), and while the isentropic and mass average calculations account from entire area flow, the CFD values are provided for a reference to the entire C_P vs. $\hat{S}$ profile derived from CFD.

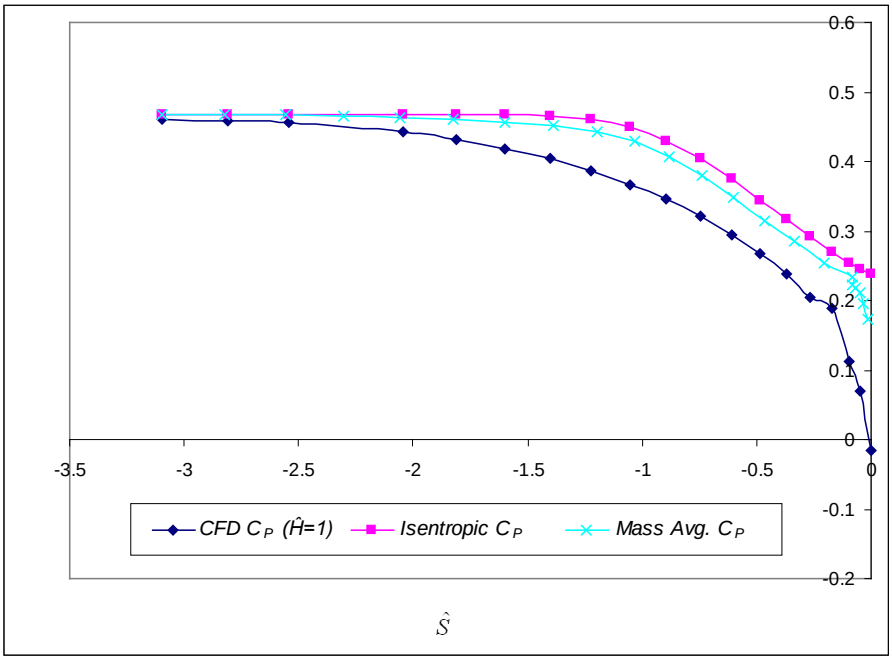

Figure 2-16 A comparison of representative C_P streamwise distributions derived from 1) CFD at $\hat{H}$= 1, 2) the isentropic assumption, and 3) the mass averaged value derived from CFD.

With increasing streamwise position, $\hat{S}$, the mass averaged C_P deviates increasingly from the 1-D isentropic calculation. The deviation is nonexistent at the beginning of the computational domain, but grows continuously as the flow traverses streamwise toward the impeller leading edge. Because losses are inherent, P_M will deviate from P_I and a direct comparison between the two reveals a measure of the

irreversible loss. Similar figures are provided for each machine considered, allowing for a qualitative investigation into the non-isentropic behavior of varying inlet geometries.

2.5.5 CFD Sensitivity Study

The computational domain ignores some portion of the actual experimental setup upstream, in order to save computation time and avoid computational challenges. One concern with excluding upstream domain from the computational domain is that this would also impact the boundary layer which may have physically developed on the shroud surface. For all cases a uniform velocity profile was initialized at the inlet of the computational domain, with the understanding that the effects would be minimal. To ensure that neglecting the boundary layer as an initial condition exerts minimal influence on the dynamics near the blade leading edge, a velocity distribution based on a turbulent boundary layer was specified at the inlet. The turbulent boundary layer assumes a classical 1/7 power law[19] and was specified based on the assumption that some aerodynamic blockage, or boundary layer displacement thickness (δ^*) exists. Two values of inlet blockage were explored as part of a sensitivity study. These values were 1% and 5% blockage. The study was conducted on all machines, and a negligible difference in the shroud and hub static pressures was observed for both assumed blockage values. Figure 2-17 depicts the overlay of the C_P profiles for the uniform profile and initialized boundary layers along the shroud (top) and hub (bottom) of a representative machine. For this representative case the deviation between tests is less than 1%, and for all cases is no more than 3%.

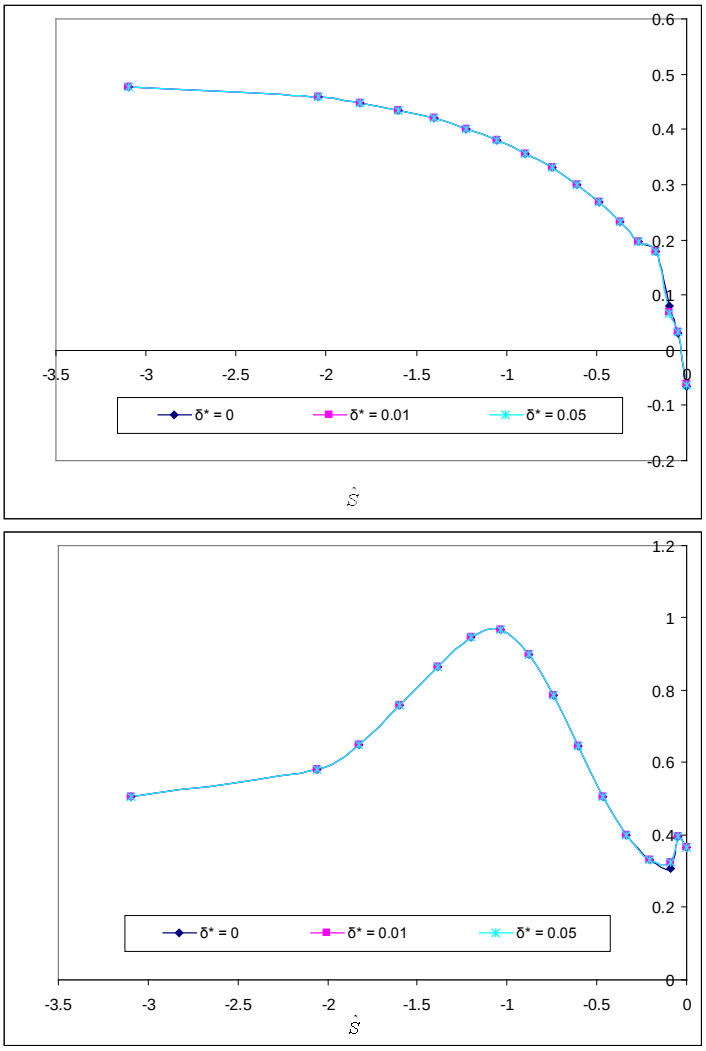

Figure 2-17 Overlay of representative C_P vs. $\hat{S}$ behavior for the assumed uniform inlet velocity profile and initialized boundary layer profiles with δ* = 0.01 and 0.05. The top panel shows the shroud ($\hat{H}$=1) and the bottom panel shows the hub line ($\hat{H}$=0).

2.5.6 Uncertainty Analysis

The greatest source of uncertainty in the C_P value comes from the experimental uncertainty of the P_{1t} measurement. Researchers who directed the experimental program have specified the maximum uncertainty is on the order of ±0.05 psi[20]. To calculate the subsequent uncertainty in the C_P calculation, reconsider the definition of C_P. Using standard error analysis, the uncertainty in C_P is defined as

$$U_{C_P} = \sqrt{\left(\frac{\partial C_P}{\partial P_{1t}}\right)^2 U_{P_{1t}}{}^2} = \left(\frac{\partial C_P}{\partial P_{1t}}\right) U_{P_{1t}} \qquad \textbf{(2-25)}$$

where U_{P1t} is ±0.05 psi. After some manipulation U_{Cp} may be expressed as

$$U_{C_P} = \left[\frac{P - P_{1t}}{\left(P_0 - P_{1t}\right)^2} - \frac{1}{P_0 - P_{1t}}\right] U_{P_{1t}} \qquad \textbf{(2-26)}$$

P is the local value of the static pressure derived from the CFD solution and P_0 is the specified upstream stagnation pressure. Figure 2-18 depicts C_P along the hub and shroud lines for a representative machine with error bars included denoting the uncertainty. U_{Cp} for this case is on the order of 0.02. All other machines exhibit comparable results.

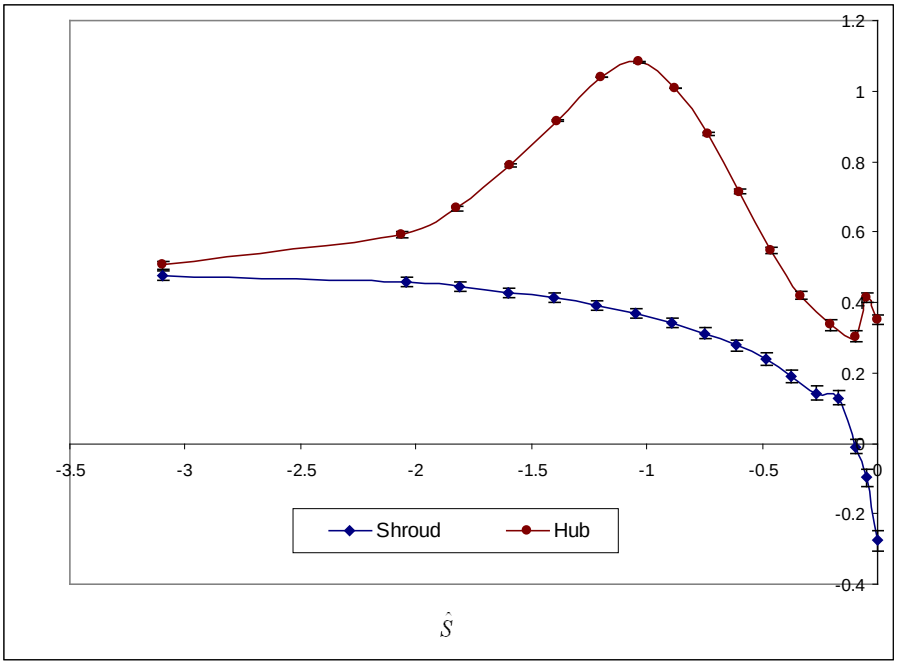

Figure 2-18 Representative variation of C_P with $\hat{S}$ along the hub and shroud lines with uncertainty bars shown denoting the overall uncertainty.

3 Results

3.1 Detailed Results of a Representative Machine

A representative machine has been selected, for which detailed information is provided. Subsequently the rest of the machines are represented, but in less detail. Significant details not presented in the text will be provided in Appendix A.

The representative machine is Centrifugal Compressor Number 30 (CCN30). Table 3-1 provides some general information about this machine.

Table 3-1 General information for CCN30.

R1 tip (in)	R1 hub (in)	R2 (in)	N (rpm)	operating mflow (lbm/s)	P_0 (psi)	T_0 (deg R)	Grid Density (hs x bb x sw)	File Name
0.95	0.31	1.35	120k	0.51	13.88	545.7	21 x 17 x 113	CCN30-2.des

CCN30 is a small compressor stage with an impeller exit diameter of only 2.7 inches, and the mass flow through the machine is relatively small at nominally 0.51 lbm/s. The grid density denotes the number of nodes in the spanwise (hub-shroud) x pitchwise (blade-blade) x streamwise (inlet-exit) directions.

Figure 3-1 is a 1-dimensional depiction of CCN30. Identification of the computational domain is provided. As a general rule for each machine considered, the computational domain extends at least three blade heights upstream and continues until

the end of a small vaneless diffuser after the impeller exit. Figure 3-2 provides a 3-D image of the inlet and impeller of CCN30.

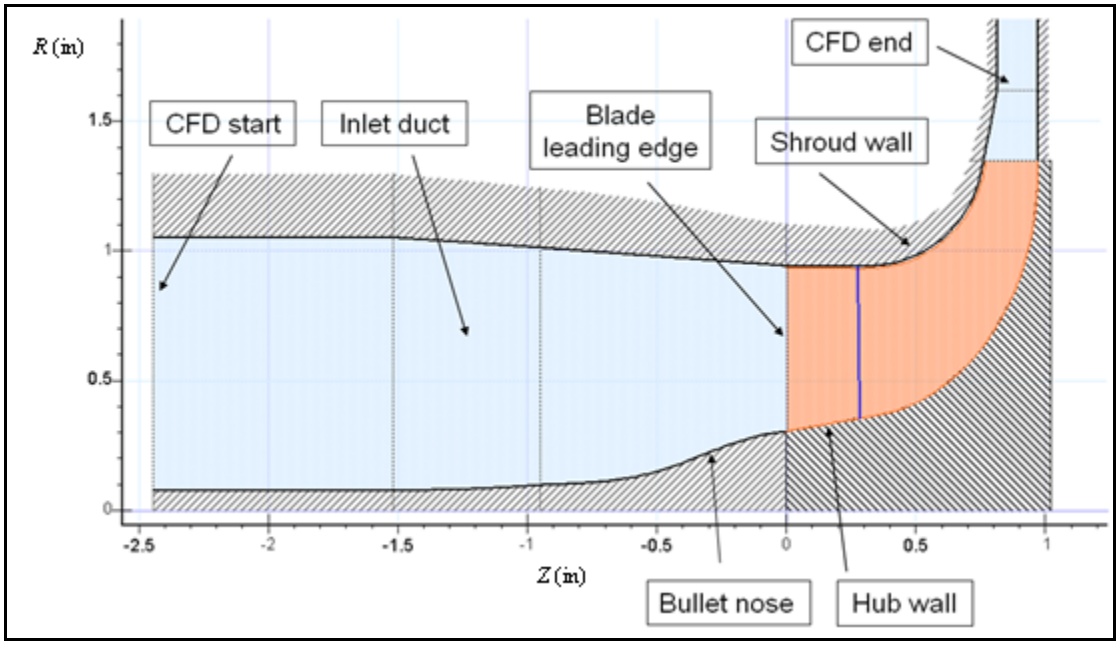

Figure 3-1 1-D representation of CCN30.

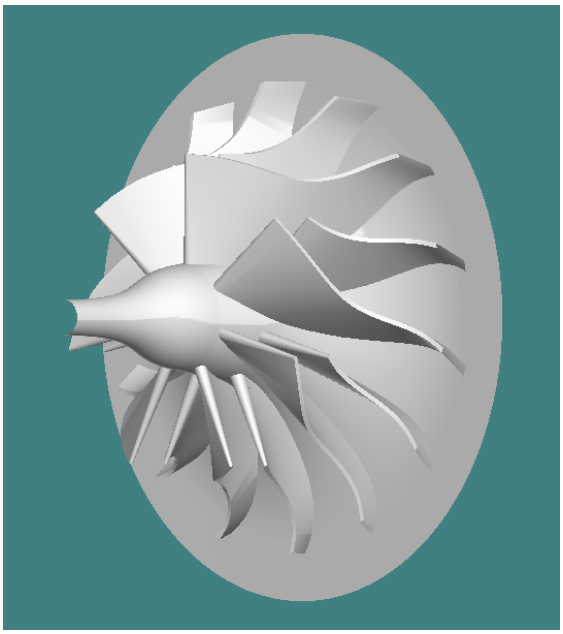

Figure 3-2 3-D illustration of the CCN30 impeller.

Figure 3-3 details experimental data as a function of mass flow through the machine. The impeller rotation rate was 120,000 rpm and all data was collected by researchers at ConceptsNREC.

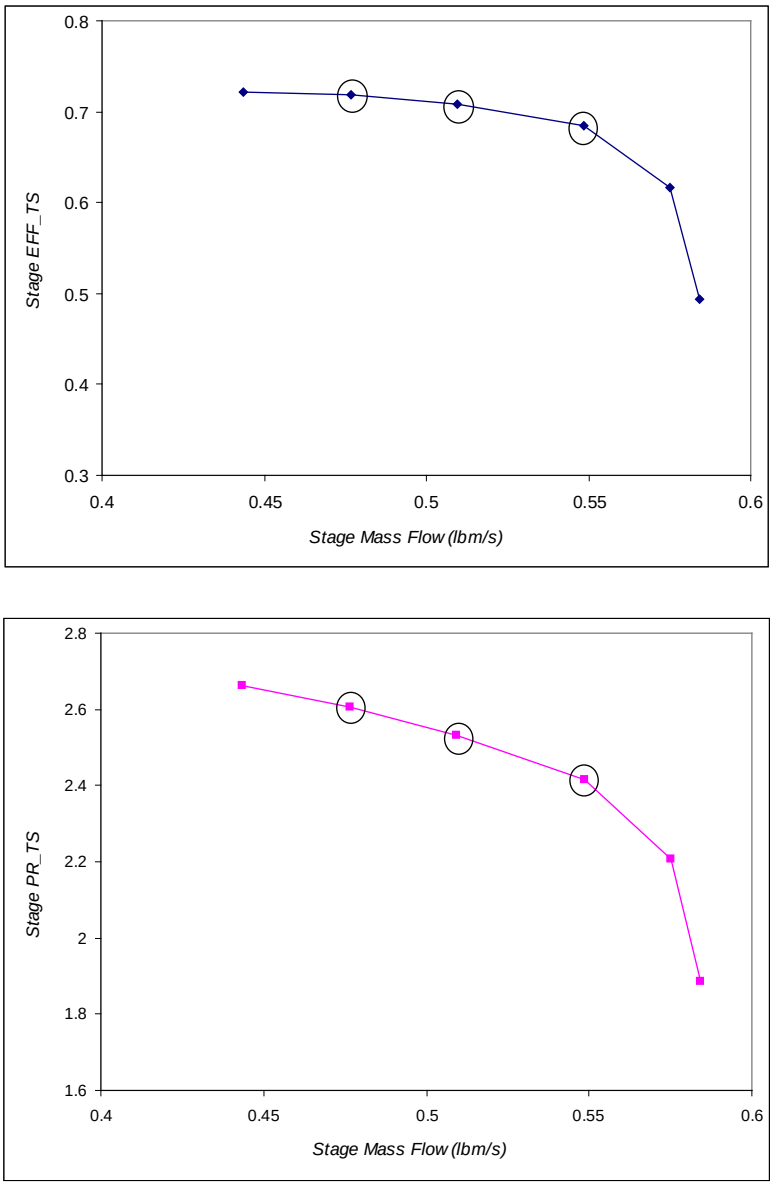

Figure 3-3 Stage total-to-static efficiency (top) and pressure ratio (bottom) maps for CCN30 operating at 120k rpm.

Shown in the top panel is the total-to-static stage efficiency (*EFF_TS*) map for this speedline and the bottom panel shows the total-to-static stage pressure ratio (*PR_TS*). *EFF_TS* and *PR_TS* are defined as[7]

$$EFF\_TS = \frac{\left(\frac{P_{ex}}{P_{0in}}\right)^{\frac{\gamma-1}{\gamma}} - 1}{\left(\frac{T_{0ex}}{T_{0in}}\right) - 1} \qquad \textbf{(3- 1)}$$

$$PR\_TS = \frac{P_{ex}}{P_{0in}} \qquad \textbf{(3- 2)}$$

where γ is the specific heat ratio, P_{ex} is the static pressure at the stage exit, P_{0in} is the total pressure at the stage inlet and T_{0ex} and T_{0in} are the total temperatures at the stage exit and inlet, respectively. The circles on each image represent the mass flows at which the CFD and MST analysis were run, matching the experimental operating conditions. At low mass flow the stage efficiency flattens out as stall approaches and at large mass flow it drops in the classical manner as choke is approached.

Figure 3-4 plots the pressure coefficient, C_P (defined in Equation 2-1), derived from the CFD simulations versus the nondimensional upstream distance, $\hat{S}$ (defined in Equation 2-2). These results correspond to a mass flow rate of 0.51 lbm/s, and from the experiment correspond to the middle circled point in Fig. 3-3. Again the C_P values represent a blade-to-blade average (pitch-average) and profiles of C_P vs. $\hat{S}$ are shown for six spanwise locations running from the shroud to the hub. A small peak is evident along the shroud ($\hat{H}$ = 1) at about 2.5 blade heights upstream ($\hat{S} \approx$ -2.5) and along the hub ($\hat{H}$ = 0) at about 0.75 blade heights upstream of the impeller leading edge ($\hat{S} \approx$ -0.75). This is a result of the shroud area contraction and the bulletnose on the hub momentarily slowing

down the flow. However, the area contraction along the length of the inlet passage causes the flow to accelerate, resulting in an increasing gradient as the flow approaches $\hat{S}$ = 0.

With regard to the appropriateness of the historical pressure tap location, Fig. 3-4 reveals the tap location to be in a region of high gradient. The steep gradient is the result of rapid acceleration into the impeller inlet due to the inlet passage area contraction and the entrainment of the flow resulting from the high speed impeller rotation. In addition, large spanwise variation exists, with a shroud C_P value of about 0.18 and a hub C_P value of about 0.35. In the near vicinity of the tap location the variation is more extreme, with a C_P difference on the order of 0.3. However, a region of near zero gradient is observed well upstream of the impeller leading edge, beginning at about 3 blade heights upstream ($\hat{S} \approx$ -3) and continuing upstream to the beginning of the computational domain. Further, the region of near zero gradient has a near uniform spanwise profile, wherein all 6 spanwise ($\hat{H}$) lines in essence collapse to a single value. This region would appear to be a more stable location for the TEIS model formulation.

CFD simulations at three mass flow rates were performed on the lone speedline and each yielded results similar to those shown in Fig. 3-4. To illustrate the similarity, Fig. 3-5 presents the C_P profile at the shroud ($\hat{H}$ = 1) for each mass flow rate considered and Fig. 3-6 presents the C_P profiles along the hub ($\hat{H}$ = 0).

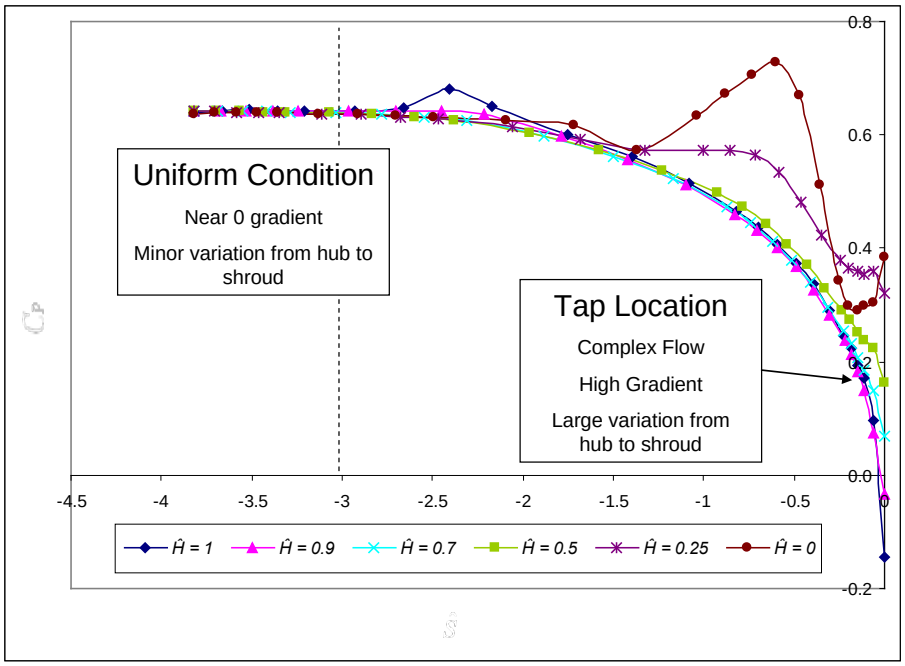

Figure 3-4 Blade-to-blade average C_P as a function of $\hat{S}$ for CCN30 at $\dot{m}$ = 0.51 lbm/s and N = 120k rpm for $\hat{H}$ = 0, 0.25, 0.5, 0.7, 0.9 and 1.

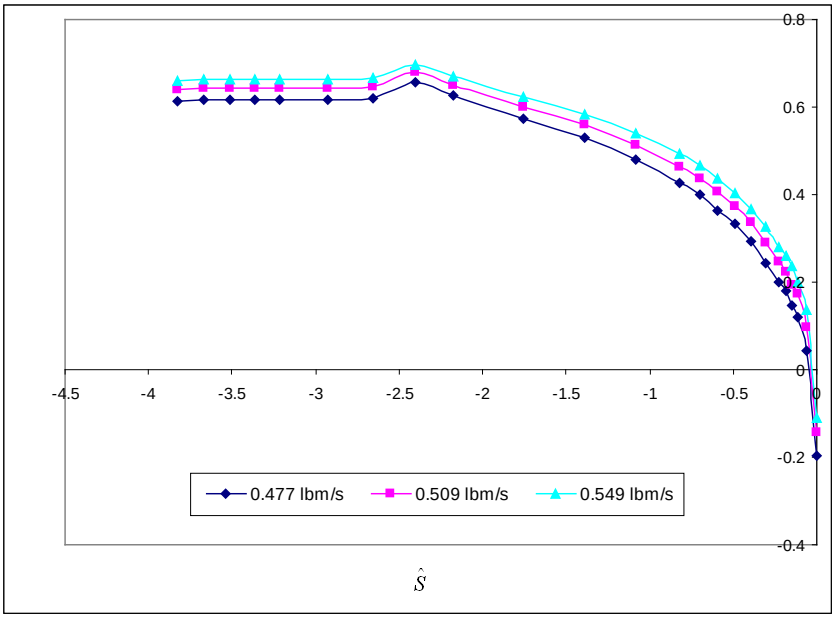

Figure 3-5 Blade-to-blade average C_P as a function of $\hat{S}$ along the shroud ($\hat{H}$ = 1) at all mass flow rates considered and N = 120k rpm for CCN30.

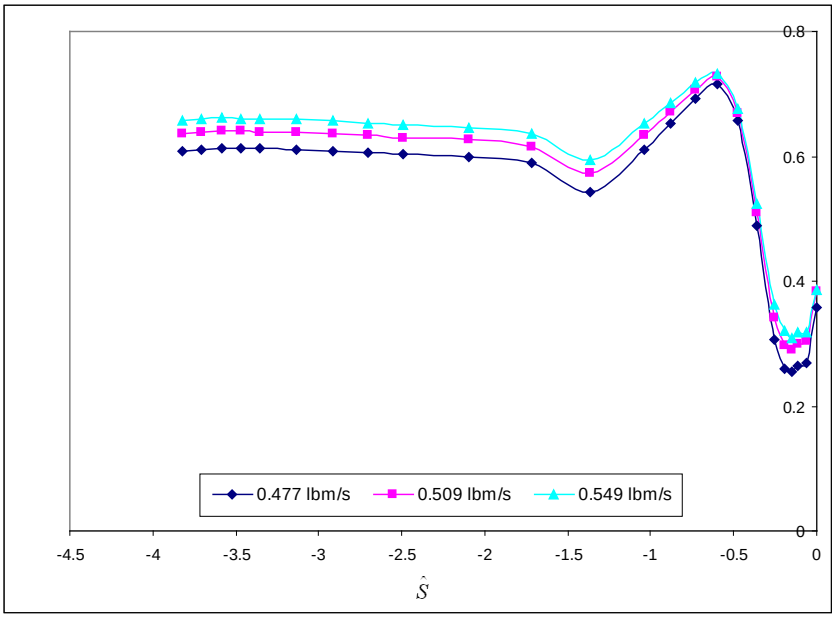

Figure 3-6 Blade-to-blade average C_P as a function of $\hat{S}$ along the hub ($\hat{H}$ = 0) at all mass flow rates considered and N = 120k rpm for CCN30.

Figure 3-7 demonstrates that the variation in C_P observed in Fig. 3-5 is primarily due to the chosen reference pressure. By changing the reference pressure to the CFD value of the impeller leading edge tip pressure, P_{1tc}, the variation with mass flow rate becomes quite small. Similar analysis at the other spanwise locations yields similar results, where the C_P vs. $\hat{S}$ distribution is nominally the same at a fixed $\hat{H}$ location for all flow rates explored.

Other useful information derived from results of the CFD simulations include full field contour plots of the static pressure and velocity magnitude near the leading edge of the impeller. Much of the inlet passage upstream of the leading edge features a fairly uniform spanwise pressure distribution. It is near the impeller leading edge that large gradients are present and where historical measurements of a static pressure have been made. Thus, attention is given to this region.

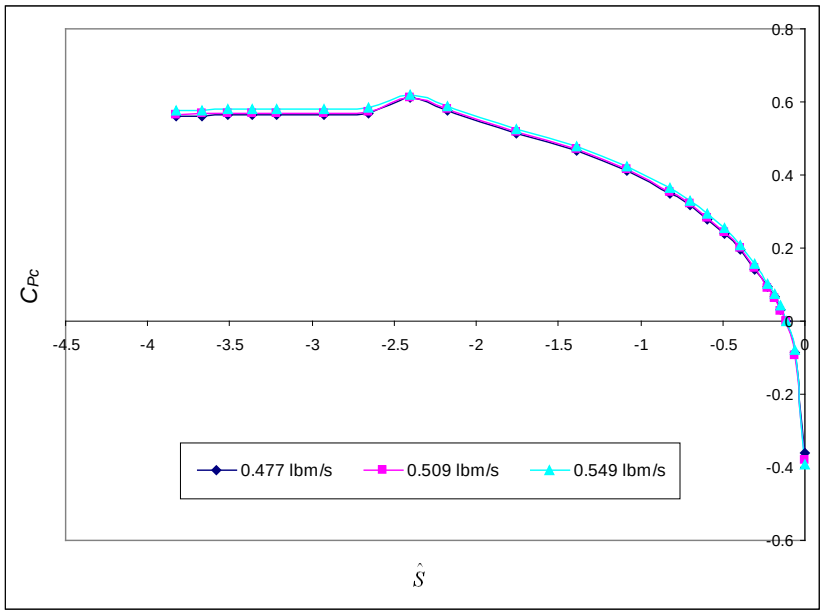

Figure 3-7 Blade-to-blade average C_{Pc} as a function of $\hat{S}$ along the shroud ($\hat{H}$ = 1) at all mass flow rates considered and N = 120k rpm for CCN30.

Figure 3-8 shows the static pressure in the inlet region and near the impeller leading edge for CCN30 at the operating mass flow rate of 0.51 lbm/s. Each panel shows a 2-D image of the static pressure field extending over the entire passage. Contour maps are shown at the hub ($\hat{H}$ = 0), $\hat{H}$ = 0.25, $\hat{H}$ = 0.5, $\hat{H}$ = 0.7, $\hat{H}$ = 0.9 and shroud ($\hat{H}$ = 1). The flow direction is from left to right and the white bars in the center of each image space are the impeller blades. The edges (top and bottom) of each colored space denote the ending of one bladed passage. A number of these identical passages wrap around the impeller resulting in a circumferentially uniform flow. Likewise, Fig. 3-9 illustrates 2-D contour maps of the velocity magnitude following the same format.

Figure 3-10 provides a streamwise viewpoint of the variation in static pressure at discrete slices moving into the passage. These results correspond to the same mass flow rate and wheel speed as the data of Fig. 3-8 and Fig. 3-9. The image slices yield 2-D contours extending from blade-to-blade (left-to-right) and hub-to-shroud (bottom-to-top).

The consecutive images step through the inlet passage, starting at the beginning of the computational domain and ending near the impeller leading edge. Figure 3-11 provides the same perspective, but depicts contours of velocity magnitude.

Figure 3-8 and Fig. 3-9 provide 2-D contour images of the static pressure and velocity magnitude, moving spanwise from hub ($\hat{H}$ = 0) to shroud ($\hat{H}$ = 1). It is evident that in the near vicinity of the impeller leading edge there are pitchwise variations, which is a result of the stagnation point. This causes a dramatic change in pressure and results in a high gradient in this region, making the historical experimental tap location less than ideal. In addition, downstream of the impeller leading edge the expected pressure and suction side variations are evident. However, further upstream of the leading edge the flow appears fairly simple. While the flow is decelerating as it moves upstream, the pitchwise variation is minimal and more ideal for flow measurements.

Figure 3-10 and Fig. 3-11 likewise provide 2-D contour images of the static pressure and velocity magnitude, but moving streamwise from the beginning of the inlet ($\hat{S}$ = -3.82) to the near leading edge ($\hat{S}$ = -0.05). The pressure contours visualize a stagnation point running the height of the leading edge. There appears to be a spanwise variation in the pressure and velocity at the stagnation point for the last image ($\hat{S}$ = -0.05). This is a result of the streamwise slice taken by the CFD software, which is not exactly parallel to the blade leading edge. A slight inclination on the streamwise slice exists as a result of the software attempting to adjust to the area changes along the hub and shroud. While variation is apparent at the impeller leading edge, the pressure contours indicate that the flow is uniform when well upstream, providing a more welcome location for anchoring the TEIS model.

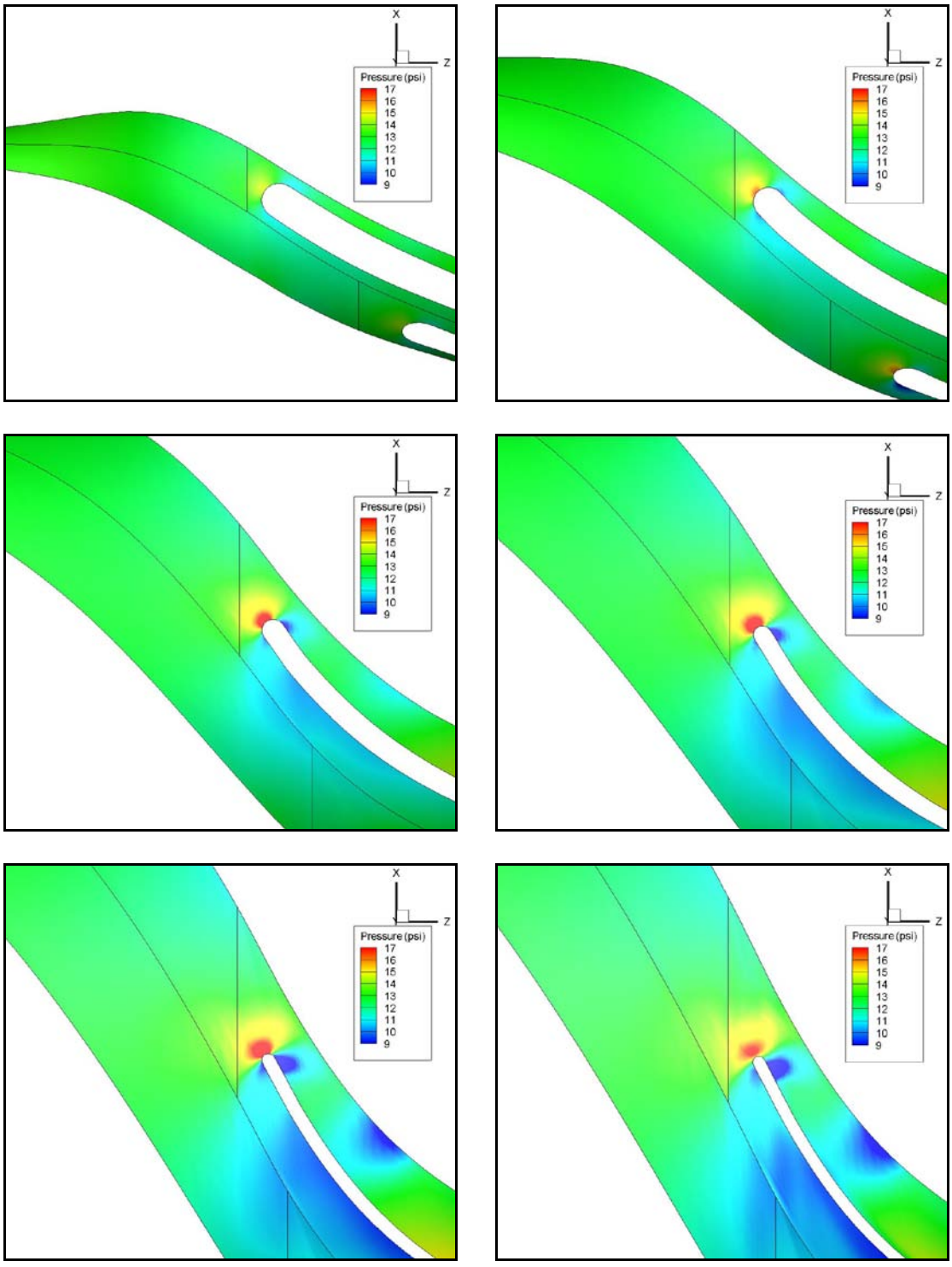

Figure 3-8 Static pressure 2-D contour plots for CCN30 at a mass flow rate of 0.51 lbm/s at six spanwise positions progressing from hub-to-shroud. The upper left panel corresponds to the hub with successive panels moving from left to right and top to bottom, in the following order: $\hat{H}$ = 0, $\hat{H}$ = 0.25, $\hat{H}$ = 0.5, $\hat{H}$ = 0.7, $\hat{H}$ = 0.9 and $\hat{H}$ = 1.

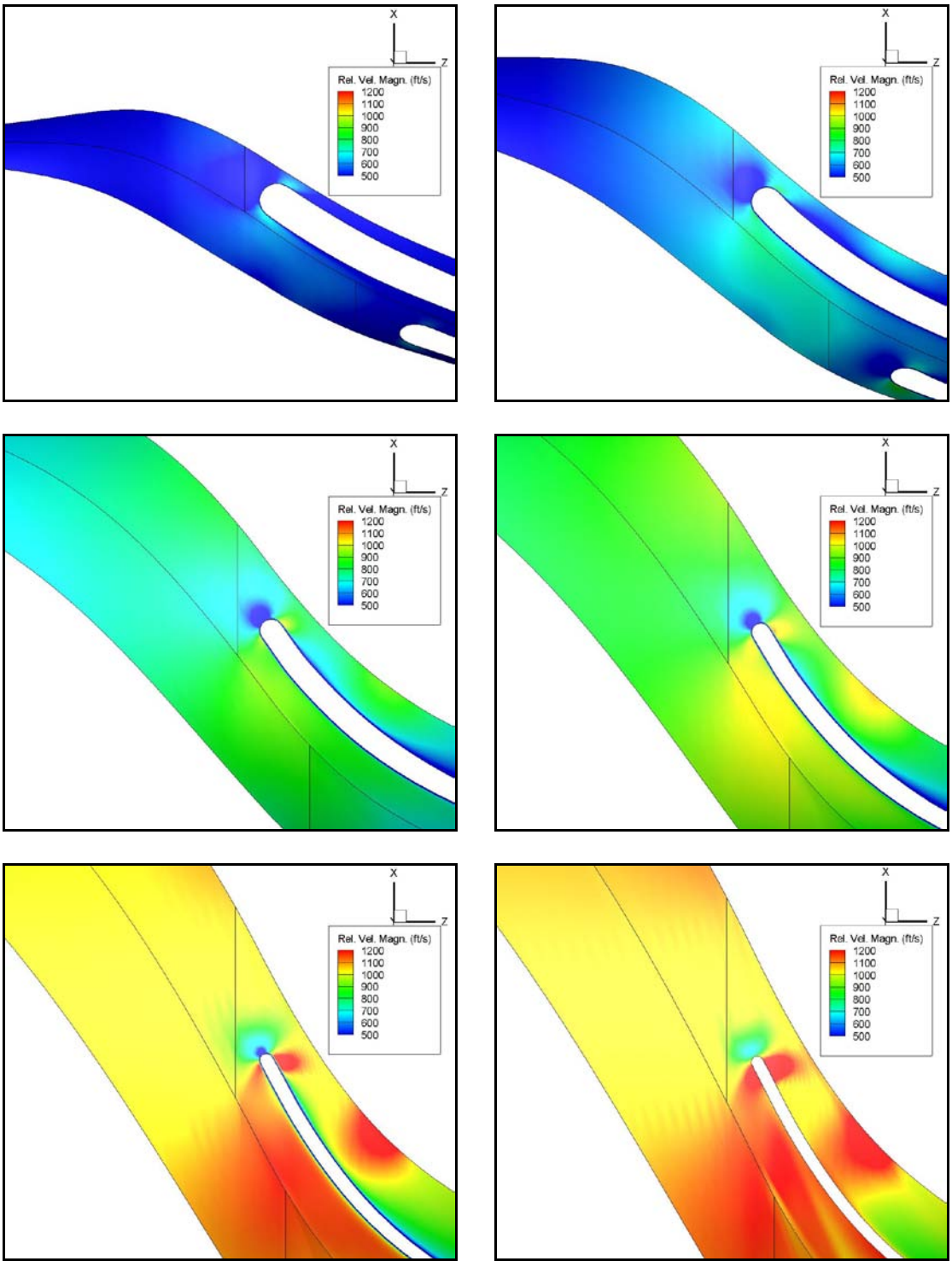

Figure 3-9 Velocity magnitude 2-D contour plots for CCN30 at a mass flow rate of 0.51 lbm/s at six spanwise positions progressing from hub-to-shroud. The upper left panel corresponds to the hub with successive panels moving from left to right and top to bottom, in the following order: $\hat{H}$ = 0, $\hat{H}$ = 0.25, $\hat{H}$ = 0.5, $\hat{H}$ = 0.7, $\hat{H}$ = 0.9 and $\hat{H}$ = 1.

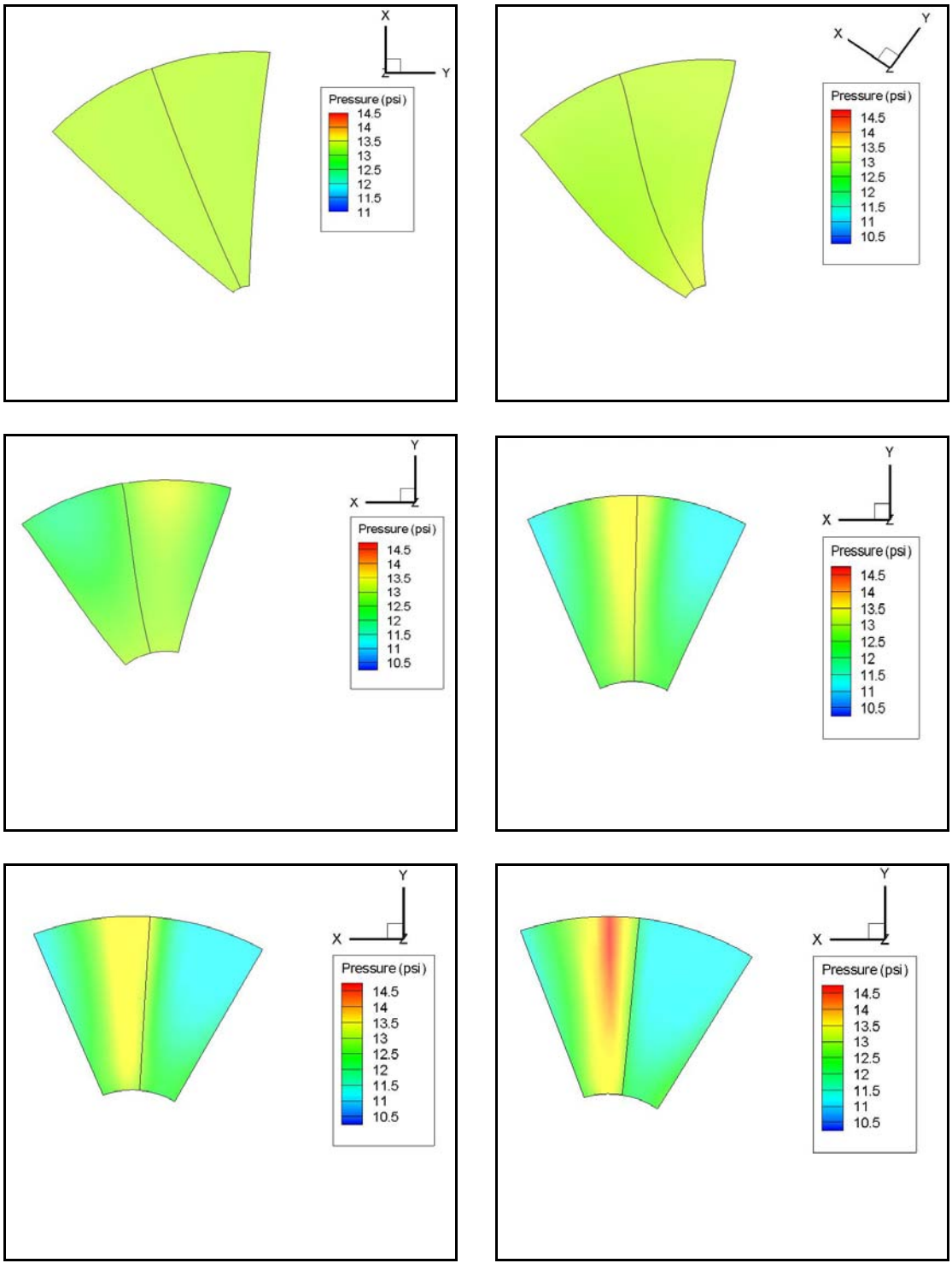

Figure 3-10 Static pressure 2-D contour plots at six streamwise locations moving from the beginning of the computational domain to the impeller leading edge. The upper left panel corresponds to $\hat{S}$ = -3.82 with successive panels moving from left to right and top to bottom, in the following order: $\hat{S}$ = -3.82, $\hat{S}$ = -1.0, $\hat{S}$ = -0.30, $\hat{S}$ = -0.15, $\hat{S}$ = -0.10, and $\hat{S}$ = -0.05.

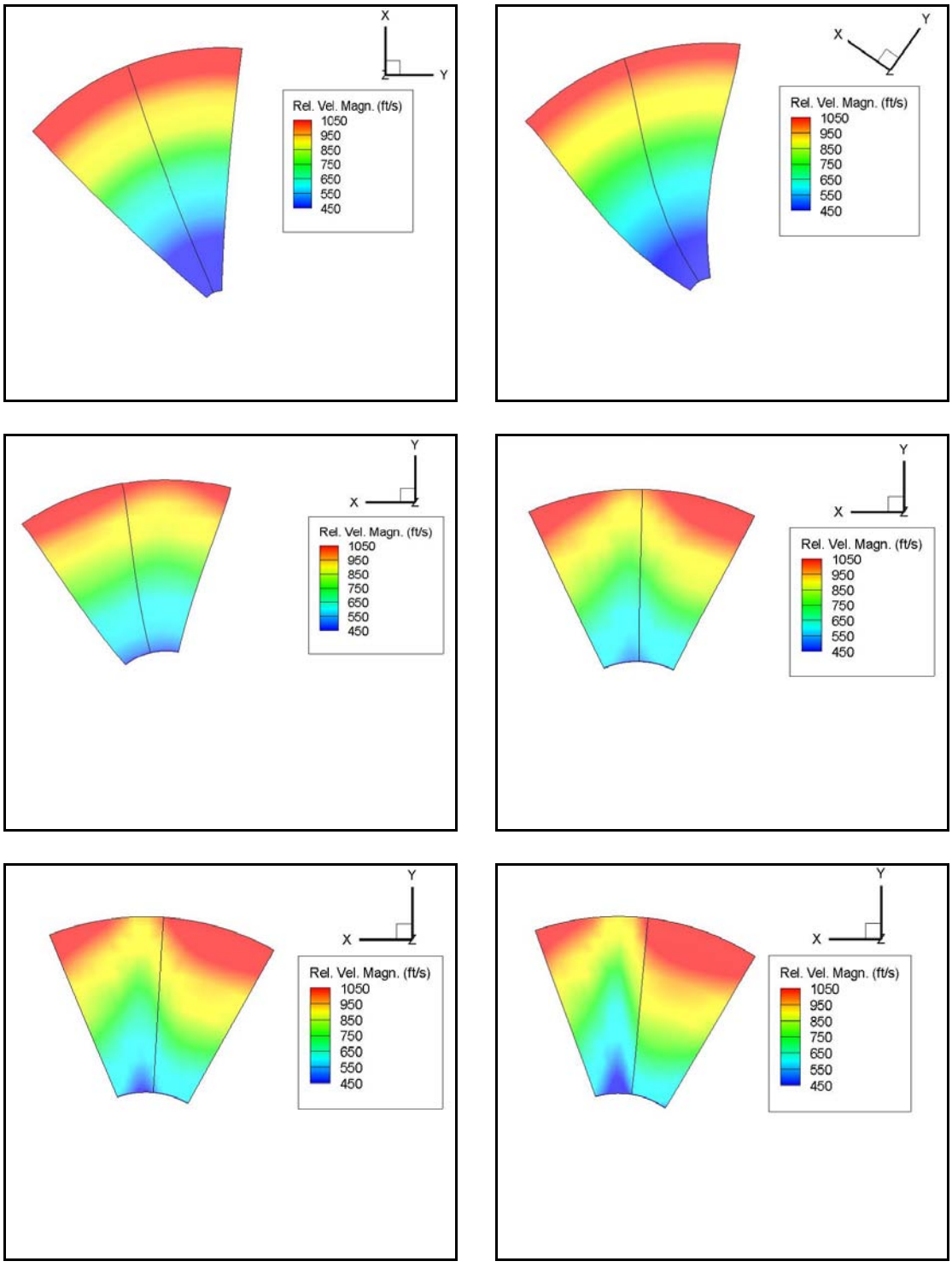

Figure 3-11 Velocity magnitude 2-D contour plots at six streamwise locations moving from the beginning of the computational domain to the impeller leading edge. The upper left panel corresponds to $\hat{S}$ = -3.82with successive panels moving from left to right and top to bottom, in the following order: $\hat{S}$ = -3.82, $\hat{S}$ = -1.0, $\hat{S}$ = -0.30, $\hat{S}$ = -0.15, $\hat{S}$ = -0.10, and $\hat{S}$ = -0.05.

3.2 Analysis of CCN30

Analysis of the CFD results lead to the conclusion that the historically placed experimental tap location is non-ideal. Researchers have historically assumed that the tap location employed would be one where inlet distortion was not significant and large streamwise gradients in the pressure field would not exist[2], and consequently would be statistically dependable for modeling purposes. However, the C_P plot, as seen in Fig. 3-4, shows that the tap location is in a region of a steep pressure gradient. The implication of this is that measurement in such a location produces a high degree of variability in measurements taken on different machines. Consequently this "noise" will propagate through any model building exercise that relies on those measurements.

If the experimental tap location is a poor choice for modeling intentions, a more suitable location would be where the streamwise gradient is much smaller, or at least well predicted. Review of the C_P vs. $\hat{S}$ behavior (Fig. 3-4) reveals a region of flow void of large gradients in C_P, starting at about three blade heights upstream of the impeller leading edge and continuing upstream to the beginning of the computational domain ($\hat{S}$ = -3, -4, -5…). In this region the velocity profile is nominally uniform with only minor change locally moving towards the impeller. This region appears to be an attractive alternative location for anchoring the TEIS modeling procedure.

To provide another analysis tool, MST was also employed for each machine and each mass flow rate. Figure 3-12 shows a comparison of results derived from MST to those from CFD for CCN30 along the shroud ($\hat{H}$ = 1), while Fig. 3-13 shows the same comparison but along the hub ($\hat{H}$ = 0). The mass flow rate was 0.51 lbm/s and the wheel speed was 120,000 rpm. Attention is focused on the shroud C_P profile since it is along

the shroud that measurements must be made and the hub profile is presented in order to illustrate the quality of the MST analysis through the entire inlet passage. The MST analysis was run utilizing the boundary layer calculation option which requires an initialized inlet aerodynamic blockage. This initial blockage value is user specified and determined by iteration until MST matches the CFD value at the beginning of the computational domain. For this scenario the inlet blockage was set at 5% ($\delta^* = 0.05$) and the boundary layer calculation determined the blockage at the exit of the inlet passage (the impeller leading edge) to be 6% ($\delta^* = 0.06$).

While there are some relatively minor oscillations in the MST profile, resulting from numerical anomalies caused by the streamwise curvature, the general behavior shows good agreement with the CFD results. Inlet and exit values are consistent between the two sets of results, as are the general slopes throughout most of the profile. The peak in the hub line from MST appearing out of phase from the CFD result is the product of the bullet nose smoothing discussed in section 2.4.4. Smoothing the bullet nose moves the effective stagnation point further upstream; hence the upstream shift in the hub profile. Similar to the CFD calculations, the MST results suggest a safe modeling location exists at about 3 blade heights upstream. The goodness of the comparison of the MST and CFD C_P results provides assurance that pertinent flow features are not being neglected.

Recall the method described in section 2.5.3 for a 1-D isentropic calculation. Figure 3-14 depicts the comparison of the C_P vs. $\hat{S}$ profiles for the CFD results at the shroud ($\hat{H} = 1$), the isentropic assumption and mass average for CCN30. Similar to the

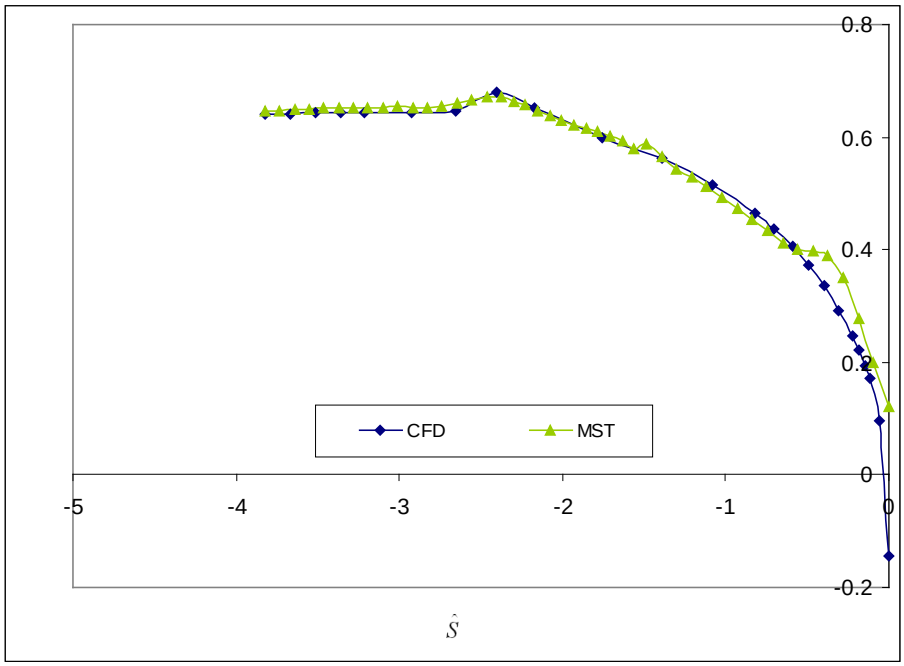

Figure 3-12 Comparison of C_P vs. $\hat{S}$ profiles derived from CFD and MST, along the shroud ($\hat{H}$ = 1), for CCN30 at a mass flow rate of 0.51 lbm/s and a wheel speed of 120k rpm.

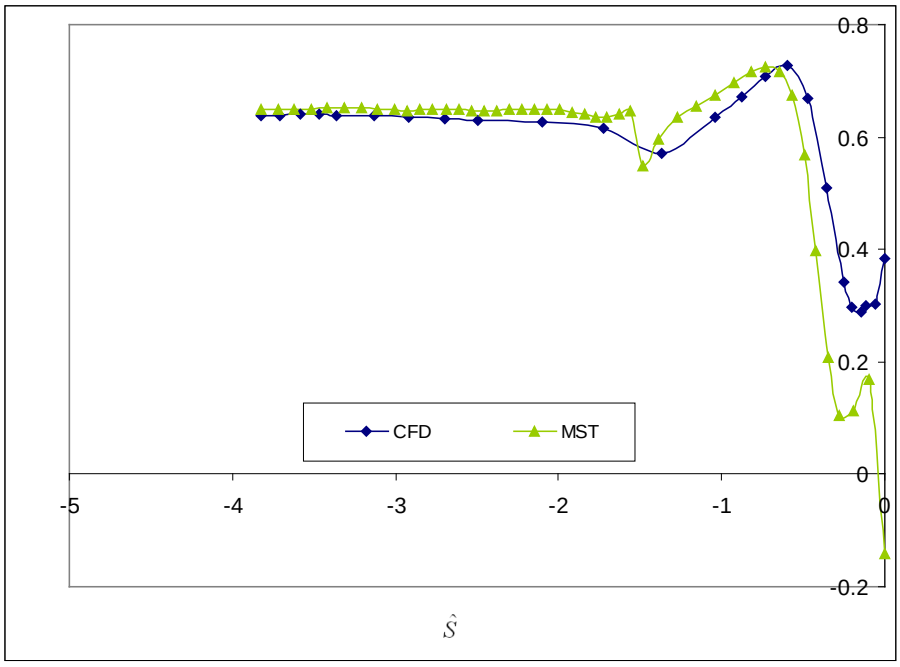

Figure 3-13 Comparison of C_P vs. $\hat{S}$ profiles derived from CFD and MST, along the hub ($\hat{H}$ = 0), for CCN30 at a mass flow rate of 0.51 lbm/s and a wheel speed of 120k rpm.

previous figures, Fig. 3-14 illustrates results for a mass flow rate of 0.51 lbm/s and a wheel speed of 120,000 rpm. The C_P derived from the mass averaged pressure deviates, as predicted, from the C_P derived from the isentropic calculation indicating that there are irreversible losses which are increasing as the flow approaches the impeller leading edge.

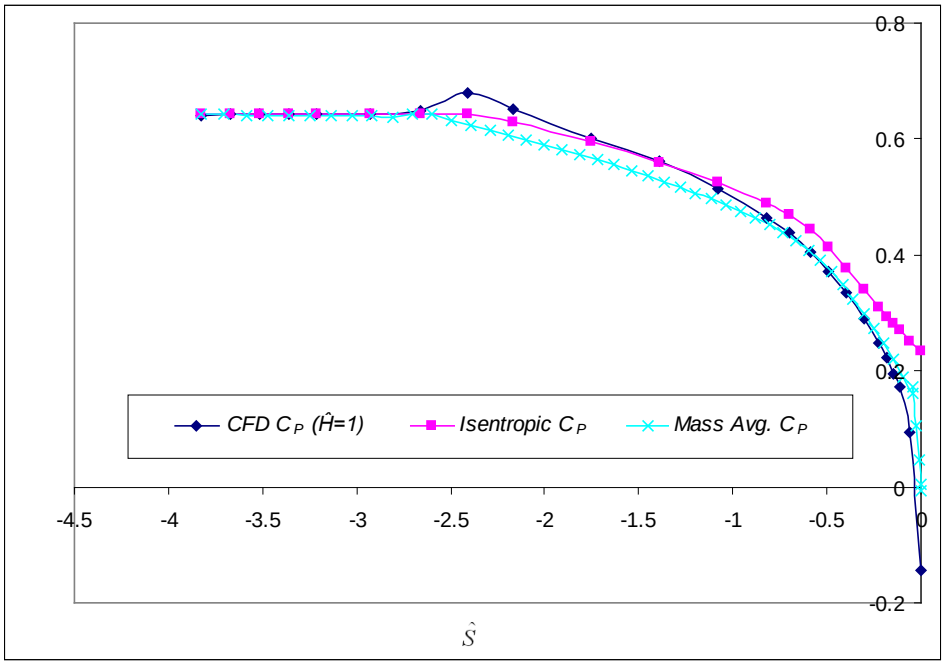

Figure 3-14 A comparison of representative C_P streamwise distributions derived from 1) CFD at $\hat{H}$= 1, 2) the isentropic assumption, and 3) the mass averaged value derived from CFD for CCN30.

3.3 Results and Analysis of the Remaining Designs

For each machine a table of general information, a 1-D representation (only the start and end of the computational domain are noted- all other features are indicated in Fig. 3-1), and pressure and efficiency maps are presented. In addition the C_P profile (to make the results easier to discern only three spanwise locations are shown: $\hat{H}$ = 0, $\hat{H}$ = 0.5, and $\hat{H}$ = 1), and a comparison of the MST and CFD results along the shroud are provided, along with the variation in C_P with $\hat{S}$ for C_P values derived from CFD, the 1-D

isentropic assumption, and the mass averaged pressure. Contour plots of the pressure and velocity will be provided in Appendix A.

3.3.1 CCN32

The CCN32 impeller is a longer and more slender than CCN30, with an exit diameter of 4.06 inches. Figure 3-15 reveals the 1-D geometry. The nominal mass flow rate is about half of CCN30, about 0.25 lbm/s, and the wheel speed is 76,000 rpm. Table 3-2 summarizes the general information for CCN32. Further, pressure and efficiency maps are found in Fig. 3-16.

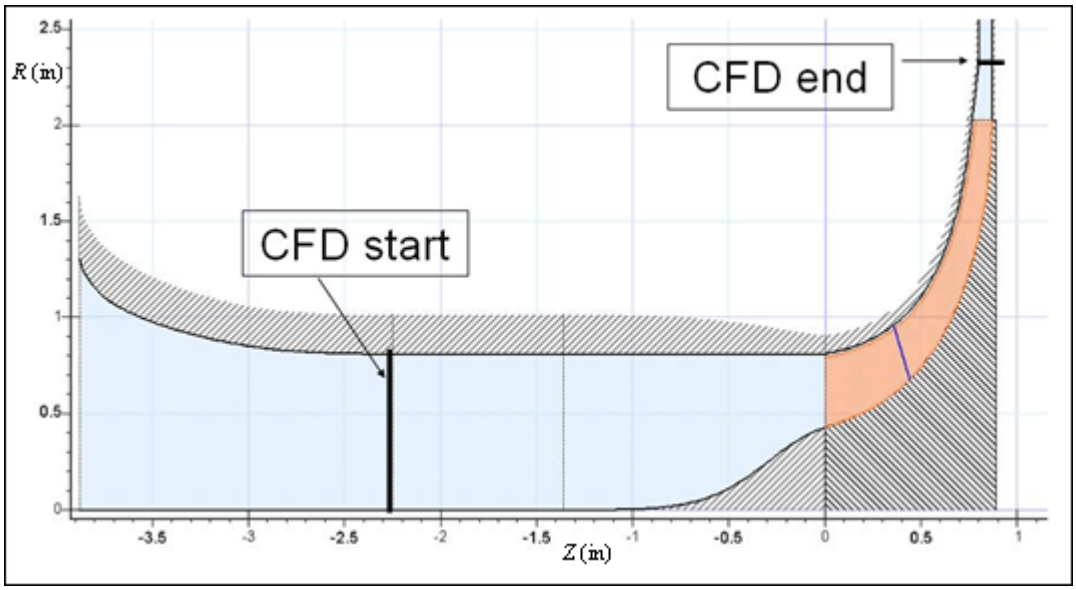

Figure 3-15 1-D representation of CCN32.

Table 3-2 General information for CCN32.

R1 tip (in)	R1 hub (in)	R2 (in)	N (rpm)	operating mflow (lbm/s)	P_0 (psi)	T_0 (deg R)	Grid Density (hs x bb x sw)	File Name
0.82	0.43	2.03	76k	0.23	14.50	555	25 x 21 x 173	CCN32-1.des

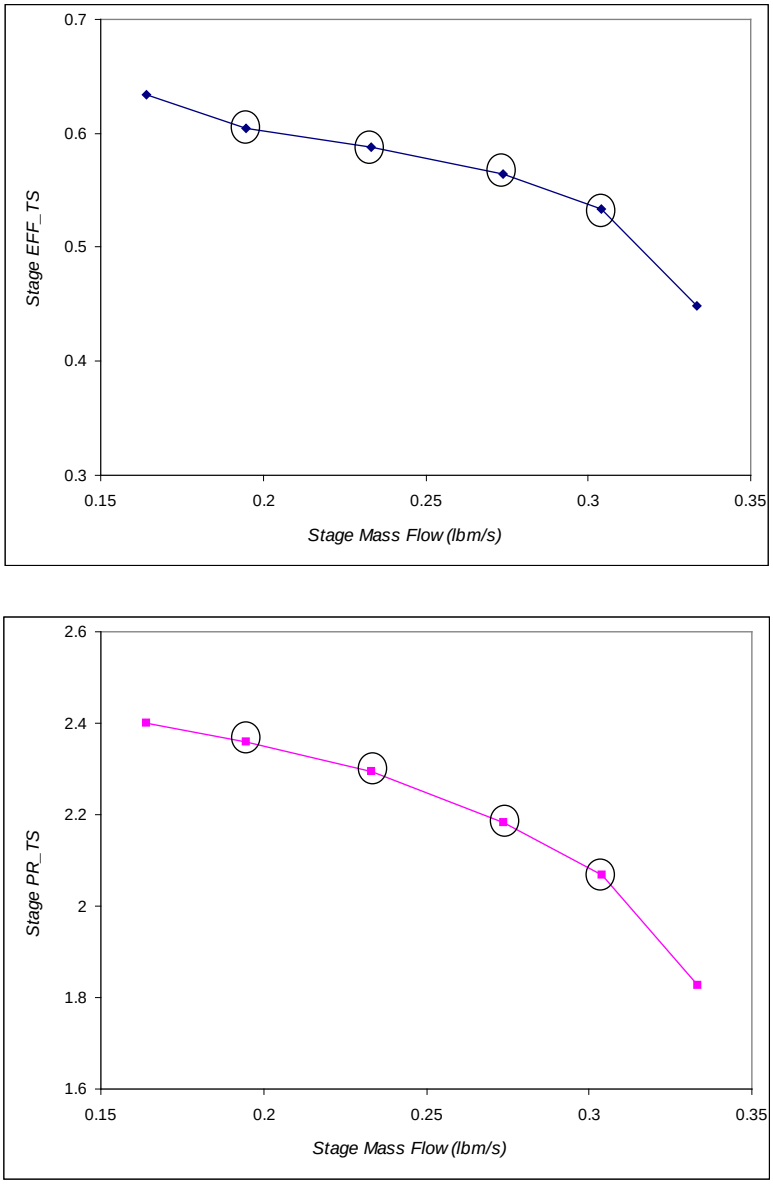

Figure 3-16 Stage total-to-static efficiency (top) and pressure ratio (bottom) maps for CCN32 operating at 76k rpm.

Figure 3-17 depicts the C_P vs. $\hat{S}$ variation for CCN32 for a mass flow rate of 0.23 lbm/s (the circled point 2nd from the left in Fig. 3-16) and a wheel speed of 76,000 rpm. The general trends observed for CCN30 are followed here; there is a high gradient in the near blade region suggesting that the historical tap location is inappropriate, and the

spanwise C_P lines converge at about 3 blade heights upstream ($\hat{S} \approx -3$). This converging location is a general trend for all straight inlet designs investigated suggesting that there is a region well upstream of the impeller leading edge where the flow is nearly uniform, making it a suitable location for the TEIS model reformation.

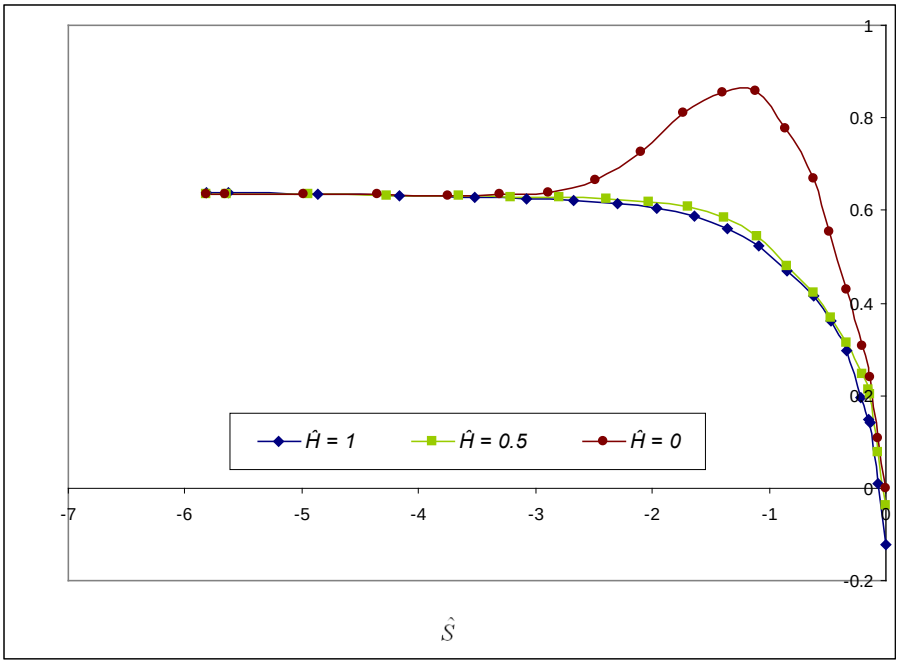

Figure 3-17 Blade-to-blade average C_P as a function of $\hat{S}$ for CCN32 at $\dot{m}$ = 0.23 lbm/s and N = 76k rpm for $\hat{H}$ = 0, 0.5 and 1.

The comparison of the C_P vs. $\hat{S}$ profiles for results derived from MST and CFD is depicted in Fig. 3-18. This comparison is also for a mass flow rate of 0.23 lbm/s and a wheel speed of 76,000 rpm. Inlet and exit values are consistent between the two sets of results, as well as the average slopes and general trend.

The comparison of the C_P vs. $\hat{S}$ profiles for the CFD results at the shroud ($\hat{H}$ = 1), the isentropic assumption and mass average for CCN32 is shown in Fig. 3-19. The relative deviation of the P_M from P_I is similar to CCN30, with irreversible losses present.

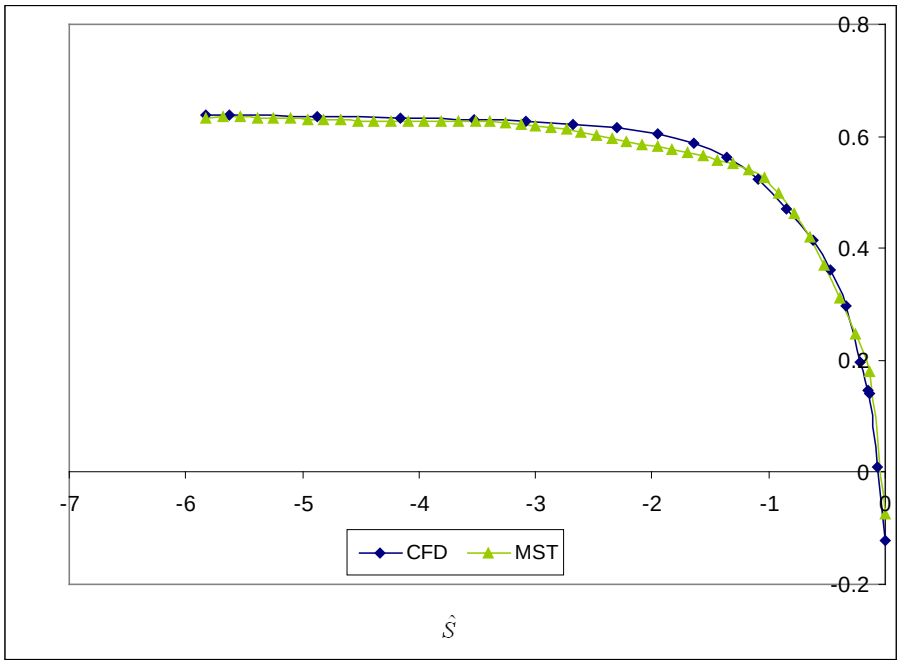

Figure 3-18 Comparison of C_P vs. $\hat{S}$ profiles derived from CFD and MST, along the shroud ($\hat{H}$ = 1), for CCN32 at a mass flow rate of 0.23 lbm/s and a wheel speed of 76k rpm.

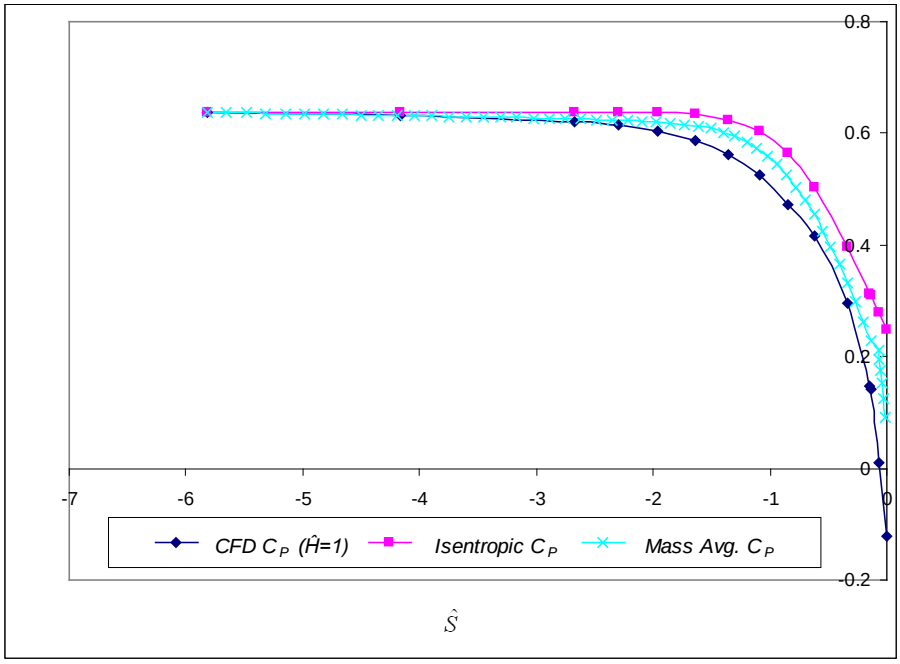

Figure 3-19 A comparison of representative C_P streamwise distributions derived from 1) CFD at $\hat{H}$= 1, 2) the isentropic assumption, and 3) the mass averaged value derived from CFD for CCN32.

3.3.2 CCN38

CCN38 has an exit diameter of 2.88 inches, operates at a wheel speed of 110,000 rpm and a mass flow rate of nominally 0.66 lbm/s. Table 3-3 lists some general information about the machine.

Table 3-3 General information for CCN38.

R1 tip (in)	R1 hub (in)	R2 (in)	N (rpm)	operating mflow (lbm/s)	P_0 (psi)	T_0 (deg R)	Grid Density (hs x bb x sw)	File Name
0.97	0.32	1.44	110k	0.66	14.69	527.4	33 x 21 x 173	CCN38-1.des

CCN38 features a different C_P profile than the previous designs, an apparent by product of the differing passage geometry, as illustrated in Fig. 3-20.

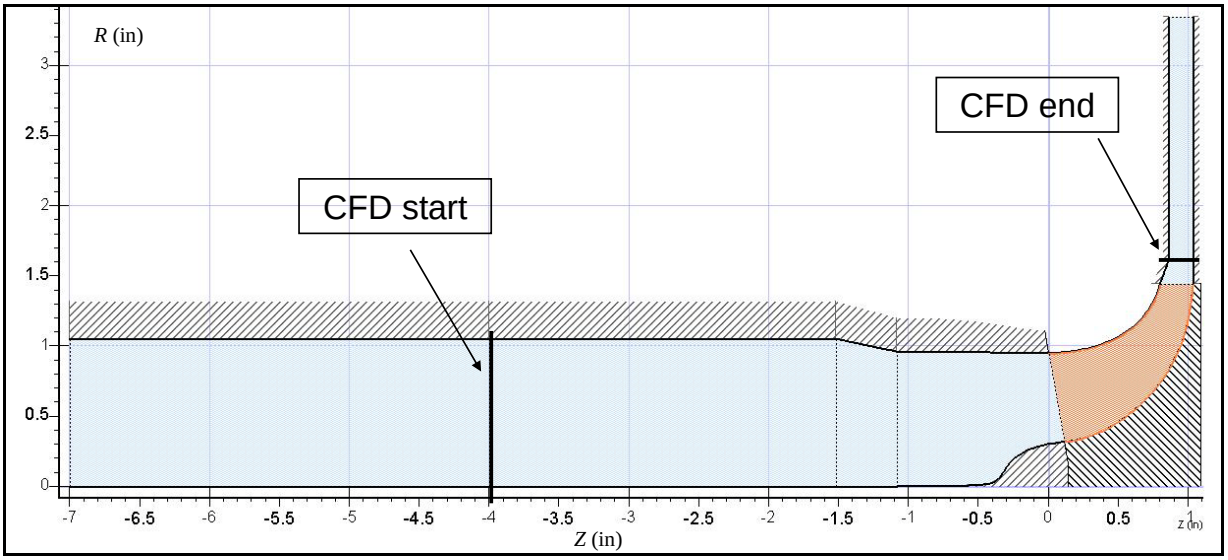

Figure 3-20 1-D representation of CCN38.

One item of note is the fluctuation in the C_P profile on the shroud line ($\hat{H} = 1$) at about 2 blade heights upstream of the impeller leading edge ($\hat{S} \approx -2$), as seen in Fig. 3-21.

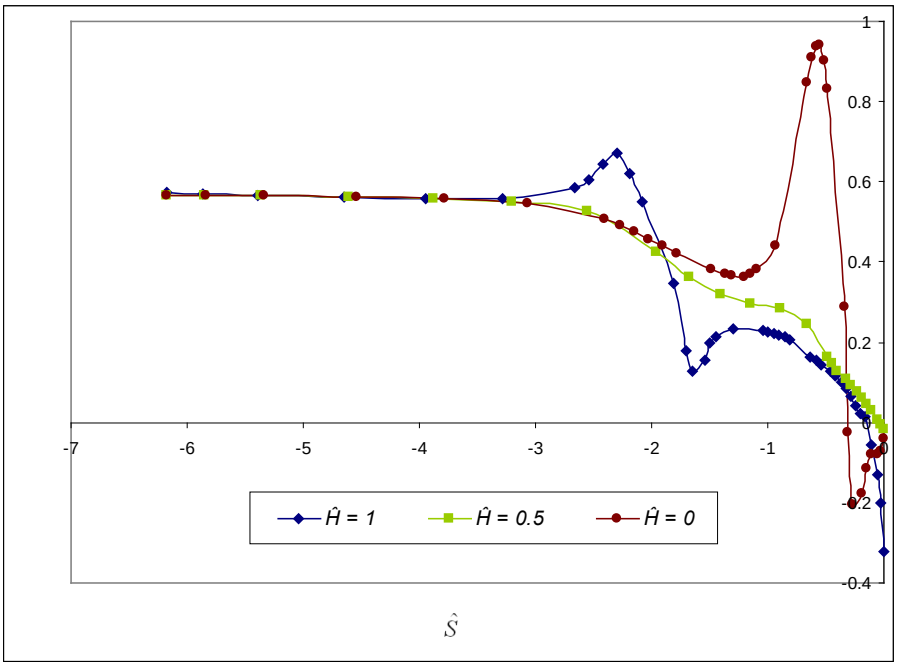

Figure 3-21 Blade-to-blade average C_P as a function of $\hat{S}$ for CCN38 at $\dot{m}$ = 0.66 lbm/s and N = 110k rpm for $\hat{H}$ = 0, 0.5 and 1.

The CCN38 design utilizes a very short and steep bullet nose and consequently the pressure coefficient quickly rises and falls from the high peak. After the area contraction the shroud profile is consistent with other machines, wherein heavy acceleration is visible as the flow navigates toward the impeller leading edge. Contour plots of the pressure and velocity help illustrate these fluctuations, and can be found in Appendix A. The results depicted are for a mass flow rate of 0.66 lbm/s and a wheel speed of 110,000 rpm. For a depiction of where this point lies on the efficiency and pressure map see Fig. 3-22.

The results retrieved from the MST and CFD analysis reveal excellent agreement between the two approaches, as seen in Fig. 3-23. While the amplitude of the fluctuation of the MST profile, caused by the shroud contraction, is not as distinguished, the similarity of the general trend is evident.

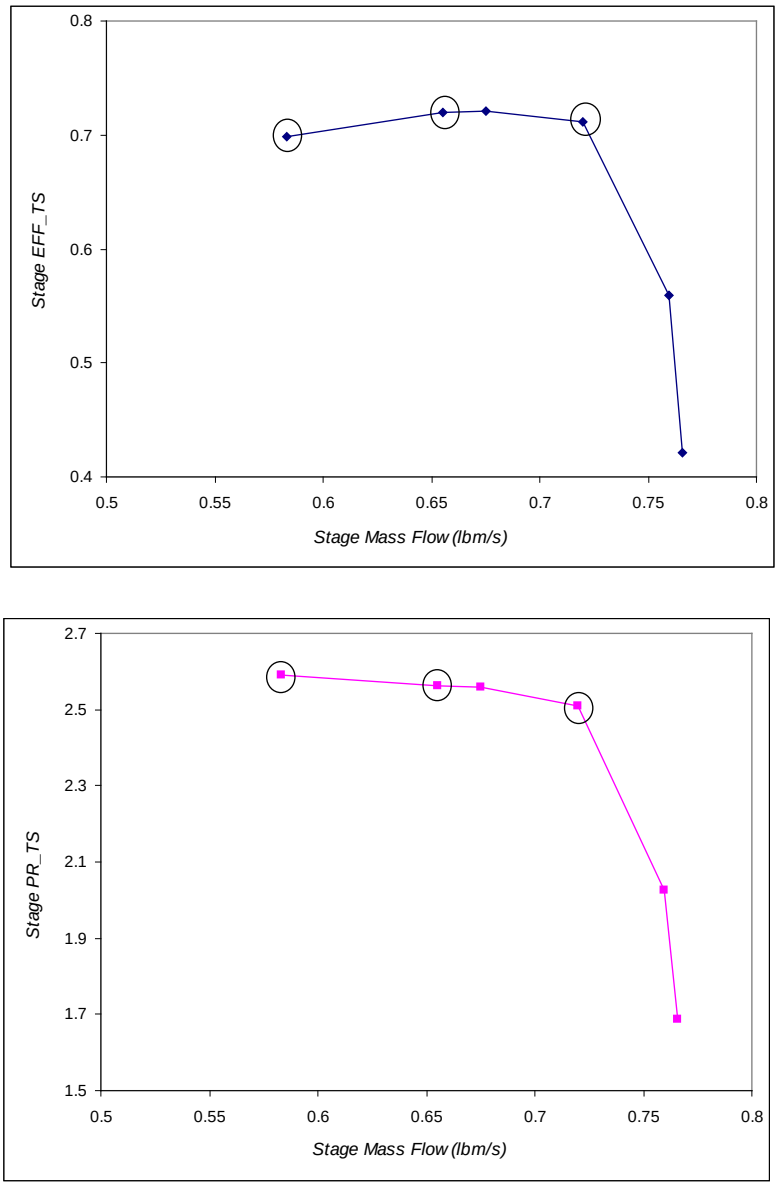

Figure 3-22 Stage total-to-static efficiency (top) and pressure ratio (bottom) maps for CCN38 operating at 110k rpm.

Figure 3-24 reveals the comparison of the C_P vs. $\hat{S}$ profiles for the CFD results at the shroud ($\hat{H}$ = 1), the isentropic assumption and mass average for CCN38. The results are given for a mass flow rate of 0.66 lbm/s and a wheel speed of 110,000 rpm.

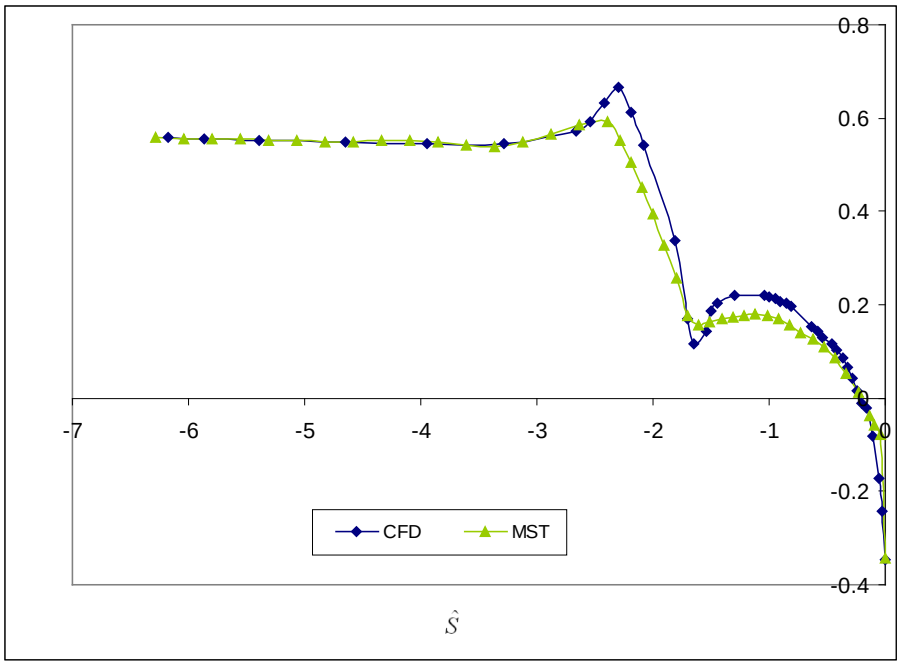

Figure 3-23 Comparison of C_P vs. $\hat{S}$ profiles derived from CFD and MST, along the shroud ($\hat{H}$ = 1), for CCN38 at a mass flow rate of 0.66 lbm/s and a wheel speed of 110k rpm.

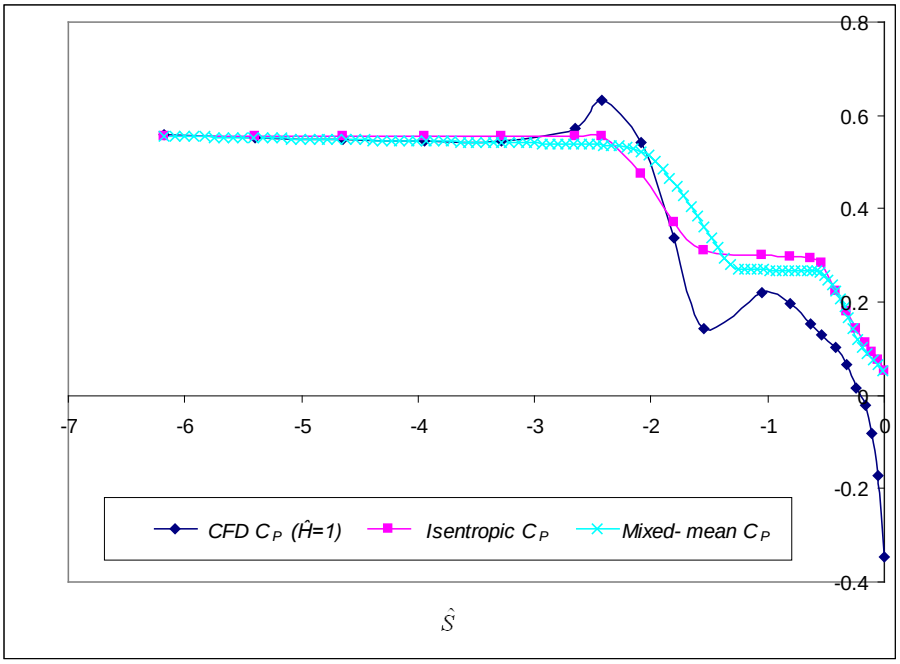

Figure 3-24 A comparison of representative C_P streamwise distributions derived from 1) CFD at $\hat{H}$= 1, 2) the isentropic assumption, and 3) the mass averaged value derived from CFD for CCN38.

Irreversible losses are easily identifiable. The two calculations result in a good match, especially in the regions far upstream and near the impeller leading edge. Recalling Fig. 3-14 and Fig. 3-19, the mass averaged C_P profile notably dives immediately at the impeller leading edge for CCN30 and CCN32. This dive is not apparent in the data of Fig. 3-24 corresponding to CCN38. The cause for this phenomenon is explained as follows. The impeller leading edge has an inclination angle, as seen in the 1-D representation. The consequence is that the core flow, which is well represented in the mass averaged C_P, exhibits this dive only after the shroud leading edge streamwise location ($\hat{S} \approx 0.2$).

3.3.3 CCN39

The design of CCN39 is identical to that of CCN38, except CCN39 employs splitter blades, while CCN38 has only full blades. Therefore the exit diameter of 2.888 inches and the wheel speed of 110,000 rpm are unchanged. The nominal mass flow rate of 0.72 lbm/s is slightly higher, which is a product of the reduced blade blockage at the impeller inlet. Table 3-4 provides general information for CCN39.

Table 3-4 General information for CCN39.

R1 tip (in)	R1 hub (in)	R2 (in)	N (rpm)	operating mflow (lbm/s)	P_0 (psi)	T_0 (deg R)	Grid Density (hs x bb x sw)	File Name
0.97	0.32	1.44	110k	0.73	14.69	527.4	33 x 21 x 173	CCN39-1.des

Figure 3-25 depicts the 1-D geometry, where the vertical line just downstream of the impeller leading edge denotes the beginning of the splitter blades. The 3-D image of

CCN38 (left) and CCN39 (right) is provided in Fig. 3-26 in order to illustrate the difference between full and splitter blades. Information regarding the purpose and effect of splitter blades can be found in Japikse's compressor design book[2]. Pressure and efficiency maps are provided in Fig. 3-27.

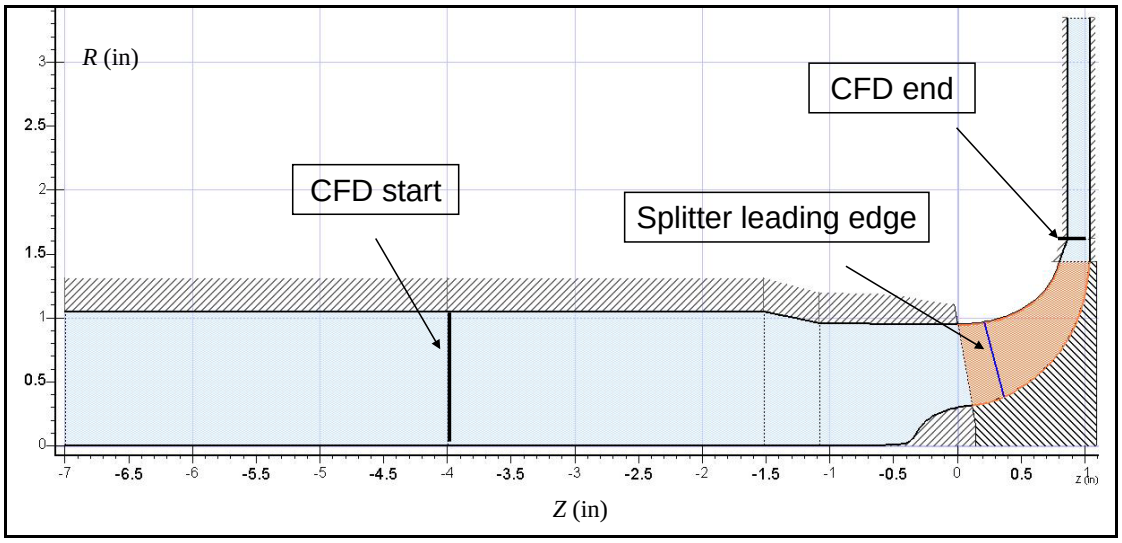

Figure 3-25 1-D representation of CCN39.

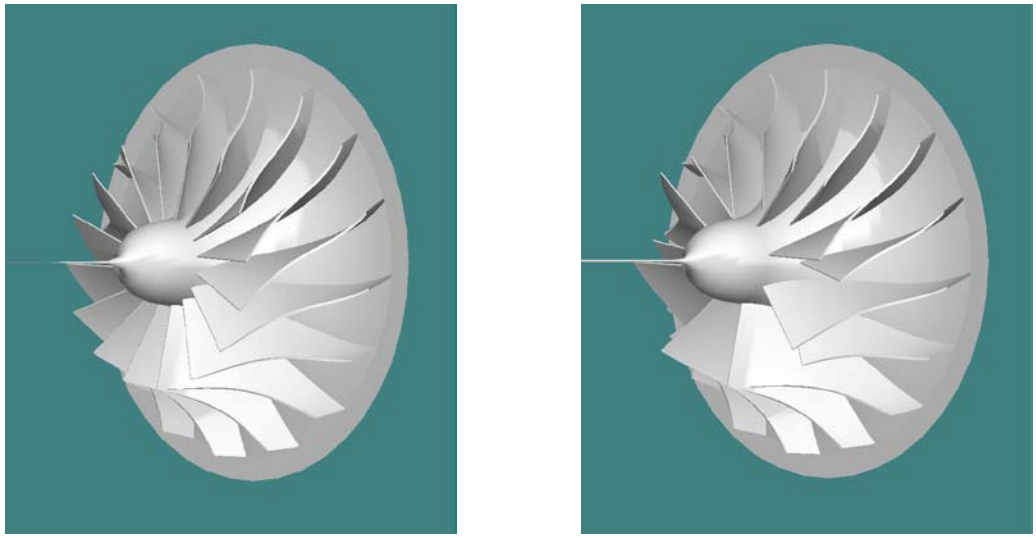

Figure 3-26 3-D representation of CCN38 (left, whole blades) and CCN39 (right, splitter blades).

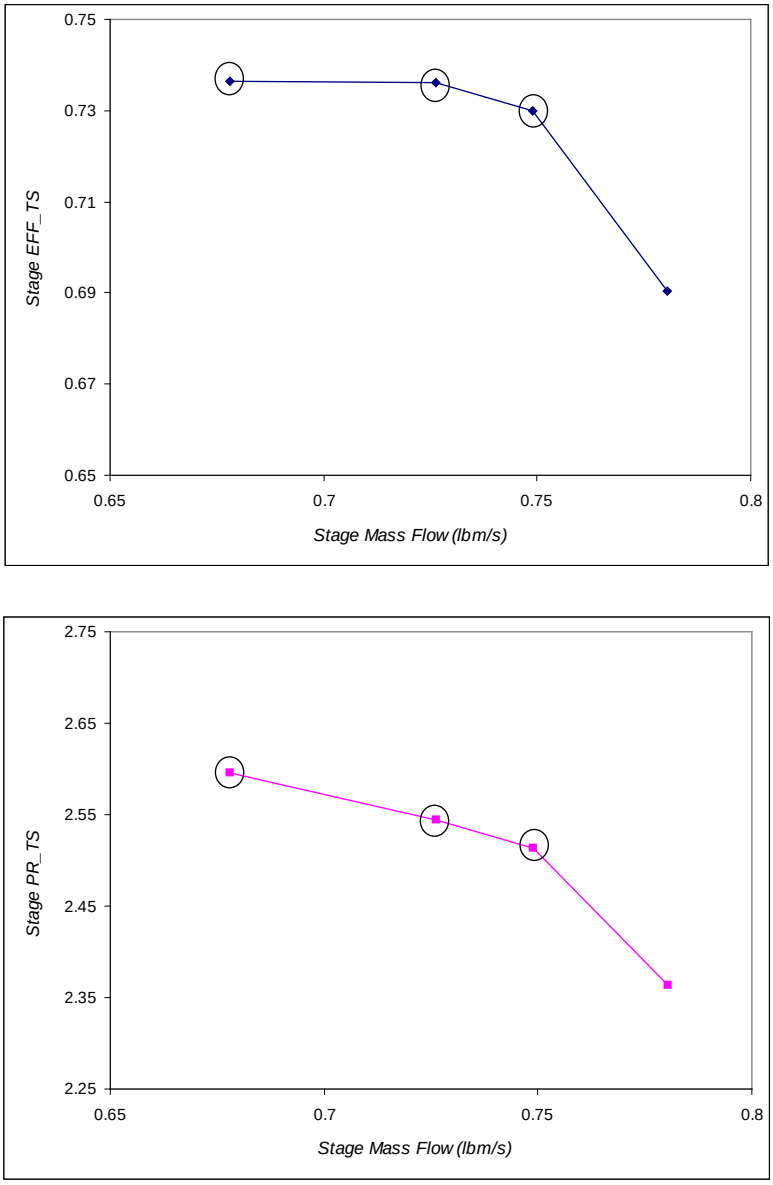

Figure 3-27 Stage total-to-static efficiency (top) and pressure ratio (bottom) maps for CCN39 operating at 110k rpm.

The C_P vs. $\hat{S}$ profile from CCN39 is comparable to the same from CCN38, as depicted in Fig. 3-28.

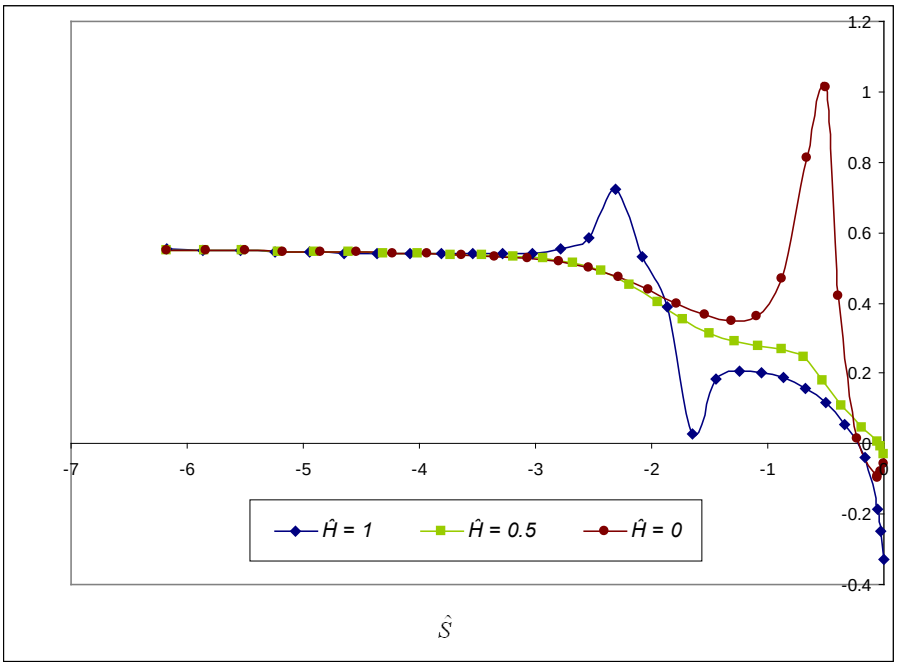

Figure 3-28 Blade-to-blade average C_P as a function of $\hat{S}$ for CCN39 at $\dot{m}$ = 0.73 lbm/s and N = 110k rpm for $\hat{H}$ = 0, 0.5 and 1.

Experimentally the performance of the CCN39 and CCN38 impellers varied notably, wherein a shift in the stall and choke lines was evident along with significant adjustments in the overall stage efficiency and pressure ratios, with the disparity attributed to the impeller inlet effects[21]. To compare CCN39 results with those of CCN38, Fig. 3-29 compares the shroud ($\hat{H}$ = 1) and Fig. 3-30 compares the hub ($\hat{H}$ = 0) profiles of the two similar designs. The CFD results suggest that the distortion within the inlet passage region which would result from varying blade blockage at the impeller leading edge is likely not the cause of the observed variation. A subtle disparity exists near the leading edge, yet this does not seem significant enough to cause the drastic differences in impeller performance.

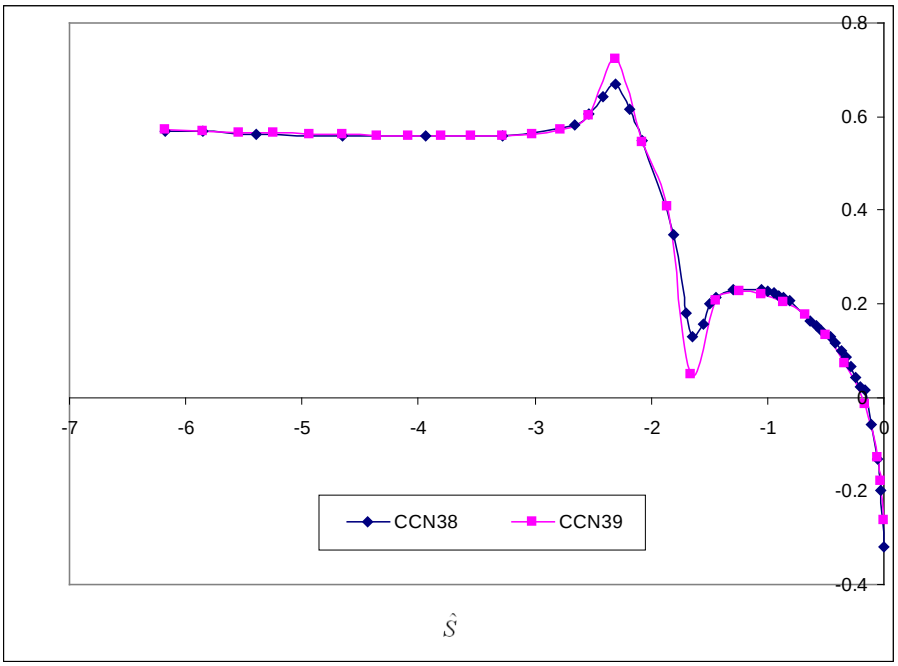

Figure 3-29 Comparison of the C_P vs. $\hat{S}$ profiles along the shroud ($\hat{H}$ = 1) for CCN38 and CCN39. These results are derived from analysis at comparable mass flow rates (0.72 lbm/s and 0.73 lbm/s, respectively) and the same wheel speed (110k rpm).

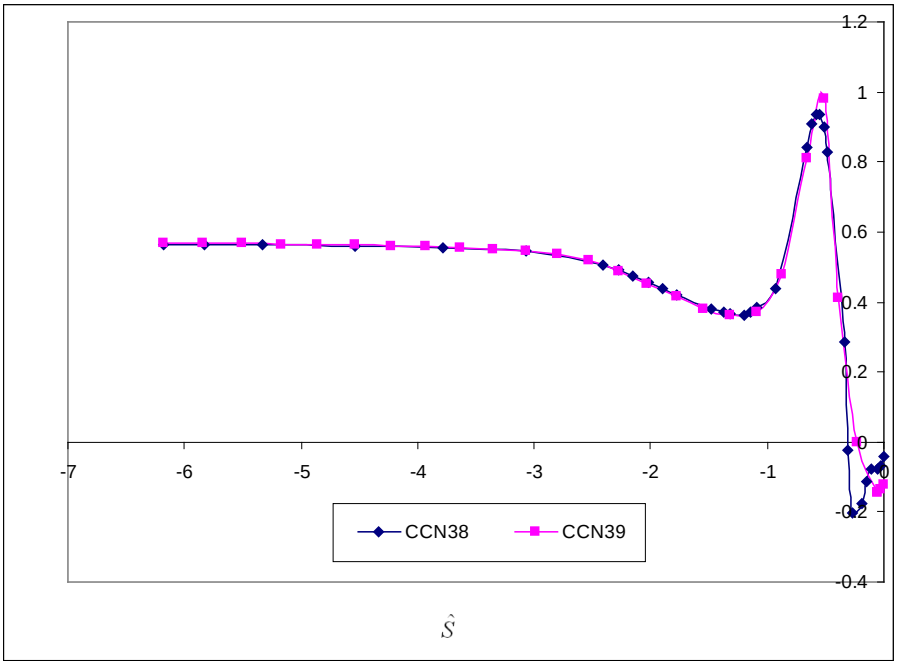

Figure 3-30 Comparison of the C_P vs. $\hat{S}$ profiles along the hub ($\hat{H}$ = 0) for CCN38 and CCN39. These results are derived from analysis at comparable mass flow rates (0.72 lbm/s and 0.73 lbm/s, respectively) and the same wheel speed (110k rpm).

Similar to CCN38, the C_P vs. $\hat{S}$ profile from the MST analysis matches very well with that from CFD, as depicted in Fig. 3-31. A slight bump exists in the MST profile (at about $\hat{S} \approx -1.2$), a result of a numerical irregularity in the streamline curvature in a portion of the MST calculation process. Additionally, the MST analysis fails to capture the full magnitude of the fluctuation seen in the CFD profile around $\hat{S} = -2$, although the overall trends are matched well.

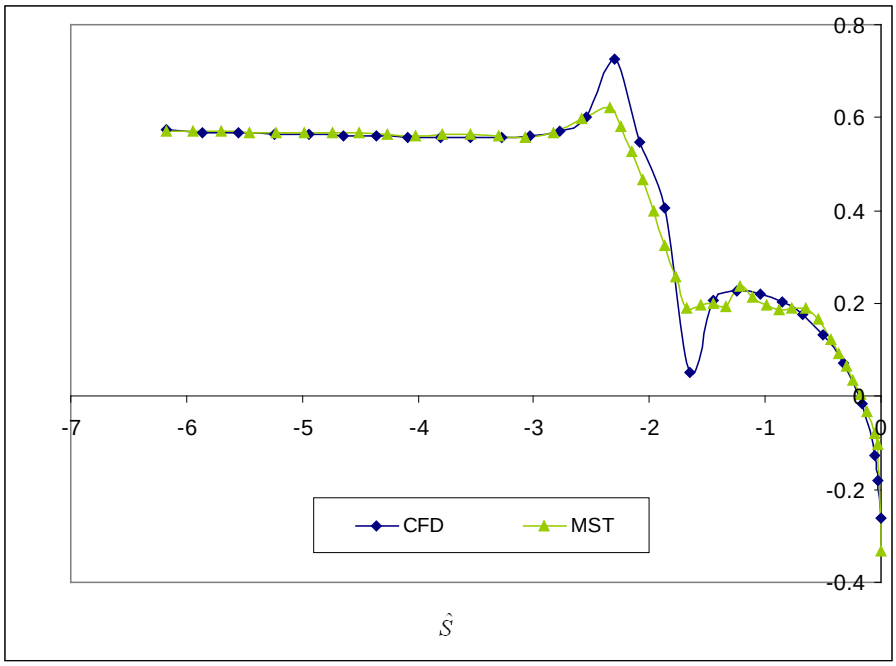

Figure 3-31 Comparison of C_P vs. $\hat{S}$ profiles derived from CFD and MST, along the shroud ($\hat{H} = 1$), for CCN39 at a mass flow rate of 0.73 lbm/s and a wheel speed of 110k rpm.

Figure 3-32 reveals the comparison of the C_P vs. $\hat{S}$ profiles for the CFD results at the shroud ($\hat{H} = 1$), the isentropic assumption and mass average for CCN39. The results are given for a mass flow rate of 0.73 lbm/s and a wheel speed of 110,000 rpm.

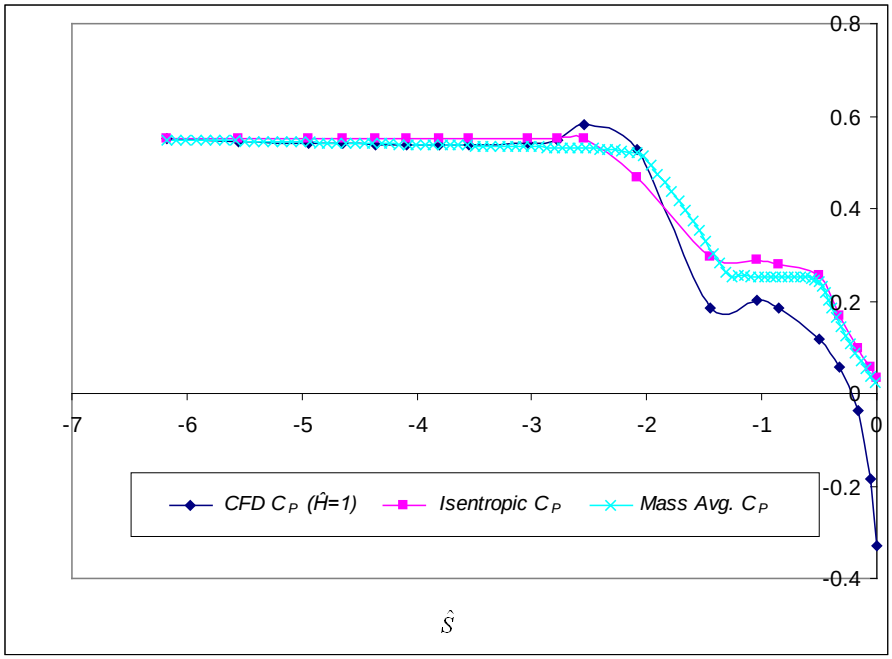

Figure 3-32 A comparison of representative C_P streamwise distributions derived from 1) CFD at $\hat{H}$ = 1, 2) the isentropic assumption, and 3) the mass averaged value derived from CFD for CCN39.

As with CCN38, the mass averaged C_P profile in CCN39 experiences a dive after the impeller shroud leading edge streamwise location. Once again the leading edge for this machine has an inclination angle, and this pushes the core flow (mass averaged flow) to dive just downstream of the shroud leading edge streamwise location ($\hat{S} \approx 0.2$).

The results derived from all approaches continue to suggest that the historical location of the impeller inlet tap pressure is inappropriate for the TEIS modeling formulation. The high gradient at the near leading edge region is a cause for serious concern as "noise" will be added to any model anchored in this region. Alternatively at about three blade heights upstream of the leading edge ($\hat{S} \approx -3$) a state of uniformity is evident, a more trustworthy location for an anchor for the TEIS model.

3.3.4 CCN40

CCN40 has an exit diameter of 5.449 inches and operates at a nominal mass flow rate of 0.42 lbm/s and a wheel speed of 58,000 rpm. Table 3-5 summarizes the general information, and Fig. 3-33 depicts the pressure and efficiency maps.

Table 3-5 General information for CCN40.

R1 tip (in)	R1 hub (in)	R2 (in)	N (rpm)	operating mflow (lbm/s)	P_0 (psi)	T_0 (deg R)	Grid Density (hs x bb x sw)	File Name
1.02	0.50	2.72	58k	0.4	14.10	555	33 x 29 x 241	CCN40-1.des

CCN40 is unique in its design in that a continuous area contraction on the shroud occurs immediately upstream of the impeller inlet. The area contraction on the shroud resulted in an increased grid density as the shroud pressure needed increased resolution for convergence to be achieved. Figure 3-34 provides a 1-D representation of the geometry.

The C_P vs. $\hat{S}$ behavior for this machine is markedly different than for the previously described machines, as revealed in Fig. 3-35. The dual-sided contraction causes a more rapid acceleration than was present in the previously investigated designs. Further, the dual contraction tends to thrust more fluid toward the 50% span line, in contrast to previous designs which exclusively pushed fluid away from the hub and toward the shroud. This rapid acceleration results in a C_P change of about 1 (-0.2 to 0.8).

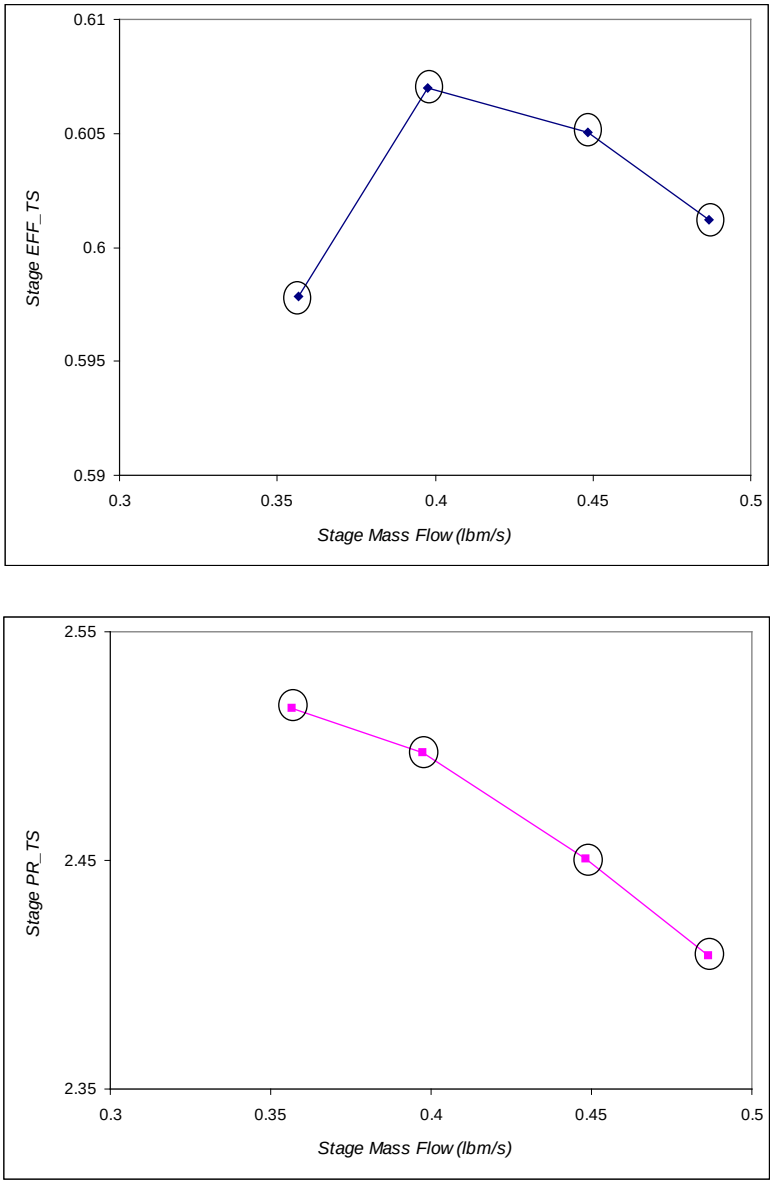

Figure 3-33 Stage total-to-static efficiency (top) and pressure ratio (bottom) maps for CCN40 operating at 58k rpm.

The only lack of correspondence between the C_P vs. $\hat{S}$ profiles derived from the MST and CFD results is the result of the need to slightly modify the area contraction profile. As was previously mentioned, this is occasionally necessary to achieve smooth streamlines in the MST calculation, and thereby produce physically sensible and

numerically stable results. Figure 3-36 demonstrates the slight inconsistency between the MST and CFD calculations along the shroud of CCN40 for a mass flow rate of 0.40 lbm/s and a wheel speed of 58,000 rpm.

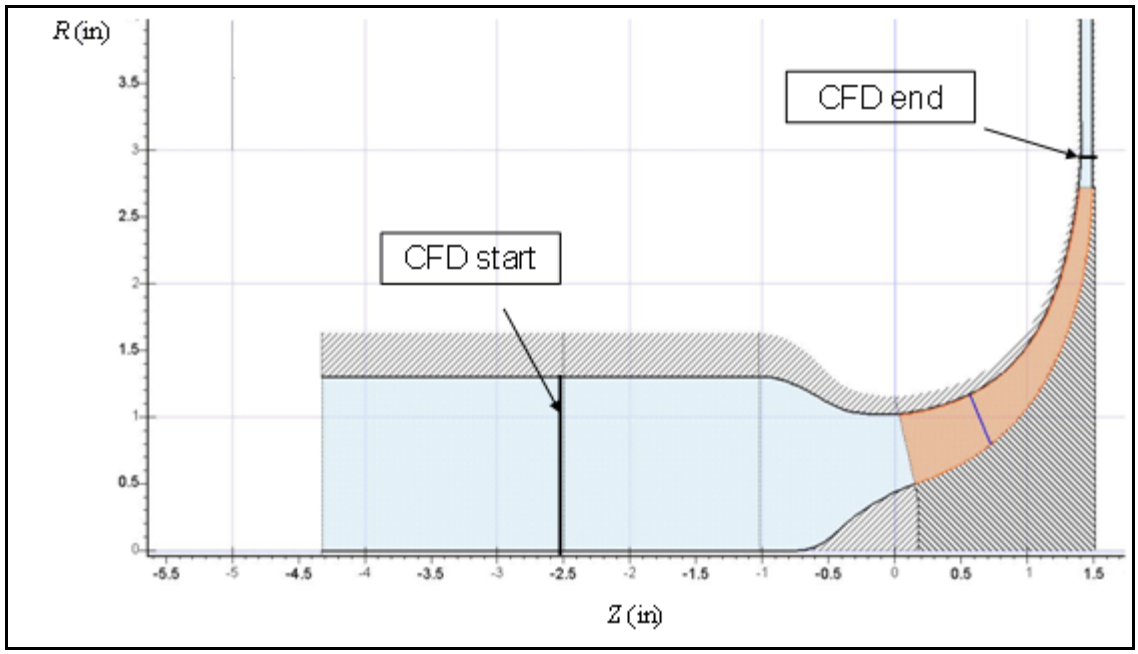

Figure 3-34 1-D representation of CCN40.

The C_P vs. $\hat{S}$ profiles for the CFD results at the shroud ($\hat{H} = 1$), the isentropic assumption, and the mass average values for CCN40 are compared in Fig. 3-37. The results are given for a mass flow rate of 0.40 lbm/s and a wheel speed of 58,000 rpm. Again the impeller leading edge has an inclination angle which causes the mass averaged C_P profile to dive downstream of the impeller leading edge shroud location ($\hat{S} > 0$).

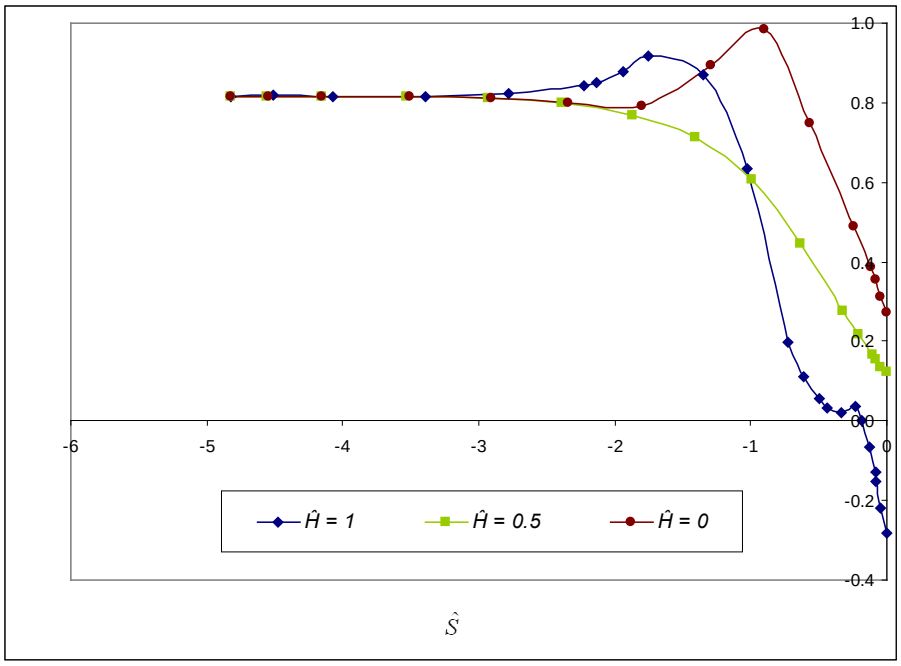

Figure 3-35 Blade-to-blade average C_P as a function of $\hat{S}$ for CCN40 at $\dot{m}$ = 0.40 lbm/s and N = 58k rpm for $\hat{H}$ = 0, 0.5 and 1.

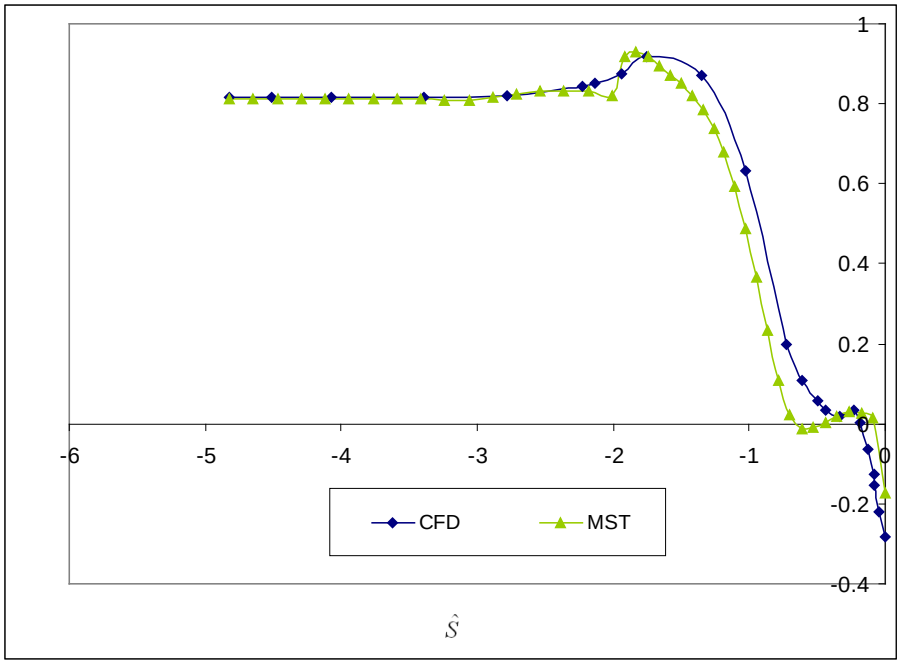

Figure 3-36 Comparison of C_P vs. $\hat{S}$ profiles derived from CFD and MST, along the shroud ($\hat{H}$ = 1), for CCN40 at a mass flow rate of 0.40 lbm/s and a wheel speed of 58k rpm.

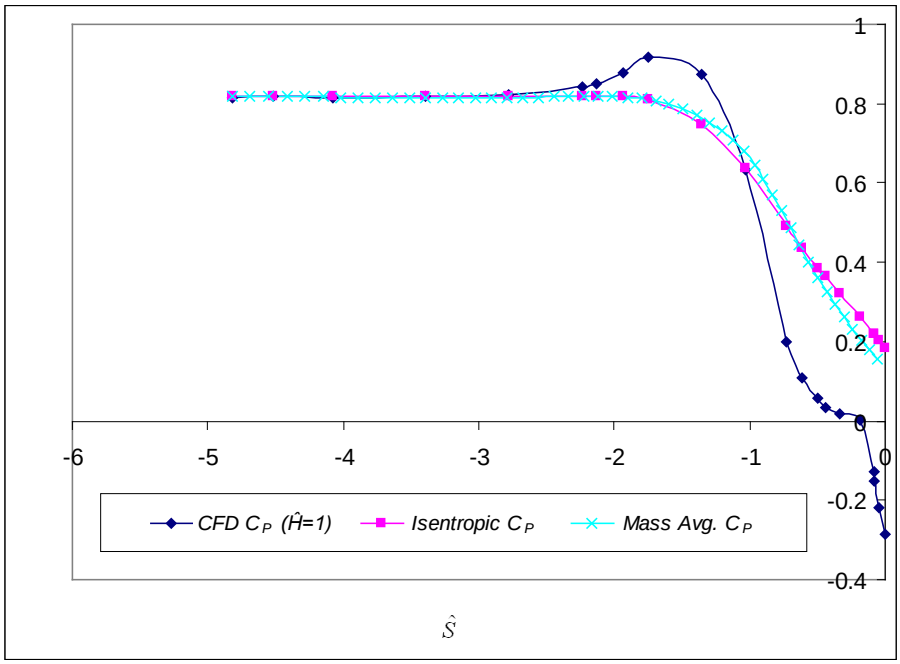

Figure 3-37 A comparison of representative C_P streamwise distributions derived from 1) CFD at $\hat{H}$ = 1, 2) the isentropic assumption, and 3) the mass averaged value derived from CFD for CCN40.

3.3.5 CCN42

Similar to machines CCN38 and CCN39 the shroud radius increases upstream of the impeller, as is disclosed in the 1-D representation of the geometry in Fig. 3-34.

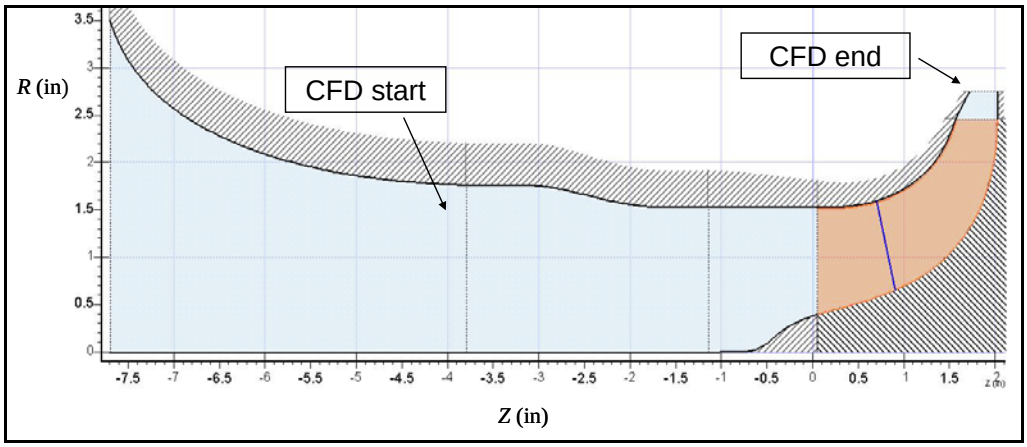

Figure 3-38 1-D representation of CCN42.

This impeller has an exit diameter of 4.918 inches, has a wheel speed of 53,000 rpm and operates at a nominal mass flow rate of 1.38 lbm/s. Table 3-6 summarizes the general information for CCN42. Figure 3-39 reveals the pressure and efficiency maps for CCN42.

Table 3-6 General information for CCN42.

R1 tip (in)	R1 hub (in)	R2 (in)	N (rpm)	operating mflow (lbm/s)	P_0 (psi)	T_0 (deg R)	Grid Density (hs x bb x sw)	File Name
1.54	0.39	2.46	53k	1.25	14.76	545.7	21 x 13 x 101	CCN42-1.des

This geometry produces an interesting result; as seen in Fig. 3-40 the shroud ($\hat{H}$ = 1), 50% span ($\hat{H}$ = 0.5) and hub ($\hat{H}$ = 0) C_P vs. $\hat{S}$ profiles do not converge at the furthest upstream location as well as was evidenced by previously considered designs. Upstream of the radius increase is a very short region of constant area duct. Moving further upstream is a large bell mouth contraction. The computational domain does not extend into the bell mouth region, as the solver has a difficult time converging when this region is included. Consequently the short constant area duct does not allow for a near uniform profile at any point upstream of the impeller leading edge. However, the results suggest that placing an anchor point for the TEIS modeling at about 3 blade heights upstream is still a better location than use of the historical tap region.

The comparison of the C_P vs. $\hat{S}$ profiles derived from the MST and CFD analysis results are shown in Fig. 3-41 with a trend similar to what is found in previous designs where good agreement is found between the two analysis methods. Irregularities

observed at $\hat{S} \approx$ -0.75 and $\hat{S} \approx$ -0.25 are the result of numerical instability caused by difficult streamline curvature.

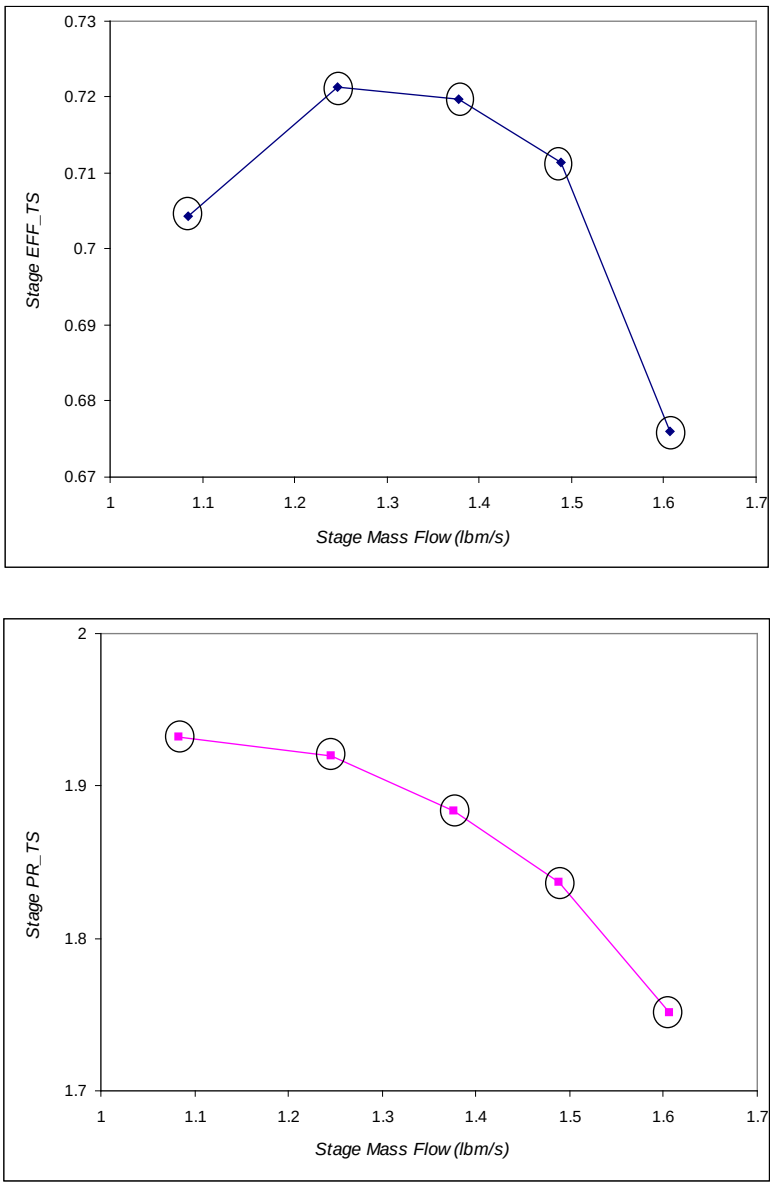

Figure 3-39 Stage total-to-static efficiency (top) and pressure ratio (bottom) maps for CCN42 operating at 53k rpm.

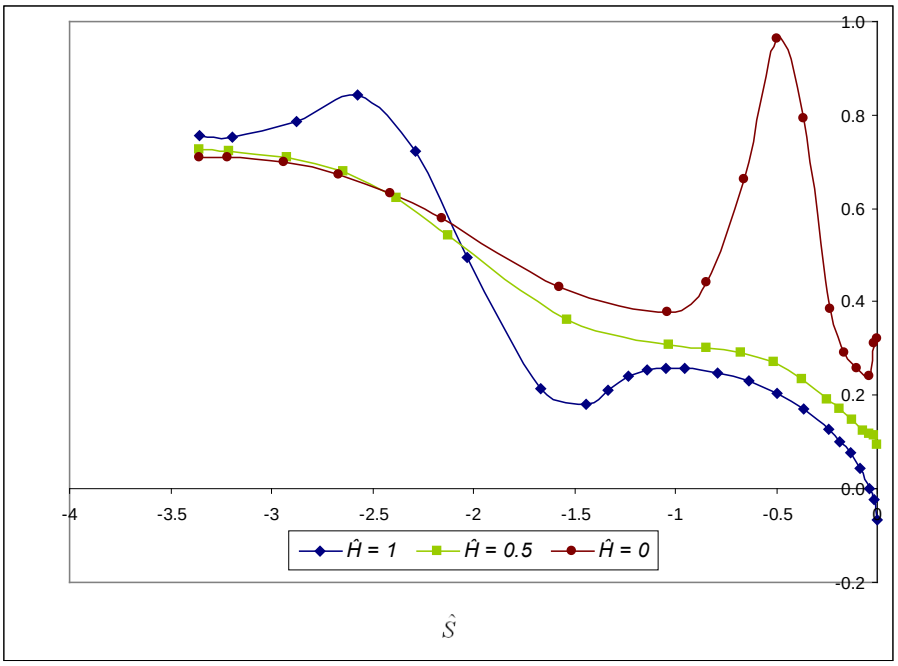

Figure 3-40 Blade-to-blade average C_P as a function of $\hat{S}$ for CCN42 at $\dot{m}$ = 1.25 lbm/s and N = 53k rpm for $\hat{H}$ = 0, 0.5 and 1.

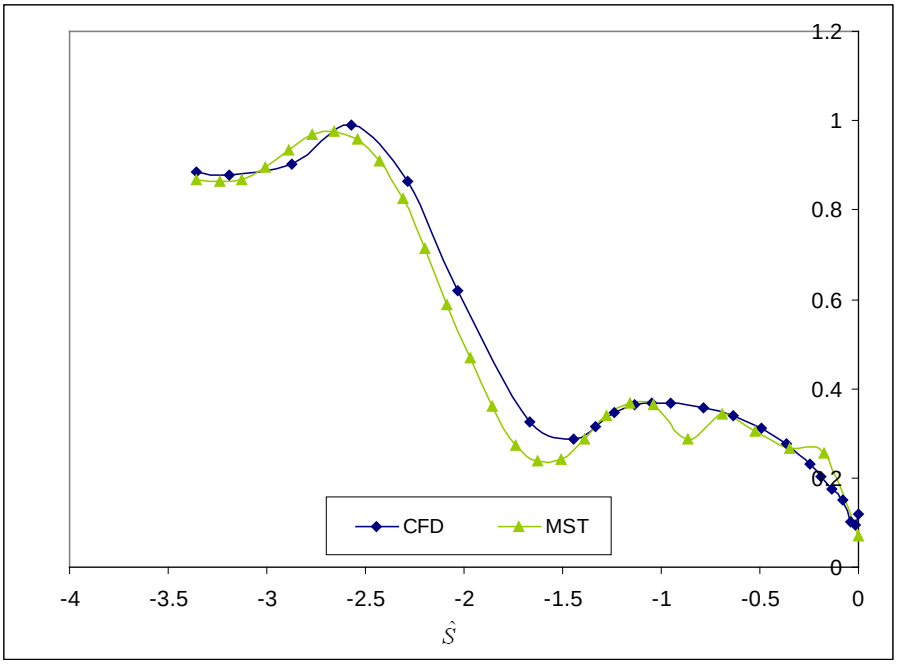

Figure 3-41 Comparison of C_P vs. $\hat{S}$ profiles derived from CFD and MST, along the shroud ($\hat{H}$ = 1), for CCN42 at a mass flow rate of 1.25 lbm/s and a wheel speed of 53k rpm.

Figure 3-42 likewise follows the now expected pattern found in comparing the C_P vs. $\hat{S}$ profiles for the CFD results at the shroud ($\hat{H}$ = 1), the isentropic assumption and mass average for CCN42. The results are given for a mass flow rate of 1.25 lbm/s and a wheel speed of 53,000 rpm. The continuous deviation of P_M from P_I illustrates the increase of the irreversible loss as the flow traverses through the inlet passage.

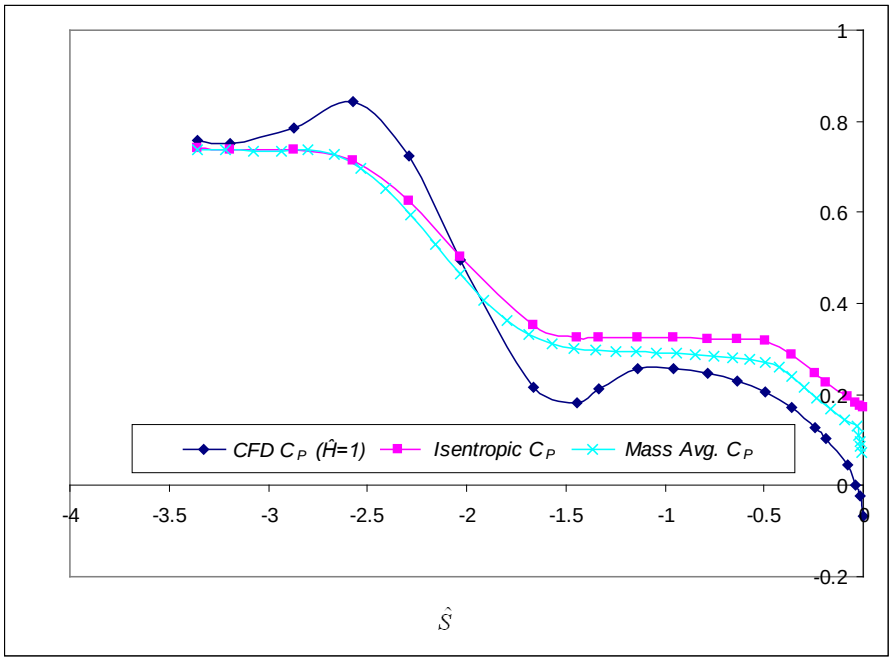

Figure 3-42 A comparison of representative C_P streamwise distributions derived from 1) CFD at $\hat{H}$ = 1, 2) the isentropic assumption, and 3) the mass averaged value derived from CFD for CCN42.

3.3.6 CCN66

CCN66 is a larger compressor than those explored thus far with an impeller exit diameter of 6.884 inches, a nominal mass flow rate of 5.0 lbm/s and a wheel speed of 39,000 rpm. A summary of the information can be found in Table 3-7. Figure 3-43 presents the pressure and efficiency maps.

Table 3-7 General information for CCN66.

R1 tip (in)	R1 hub (in)	R2 (in)	N (rpm)	operating mflow (lbm/s)	P_0 (psi)	T_0 (deg R)	Grid Density (hs x bb x sw)	File Name
1.71	0.60	3.44	39k	5.20	14.10	564	29 x 21 x 177	CCN66-1.des

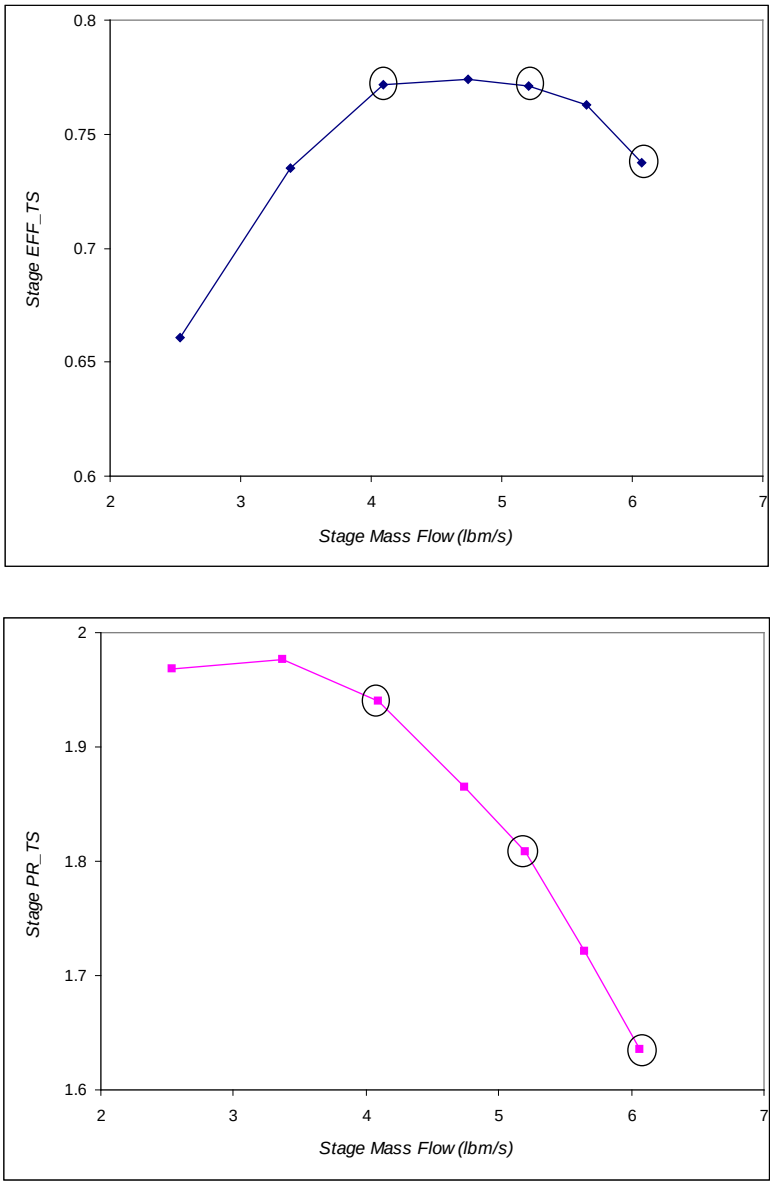

Figure 3-43 Stage total-to-static efficiency (top) and pressure ratio (bottom) maps for CCN66 operating at 39k rpm.

Similar to CCN42 a limited region of constant area duct, as seen in Fig. 3-44, prohibits the flow from reaching a condition of uniform flow, as depicted by the C_P vs. $\hat{S}$ results of Fig. 3-45. However, the results suggest that beginning of the computational domain still provides a better anchor point for reformulating the TEIS model than the historical tap location.

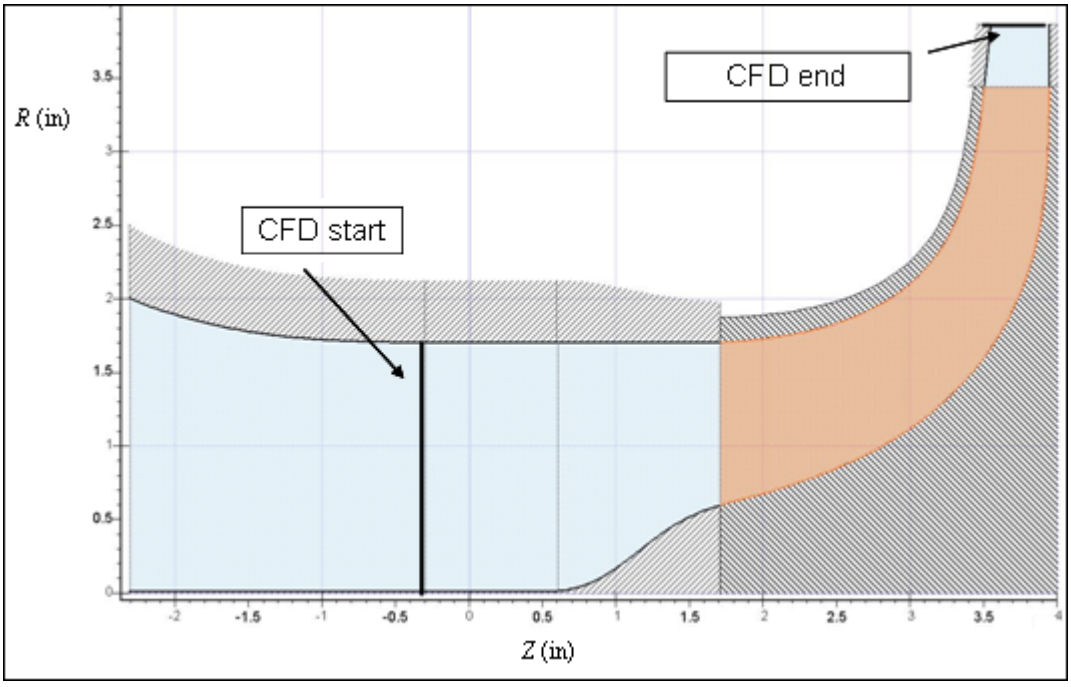

Figure 3-44 1-D representation of CCN66.

A comparison of the C_P vs. $\hat{S}$ profiles along the shroud for the MST and CFD analysis reveals another good match of results from the two methods, as seen in Fig. 3-40. These results are for a mass flow rate of 5.2 lbm/s and a wheel speed of 39,000 rpm. Figure 3-47 again illustrates that P_M increasingly deviates from P_I as the flow moves from the inlet toward the impeller leading edge with irreversible losses again the likely cause.

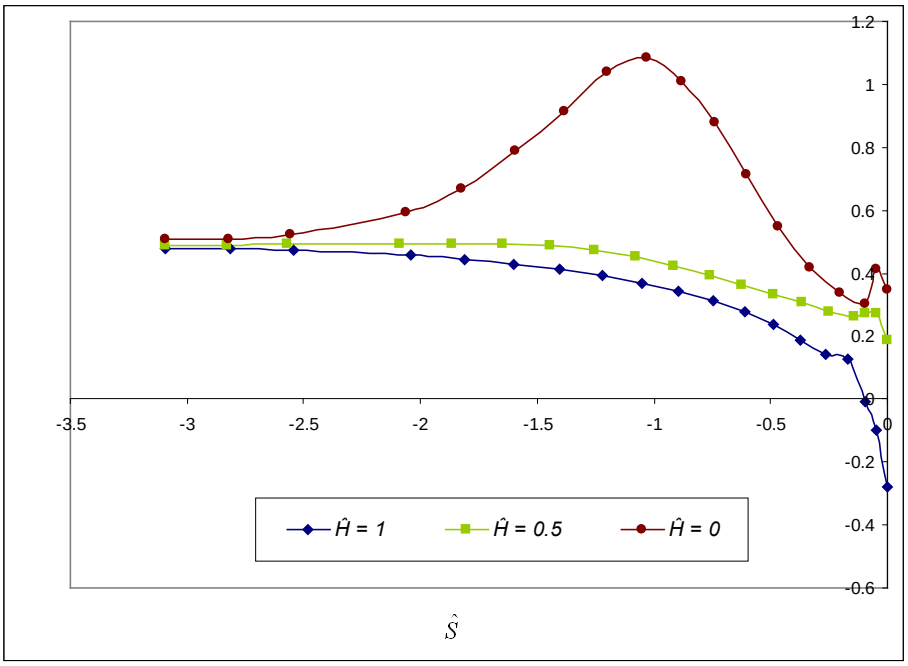

Figure 3-45 Blade-to-blade average C_P as a function of $\hat{S}$ for CCN66 at $\dot{m}$ = 5.2 lbm/s and N = 39k rpm for $\hat{H}$ = 0, 0.5 and 1.

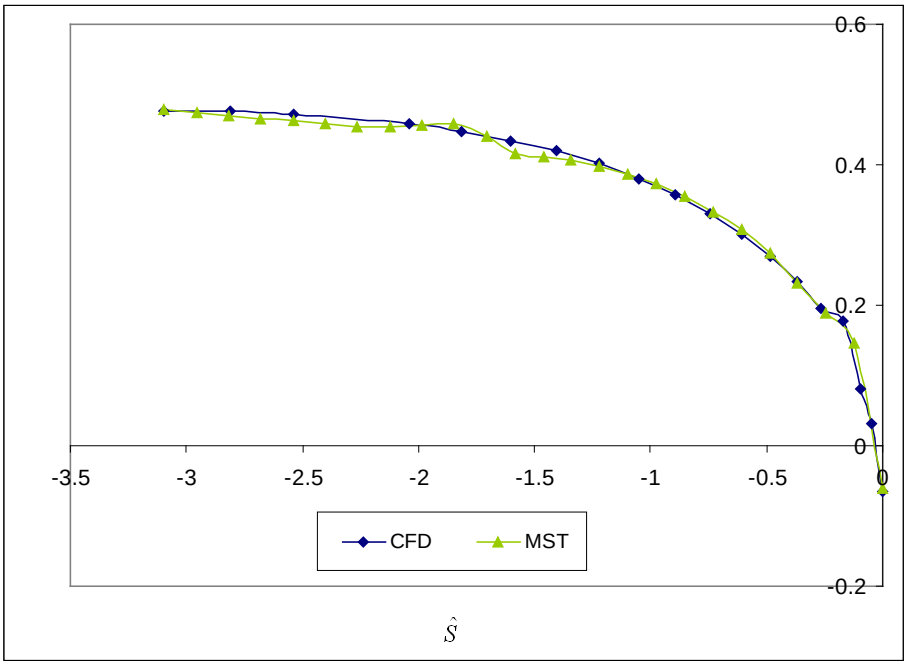

Figure 3-46 Comparison of C_P vs. $\hat{S}$ profiles derived from CFD and MST, along the shroud ($\hat{H}$ = 1), for CCN66 at a mass flow rate of 5.2 lbm/s and a wheel speed of 39k rpm.

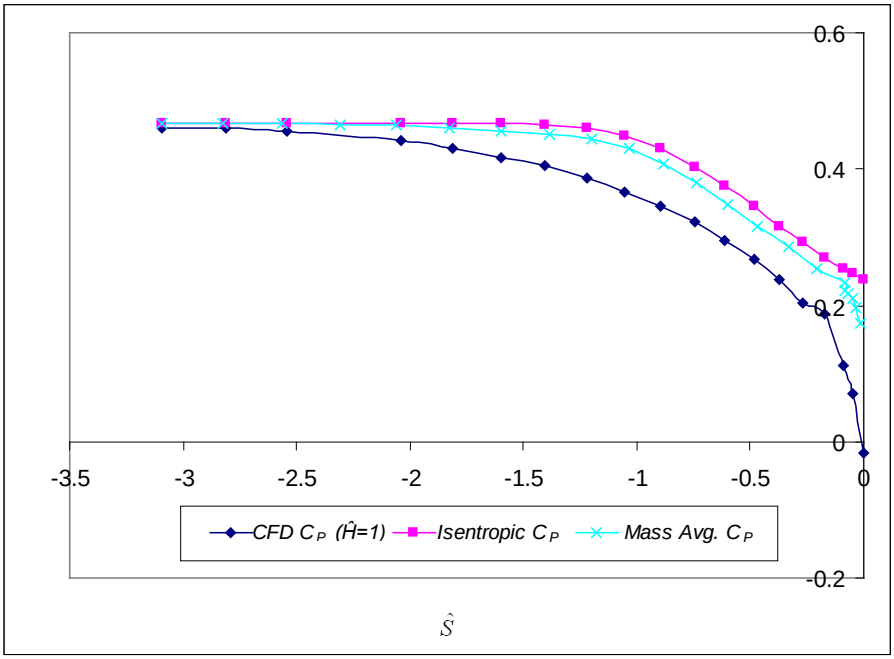

Figure 3-47 A comparison of representative C_P streamwise distributions derived from 1) CFD at $\hat{H}$ = 1, 2) the isentropic assumption, and 3) the mass averaged value derived from CFD for CCN66.

3.3.7 CCN74

CCN74 is the most unique design considered in this study. Obvious differences in geometry are illustrated in Fig. 3-42.

The u-bend upstream of the impeller is a result of size restrictions and the axial inflow to the impeller is unique to this study. The impeller has an exit diameter of 6.0 inches, a nominal mass flow rate of 0.3 lbm/s and a wheel speed of 39,000 rpm. A summary of the machine specifications is found in Table 3-8. For this case the impeller inlet radius at the tip and hub (R_{1t} and R_{1h}) are the same, and the inlet blade height is represented by B_1, the inlet passage height.

Figure 3-49 provides the pressure and efficiency maps for CCN74.

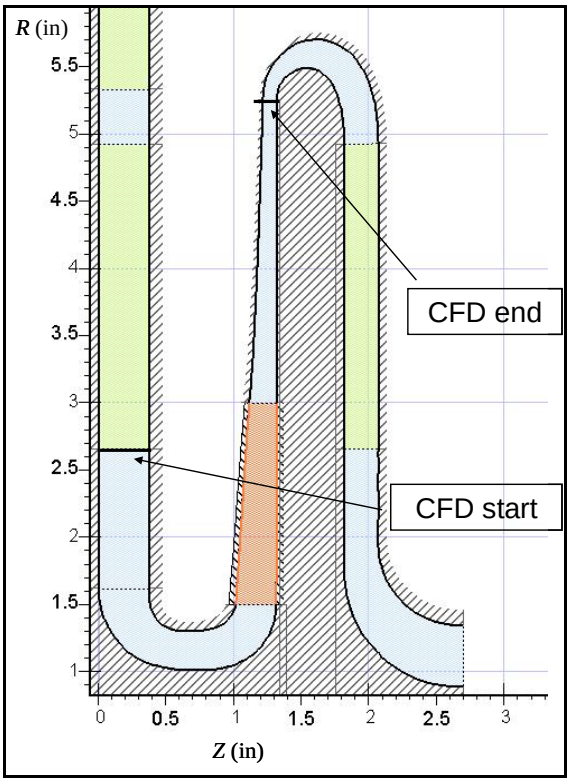

Figure 3-48 A 1-D representation of CCN74.

Table 3-8 General information for CCN74.

R1 tip (in)	B1 (in)	R2 (in)	N (rpm)	operating mflow (lbm/s)	P_0 (psi)	T_0 (deg R)	Grid Density (hs x bb x sw)	File Name
1.50	0.30	3.00	39k	0.30	16.00	540	25 x 33 x 241	CCN74-1.des

The u-bend inlet, in combination with the radial inlet impeller, provides a different perspective on the flow physics involved in a turbomachine inlet. The fundamental principles of flow through a curved duct necessarily result in a different profile than the rest of the designs in this work, as is evident in the C_P vs. $\hat{S}$ results shown in Fig. 3-50. The data presented represents flow conditions for a mass flow rate of 0.30 lbm/s and a wheel speed of 39,000 rpm. For this scenario all six spanwise locations ($\hat{H}$ = 0, 0.25, 0.5, 0.7, 0.9, and 1) are presented, allowing for a more complete understanding of

the differing flow physics caused by the u-bend. Particularly the curvature of the passage results in the 90% span ($\hat{H}$ = 0.9) profile behaving fairly differently than the shroud line ($\hat{H}$ = 1), whereas for all the previous machines investigated the $\hat{H}$ = 0.9 was nearly identical to the flow at $\hat{H}$ = 1.

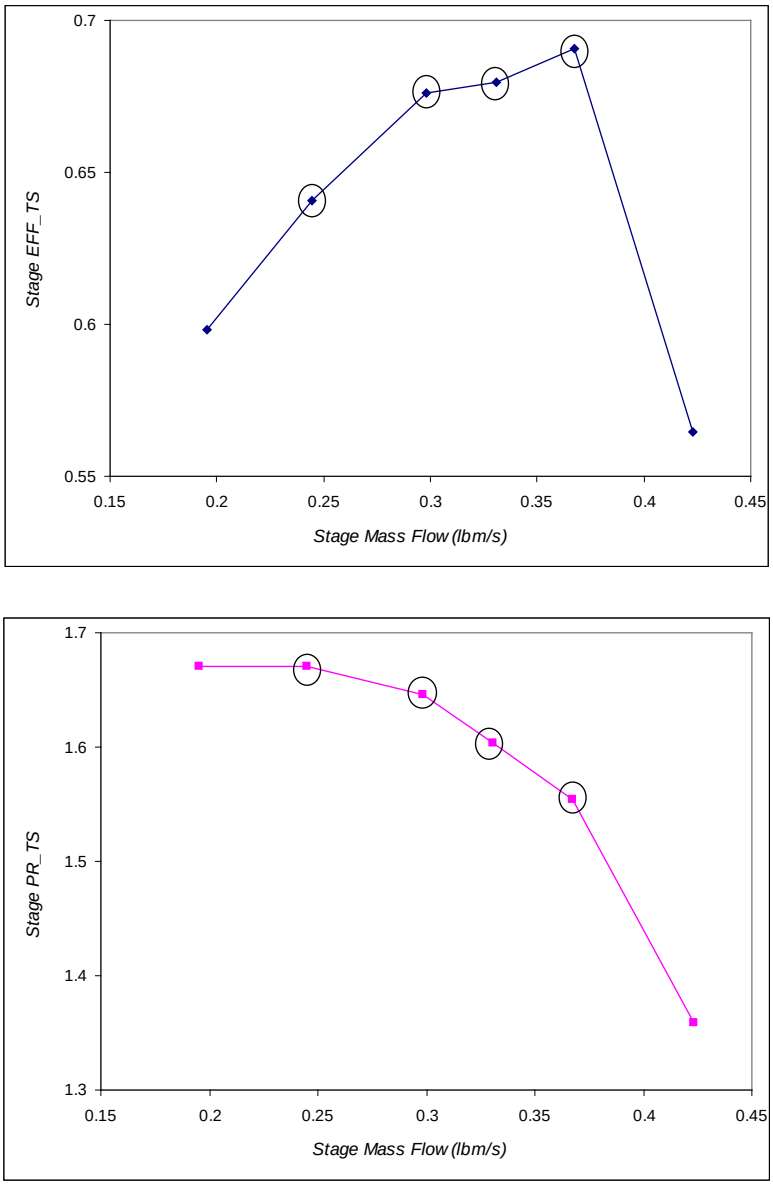

Figure 3-49 Stage total-to-static efficiency (top) and pressure ratio (bottom) maps for CCN74 operating at 39k rpm.

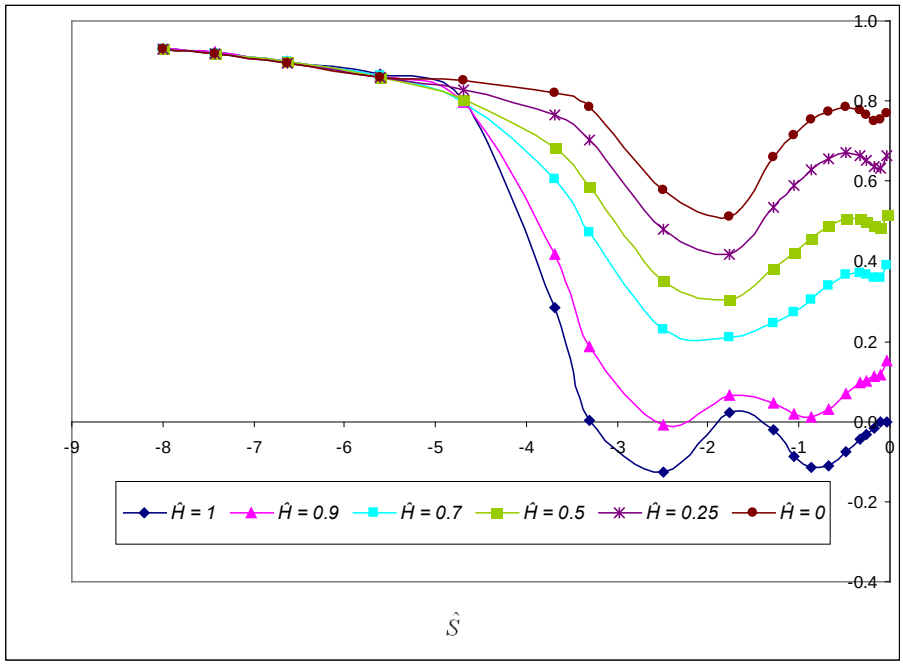

Figure 3-50 Blade-to-blade average C_P as a function of $\hat{S}$ for CCN74 at $\dot{m}$ = 0.24 lbm/s and N = 39k rpm for $\hat{H}$ = 0, 0.25, 0.5, 0.7, 0.9 and 1.

Although the flow exhibits a condition of spanwise uniform flow far upstream of the blade leading edge, this occurs about 1 blade height upstream of the u-bend ($\hat{S} \approx$ -5.5), which is well upstream of the typical 3 blade height location ($\hat{S} \approx$ -3). While this is an anomaly due to the u-bend geometry, the important conclusion is that there is a location upstream of the impeller leading edge in which the flow can be approximated as uniform. $\hat{S} \approx$ -3 can be used as a general rule for the classic centrifugal turbomachine design, and about 1 blade height upstream of the actual u-bend is appropriate for u-bend inlet geometries.

Despite the complexity of the u-bend inlet, the C_P vs. $\hat{S}$ profiles derived from results from the MST and CFD analysis match quite well, as illustrated in Fig. 3-51.

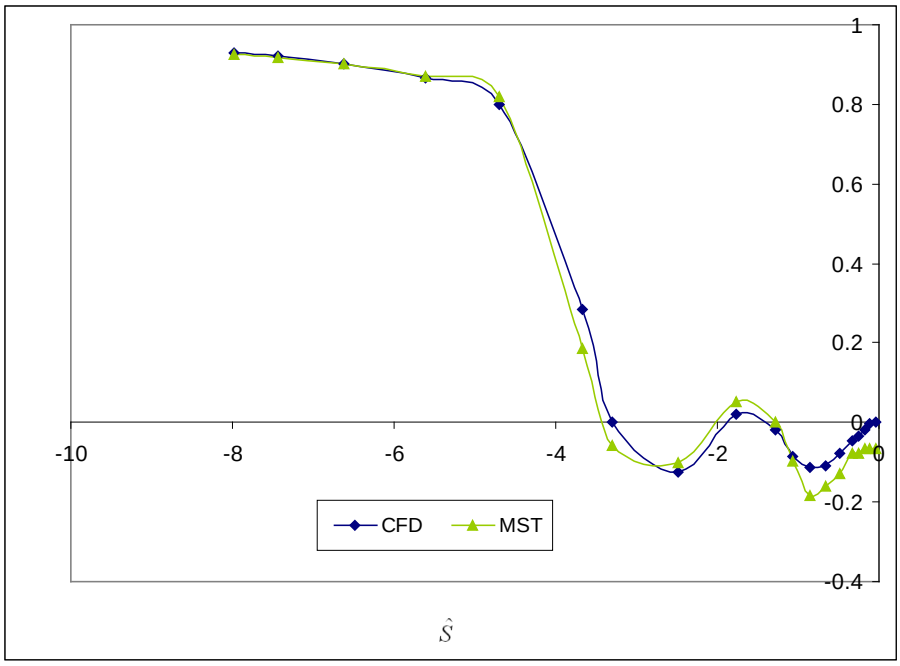

Figure 3-51 Comparison of C_P vs. $\hat{S}$ profiles derived from CFD and MST, along the shroud ($\hat{H}$ = 1), for CCN74 at a mass flow rate of 0.24 lbm/s and a wheel speed of 39k rpm.

Excellent agreement is reached at the beginning of the computational domain and the acceleration in the pre-u-bend region is also modeled very well. Further, the MST analysis appears to capture the acceleration and curvature of the u-bend flow as well as the CFD analysis does.

Figure 3-52 presents the now expected pattern in comparing the C_P vs. $\hat{S}$ profiles for the CFD results at the shroud ($\hat{H}$ = 1), the isentropic assumption and mass average for CCN74. The results are given for a mass flow rate of 0.30 lbm/s and a wheel speed of 39,000 rpm. The mass average C_P deviates from the isentropic C_P for CCN74 more than any other machine, with a deviation at the leading edge of 0.15 units. As the deviation is a measure of the irreversible losses in the flow, it is logical that the u-bend geometry experiences the most deviation.

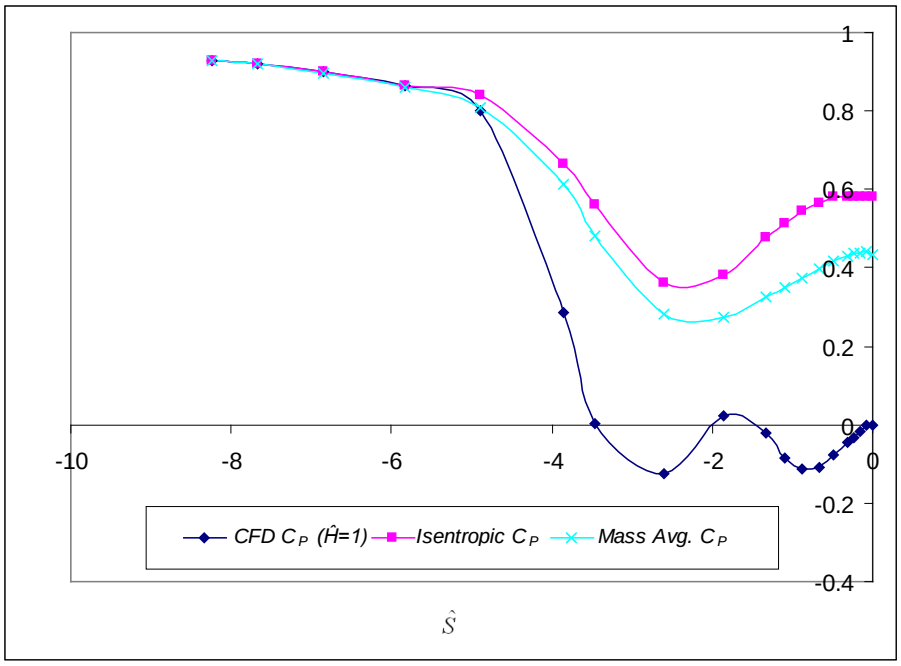

Figure 3-52 A comparison of representative C_P streamwise distributions derived from 1) CFD at $\hat{H}$ = 1, 2) the isentropic assumption, and 3) the mass averaged value derived from CFD for CCN74.

3.3.8 CCN95

CCN95 has an impeller exit diameter of 5.64 inches and operates at a nominal mass flow rate of 0.55 lbm/s and a wheel speed of 34,000 rpm. Table 3-9 provides general information for this machine. The geometry of CCN95 is similar to the majority of the designs in this investigation, as evidenced in Fig. 3-53. Further, Fig. 3-54 provides the pressure and efficiency maps for CCN95.

Table 3-9 General information for CCN95.

R1 tip (in)	R1 hub (in)	R2 (in)	N (rpm)	operating mflow (lbm/s)	P_0 (psi)	T_0 (deg R)	Grid Density (hs x bb x sw)	File Name
1.41	0.49	2.82	34k	0.55	14.10	554.7	29 x 25 x 169	CCN95-1.des

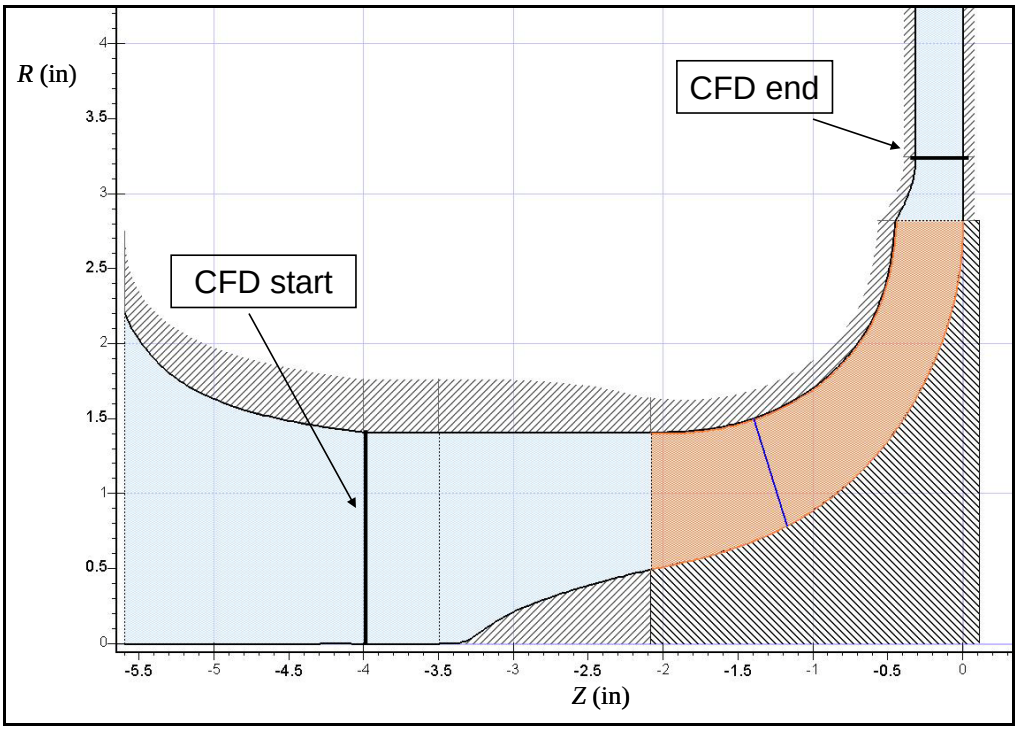

Figure 3-53 1-D representation of CCN95.

The C_P vs. $\hat{S}$ profile results for CCN95 follow a similar trend to those observed previously. However, consideration of the scale is imperative as Fig. 3-55 reveals an ordinate scale of 0.85 to 0.95. Reviewing previous design C_P vs. $\hat{S}$ data shows a typical C_P change of nearly an order of magnitude higher than observed for this machine. The minor change in C_P indicates that there is very little flow acceleration occurring through the CCN95 inlet passage. Further, the short constant area duct upstream of the bulletnose does not provide ample distance for the uniform spanwise flow condition to occur, as the spanwise locations ($\hat{H}$ = 0, 0.25, 0.5, 0.7, 0.9, 1) have yet to converge.

Another feature to consider while reviewing this machine is that while all other designs have a C_P value of nominally zero in the near blade region, CCN95 fails in this respect as the CFD does not accurately predict the static pressure measurement at the historically placed tap location. However, the 1-D isentropic calculation matches the

CFD results very well, indicating that error lies with either the actual experimental tap pressure measurement or in some flow phenomena which was not detected in the CFD analysis.

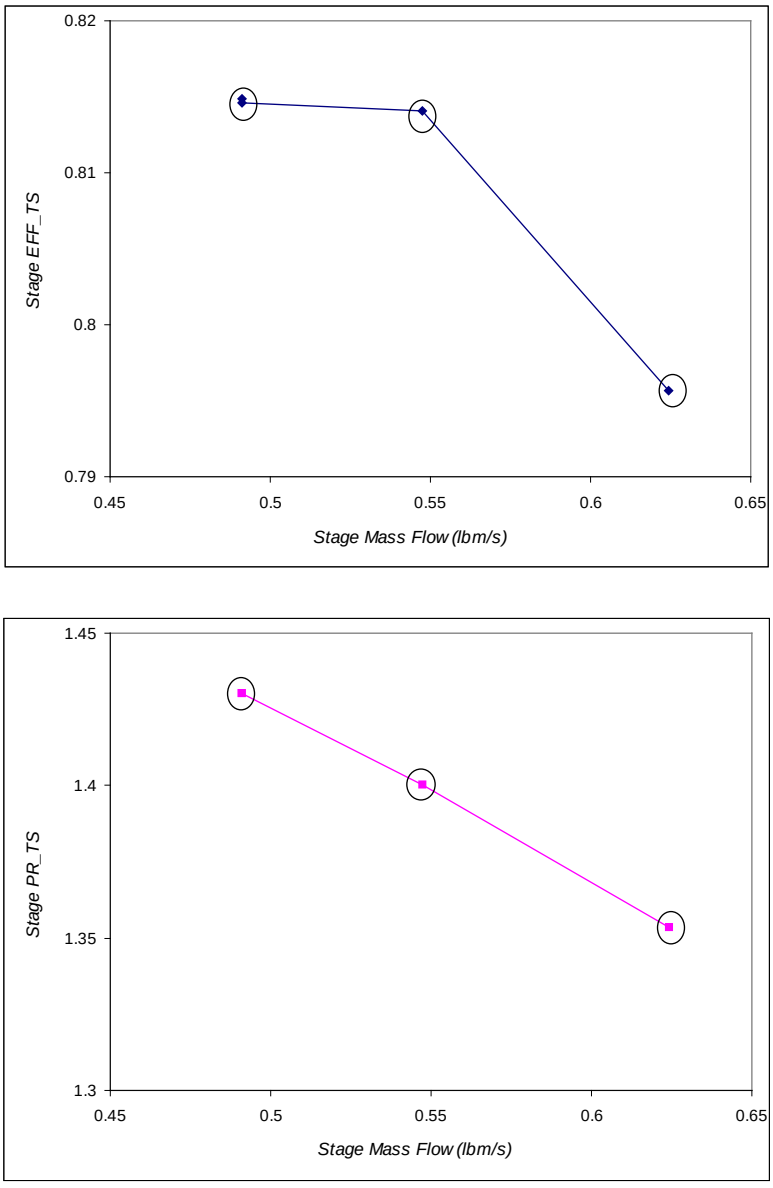

Figure 3-54 Stage total-to-static efficiency (top) and pressure ratio (bottom) maps for CCN95 operating at 34k rpm.

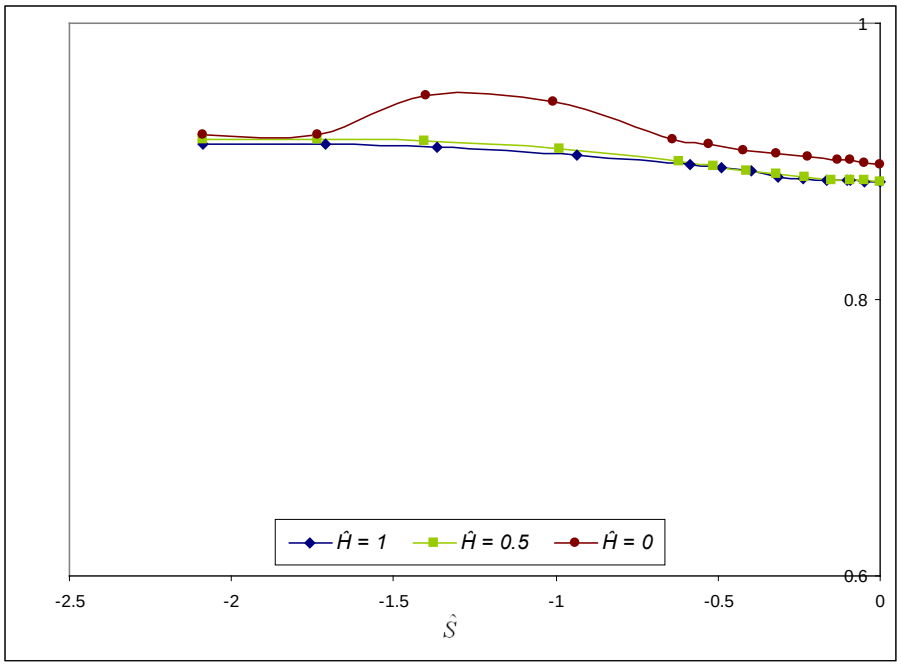

Figure 3-55 Blade-to-blade average C_P as a function of $\hat{S}$ for CCN95 at $\dot{m}$ = 0.55 lbm/s and N = 34k rpm for $\hat{H}$ = 0, 0.5 and 1.

Figure 3-56 reveals the comparison of the C_P vs. $\hat{S}$ profiles along the shroud ($\hat{H}$ = 1) for results derived from the CFD and MST analysis. The two numerical approaches agree on the C_P value at the beginning of the computational domain, and good agreement continues throughout the inlet passage. Results are presented for an operating mass flow rate of 0.55 lbm/s and wheel speed of 34,000 rpm.

The minor deviation of P_M from P_I in Fig. 3-57 illustrates that not only does CCN95 experience minimal acceleration, but it also indicates that the minor deviation of the mass average C_P from the isentropic C_P (measured just before the mass average dive) is a result of minimal irreversible losses in the inlet passage. Results are presented for the same conditions listed previously.

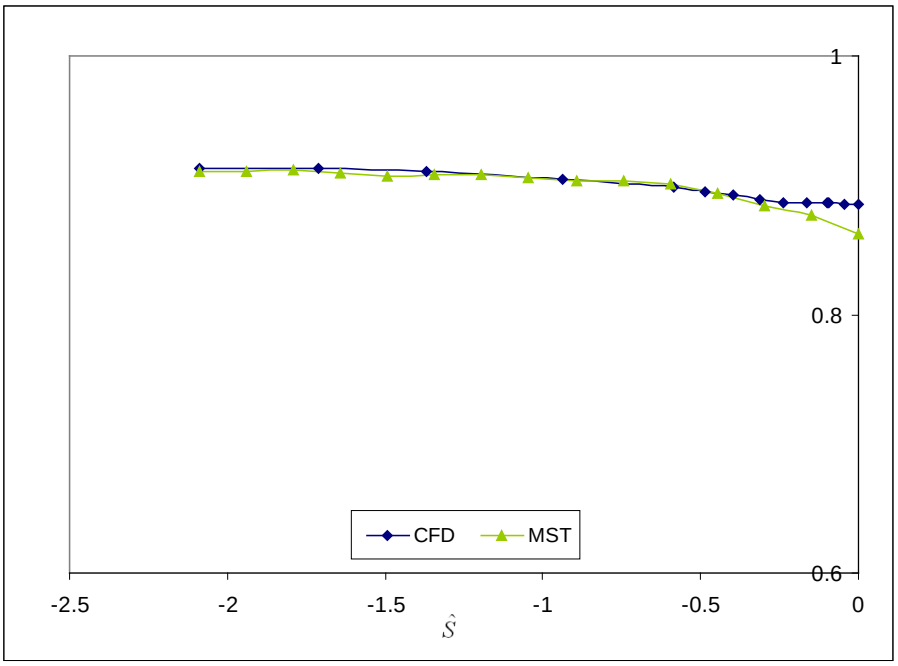

Figure 3-56 Comparison of C_P vs. $\hat{S}$ profiles derived from CFD and MST, along the shroud ($\hat{H}$ = 1), for CCN95 at a mass flow rate of 0.55 lbm/s and a wheel speed of 34k rpm.

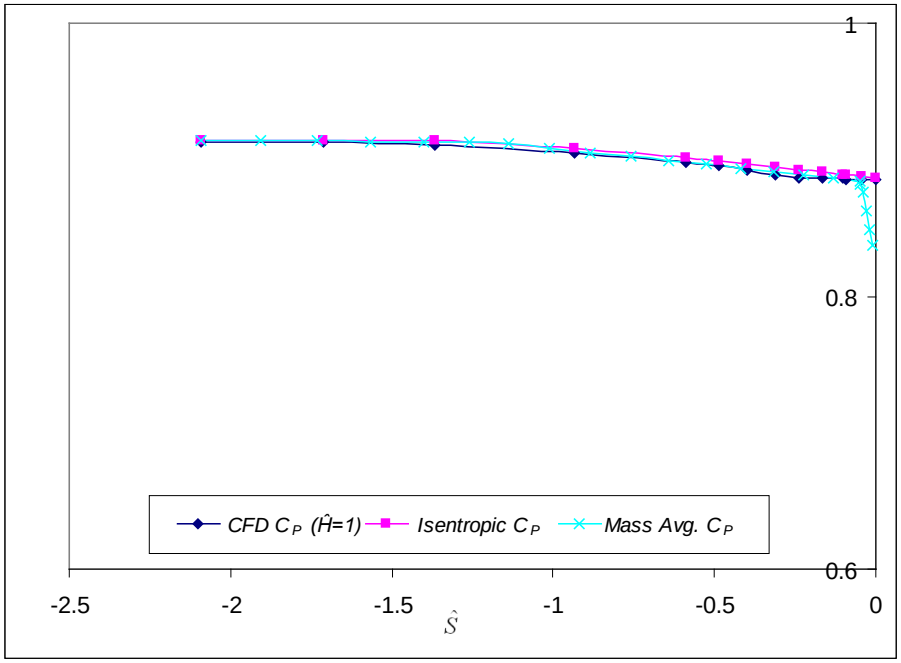

Figure 3-57 A comparison of representative C_P streamwise distributions derived from 1) CFD at $\hat{H}$ = 1, 2) the isentropic assumption, and 3) the mass averaged value derived from CFD for CCN95.

3.3.9 CPN7

CPN7 is the first pump investigated in this study. Figure 3-58 presents the 1-D representation of CPN7. While the 1-D pump representation appears to be very similar to the compressor designs, there are significant differences when viewed in 3-D, as illustrated in Fig. 3-51.

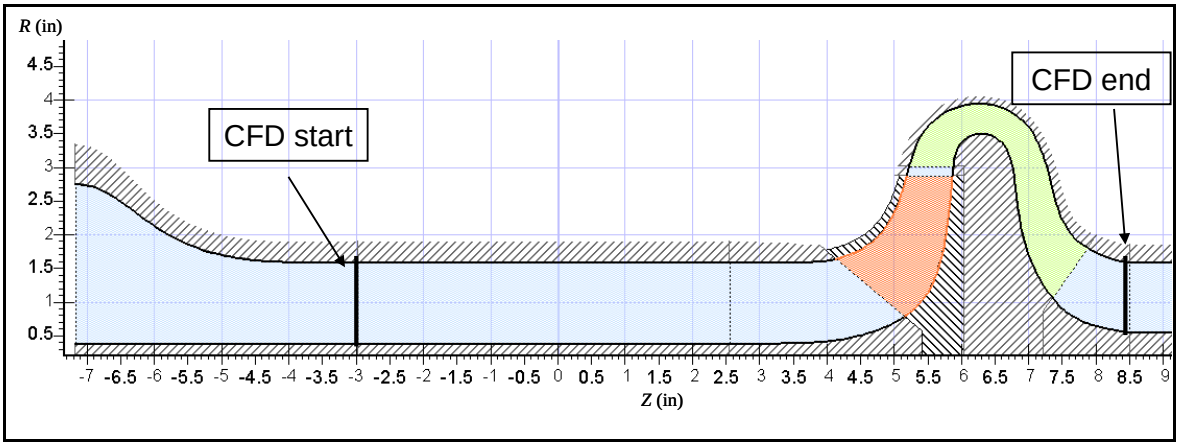

Figure 3-58 1-D representation of CPN7.

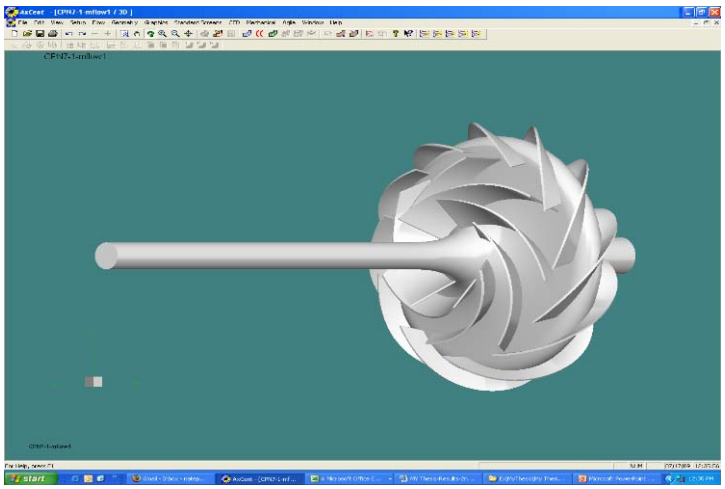

Figure 3-59 3-D representation of CPN7.

Geometrically, pumps are similar to compressors except that substantially more blade backsweep is employed and the rotors are usually shrouded on both sides, whereas the centrifugal compressor frequently has an unshrouded front face. For a detailed understanding of the function of pumps, the reader is recommended to pursue the introductory turbomachinery book by Japikse and Baines[7].

CPN7 has an exit diameter of 5.76 inches and operates at a nominal mass flow rate of 90 lbm/s and a wheel speed of 3,000 rpm. Of note is the design of the impeller blades as well as the radius of the hub. Physically the compressors have a zero radius hub until the bulletnose, whereas for this case an inlet hub radius of 0.4 inches prevails. Further, the computational domain extends much further downstream of the impeller exit, unlike previously considered machines where the computational domain extended only to the end of a short vaneless diffuser downstream of the impeller exit. Ending the domain at the end of the short diffuser present in this design prohibited the solver from converging. The general information of CPN7 is summarized in Table 3-10. Figure 3-60 presents the efficiency and head maps for CPN7. The stage total dynamic head (TDH), instead of the pressure ratio, is a standard parameter for pumps, and is defined as[19]

$$TDH = \frac{P_{in} - P_{out}}{\rho g} \qquad \textbf{(3- 3)}$$

It represents the total equivalent height that a fluid is to be pumped.

Table 3-10 General information for CPN7.

R1 tip (in)	R1 hub (in)	R2 (in)	N (rpm)	operating mflow (lbm/s)	P_0 (psi)	T_0 (deg R)	Grid Density (hs x bb x sw)	File Name
1.65	0.79	2.88	3k	90.26	14.10	540	33 x 29 x 185	CPN7-1.des

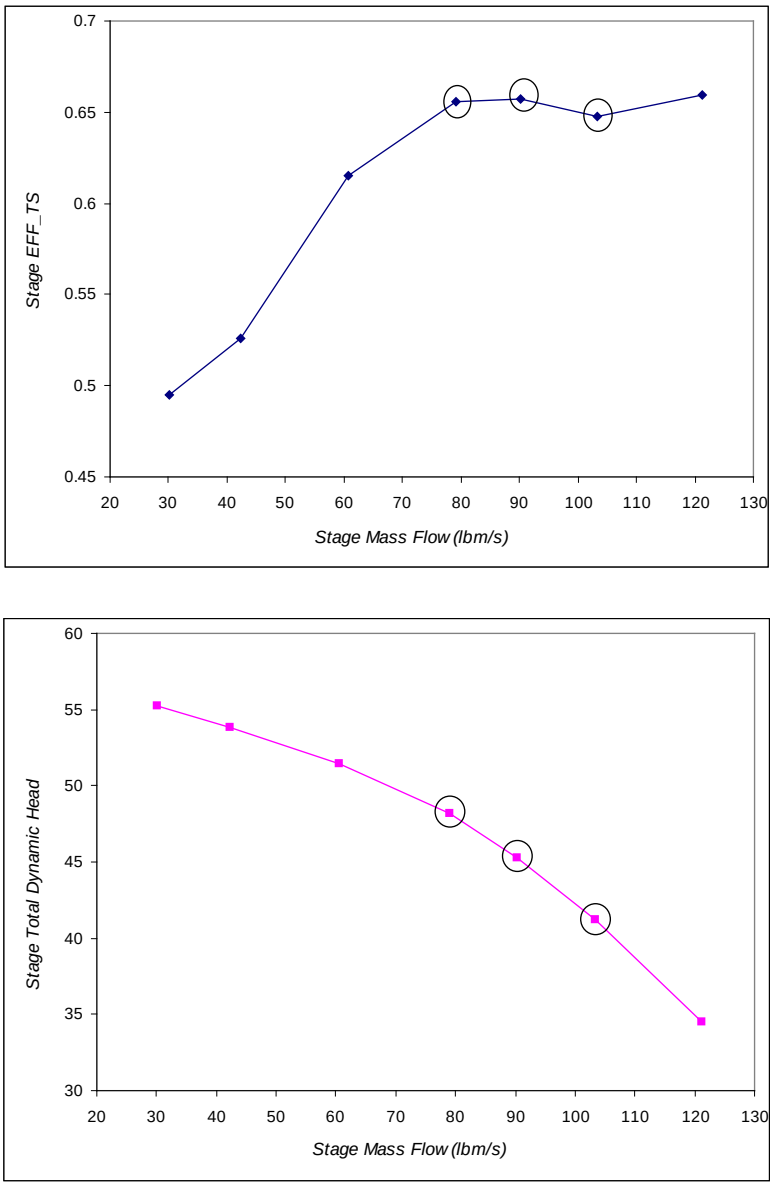

Figure 3-60 Stage total-to-static efficiency (top) and total dynamic head (bottom) maps for CPN7 operating at 3k rpm.

A unique C_{Pc} vs. $\hat{S}$ profile for CPN7 is observed in Fig. 3-61. For this scenario C_{Pc} is plotted instead of C_P because the experimental pressure value for this machine could not be trusted. The results correspond to a mass flow rate of 90.26 lbm/s and a

wheel speed of 3,000 rpm. The large inclination angle (40 degrees) of the impeller blade leading edge results in the hub stagnation point existing downstream of the streamwise shroud leading edge location ($\hat{S} > 0$). However the pump acts in a manner similar to the compressors in that there are high gradients in the near vicinity of the leading edge. Further, at about 3 blade heights upstream of the impeller leading edge ($\hat{S} \approx -3$) the C_{Pc} vs. $\hat{S}$ are flattening and collapsing indicating a region of uniform flow behavior.

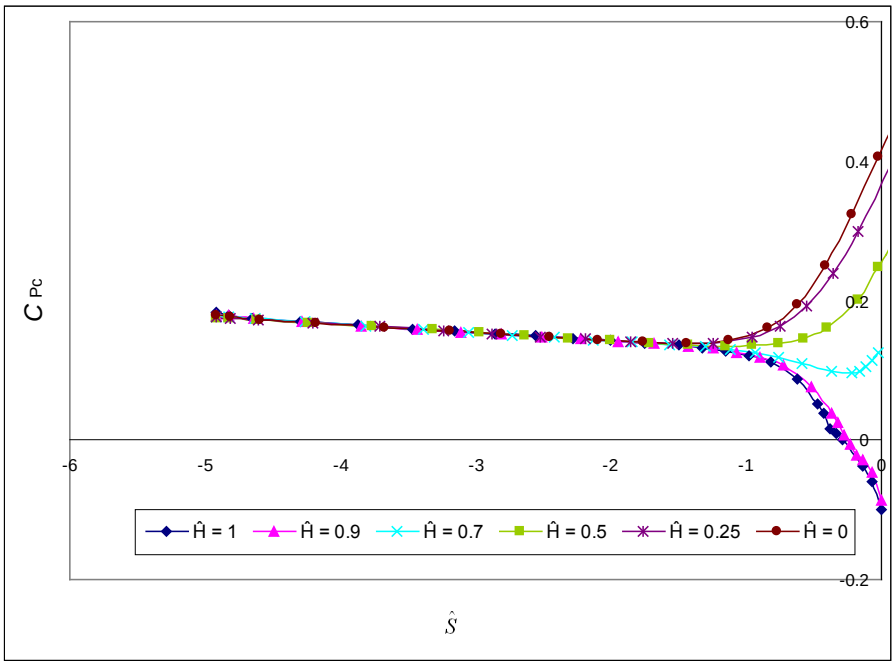

Figure 3-61 Blade-to-blade average C_{Pc} as a function of $\hat{S}$ for CPN7 at $\dot{m}$ = 90.26 lbm/s and N = 3k rpm for $\hat{H}$ = 0, 0.25, 0.5, 0.7, 0.9 and 1.

The comparison of the C_{Pc} profile derived from results of the CFD and MST analysis is presented along both the shroud ($\hat{H}$ = 1, Fig. 3-62) and hub ($\hat{H}$ = 0, Fig. 3-63) lines to depict the agreement between the two approaches at both spanwise locations. As with previously considered machines, the good agreement at both the shroud and hub for CPN7 is indicative of the agreement found across the passage in the compressor inlet.

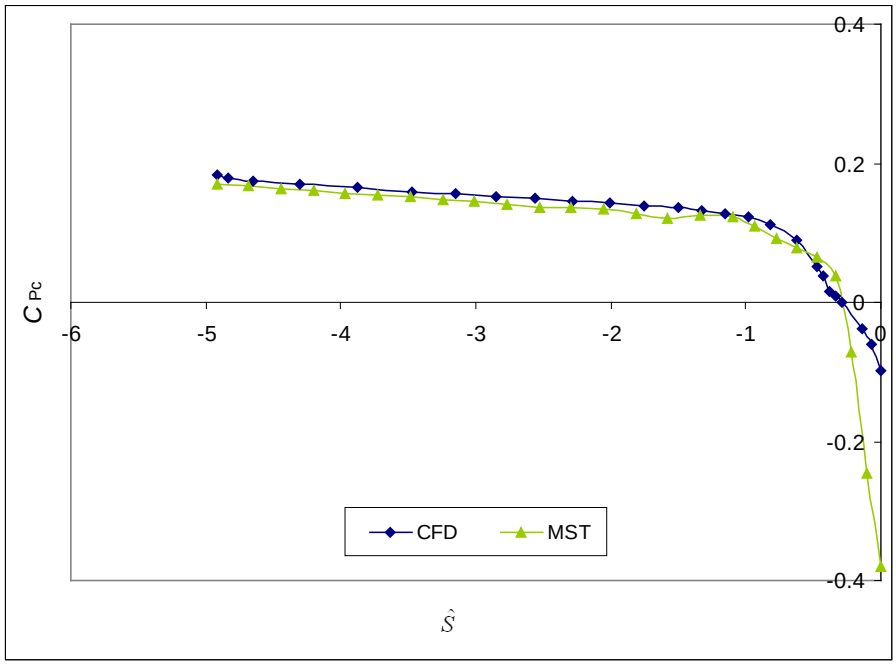

Figure 3-62 Comparison of C_{Pc} vs. $\hat{S}$ profiles derived from CFD and MST, along the shroud ($\hat{H}$ = 1), for CPN7 at a mass flow rate of 90.26 lbm/s and a wheel speed of 3k rpm.

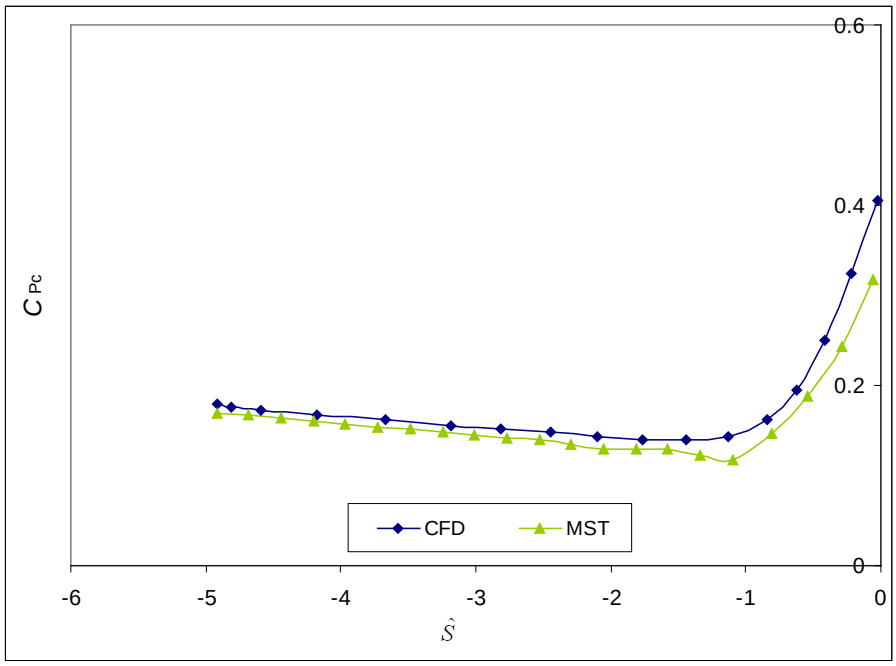

Figure 3-63 Comparison of C_{Pc} vs. $\hat{S}$ profiles derived from CFD and MST, along the hub ($\hat{H}$ = 0), for CPN7 at a mass flow rate of 90.26 lbm/s and a wheel speed of 3k rpm.

The comparison of the C_{Pc} vs. $\hat{S}$ profiles for the CFD results at the shroud ($\hat{H}$ = 1), the isentropic assumption and mass average for CPN7 is presented in Fig. 3-64. The results are extracted from analysis performed at a mass flow rate of 90.26 lbm/s and a wheel speed of 3,000 rpm. The mass averaged static pressure, P_M, deviates from the isentropic local static pressure, P_I, similar as observed for previous machines. While the entire inlet region is not presented (the inclination angle pushes some of the data downstream of the shroud leading edge streamwise location) irreversible loss again appears to be responsible for the observed deviation in the two pressure values.

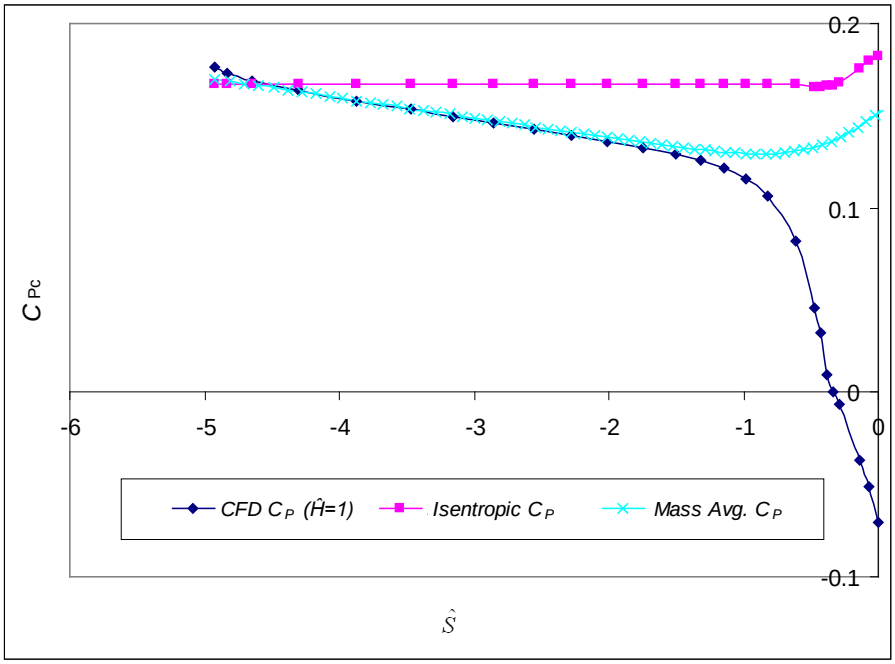

Figure 3-64 A comparison of representative C_{Pc} streamwise distributions derived from 1) CFD at $\hat{H}$ = 1, 2) the isentropic assumption, and 3) the mass averaged value derived from CFD for CPN7.

3.3.10 CPN28

CPN28 has an impeller exit diameter of 5.00 inches, a nominal mass flow rate of 130 lbm/s and an operating wheel speed of 3,000rpm. Table 3-11 summarized the basic general machine information.

Table 3-11 General information for CPN28.

R1 tip (in)	R1 hub (in)	R2 (in)	N (rpm)	operating mflow (lbm/s)	P_0 (psi)	T_0 (deg R)	Grid Density (hs x bb x sw)	File Name
2.69	1.68	3.75	3k	133.39	14.10	540	37 x 41 x 237	CPN28-1.des

Figure 3-65 presents the 1-D representation of CPN28. While there are similarities between the pump and compressor in the 1-D frame, the functionality of the machine type requires them to look fundamentally different in 3-D, as seen in Fig. 3-66. Figure 3-67 depicts the efficiency and head maps for CPN28.

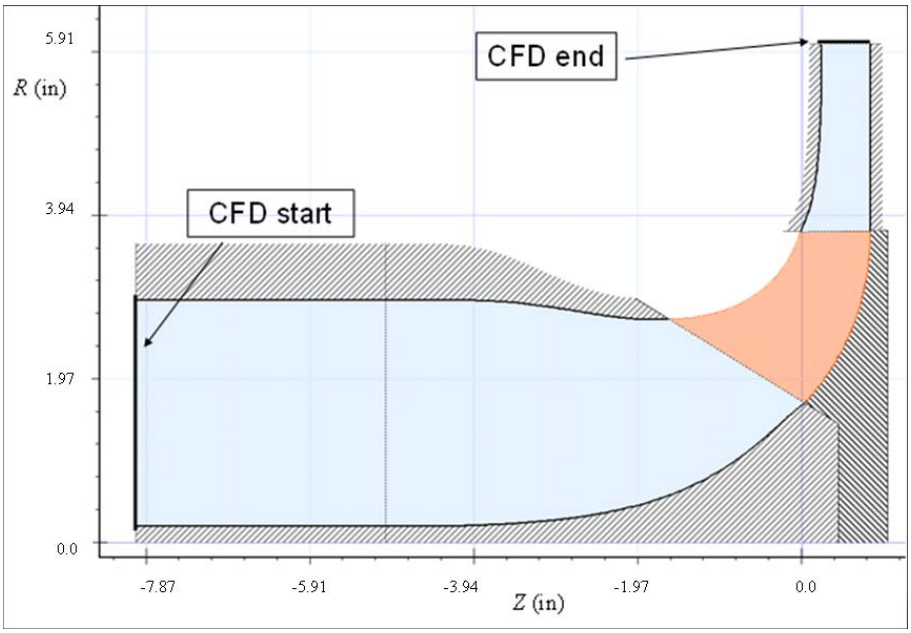

Figure 3-65 1-D representation of CPN28.

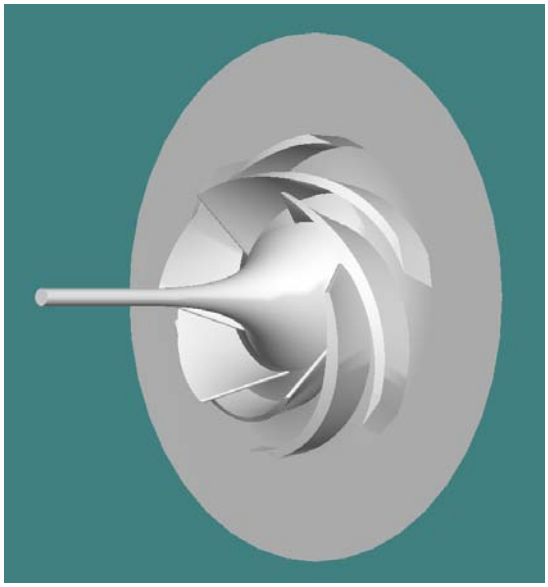

Figure 3-66 3-D representation of CPN28.

The C_P vs. $\hat{S}$ profile from the CFD analysis is presented in Fig. 3-68 for a mass flow rate of 133.39 lbm/s and a wheel speed of 3000 rpm. All six spanwise locations ($\hat{H}$ = 0, 0.25, 0.5, 0.7, 0.9, and 1) are presented in order to illustrate the variation of the profiles between compressors and pumps. Despite the differences in geometry, the basic trends are consistent with previous observations; the flow is nearly uniform about 3 blade heights upstream of the impeller leading edge ($\hat{S} \approx -3$) and there is a steep gradient in C_P in the vicinity of the leading edge.

Figure 3-69 compares the C_P vs. $\hat{S}$ profiles for the results derived from the CFD and MST analysis for the same flow conditions as the data of Fig. 3-68 and it is readily apparent that excellent agreement exists between the two approaches. This agreement is valuable because one secondary intent of the study is to show how MST and CFD can assist the design process of 1-D modeling procedures. MST is much easier and faster to run than CFD, and consequently if the two methods produce similar results, this provides

an opportunity for MST to be used with greater validity in future design work . Figure 3-70 compares the C_P vs. $\hat{S}$ profiles for the CFD results at the shroud ($\hat{H}$ = 1), the isentropic and mass average calculations. The deviation of P_M from P_I is minor for this case, and again the impeller inclination angle causes the dive in P_M to occur at $\hat{S} > 0$.

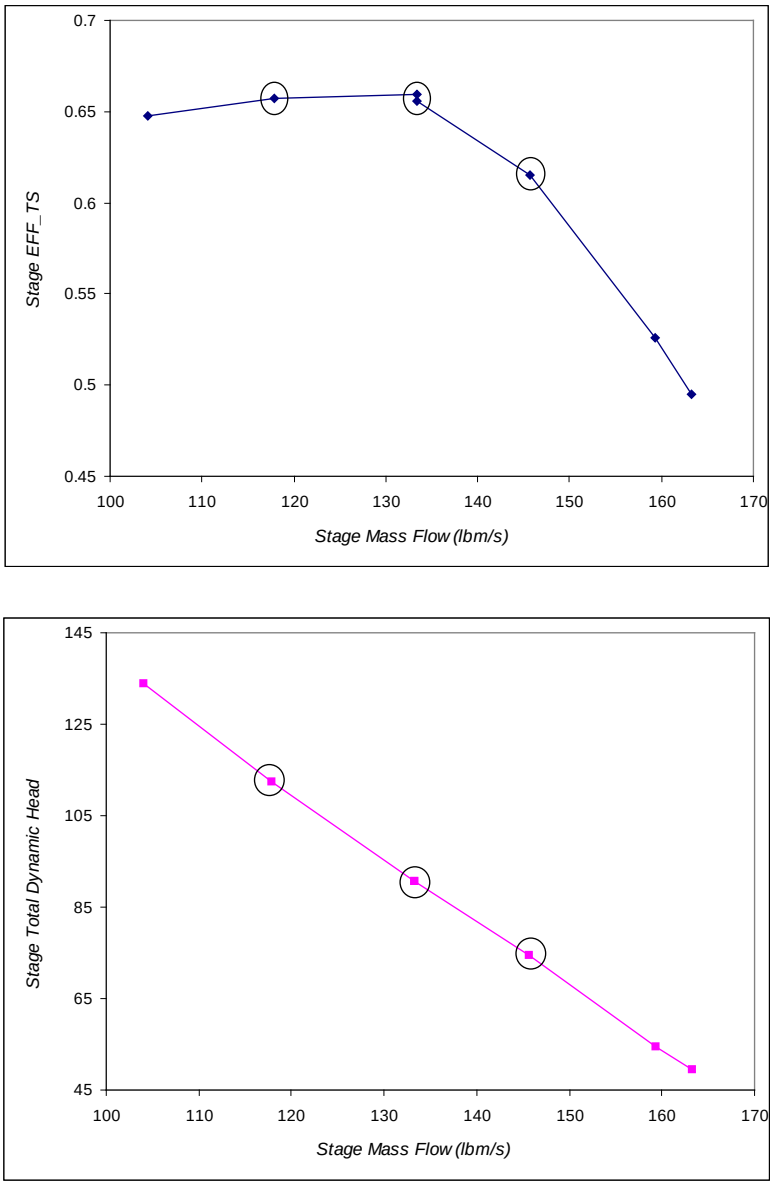

Figure 3-67 Stage total-to-static efficiency (top) and total dynamic head (bottom) maps for CPN28 operating at 3k rpm.

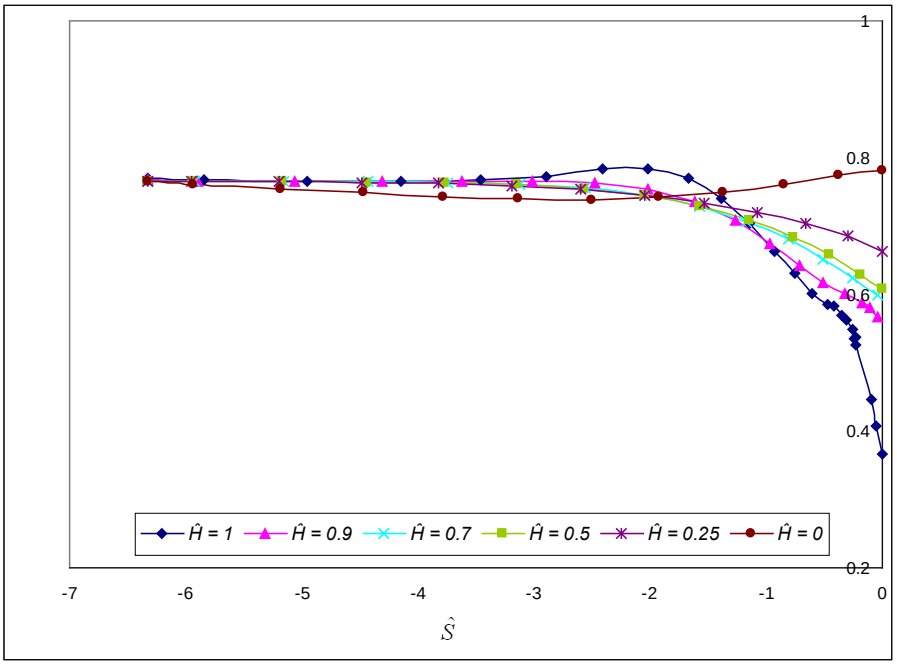

Figure 3-68 Blade-to-blade average C_P as a function of $\hat{S}$ for CPN28 at $\dot{m}$ = 133.39 lbm/s and N = 3k rpm for $\hat{H}$ = 0, 0.25, 0.5, 0.7, 0.9 and 1.

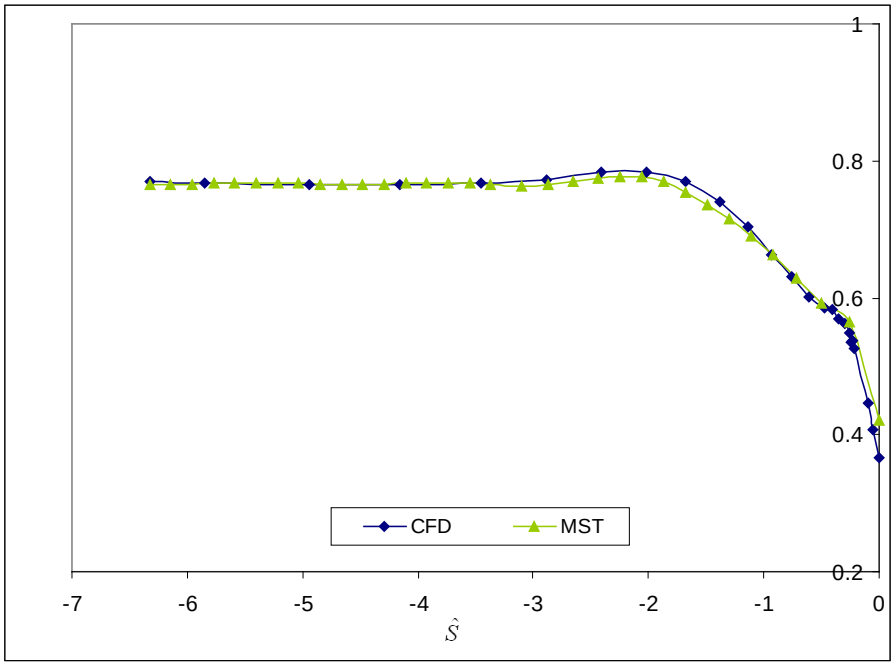

Figure 3-69 Comparison of C_P vs. $\hat{S}$ profiles derived from CFD and MST, along the shroud ($\hat{H}$ = 1), for CPN28 at a mass flow rate of 133.39 lbm/s and a wheel speed of 3k rpm.

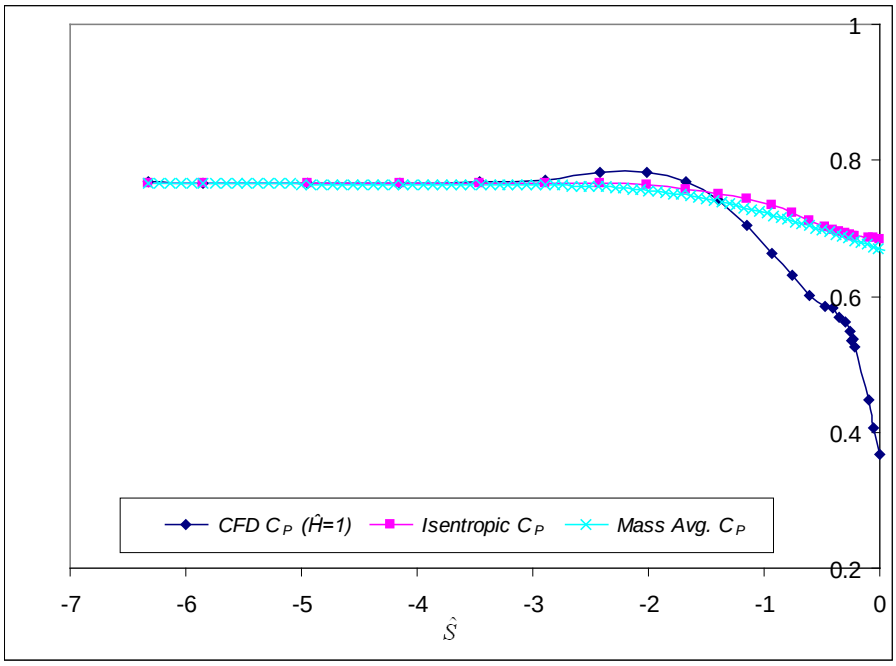

Figure 3-70 A comparison of representative C_P streamwise distributions derived from 1) CFD at $\hat{H}$ = 1, 2) the isentropic assumption, and 3) the mass averaged value derived from CFD for CPN28.

3.4 Recapitulation

Extensive CFD analysis has been conducted for 11 centrifugal turbomachines. Summary results have been presented herein with regard to streamwise variations in the static pressure. Experimental data at 1 location is compared to information gleaned from the CFD and MST solutions. For all scenarios the following information is available: the C_P vs. $\hat{S}$ profiles through the inlet passage, a comparison of the C_P vs. $\hat{S}$ profiles derived from the CFD and MST analysis, and a comparison of the same profiles for the CFD results at the shroud ($\hat{H}$ = 1), the isentropic assumption and mass average.

All information is provided to answer the key questions of the study: 1) is the historical experimental pressure tap location appropriate? 2) If it is not appropriate, is there a better location for the improvement of the TEIS modeling formulation?

Figure 3-71 shows the *C*P vs. $\hat{S}$ data on the shroud ($\hat{H}$ = 1) line for each machine considered. Generally simulations are compared to data at a mass flow rate about half way between stall and choke. However, based on how the results of the individual mass flow rates collapse, there is no evidence of the effects of stall or choke in the simulations. These results provide answers to the questions of interest and provide insight for some general conclusions.

3.4.1 Appropriateness of Tap Location

The appropriateness of the tap location is assessed by evaluation of the C_P vs. $\hat{S}$ profiles for the individual designs and by comparing all the designs in the study. Individual profiles reveal a high gradient often exists at the impeller leading edge region, extending from the impeller blade leading edge ($\hat{S}$ = 0) and traversing upstream at a minimum to the introduction of the bulletnose ($\hat{S} \approx -1.5$). The location of the experimental pressure tap was generally determined subjectively by the designer on the assumption that simple flow conditions existed in the near blade region. Results derived from present CFD and MST analysis counter that assumption and reveal that a relatively minor movement of the static pressure tap would significantly alter the experimental results.

Figure 3-71 shows a region of high acceleration in the vicinity of the impeller leading edge with the assumption of a simple inlet flow condition here not supported by the results. Further, the results show that significant diversity and deviation between individual designs exist and this deviation is a result of irreversible losses present in the flow.

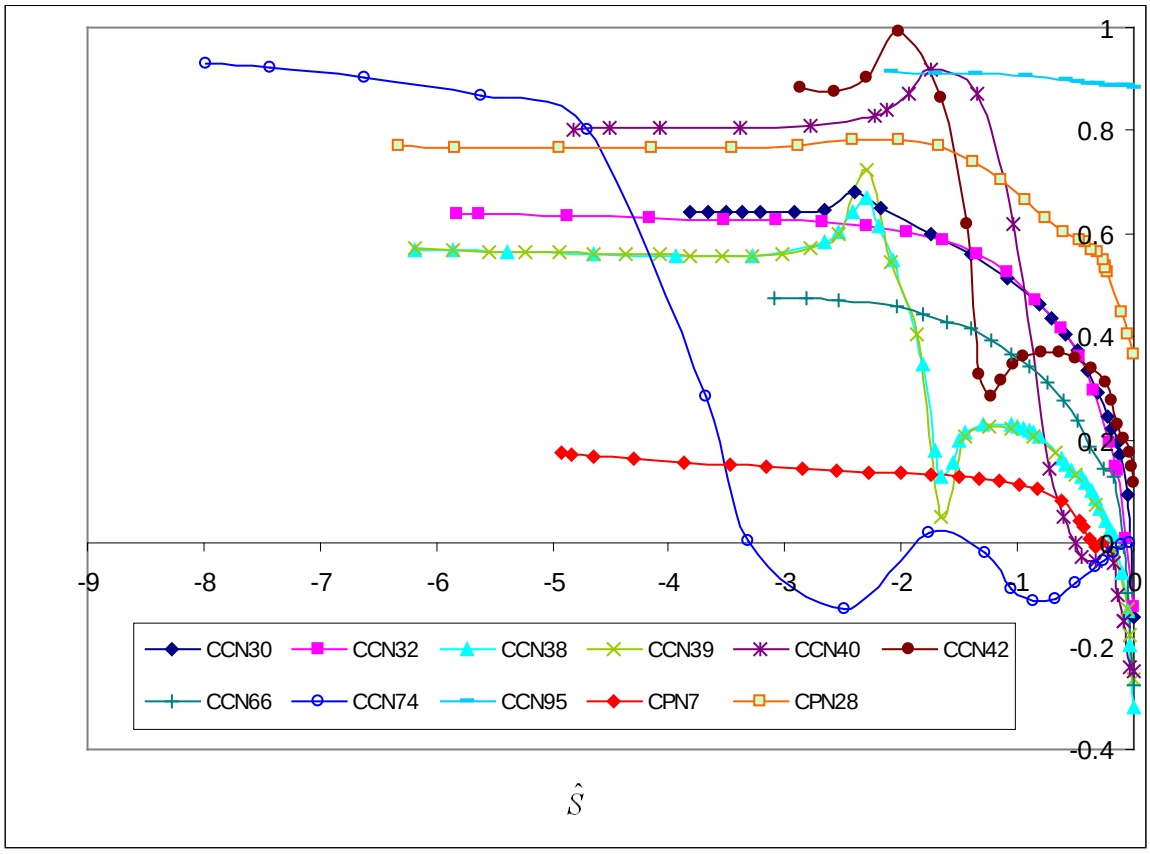

Figure 3-71 Comparison of the C_P vs. $\hat{S}$ profile along the shroud ($\hat{H}$ = 1) for each Centrifugal Compressor or Pump Number (CCN or CPN) investigated.

The results of the study show that far upstream of the blade inlet a region of nearly uniform and well predicted flow prevails. For a straight inlet (standard inlet of a radial flow centrifugal compressor, used in most of the designs in this study) this location is at about 3 blade heights upstream from the leading edge ($\hat{S} \approx -3$). For the u-bend geometry this location is about one blade height upstream of the bend. Generally, an appropriate location is at least one blade height upstream of any area contraction in the inlet region, whether it be the bullet nose or along the shroud, yet downstream of any bell mouth that may exist physically. At this location the flow for all machines explored here exhibits a nominally uniform flow condition, evidenced in the previous C_P vs. $\hat{S}$ profiles.

In addition to the investigation of the C_P vs. $\hat{S}$ profile for each machine, consideration was made regarding the static pressure at the historical pressure tap location derived from the experimental, CFD and MST analysis. While C_P traversed through nominally zero at the historical tap location, the proximity to zero is dependent upon how accurate of a match that CFD and MST predict when comparing to the experimental static pressure. Table 3-12 summarizes the results of this comparison for all mass flow rates considered for each machine. The 2nd column looks at the difference between the static pressure at the historical pressure tap location derived from the experimental and CFD analysis. The 3rd column compares the pressures derived from the CFD and MST analysis. Generally, the CFD and MST analysis are in good agreement, while the experimental and CFD analysis tend to disagree a bit more. The general discrepancy between the physical measurement and the numerical simulation suggests that while the two numerical methods agree, they fail to detect axisymmetric or unsteady distortion which may exist physically.

In addition to the comparison in the 2nd and 3rd columns, Table 3-12 compares a stage pressure ratio, of sorts. The static pressure at the impeller exit, P_2, is compared to the total pressure at the inlet of the computational domain, P_0. P_2 is greater than P_0 as a result of the energy added to the flow as it traveled through the impeller, and consequently P_0 is subtracted from P_2. This is done for both the experimental data, provided by ConceptsNREC, and for the results derived from the CFD analysis.

Table 3-12 Comparison of the static pressure derived from the experimental, CFD and MST results at the historical tap location for all mass flow rates considered.

Machine Name	mflow (lbm/s)	abs[P_{1t} (Exp.) - P_{1t} (CFD)] (psi)	abs[P_{1t} (CFD) - P_{1t} (MST)] (psi)	P_2-P_0 (Data) (psi)	P_2-P_0 (CFD) (psi)	% Difference
CCN30	0.48	0.18	0.16	10.03	9.73	2.99
	0.51	0.32	0.09	9.02	8.47	6.10
	0.55	0.47	0.26	7.25	2.1	71.03
CCN32	0.19	0.07	0.01	13.60	13.78	-1.32
	0.23	0.16	0.04	12.83	13.00	-1.33
	0.27	0.22	0.07	11.78	11.90	-1.02
	0.30	0.21	0.06	10.82	10.79	0.28
CCN38	0.58	0.47	0.20	11.08	13.9	-25.45
	0.66	0.42	0.23	10.57	13.13	-24.22
	0.72	0.40	0.21	9.81	11.36	-15.80
CCN39	0.68	0.40	0.23	10.66	11.21	-5.16
	0.73	0.33	0.38	9.73	10.28	-5.65
	0.75	0.33	0.06	9.33	9.02	3.32
CCN40	0.36	0.11	0.05	14.52	15.41	-6.13
	0.40	0.14	0.07	14.11	14.94	-5.88
	0.45	0.21	0.11	13.46	14.1	-4.75
	0.49	0.28	0.15	12.85	13.16	-2.41
CCN42	1.08	0.04	0.02	8.76	7.81	10.84
	1.25	0.10	0.01	8.35	7.54	9.70
	1.38	0.06	0.07	7.88	7.46	5.33
	1.49	0.03	0.04	7.27	7.06	2.89
	1.61	0.00	0.06	6.26	6.45	-3.04
CCN66	4.09	0.01	0.02	9.57	9.92	-3.66
	5.20	0.09	0.02	8.32	8.95	-7.59
	6.07	0.19	0.04	6.48	7.73	-19.33
CCN74	0.24	0.01	0.04	5.79	9.06	-56.48
	0.30	0.02	0.05	5.58	8.78	-57.35
	0.33	0.03	0.04	5.23	8.46	-61.76
	0.37	0.05	0.04	4.88	8.04	-64.75
CCN95	0.49	0.64	0.08	4.18	4.34	-3.76
	0.55	0.86	0.06	3.81	4.34	-13.76
	0.62	1.22	0.02	3.29	4.30	-30.70
CPN7	79.10	N/A	1.15	23.61	20.03	15.16
	90.26	N/A	1.28	22.48	18.05	19.70
	103.37	N/A	1.23	21.28	15.38	27.71
CPN28	117.98	1.10	0.10	26.82	24.68	7.98
	133.39	1.19	0.07	21.88	18.88	13.68
	145.64	1.76	0.06	17.49	13.38	23.49

While the focus of the study is the characterization of inlet flow dynamics, checking a more global pressure variation validates the results as a whole. Generally the experimental results do not match the CFD results that well. However, the slope derived from each method is consistent for most of the designs, indicating that the CFD analysis is doing an adequate job and analyzing the flow. These slopes are compared in for CCN32 (Fig. 3-72), CCN40 (Fig. 3-73), CCN74 (Fig. 3-75) and CPN28 (Fig. 3-76).

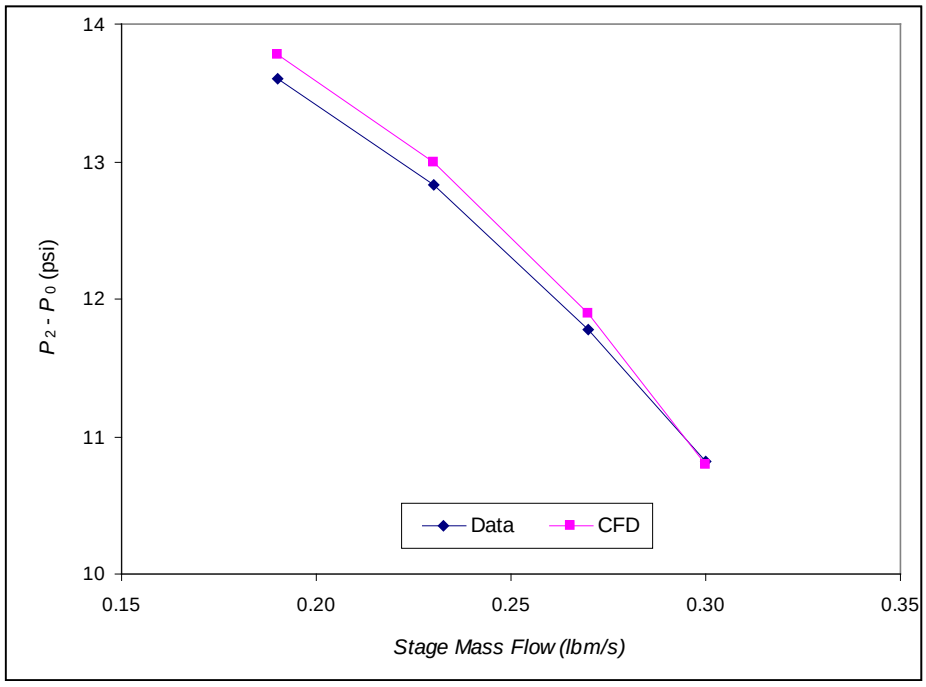

Figure 3-72 Comparison of the static pressure at the impeller exit, P_2, with the inlet total pressure, P_0, from the measured data and CFD analysis for all mass flow rates investigated in CCN32.

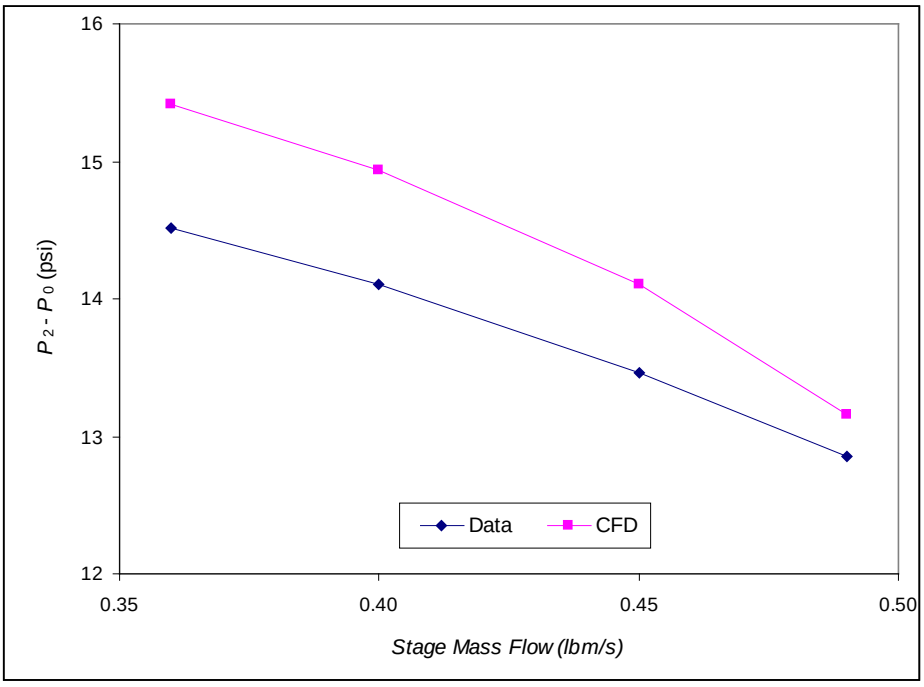

Figure 3-73 Comparison of the static pressure at the impeller exit, P_2, with the inlet total pressure, P_0, from the measured data and CFD analysis for all mass flow rates investigated in CCN40.

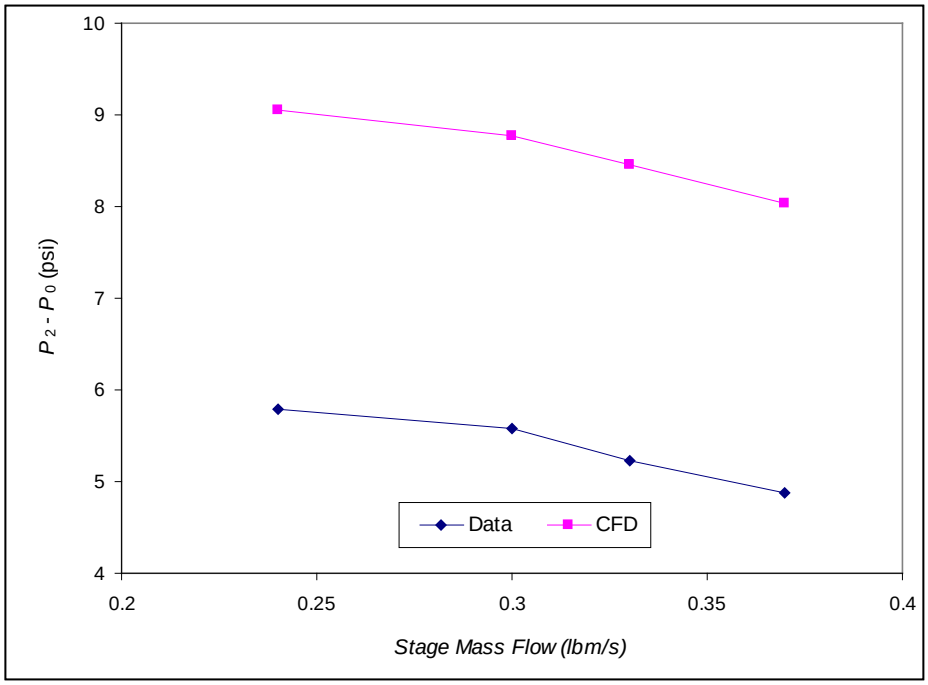

Figure 3-74 Comparison of the static pressure at the impeller exit, P_2, with the inlet total pressure, P_0, from the measured data and CFD analysis for all mass flow rates investigated in CCN74.

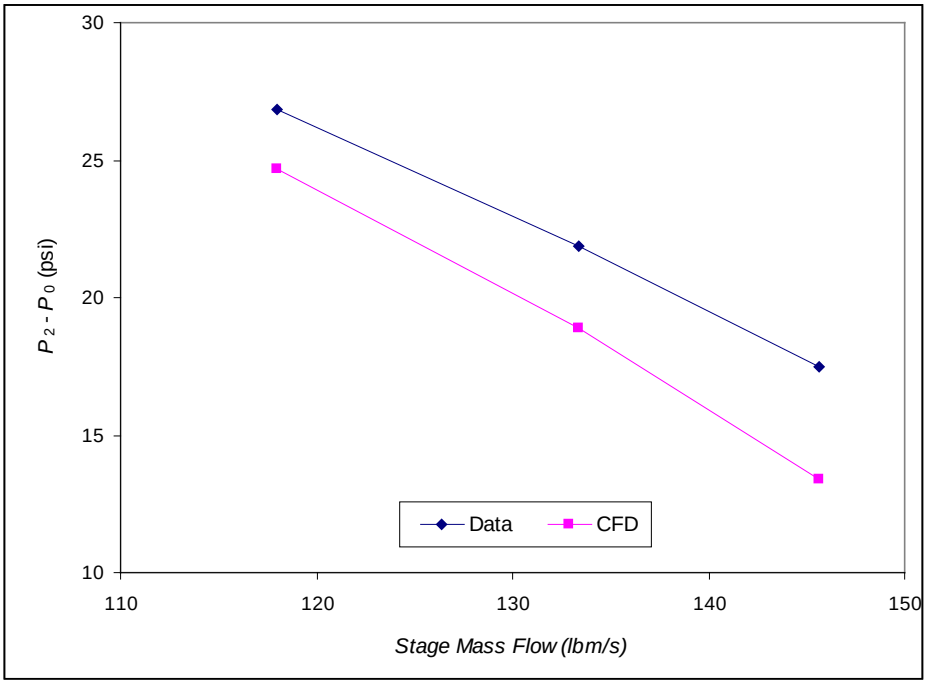

Figure 3-75 Comparison of the static pressure at the impeller exit, P_2, with the inlet total pressure, P_0, from the measured data and CFD analysis for all mass flow rates investigated in CPN28.

Of further interest is a characterization of the deviation of the mass averaged pressure coefficient, derived from $P_{M,}$ from the static pressure coefficient derived from a 1-D isentropic pressure, P_I, for each machine. The deviation is calculated just upstream of the impeller leading edge. For those cases where the dive in P_M is upstream of the shroud leading edge streamwise location ($\hat{S} < 0$) the deviation will be calculated just before the dive, whereas for all other cases the deviation will be calculated at $\hat{S} = 0$. Table 3-13 summarizes the deviation for each machine.

Table 3-13 Deviation of mass averaged C_P (from P_M) from 1-D isentropic C_P (from P_I) in the vicinity of the impeller leading edge for all mass flow rates considered.

Machine Name	mflow (lbm/s)	C_P (P_M)	C_P (P_I)	% Deviation
CCN30	0.48	0.109	0.200	45.5.
	0.51	0.166	0.247	32.9
	0.55	0.202	0.280	27.8
CCN32	0.19	0.146	0.217	32.8
	0.23	0.204	0.276	26.1
	0.27	0.209	0.279	25.2
	0.30	0.181	0.257	29.5
CCN38	0.58	-0.016	-0.009	76.5
	0.66	0.053	0.057	7.8
	0.72	0.044	0.052	16.2
CCN39	0.68	0.022	0.037	41.6
	0.73	0.034	0.047	26.5
	0.75	0.037	0.038	2.3
CCN40	0.36	0.095	0.156	39.3
	0.40	0.155	0.208	25.5
	0.45	0.186	0.233	20.1
	0.49	0.144	0.177	18.6
CCN42	1.08	0.204	0.281	27.4
	1.25	0.25	0.302	17.4
	1.38	0.114	0.163	30.0
	1.49	0.126	0.176	28.2
	1.61	0.132	0.179	26.3
CCN66	4.09	0.234	0.250	6.3
	5.20	0.249	0.271	8.2
	6.07	0.228	0.253	9.9
CCN74	0.24	0.432	0.583	25.9
	0.30	0.461	0.577	20.1
	0.33	0.391	0.513	23.8
	0.37	0.463	0.570	18.8
CCN95	0.49	0.849	0.859	1.2
	0.55	0.869	0.873	0.5
	0.62	0.883	0.887	0.5
CPN7	79.10	0.150	0.182	17.6
	90.26	0.146	0.172	15.1
	103.37	0.144	0.169	14.8
CPN28	117.98	0.667	0.684	2.5
	133.39	0.645	0.652	1.1
	145.64	0.652	0.661	1.4

3.4.2 TEIS Model Reformulation

The current TEIS model is dependent on accurate prediction of the inlet effectiveness η_a. Current calculation of η_a from experimental results is accomplished primarily by utilizing the relative velocity at the impeller leading edge tip, W_{1t}, derived from the experimentally determined static pressure at the same location, P_{1t}. This is accomplished by the conservation equations with the mass flow rate, pressure and geometry known. The present investigation and analysis has shown that the P_{1t} measurement, and consequently the W_{1t} calculation are inappropriate for the modeling procedure. The results also suggest that a location upstream of the impeller leading edge ($\hat{S} \approx -3$) provides an excellent point to anchor for the TEIS modeling procedure.

As illustrated throughout this chapter, the 1-D isentropic calculation approximates very well the CFD solution at the upstream location ($\hat{S} \approx -3$). It is suggested that the TEIS model be reformulated about this point. This study does not propose a statistically improved model for η_a. However, building a model for η_a based on this more appropriate passage location should more accurately represent the physical flow conditions, reduce noise and improve upon the accuracy of the current Pelton model.

4 Conclusions and Recommendations

4.1 Conclusions

The flow field in the inlet region of several radial flow turbomachines has been characterized in order to investigate the appropriateness of historical assumptions regarding the inlet dynamics. Specific emphasis was placed on understanding how the local static pressure varied in the vicinity of the impeller leading edge with particular attention given to variations near the historically placed experimental pressure tap location. Full computational fluid dynamics (CFD) and multi-streamtube (MST) analysis was performed on 11 previously designed and tested centrifugal turbomachines. These designs, as well as the experimental results, were supplied by the study sponsor ConceptsNREC and were selected to provide a wide variety of geometric sizes and flow conditions, with 9 compressors and 2 pumps. A pressure coefficient, C_P, was derived from the CFD and MST analysis and plotted against a nondimensional distance upstream of the impeller leading edge ($\hat{S}$). The profiles of C_P vs. $\hat{S}$ derived from the CFD and MST analysis were compared to verify agreement between the inviscid multi-streamtube analysis and the viscid, full 3-D turbulent RANS solver. Further the C_P vs. $\hat{S}$ profiles for the CFD results at the shroud ($\hat{H} = 1$), the isentropic assumption and mass average were compared in order to investigate the deviation of the mass averaged static pressure, $P_{M,}$ from the ideal local static pressure, P_I.

Investigation of flow dynamics in the vicinity of the impeller inlet reveals that the historical assumption regarding inlet dynamics was inappropriate. Steep streamwise gradients in C_P are present in the vicinity of the impeller leading edge, a by product of the inlet passage area contraction and the entrainment of flow into the impeller inlet. The wide array of geometric and flow conditions investigated in the 11 machines confirm that compressor inlet passage flow dynamics are more complex than has been previously estimated. Individually and collectively the 11 machines confirm that more effort must be exerted by turbomachine designers to adequately understand and then model the complex flow conditions in future endeavors. To help that process, the agreement between the results derived from the CFD and MST analysis encourage the use of MST for much of this design procedure, providing adequate accuracy and requiring less time than the CFD analysis.

Furthermore the results of this study show that the historical placement of the experimental static pressure tap, located on the shroud at the impeller blade leading edge, is a poor anchor for the TEIS model formulation. Steep gradients in this region likely increase the noise in previously developed statistical models. For a straight inlet duct, moving the model anchor point to a location nominally 3 blade heights upstream of the impeller leading edge ($\hat{S} \approx -3$) yields a more suitable location for the TEIS model formulation. For the u-bend geometry, 1 blade height upstream of the actual u-bend is a more suitable location.

4.2 Recommendations

Future work should focus on the statistical development of an improved η_a model. This can be accomplished by integrating the upstream anchor point and inlet passage geometric and flow parameters with those parameters already used in previous models. Application of the results of this work should reduce noise in the model and provide an improved vehicle for the matching of test data and the prediction of new turbomachine designs. Consequently, the design process should improve and enhance the ability of 1-D meanline modeling.

Improving the design process could include performing CFD analysis to determine an appropriate tap location before taking any experimental measurements. Another idea is to use a high response pressure tap at the historical tap location to see if unsteady effects may be responsible for some of the noise visible in the measurements.

References

1 Pelton, J. (2007). "One-Dimensional Radial Flow Turbomachinery Performance Modeling," MS Thesis, Brigham Young University, Provo, Utah.

2 Japikse, D. (1996). *Centrifugal Compressor Design and Performance*, Concepts ETI, Inc., Wilder, VT, USA.

3 Japikse, D., Personal Communication, October 9, 2007.

4 AxCent, ConceptsNREC software- host of PushbuttonCFD and MST, help page.

5 Dean, R. C. (1972). "The Fluid Dynamic Design of Advanced Centrifugal Compressors," Creare Technical Note 153.

6 Clements, W.W, Artt, D. W. (1987). "Performance Prediction and Impeller Diffusion Matching for Vaned Diffuser Centrifugal Compressors," *Institution of Mechanical Engineers Conference Publications*, 1987: 183-198.

7 Japikse, D., Baines, N.C. (1994). *Introduction to Turbomachinery*, Concepts ETI, Inc., Norwich, VT, and Oxford University Press, Oxford, England.

8 Zemp, A., Kammerer, A., Abhari, R. S. (2008). "Unsteady CFD Investigation on Inlet Distortion in a Centrifugal Compressor," ASME Turbo Expo 2008, *Paper No. GT2008-50744*.

9 Charalambous, N., Ghisu, T., Iurisci, G., Pachidis, V., Pilidis, P. (2004). "Axial Compressor Response to Inlet Flow Distortions by a CFD Analysis," ASME Turbo Expo 2004, *Paper No. GT2004-53846*.

10 Sonoda, T., Arima, T., Oana, M. (1999). "The Effect of Inlet Boundary Layer Thickness on the Flow within an Annular S-Shaped Duct," *Trans. ASME Journal of Turbomachinery*, Vol.121: 626-634.

11 Bernard, P. S., Wallace, J. M. (2002). *Turbulent Flow Analysis, Measurement, and Prediction*, John Wiley & Sons, Inc., Hoboken, New Jersey.

12 Spalart, P.R., and Allmaras, S.R. (1992). "A One-Equation Turbulence Model for Aerodynamic Flows." *Paper No. AIAA 92-0439*.

13 Yang, H., Nuernberger, D., Kersken, H. (2005). "Towards Excellence in Turbomachinery CFD: A Hybrid Structured-Unstructured RANS Solver," ASME Turbo Expo 2005, *Paper No. GT2005-68735*.

14 Madden, D. S., West, M. A. (2005). "Effects of Inlet Distortion on the Stability of an Advanced Military Swept Fan Stage with Casing Treatment," ASME Turbo Expo 2005, *Paper No. GT2005-68693*.

15 Vassiliev, V., Kostege, V., Pirscher, A., Chernyshev, S. (2005). "CFD Application in Design of GT Structural Components," ASME Turbo Expo 2005, *Paper No. GT2005-68950.*

16 Anderson, M. R. (2009). "Optimization of Turbomachinery – Validation Against Experimental Results," Current Trends in Design and Computation of Turbomachinery, Prague, 2009.

17 Japikse, D., Personal Communication, June, 2009.

18 John, J., Keith, T. (2006). *Gas Dynamics*, Third Ed., Pearson Education, Inc., Upper Saddle River, New Jersey.

19 Munson, B. R., Young, D. F., Okiishi, T. H. (2006). *Fundamentals of Fluid Mechanics*, Fifth Ed., John Wiley & Sons, Inc., Hoboken, New Jersey.

20 Japikse, D., Personal Communication, November 25, 2008

21 Japikse, D. (1990). “Design and Evaluation with a High Flow, High Pressure Centrifugal Compressor Stage,” TM 77, ConceptsETI. Restricted distribution; proprietary.

Appendix A

A-1 CCN32

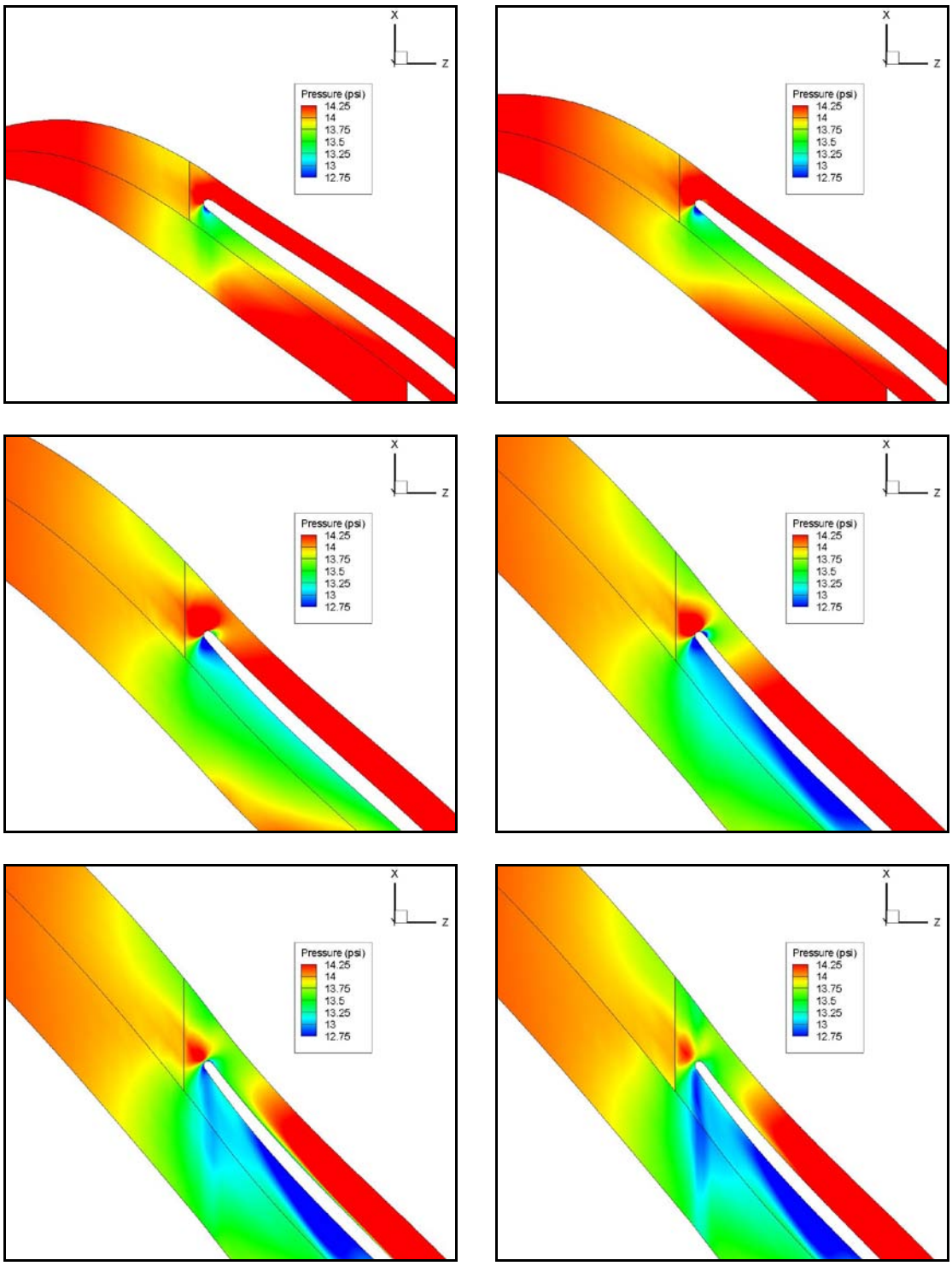

Figure A-1 Static pressure 2-D contour plots for CCN32 at a mass flow rate of 0.23 lbm/s at six spanwise positions progressing from hub-to-shroud. The upper left panel corresponds to the hub with successive panels moving from left to right and top to bottom, in the following order: $\hat{H}$ = 0, $\hat{H}$ = 0.25, $\hat{H}$ = 0.5, $\hat{H}$ = 0.7, $\hat{H}$ = 0.9 and $\hat{H}$ = 1.

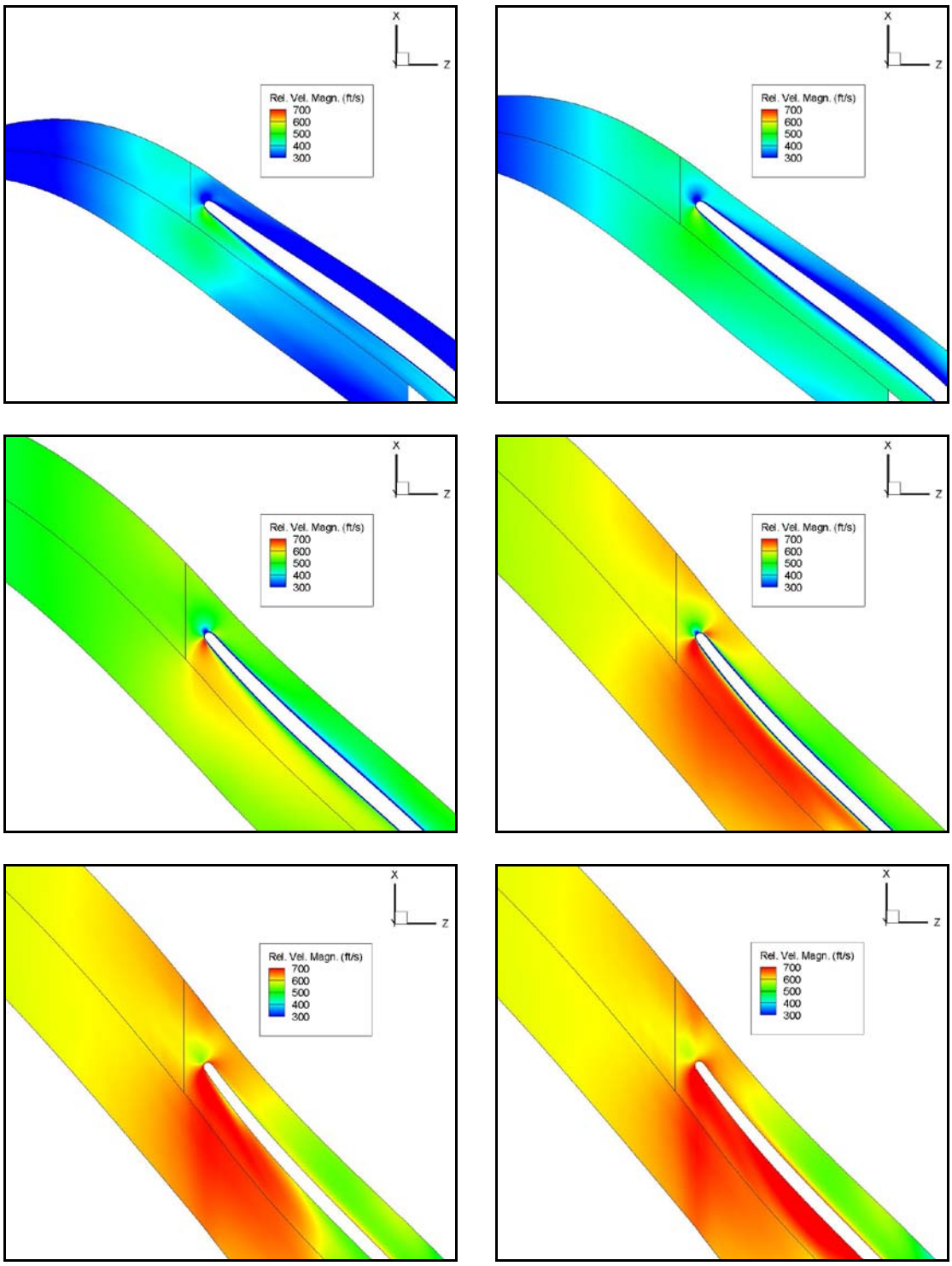

Figure A-2 Velocity magnitude 2-D contour plots for CCN32 at a mass flow rate of 0.23 lbm/s at six spanwise positions progressing from hub-to-shroud. The upper left panel corresponds to the hub with successive panels moving from left to right and top to bottom, in the following order: $\hat{H}$ = 0, $\hat{H}$ = 0.25, $\hat{H}$ = 0.5, $\hat{H}$ = 0.7, $\hat{H}$ = 0.9 and $\hat{H}$ = 1.

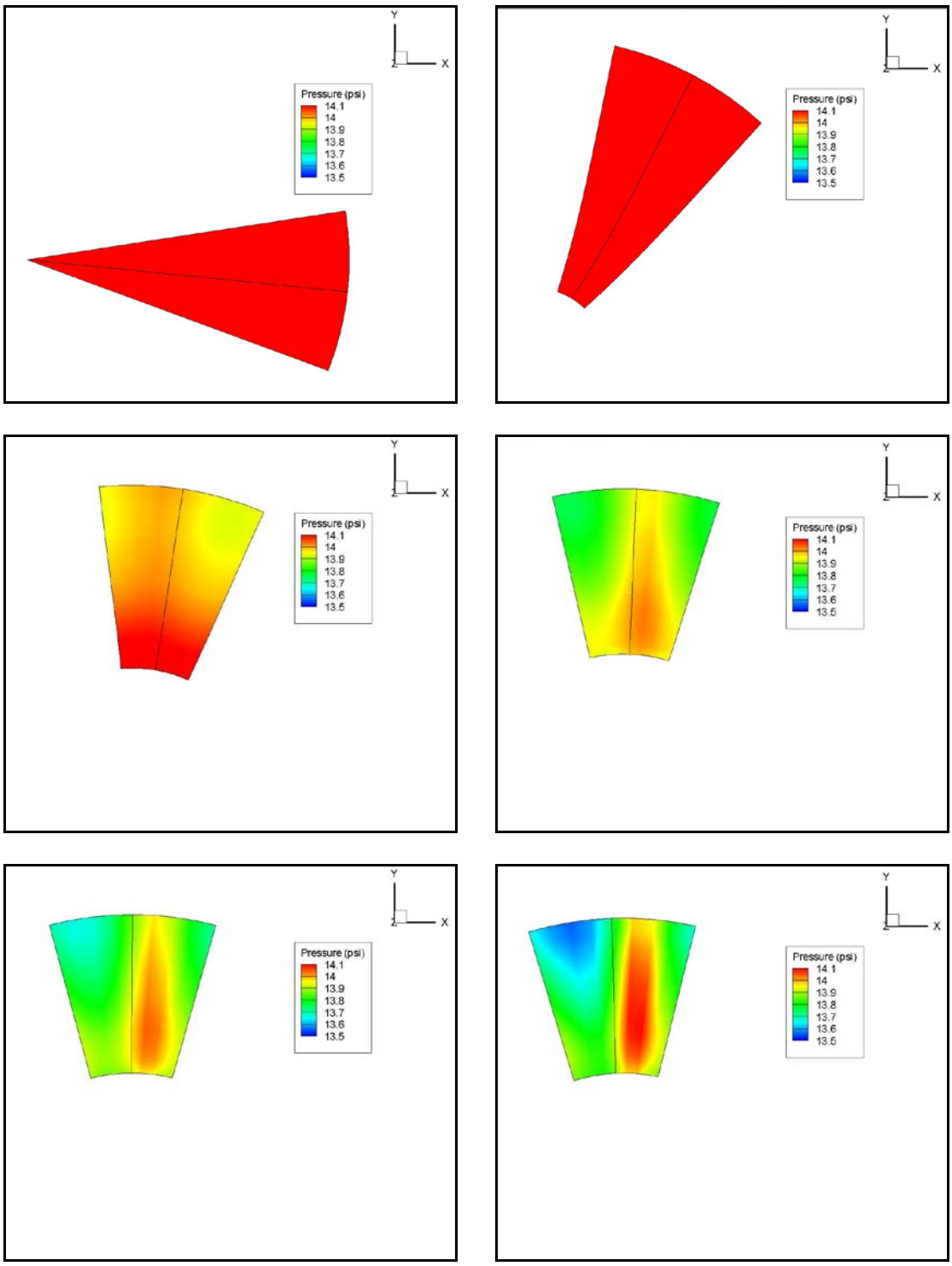

Figure A-3 Static pressure 2-D contour plots at six streamwise locations moving from the beginning of the computational domain to the impeller leading edge. The upper left panel corresponds to $\hat{S}$ = -5.82 with successive panels moving from left to right and top to bottom, in the following order: $\hat{S}$ = -5.82, $\hat{S}$ = -1.09, $\hat{S}$ = -0.48, $\hat{S}$ = -0.34, $\hat{S}$ = -0.20, and $\hat{S}$ = -0.15.

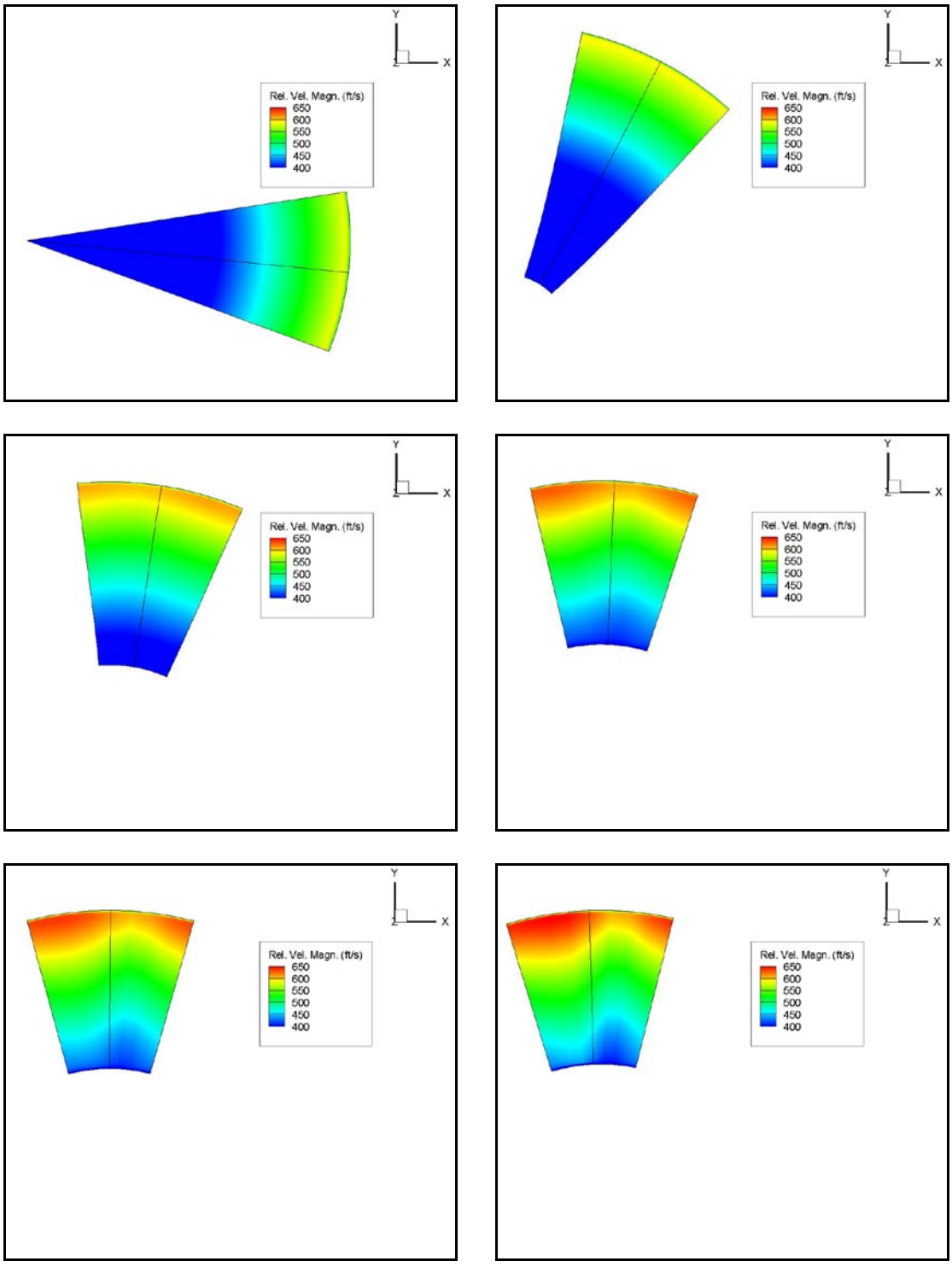

Figure A-4 Velocity magnitude 2-D contour plots at six streamwise locations moving from the beginning of the computational domain to the impeller leading edge. The upper left panel corresponds to $\hat{S}$ = -5.82 with successive panels moving from left to right and top to bottom, in the following order: $\hat{S}$ = -5.82, $\hat{S}$ = -1.09, $\hat{S}$ = -0.48, $\hat{S}$ = -0.34, $\hat{S}$ = -0.20, and $\hat{S}$ = -0.15.

A-2 CCN38

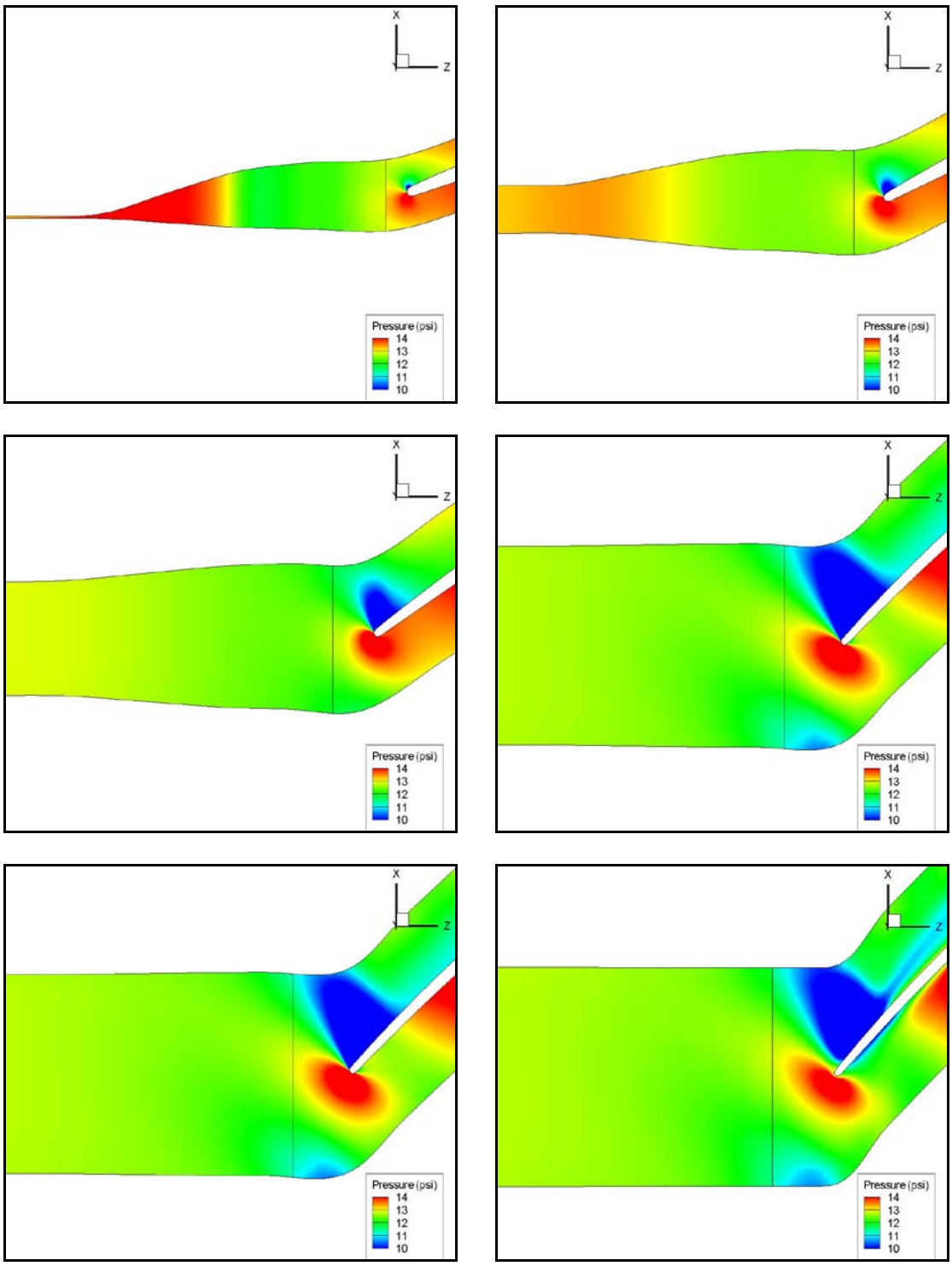

Figure A-5 Static pressure 2-D contour plots for CCN38 at a mass flow rate of 0.66 lbm/s at six spanwise positions progressing from hub-to-shroud. The upper left panel corresponds to the hub with successive panels moving from left to right and top to bottom, in the following order: $\hat{H}$ = 0, $\hat{H}$ = 0.25, $\hat{H}$ = 0.5, $\hat{H}$ = 0.7, $\hat{H}$ = 0.9 and $\hat{H}$ = 1.

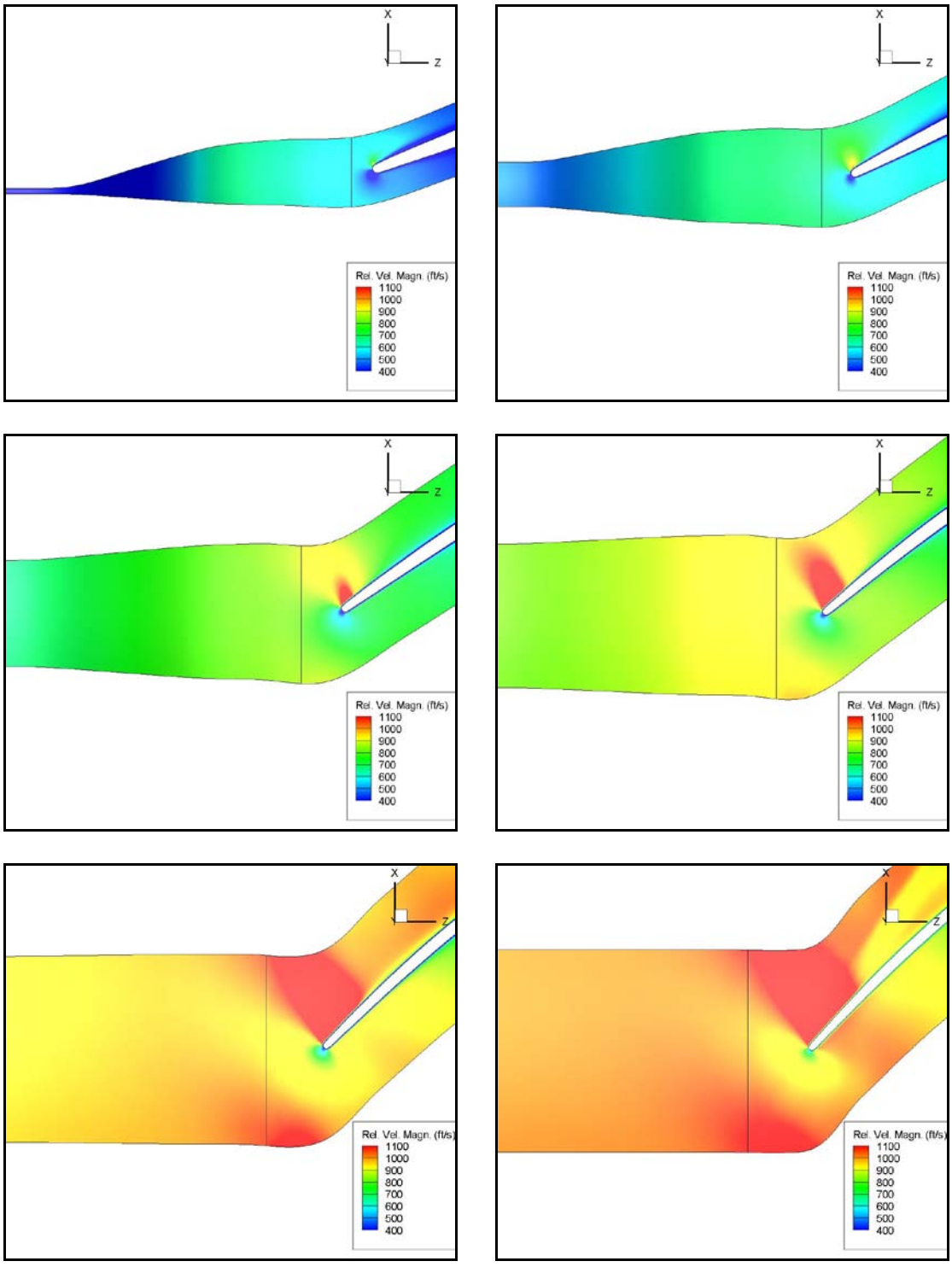

Figure A-6 Velocity magnitude 2-D contour plots for CCN38 at a mass flow rate of 0.66 lbm/s at six spanwise positions progressing from hub-to-shroud. The upper left panel corresponds to the hub with successive panels moving from left to right and top to bottom, in the following order: $\hat{H}$ = 0, $\hat{H}$ = 0.25, $\hat{H}$ = 0.5, $\hat{H}$ = 0.7, $\hat{H}$ = 0.9 and $\hat{H}$ = 1.

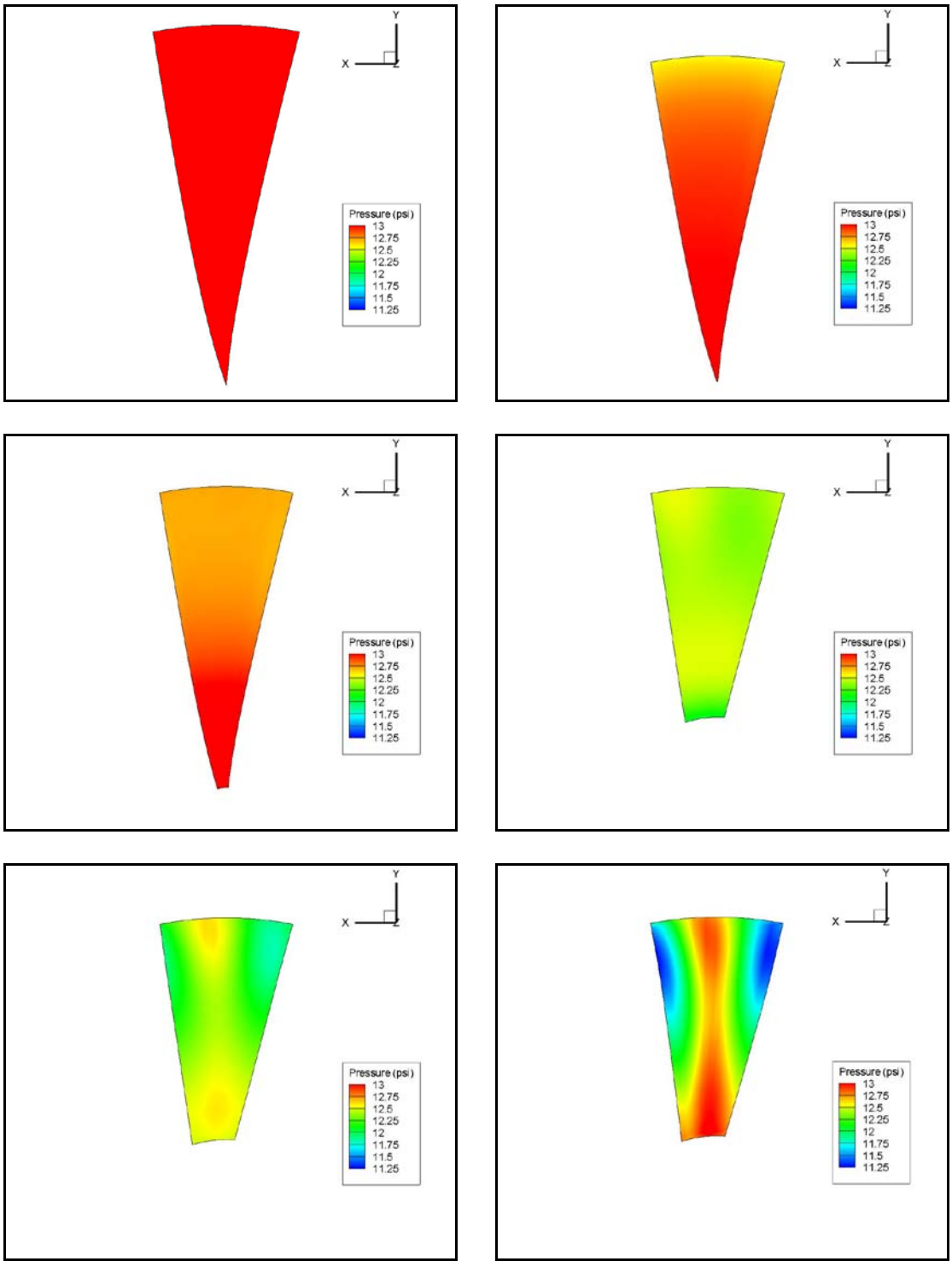

Figure A-6 Static pressure 2-D contour plots at six streamwise locations moving from the beginning of the computational domain to the impeller leading edge. The upper left panel corresponds to $\hat{S}$ = -6.18 with successive panels moving from left to right and top to bottom, in the following order: $\hat{S}$ = -6.18, $\hat{S}$ = -1.55, $\hat{S}$ = -0.90, $\hat{S}$ = -0.41, $\hat{S}$ = -0.25, and $\hat{S}$ = -0.16.

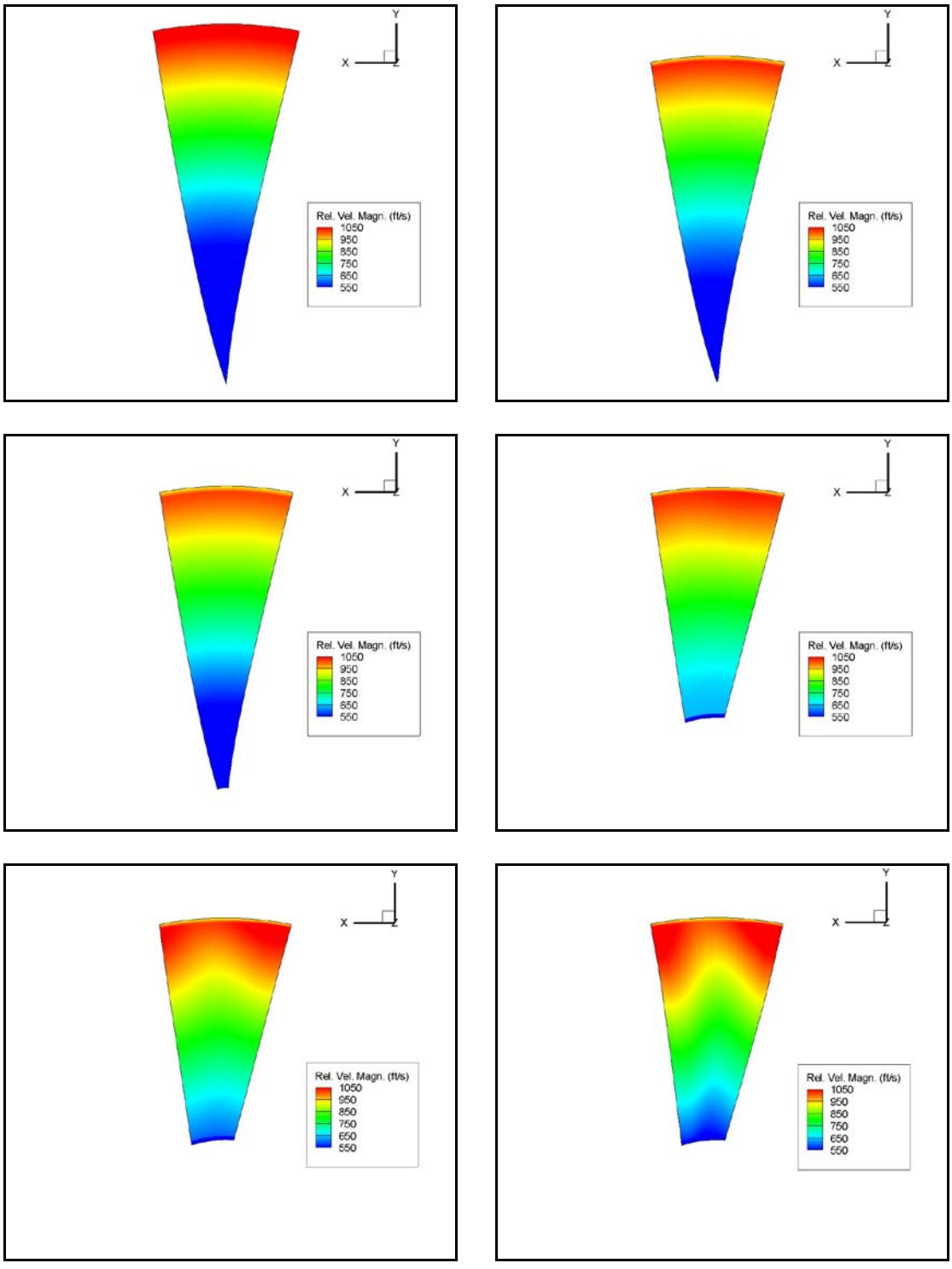

Figure A-8 Velocity magnitude 2-D contour plots at six streamwise locations moving from the beginning of the computational domain to the impeller leading edge. The upper left panel corresponds to $\hat{S}$ = -6.18 with successive panels moving from left to right and top to bottom, in the following order: $\hat{S}$ = -6.18, $\hat{S}$ = -1.55, $\hat{S}$ = -0.90, $\hat{S}$ = -0.41, $\hat{S}$ = -0.25, and $\hat{S}$ = -0.16.

A-3 CCN39

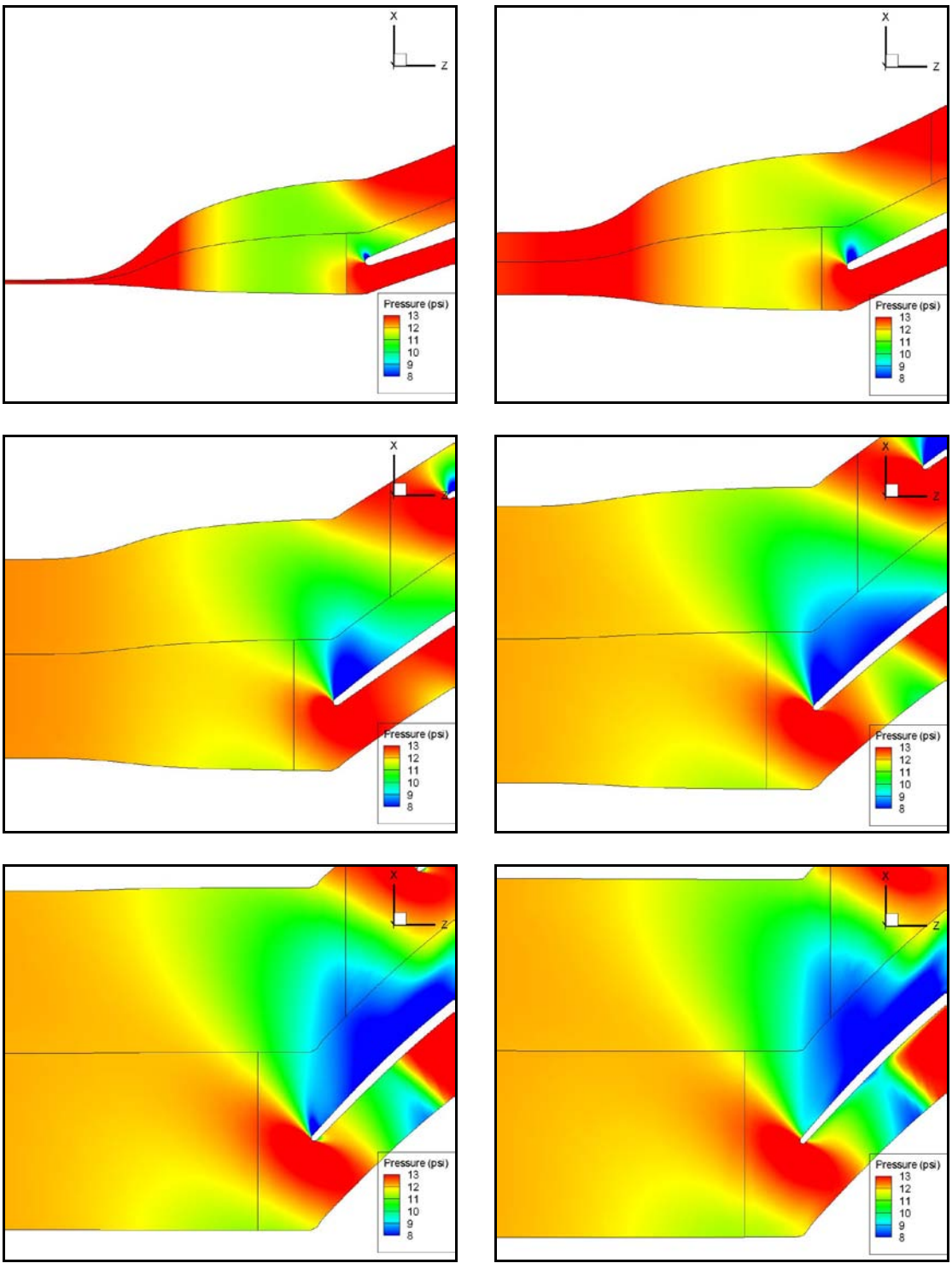

Figure A-9 Static pressure 2-D contour plots for CCN39 at a mass flow rate of 0.73 lbm/s at six spanwise positions progressing from hub-to-shroud. The upper left panel corresponds to the hub with successive panels moving from left to right and top to bottom, in the following order: $\hat{H}$ = 0, $\hat{H}$ = 0.25, $\hat{H}$ = 0.5, $\hat{H}$ = 0.7, $\hat{H}$ = 0.9 and $\hat{H}$ = 1.

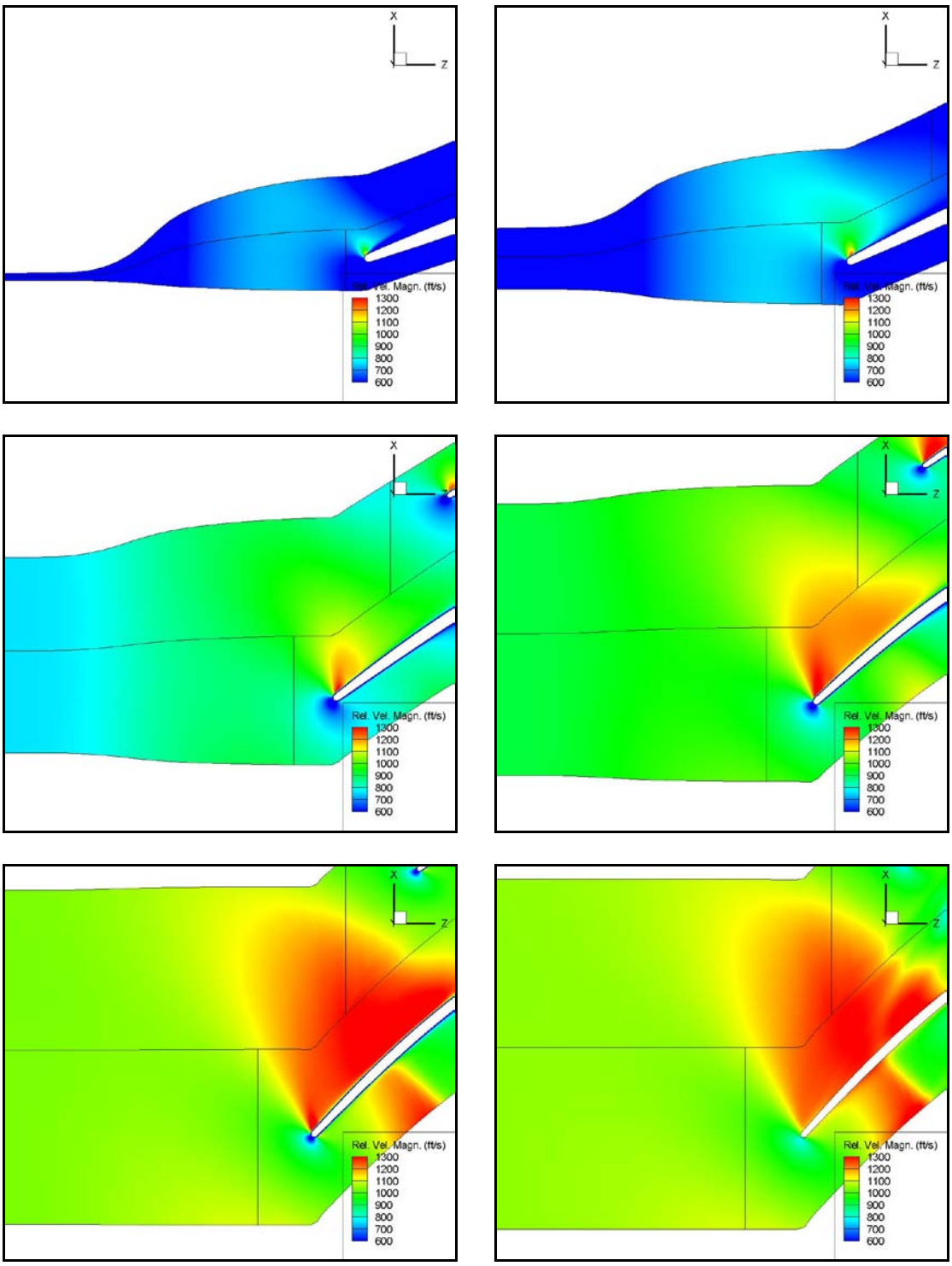

Figure A-10 Velocity magnitude 2-D contour plots for CCN39 at a mass flow rate of 0.73 lbm/s at six spanwise positions progressing from hub-to-shroud. The upper left panel corresponds to the hub with successive panels moving from left to right and top to bottom, in the following order: $\hat{H}$ = 0, $\hat{H}$ = 0.25, $\hat{H}$ = 0.5, $\hat{H}$ = 0.7, $\hat{H}$ = 0.9 and $\hat{H}$ = 1.

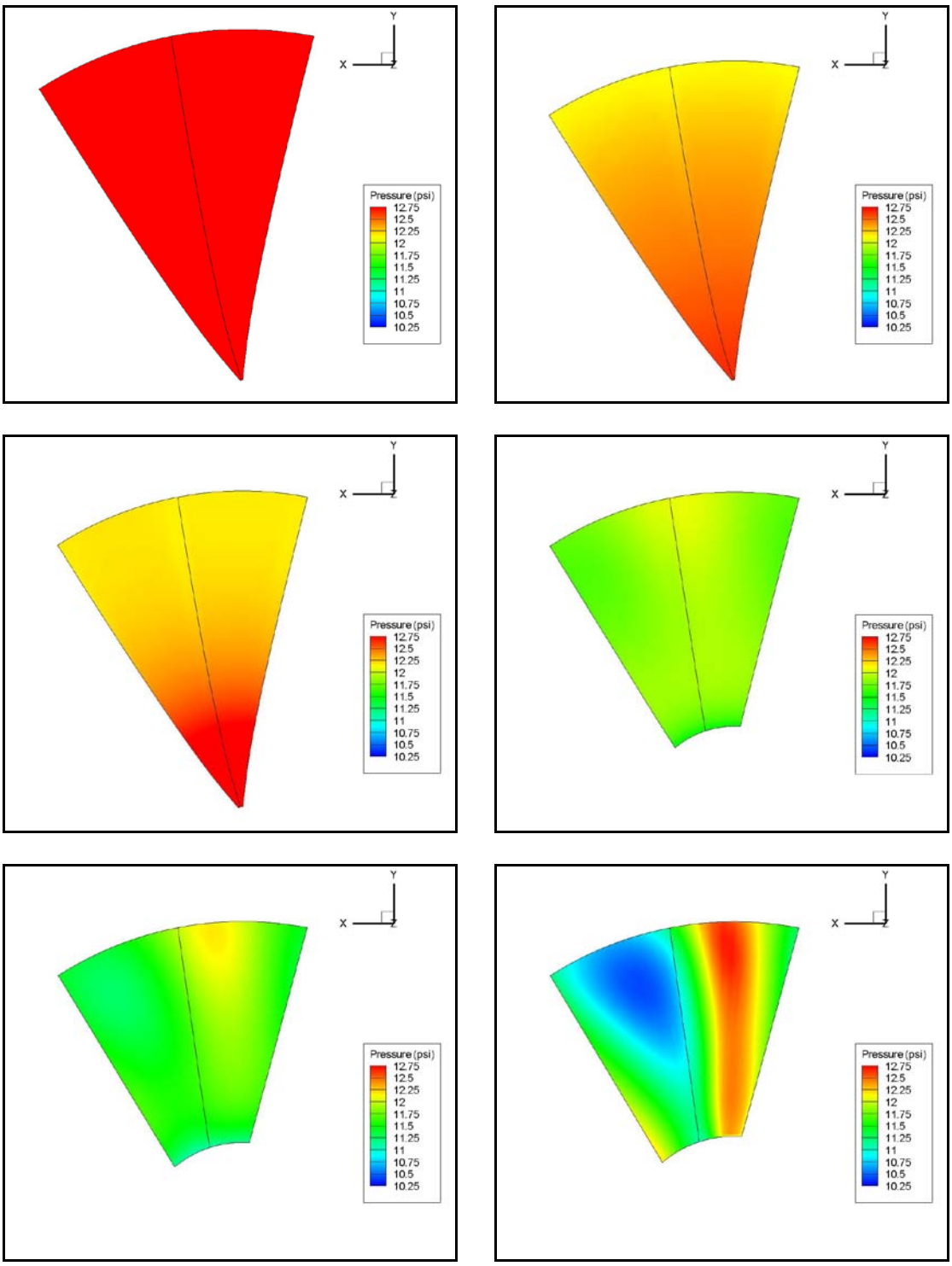

Figure A-12 Static pressure 2-D contour plots at six streamwise locations moving from the beginning of the computational domain to the impeller leading edge. The upper left panel corresponds to $\hat{S}$ = -6.18 with successive panels moving from left to right and top to bottom, in the following order: $\hat{S}$ = -6.18, $\hat{S}$ = -1.45, $\hat{S}$ = -1.05, $\hat{S}$ = -0.50, $\hat{S}$ = -0.33, and $\hat{S}$ = -0.16.

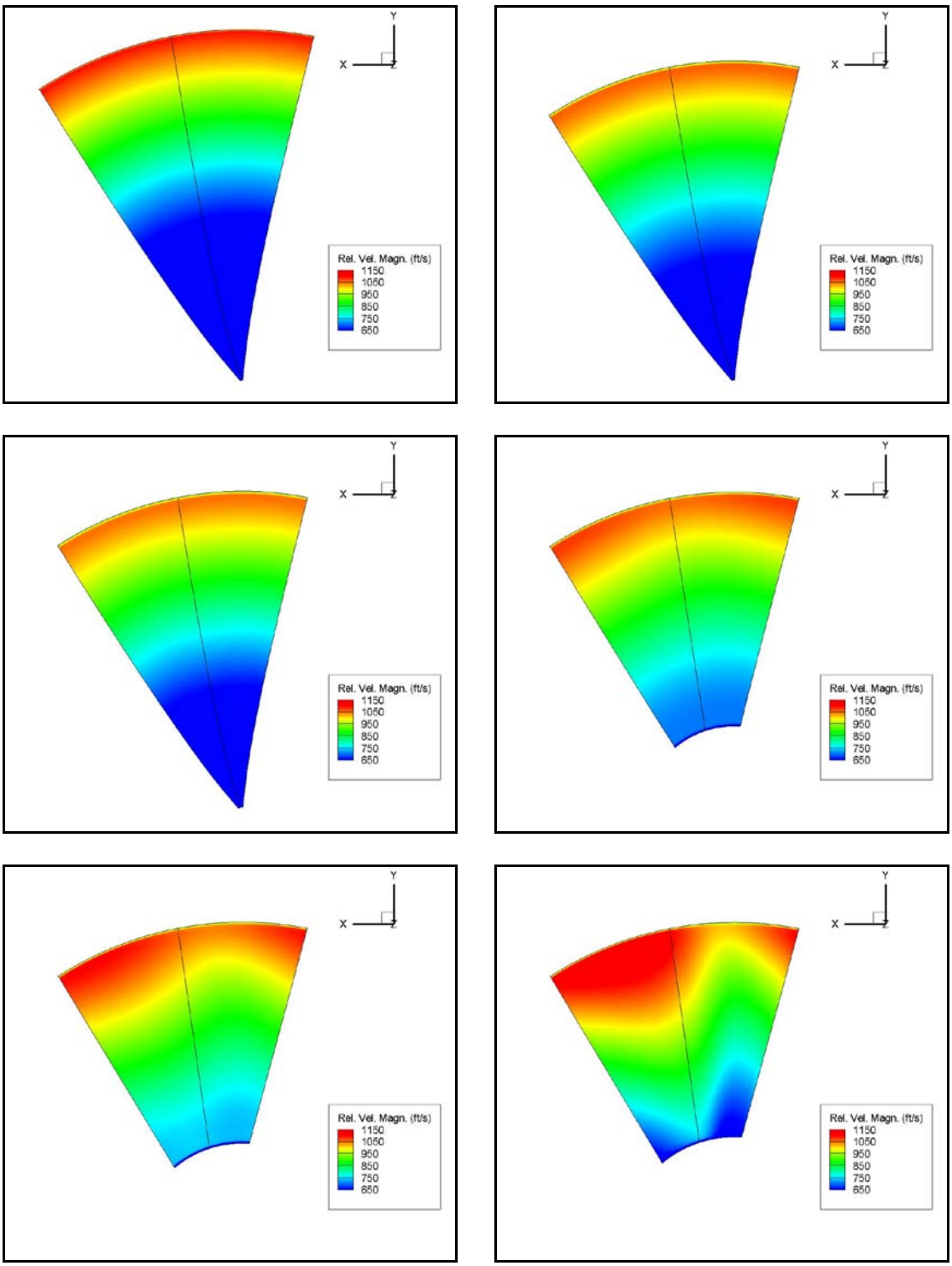

Figure A-11 Velocity magnitude 2-D contour plots at six streamwise locations moving from the beginning of the computational domain to the impeller leading edge. The upper left panel corresponds to $\hat{S}$ = -6.18 with successive panels moving from left to right and top to bottom, in the following order: $\hat{S}$ = -6.18, $\hat{S}$ = -1.45, $\hat{S}$ = -1.05, $\hat{S}$ = -0.50, $\hat{S}$ = -0.33, and $\hat{S}$ = -0.16.

A-4 CCN40

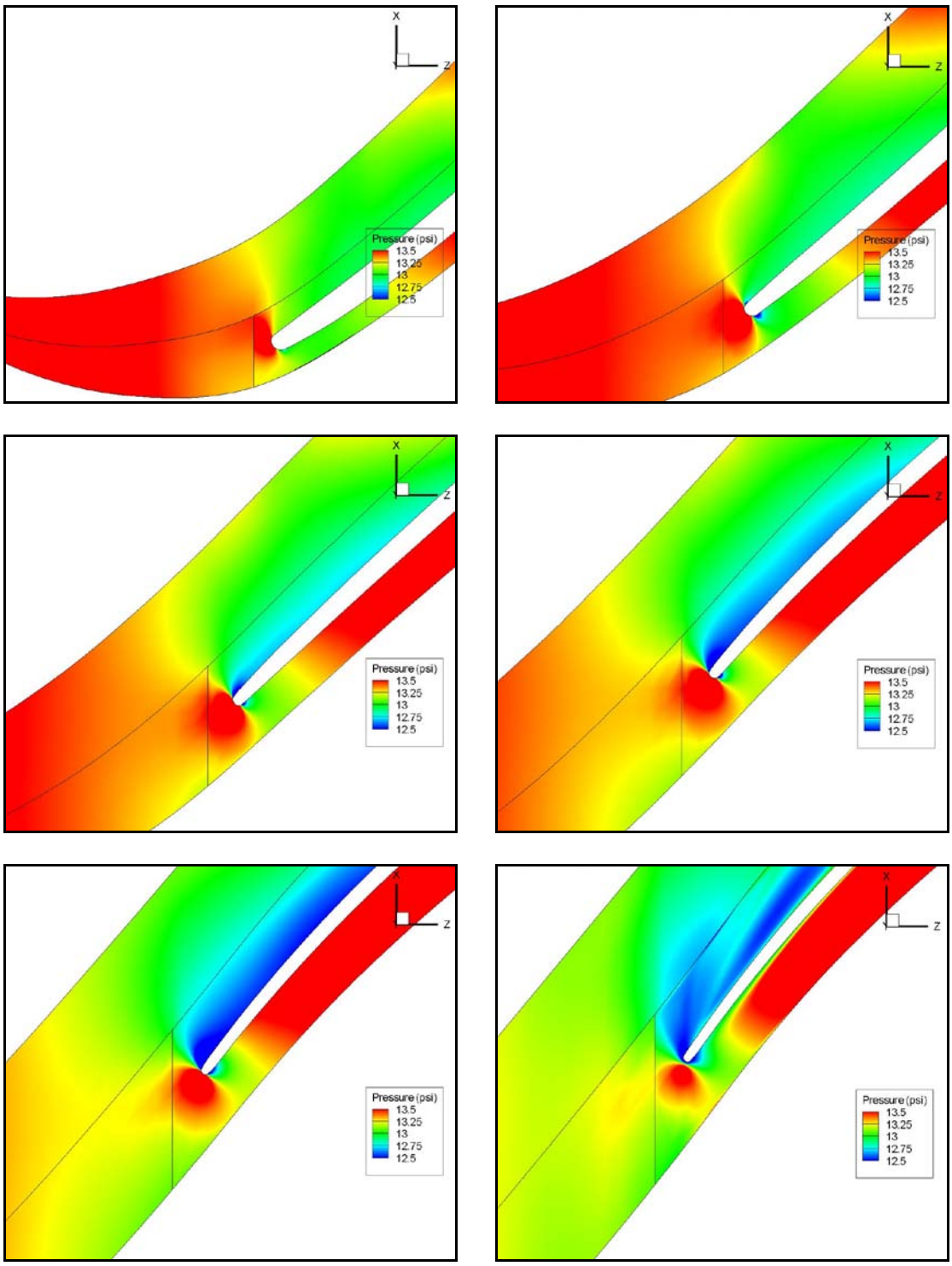

Figure A-13 Static pressure 2-D contour plots for CCN40 at a mass flow rate of 0.40 lbm/s at six spanwise positions progressing from hub-to-shroud. The upper left panel corresponds to the hub with successive panels moving from left to right and top to bottom, in the following order: $\hat{H}$ = 0, $\hat{H}$ = 0.25, $\hat{H}$ = 0.5, $\hat{H}$ = 0.7, $\hat{H}$ = 0.9 and $\hat{H}$ = 1.

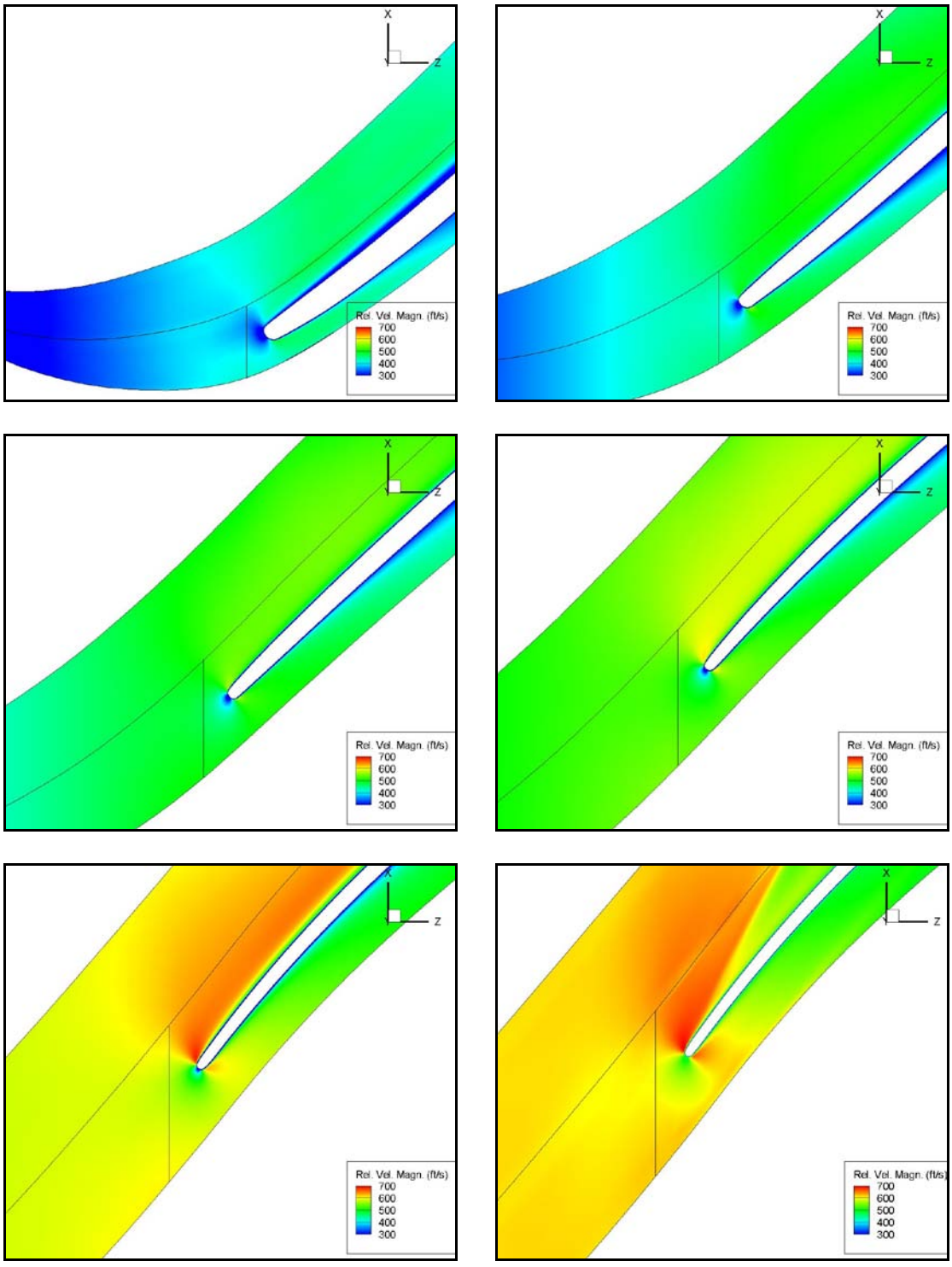

Figure A-14 Velocity magnitude 2-D contour plots for CCN40 at a mass flow rate of 0.40 lbm/s at six spanwise positions progressing from hub-to-shroud. The upper left panel corresponds to the hub with successive panels moving from left to right and top to bottom, in the following order: $\hat{H}$ = 0, $\hat{H}$ = 0.25, $\hat{H}$ = 0.5, $\hat{H}$ = 0.7, $\hat{H}$ = 0.9 and $\hat{H}$ = 1.

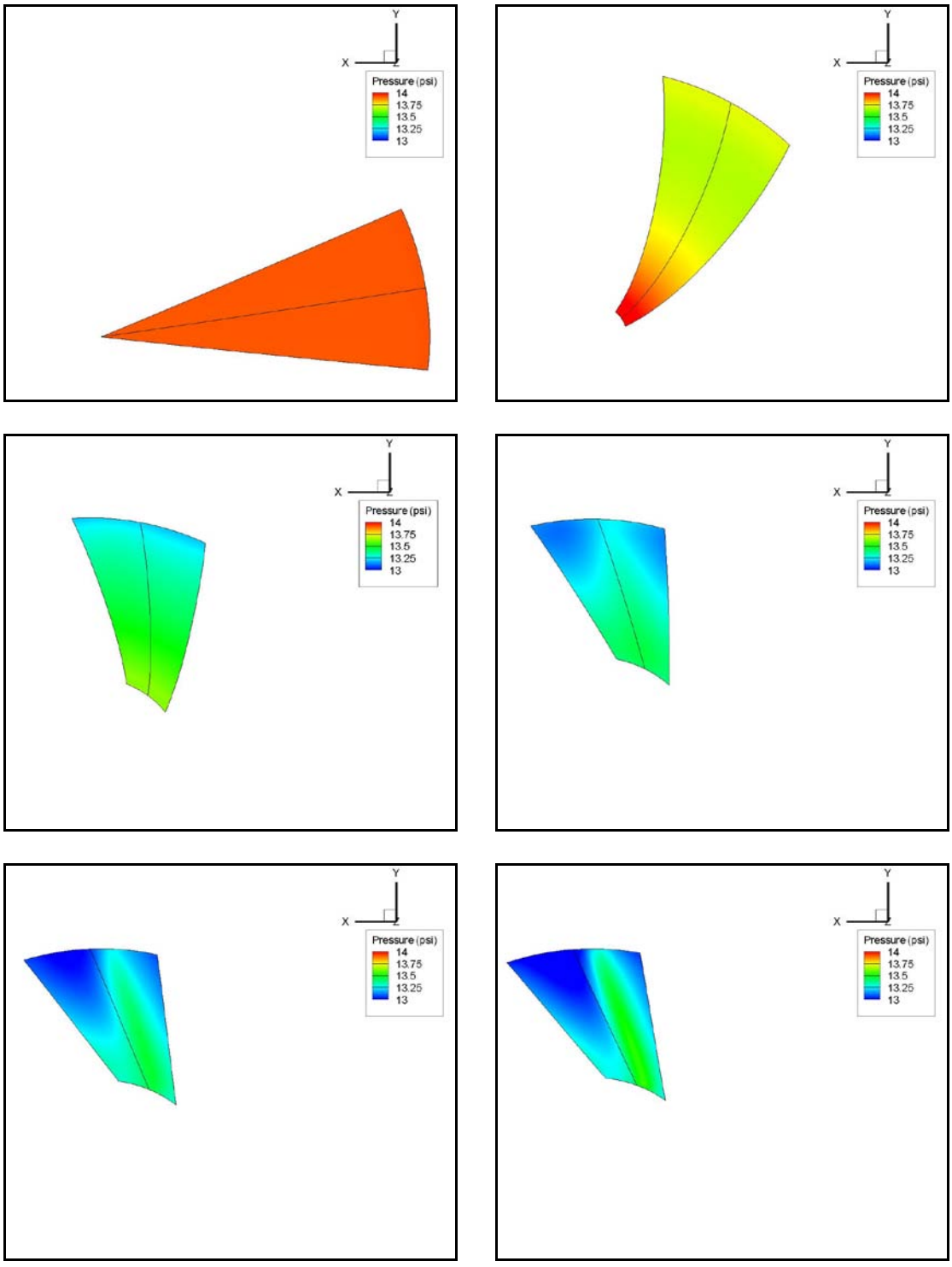

Figure A-15 Static pressure 2-D contour plots at six streamwise locations moving from the beginning of the computational domain to the impeller leading edge. The upper left panel corresponds to $\hat{S}$ = -4.82 with successive panels moving from left to right and top to bottom, in the following order: $\hat{S}$ = -4.82, $\hat{S}$ = -1.03 $\hat{S}$ = -0.50, $\hat{S}$ = -0.23, $\hat{S}$ = -0.13, and $\hat{S}$ = -0.08.

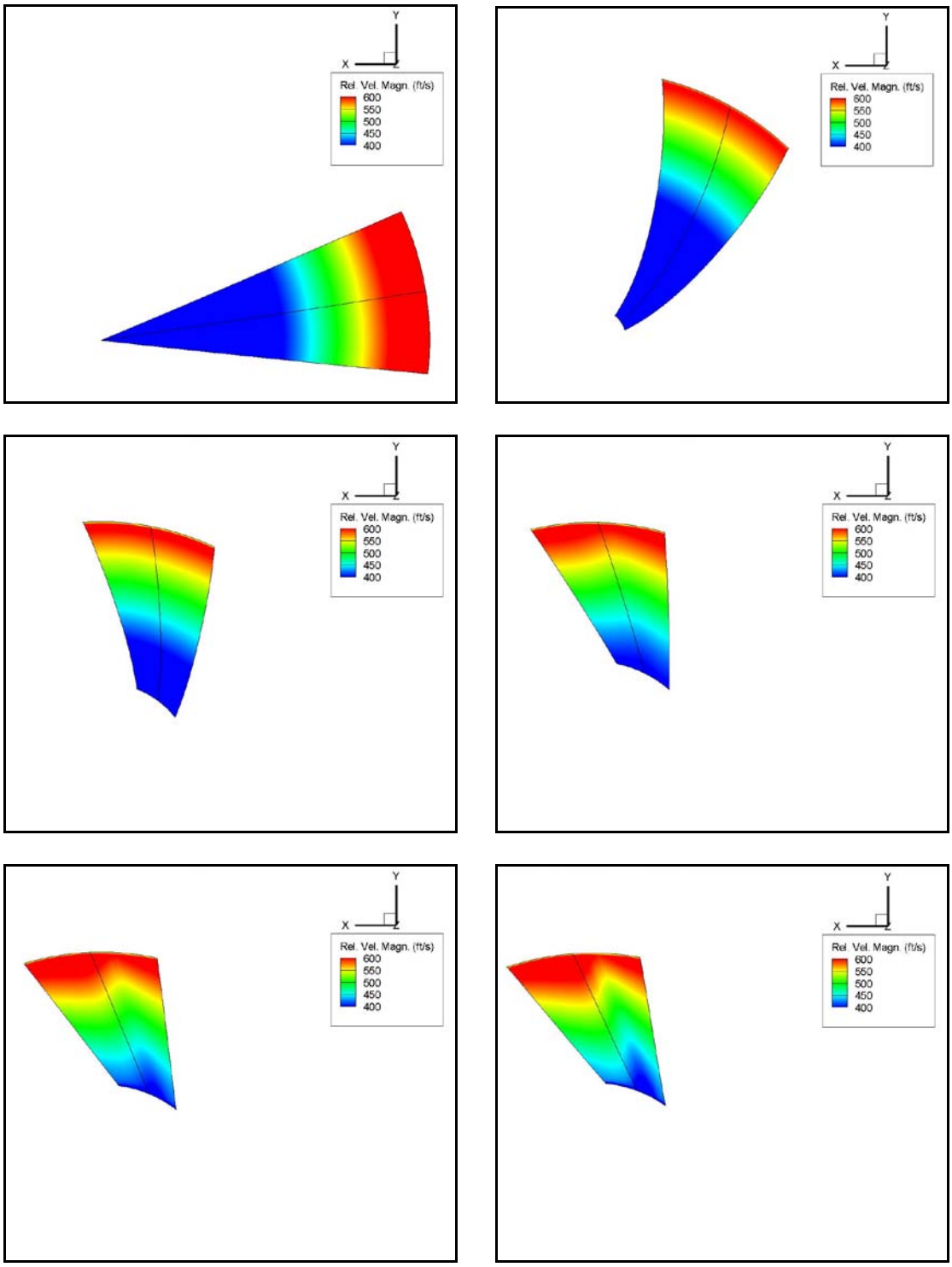

Figure A-16 Velocity magnitude 2-D contour plots at six streamwise locations moving from the beginning of the computational domain to the impeller leading edge. The upper left panel corresponds to $\hat{S}$ = -4.82 with successive panels moving from left to right and top to bottom, in the following order: $\hat{S}$ = -4.82, $\hat{S}$ = -1.03, $\hat{S}$ = -0.50, $\hat{S}$ = -0.23, $\hat{S}$ = -0.13, and $\hat{S}$ = -0.08.

A-5 CCN42

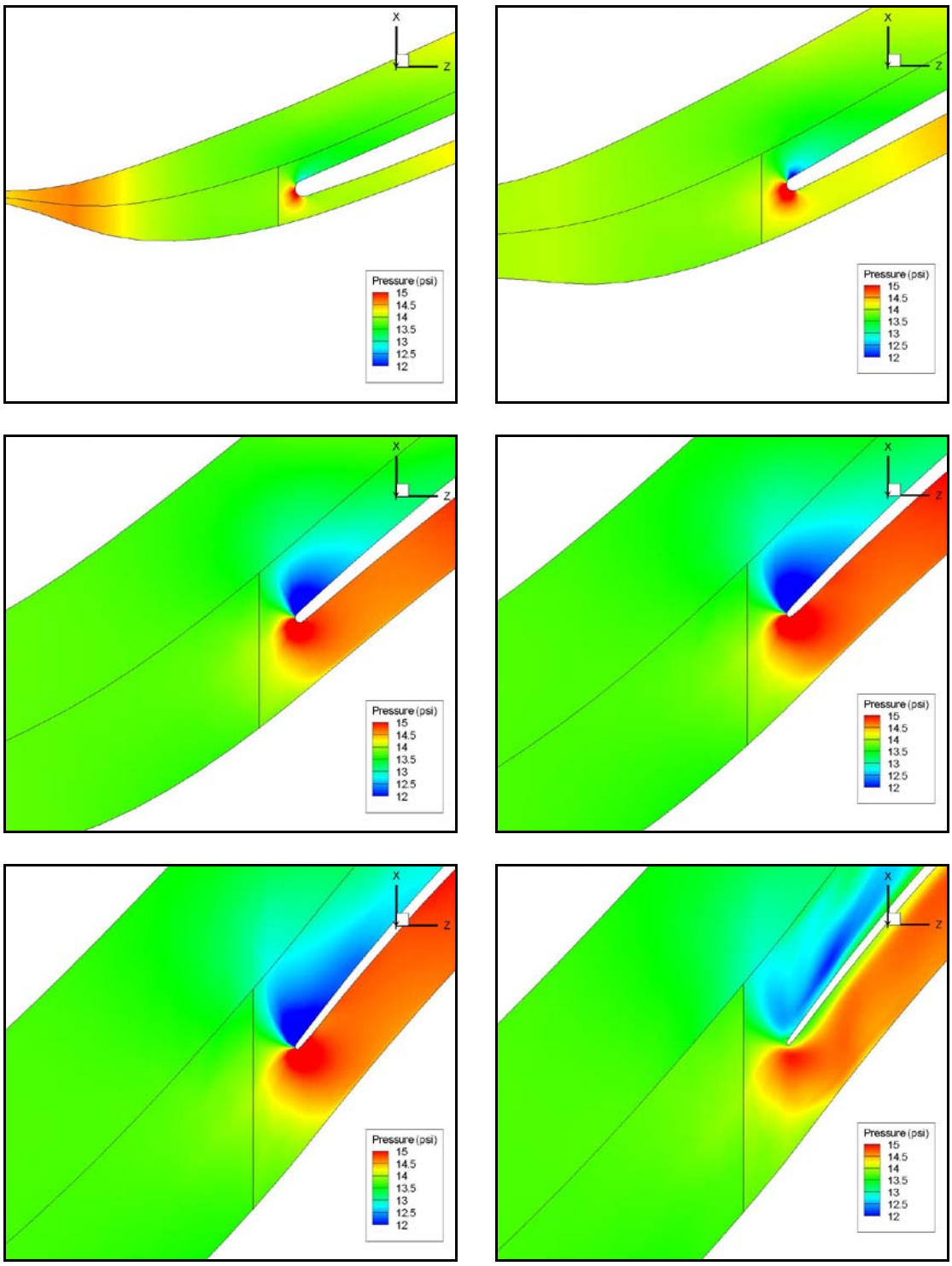

Figure A-17 Static pressure 2-D contour plots for CCN42 at a mass flow rate of 1.25 lbm/s at six spanwise positions progressing from hub-to-shroud. The upper left panel corresponds to the hub with successive panels moving from left to right and top to bottom, in the following order: $\hat{H}$ = 0, $\hat{H}$ = 0.25, $\hat{H}$ = 0.5, $\hat{H}$ = 0.7, $\hat{H}$ = 0.9 and $\hat{H}$ = 1.

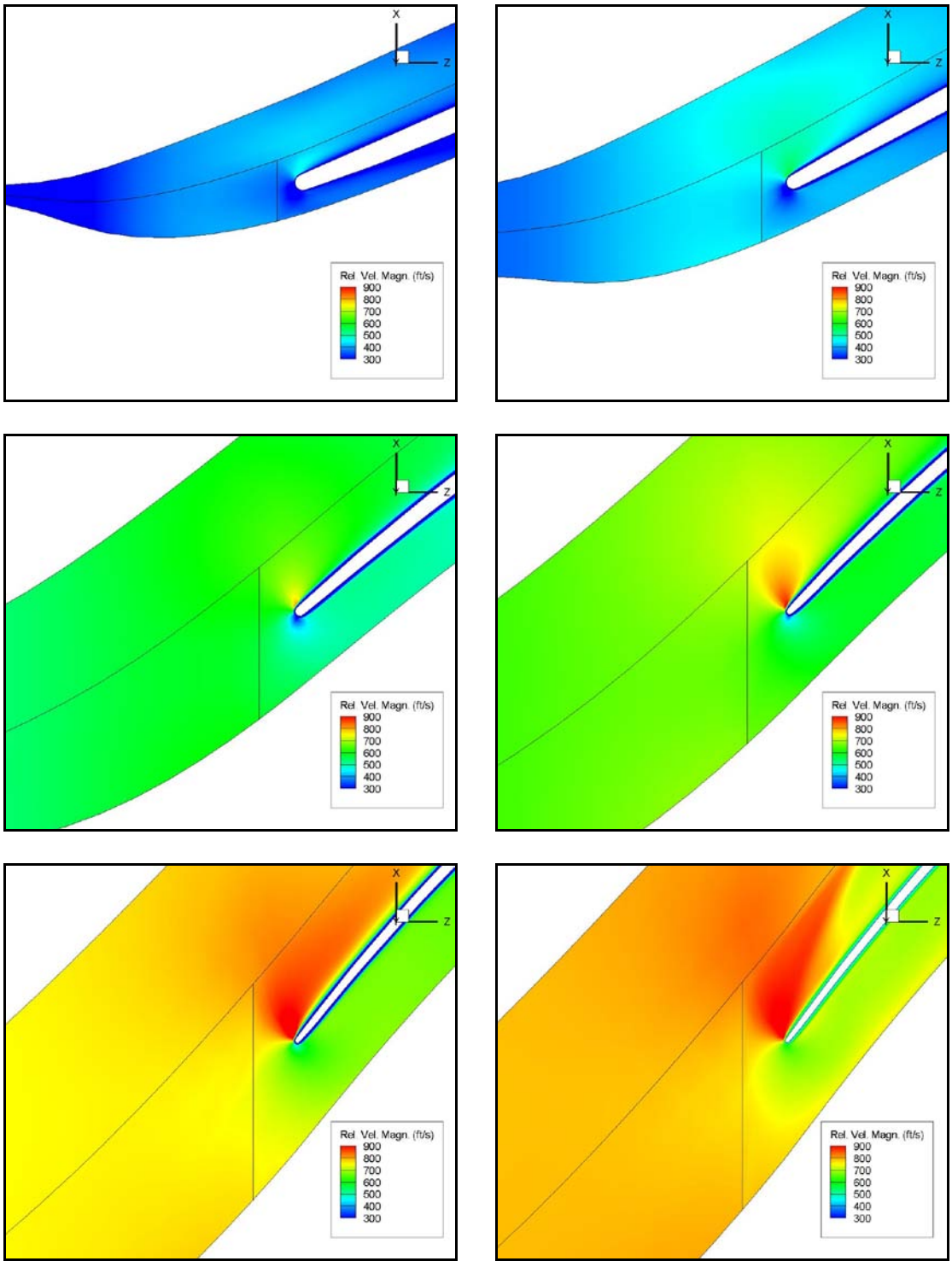

Figure A-18 Velocity magnitude 2-D contour plots for CCN42 at a mass flow rate of 1.25 lbm/s at six spanwise positions progressing from hub-to-shroud. The upper left panel corresponds to the hub with successive panels moving from left to right and top to bottom, in the following order: $\hat{H}$ = 0, $\hat{H}$ = 0.25, $\hat{H}$ = 0.5, $\hat{H}$ = 0.7, $\hat{H}$ = 0.9 and $\hat{H}$ = 1.

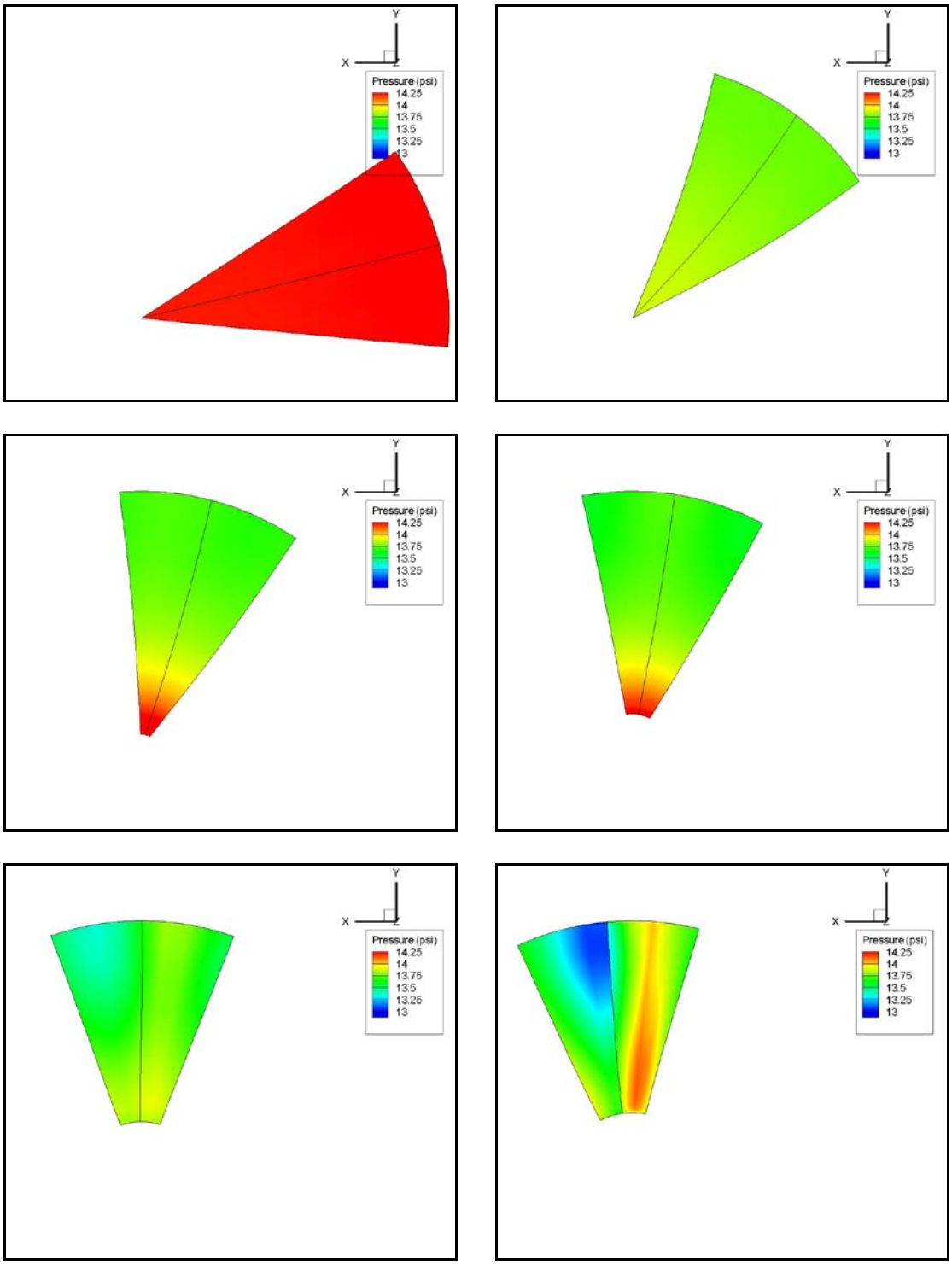

Figure A-19 Static pressure 2-D contour plots at six streamwise locations moving from the beginning of the computational domain to the impeller leading edge. The upper left panel corresponds to $\hat{S}$ = -3.36 with successive panels moving from left to right and top to bottom, in the following order: $\hat{S}$ = -3.36, $\hat{S}$ = -1.04 $\hat{S}$ = -0.49, $\hat{S}$ = -0.36, $\hat{S}$ = -0.19, and $\hat{S}$ = -0.08.

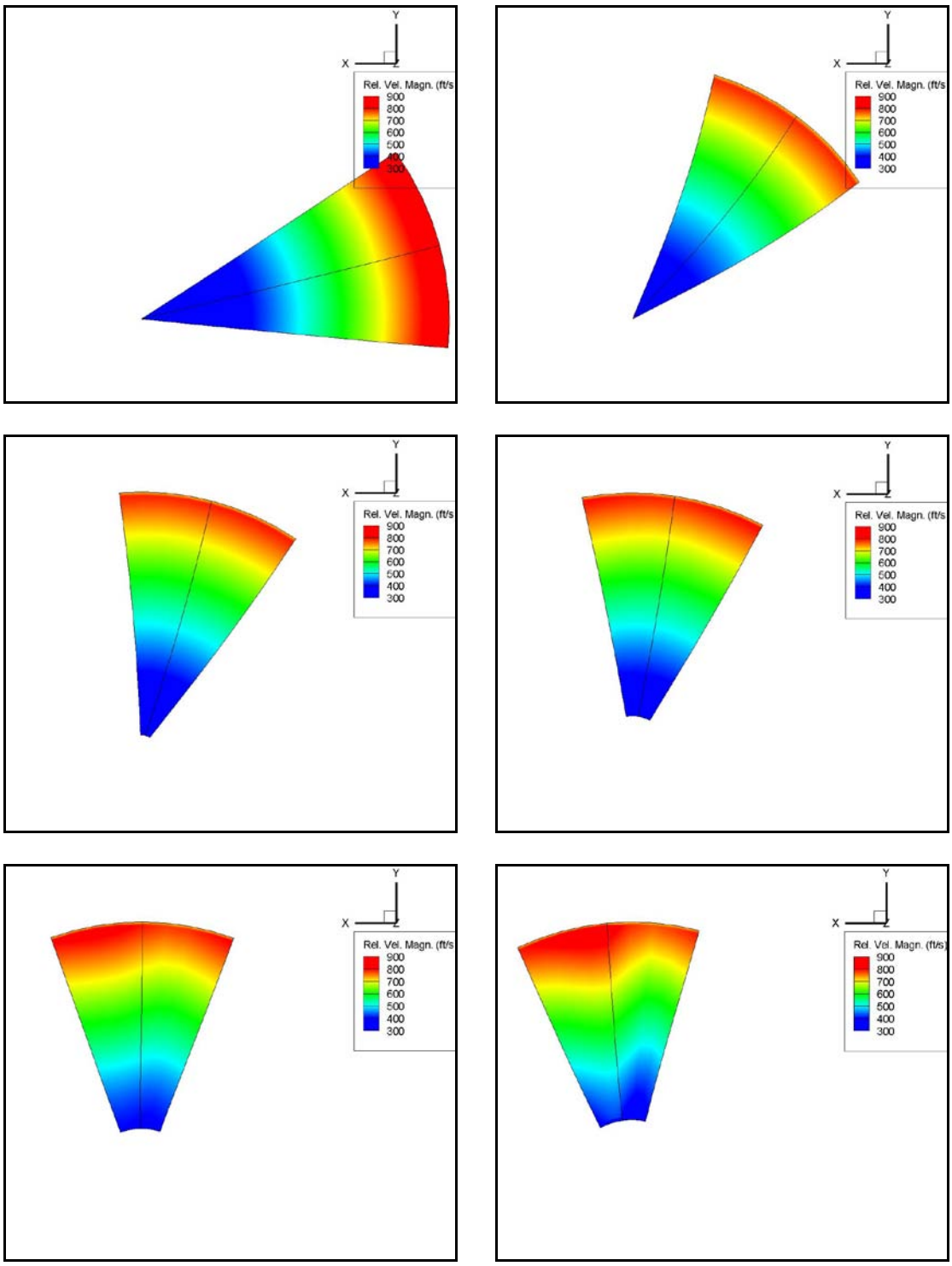

Figure A-20 Velocity magnitude 2-D contour plots at six streamwise locations moving from the beginning of the computational domain to the impeller leading edge. The upper left panel corresponds to $\hat{S}$ = -3.36 with successive panels moving from left to right and top to bottom, in the following order $\hat{S}$ = -3.36, $\hat{S}$ = -1.04 $\hat{S}$ = -0.49, $\hat{S}$ = -0.36, $\hat{S}$ = -0.19, and $\hat{S}$ = -0.08.

A-6 CCN66

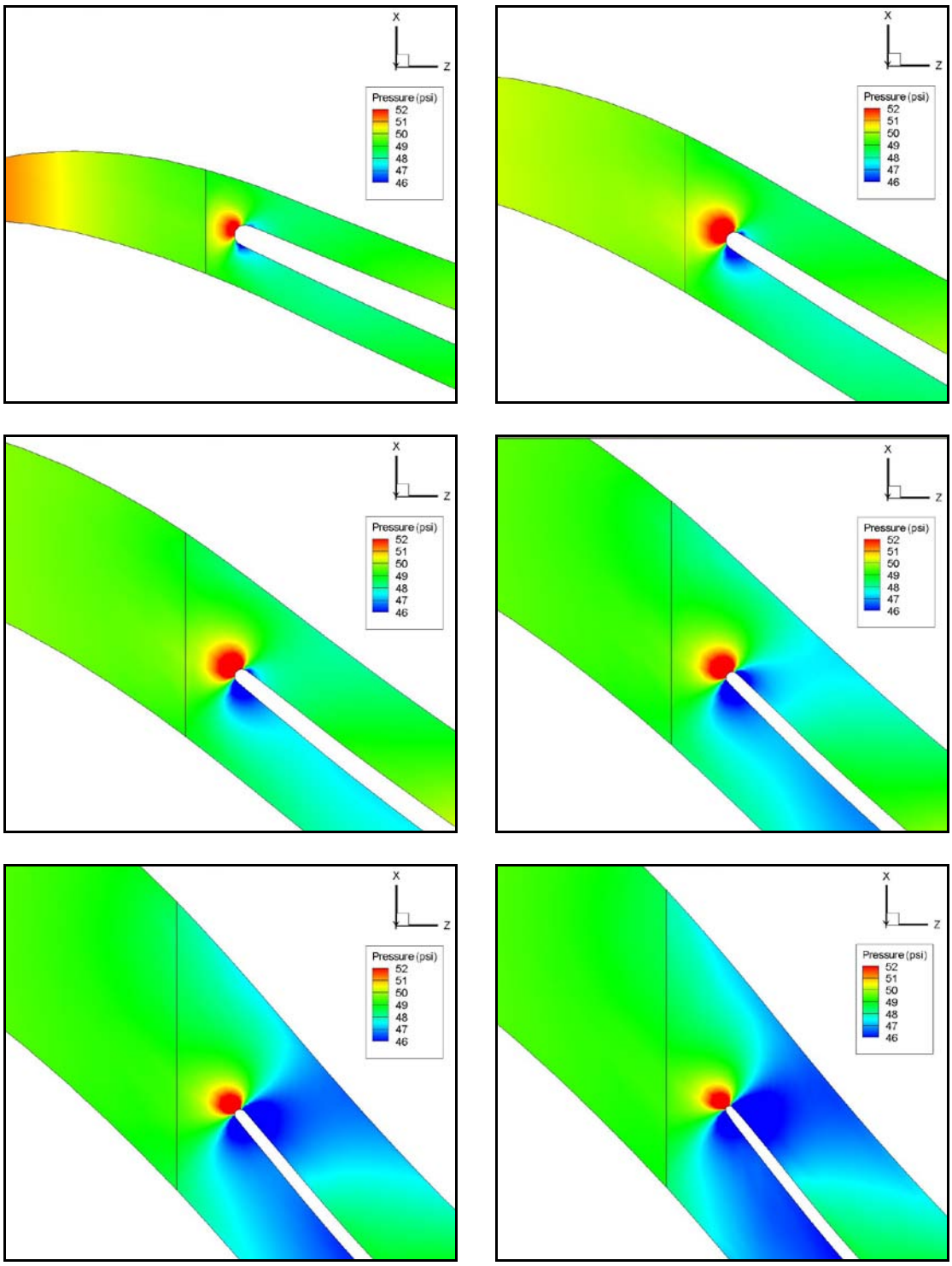

Figure A-21 Static pressure 2-D contour plots for CCN66 at a mass flow rate of 5.20 lbm/s at six spanwise positions progressing from hub-to-shroud. The upper left panel corresponds to the hub with successive panels moving from left to right and top to bottom, in the following order: $\hat{H}$ = 0, $\hat{H}$ = 0.25, $\hat{H}$ = 0.5, $\hat{H}$ = 0.7, $\hat{H}$ = 0.9 and $\hat{H}$ = 1.

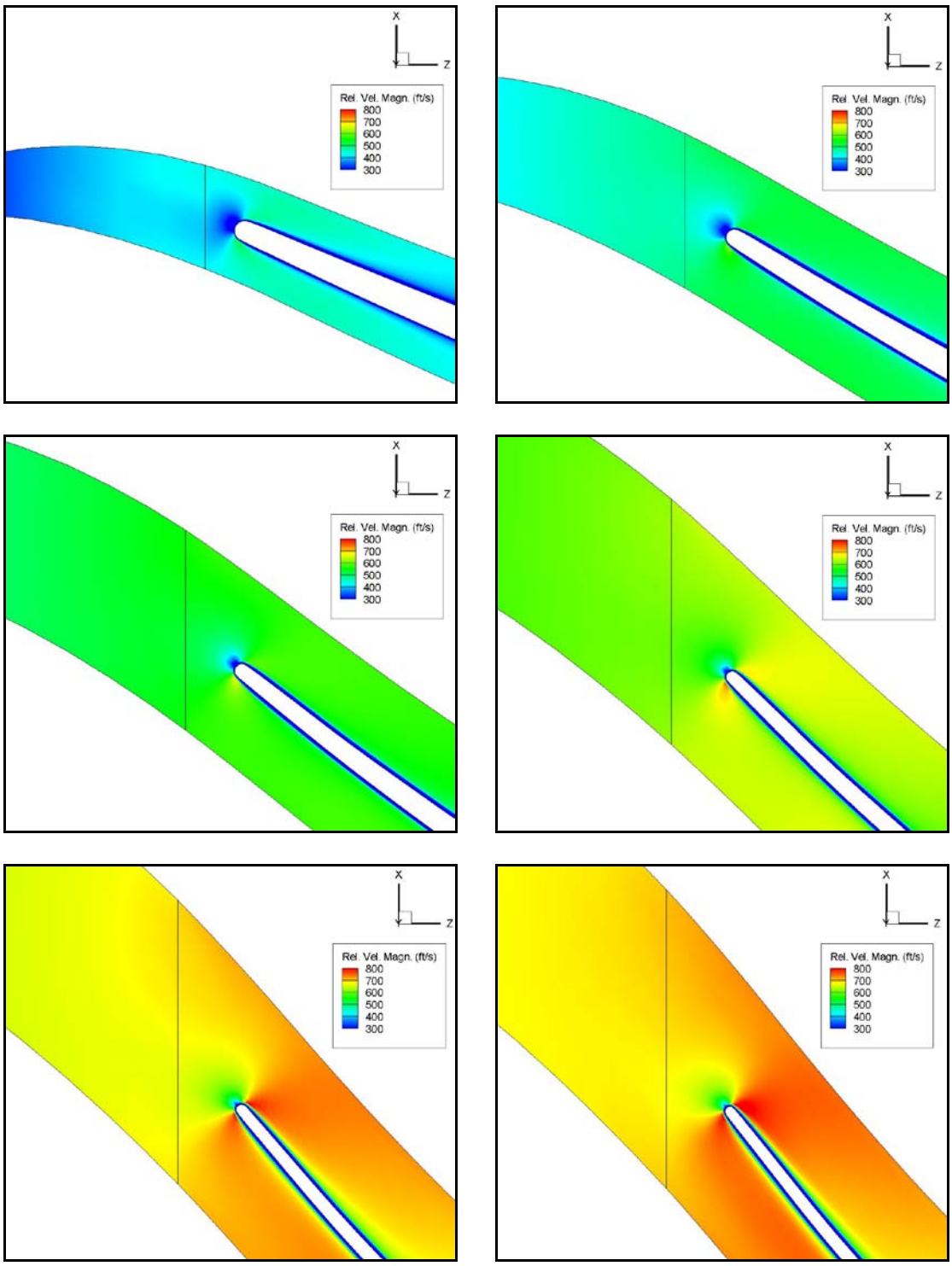

Figure A-22 Velocity magnitude 2-D contour plots for CCN66 at a mass flow rate of 5.20 lbm/s at six spanwise positions progressing from hub-to-shroud. The upper left panel corresponds to the hub with successive panels moving from left to right and top to bottom, in the following order: $\hat{H}$ = 0, $\hat{H}$ = 0.25, $\hat{H}$ = 0.5, $\hat{H}$ = 0.7, $\hat{H}$ = 0.9 and $\hat{H}$ = 1.

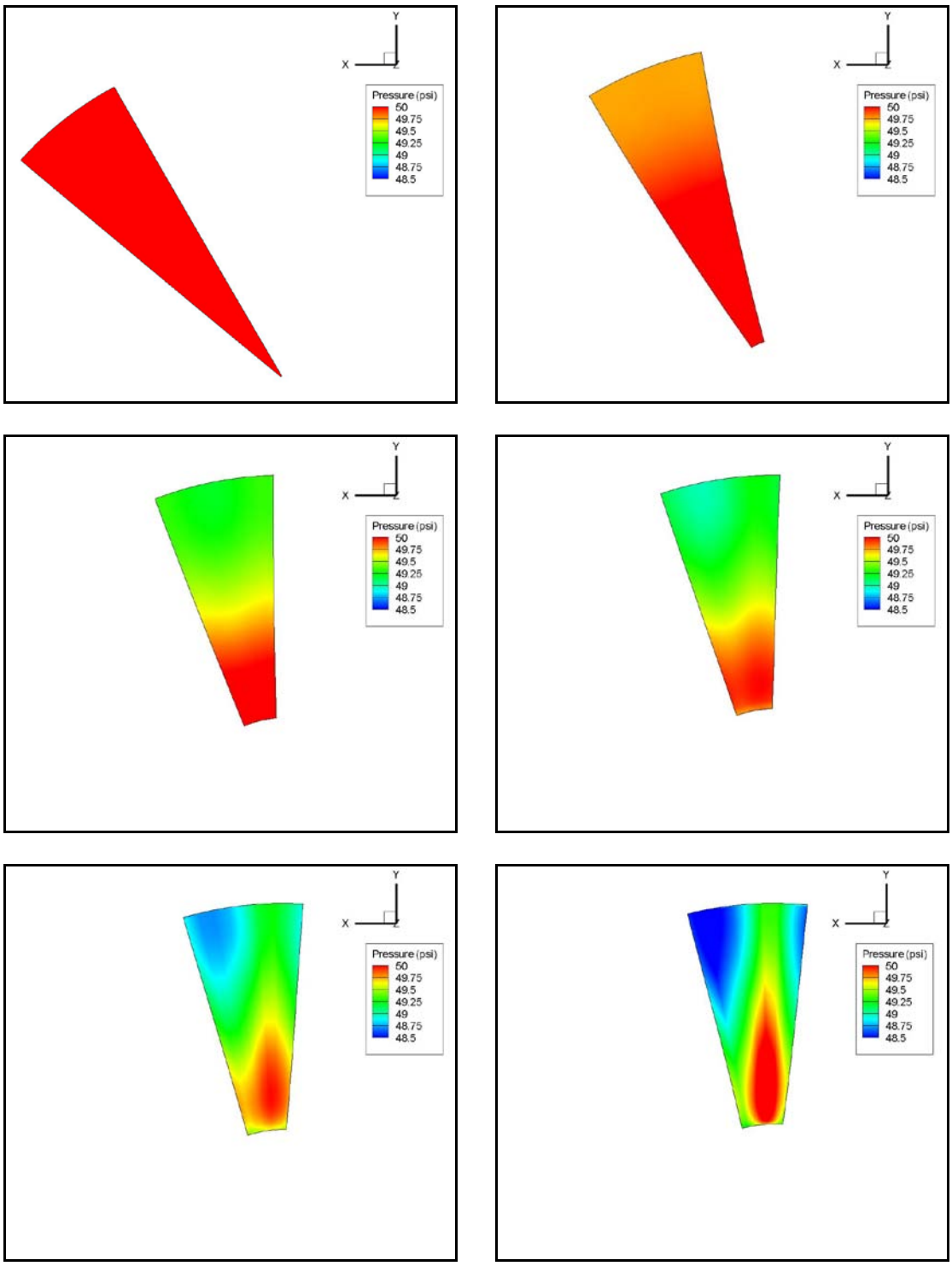

Figure A-23 Static pressure 2-D contour plots at six streamwise locations moving from the beginning of the computational domain to the impeller leading edge. The upper left panel corresponds to $\hat{S}$ = -3.09 with successive panels moving from left to right and top to bottom, in the following order: $\hat{S}$ = -3.09, $\hat{S}$ = -1.05 $\hat{S}$ = -0.49, $\hat{S}$ = -0.37, $\hat{S}$ = -0.25, and $\hat{S}$ = -0.17.

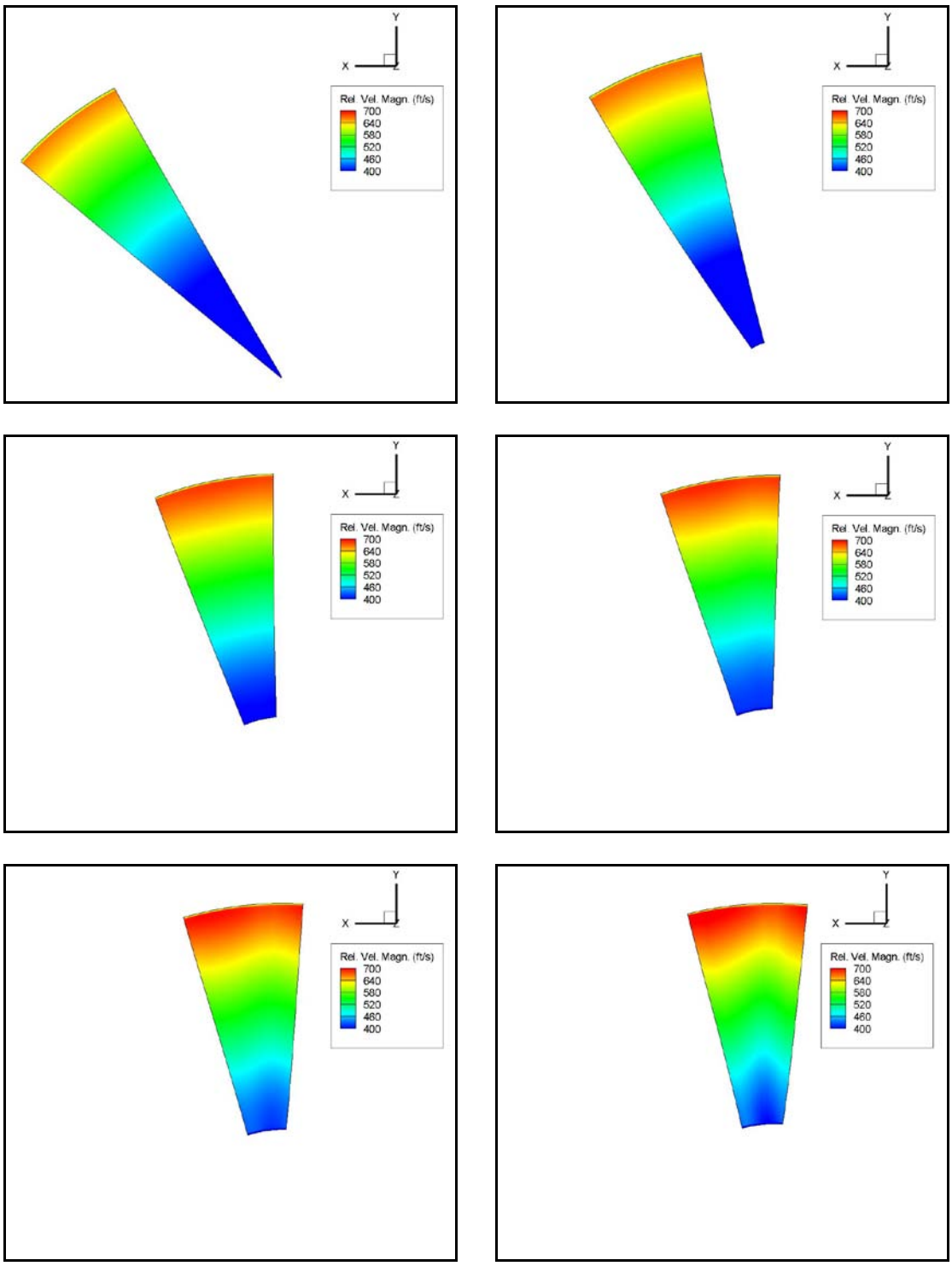

Figure A-24 Velocity magnitude 2-D contour plots at six streamwise locations moving from the beginning of the computational domain to the impeller leading edge. The upper left panel corresponds to $\hat{S}$ = -3.09 with successive panels moving from left to right and top to bottom, in the following order $\hat{S}$ = -3.09, $\hat{S}$ = -1.05 $\hat{S}$ = -0.49, $\hat{S}$ = -0.37, $\hat{S}$ = -0.25, and $\hat{S}$ = -0.17.

A-7 CCN74

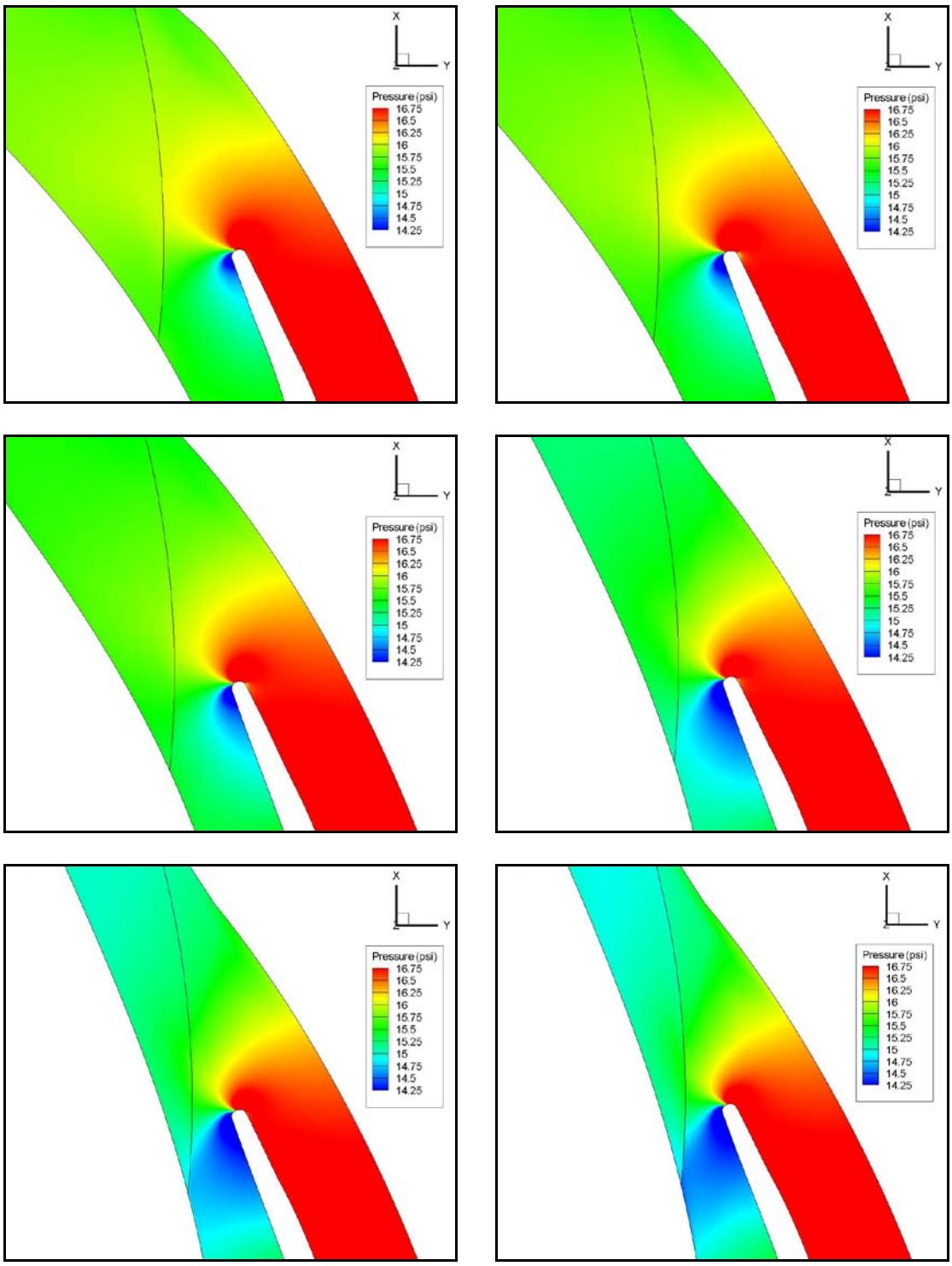

Figure A-25 Static pressure 2-D contour plots for CCN74 at a mass flow rate of 0.30 lbm/s at six spanwise positions progressing from hub-to-shroud. The upper left panel corresponds to the hub with successive panels moving from left to right and top to bottom, in the following order: $\hat{H}$ = 0, $\hat{H}$ = 0.25, $\hat{H}$ = 0.5, $\hat{H}$ = 0.7, $\hat{H}$ = 0.9 and $\hat{H}$ = 1.

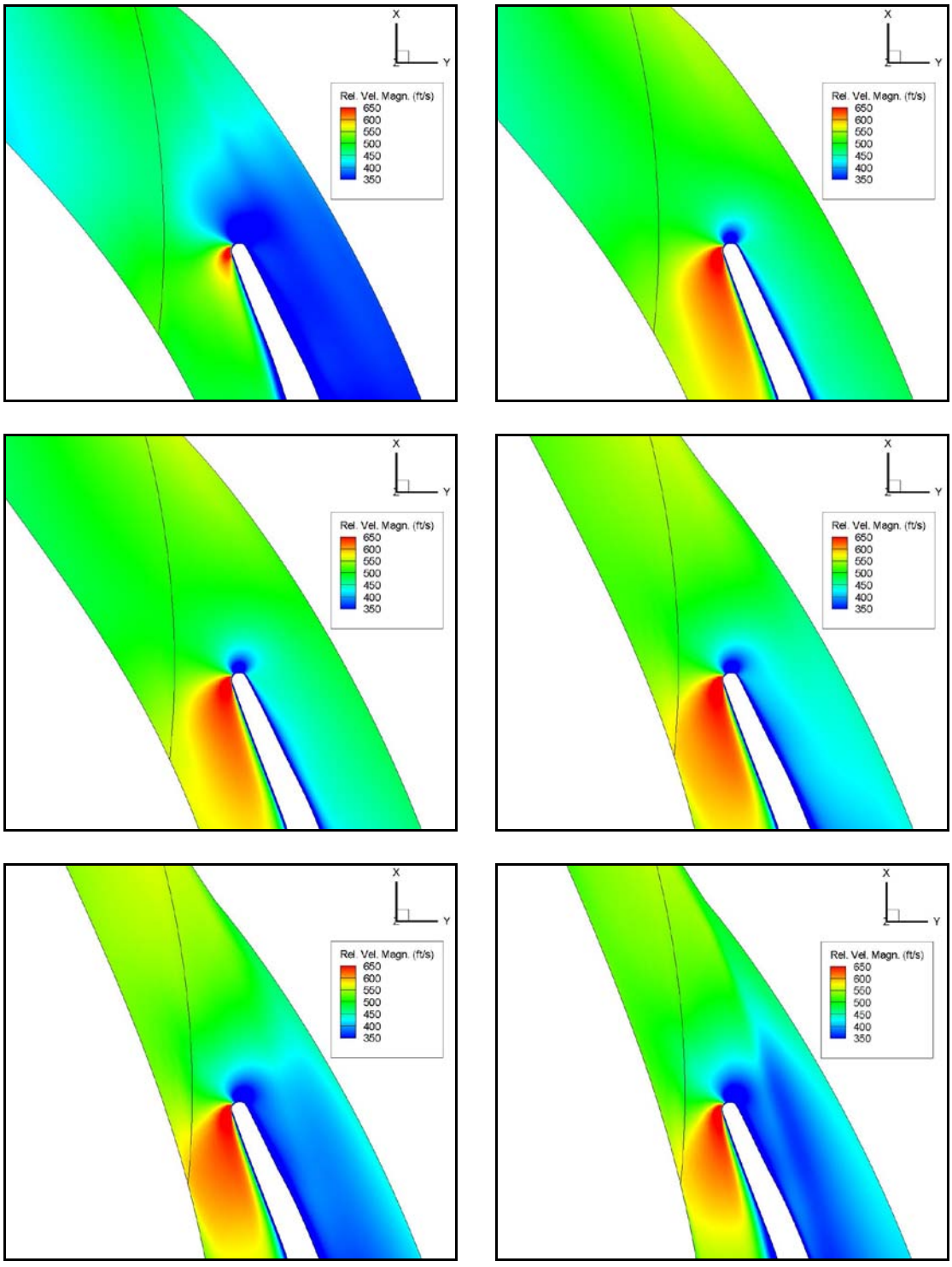

Figure A-26 Velocity magnitude 2-D contour plots for CCN74 at a mass flow rate of 0.30 lbm/s at six spanwise positions progressing from hub-to-shroud. The upper left panel corresponds to the hub with successive panels moving from left to right and top to bottom, in the following order: $\hat{H}$ = 0, $\hat{H}$ = 0.25, $\hat{H}$ = 0.5, $\hat{H}$ = 0.7, $\hat{H}$ = 0.9 and $\hat{H}$ = 1.

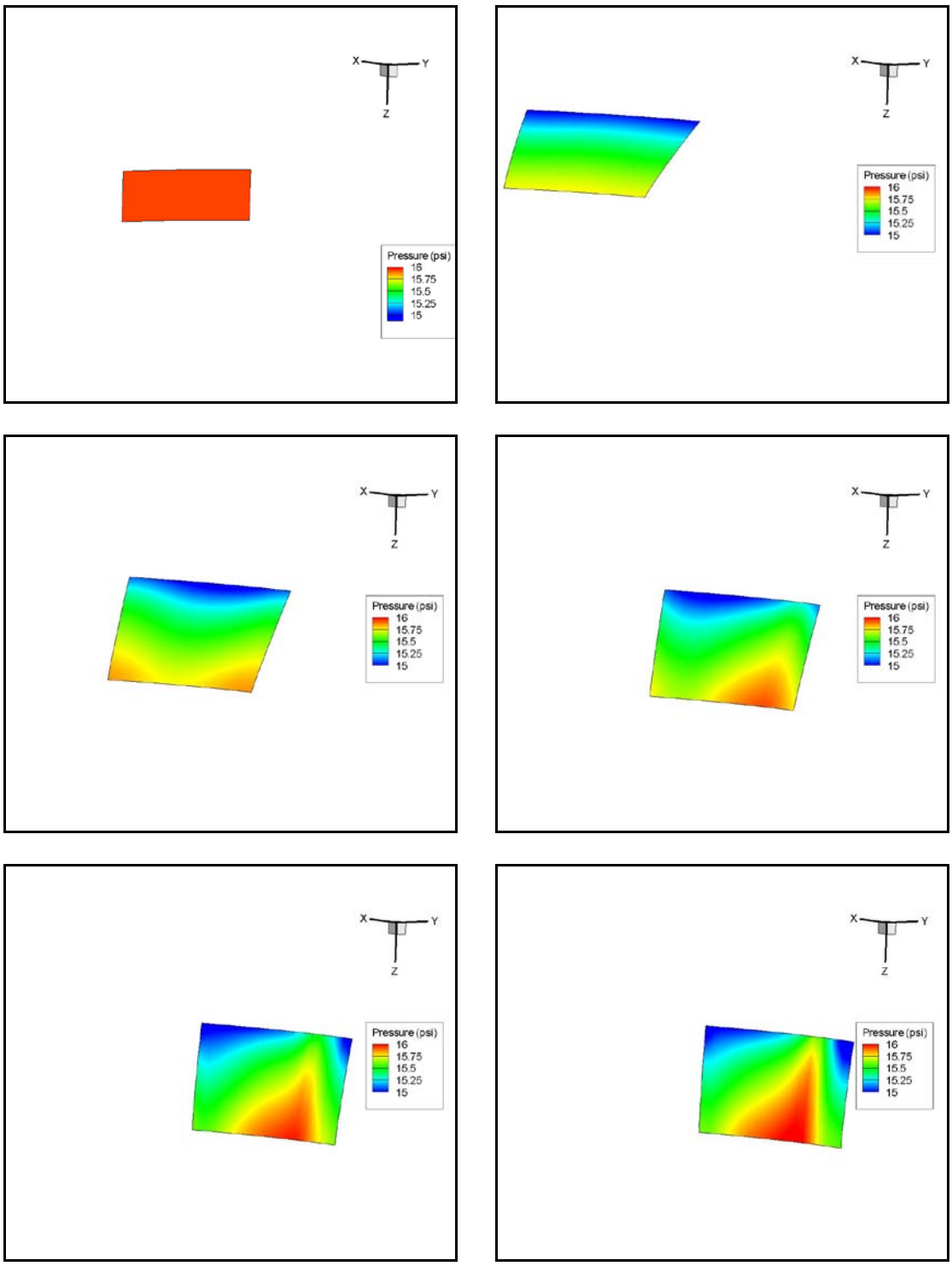

Figure A-27 Static pressure 2-D contour plots at six streamwise locations moving from the beginning of the computational domain to the impeller leading edge. The upper left panel corresponds to $\hat{S}$ = -7.99 with successive panels moving from left to right and top to bottom, in the following order: $\hat{S}$ = -7.99, $\hat{S}$ = -1.06 $\hat{S}$ = -0.49, $\hat{S}$ = -0.25, $\hat{S}$ = -0.11, and $\hat{S}$ = -0.04.

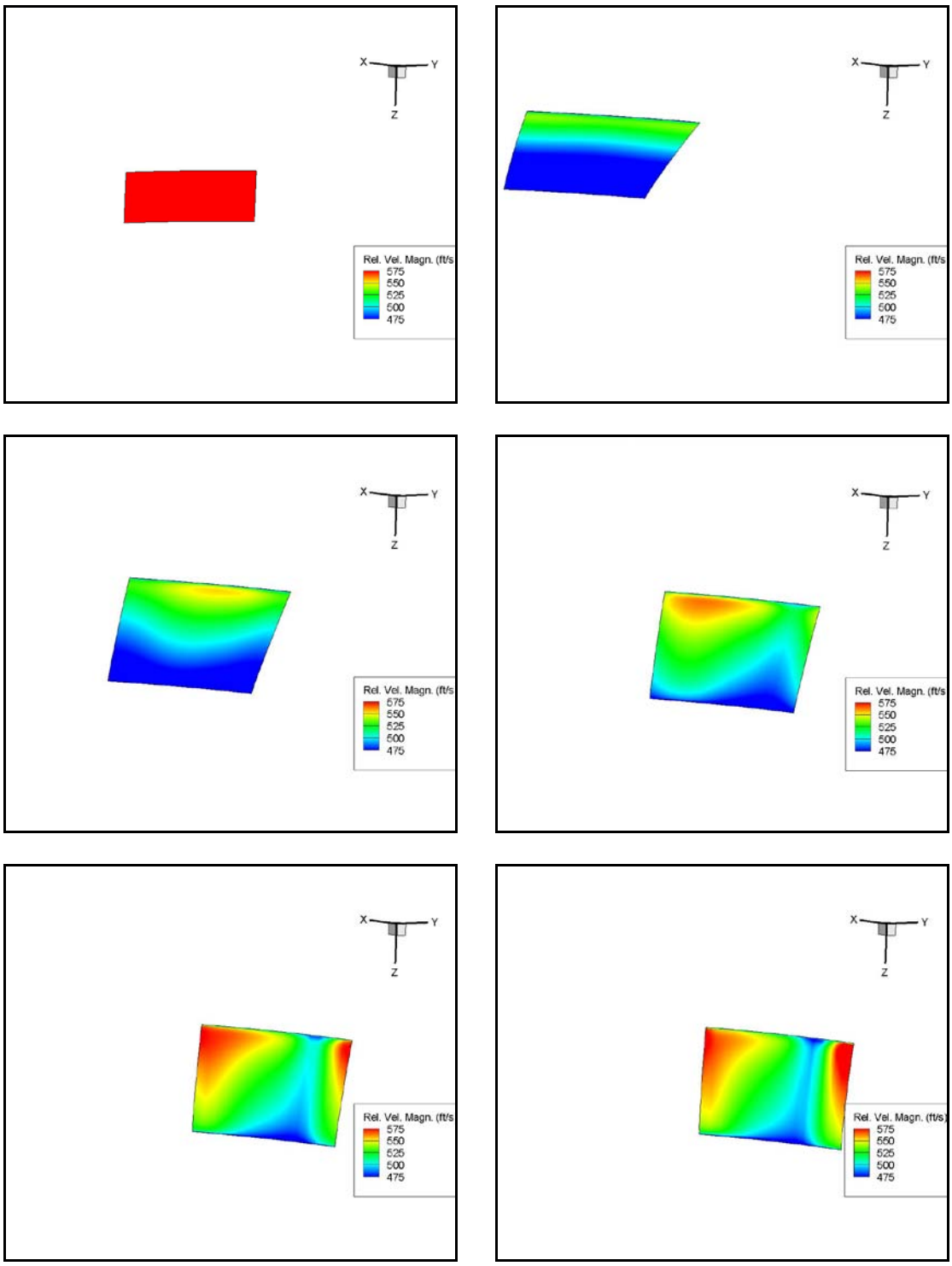

Figure A-28 Velocity magnitude 2-D contour plots at six streamwise locations moving from the beginning of the computational domain to the impeller leading edge. The upper left panel corresponds to $\hat{S}$ = -7.99 with successive panels moving from left to right and top to bottom, in the following order $\hat{S}$ = -7.99, $\hat{S}$ = -1.06 $\hat{S}$ = -0.49, $\hat{S}$ = -0.25, $\hat{S}$ = -0.11, and $\hat{S}$ = -0.04.

A-8 CCN95

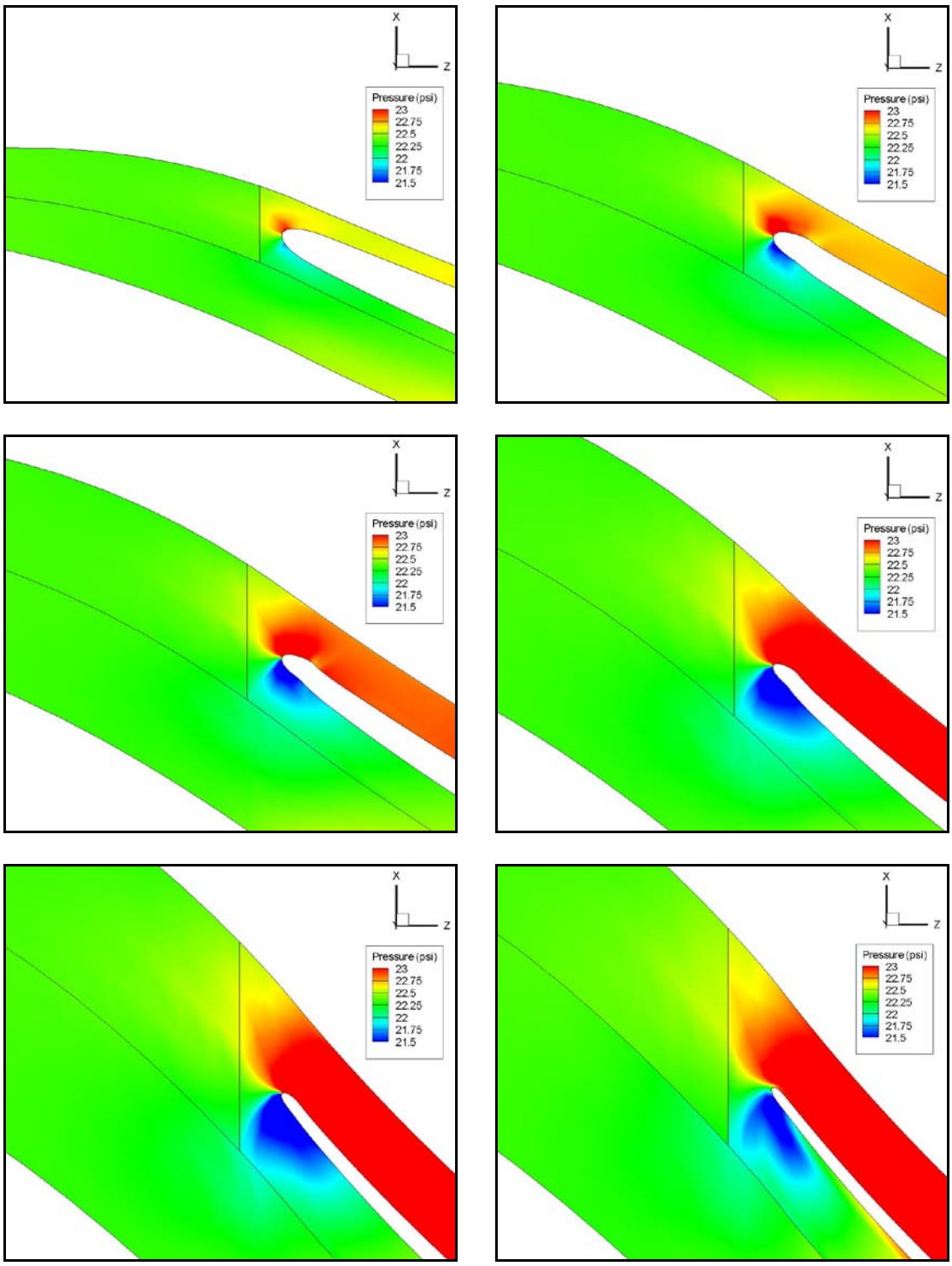

Figure A-29 Static pressure 2-D contour plots for CCN95 at a mass flow rate of 0.55 lbm/s at six spanwise positions progressing from hub-to-shroud. The upper left panel corresponds to the hub with successive panels moving from left to right and top to bottom, in the following order: $\hat{H}$ = 0, $\hat{H}$ = 0.25, $\hat{H}$ = 0.5, $\hat{H}$ = 0.7, $\hat{H}$ = 0.9 and $\hat{H}$ = 1.

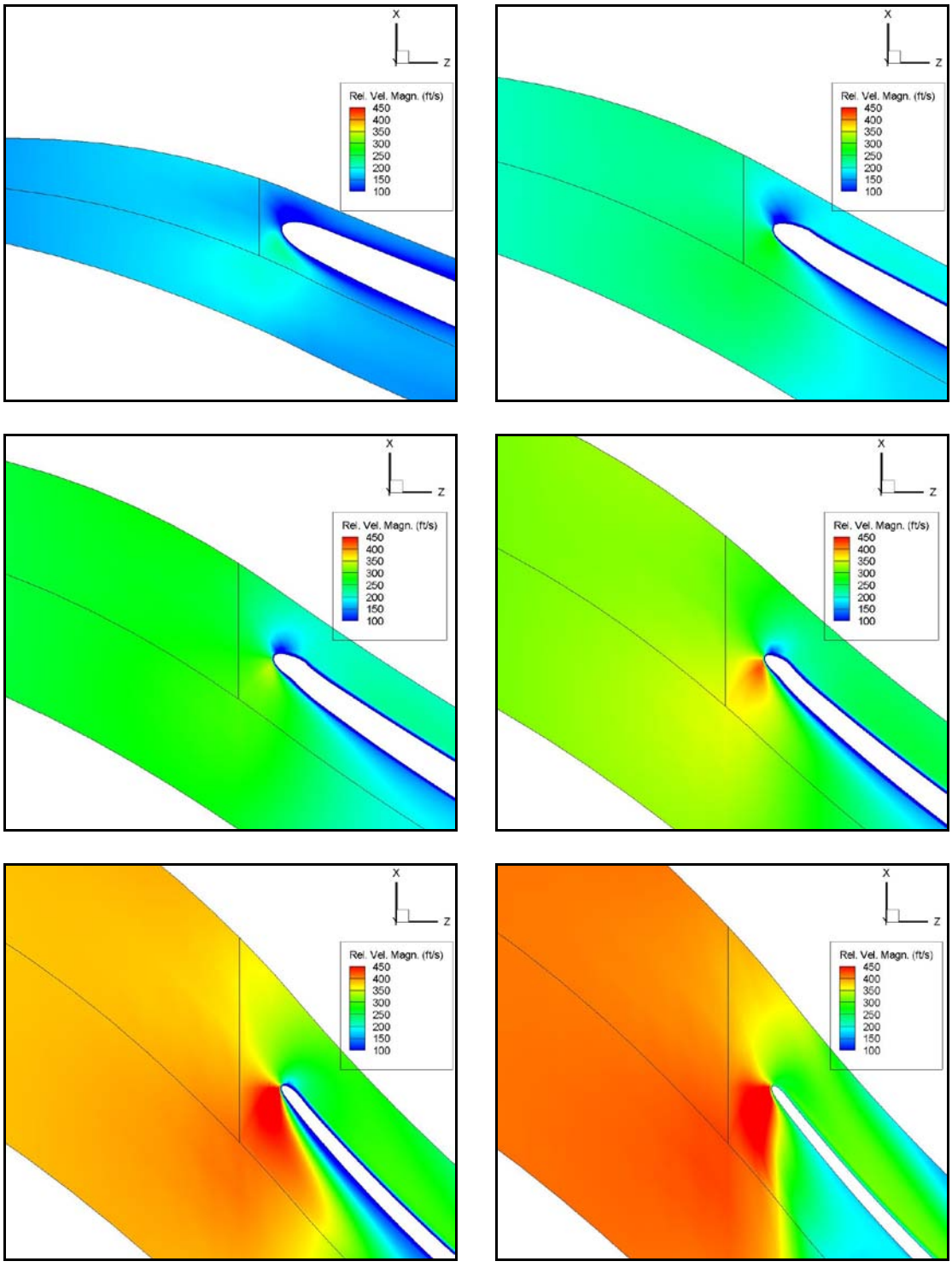

Figure A-30 Velocity magnitude 2-D contour plots for CCN95 at a mass flow rate of 0.55 lbm/s at six spanwise positions progressing from hub-to-shroud. The upper left panel corresponds to the hub with successive panels moving from left to right and top to bottom, in the following order: $\hat{H}$ = 0, $\hat{H}$ = 0.25, $\hat{H}$ = 0.5, $\hat{H}$ = 0.7, $\hat{H}$ = 0.9 and $\hat{H}$ = 1.

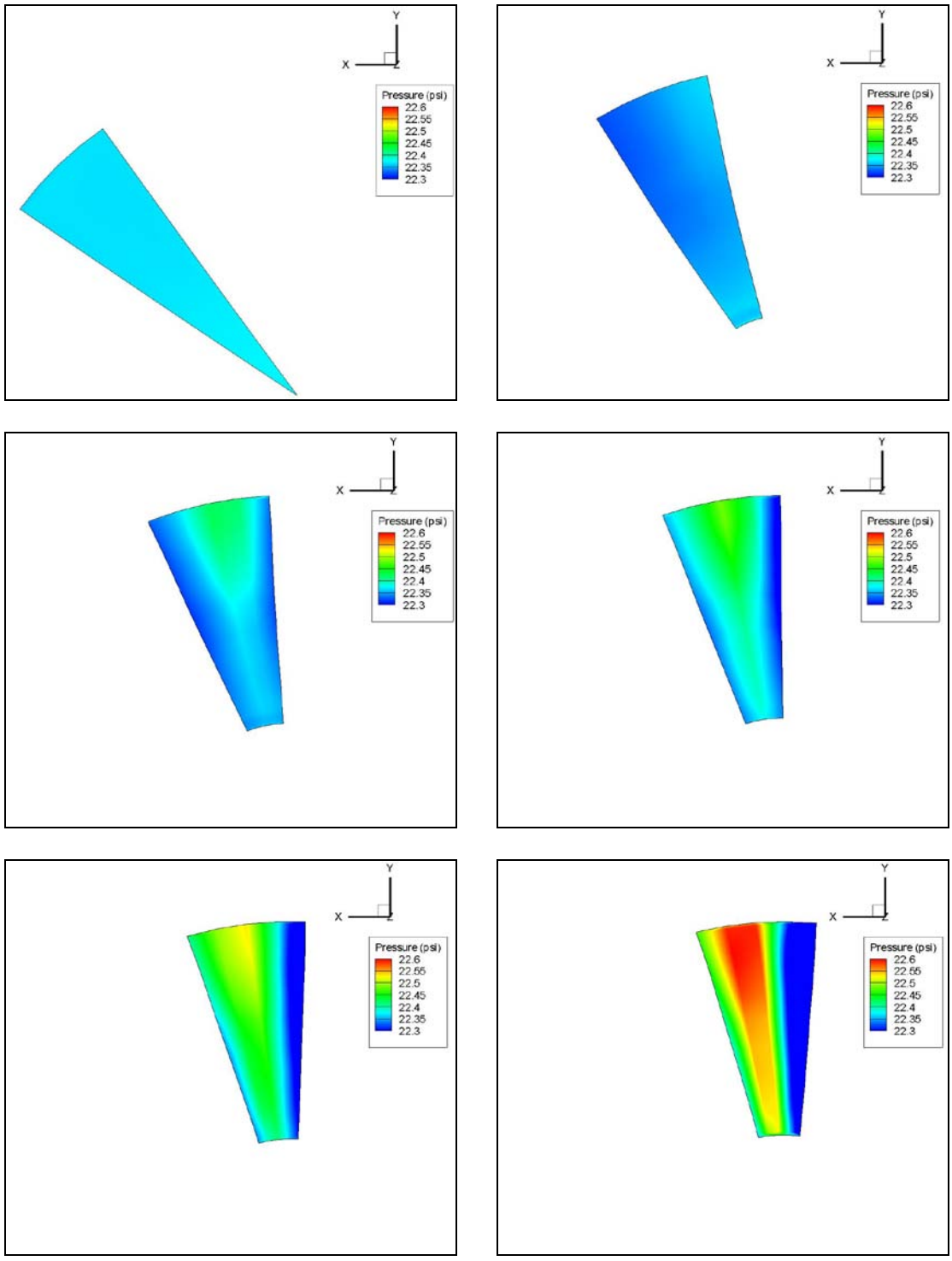

Figure A-31 Static pressure 2-D contour plots at six streamwise locations moving from the beginning of the computational domain to the impeller leading edge. The upper left panel corresponds to $\hat{S}$ = -2.09 with successive panels moving from left to right and top to bottom, in the following order: $\hat{S}$ = -2.09, $\hat{S}$ = -0.59 $\hat{S}$ = -0.31, $\hat{S}$ = -0.24, $\hat{S}$ = -0.17, and $\hat{S}$ = -0.101.

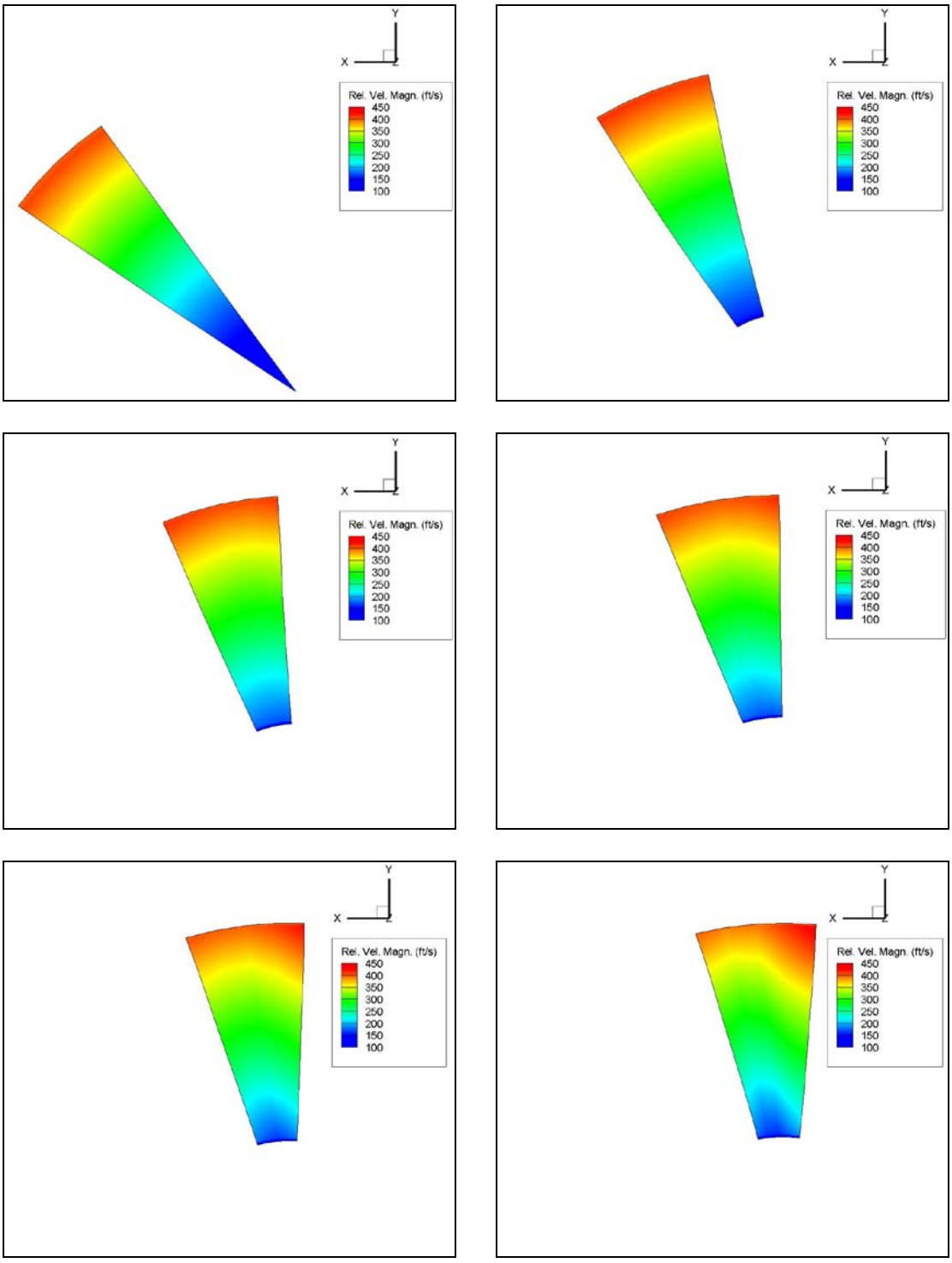

Figure A-32 Velocity magnitude 2-D contour plots at six streamwise locations moving from the beginning of the computational domain to the impeller leading edge. The upper left panel corresponds to $\hat{S}$ = -2.09 with successive panels moving from left to right and top to bottom, in the following order $\hat{S}$ = -2.09, $\hat{S}$ = -0.59 $\hat{S}$ = -0.31, $\hat{S}$ = -0.24, $\hat{S}$ = -0.17, and $\hat{S}$ = -0.10.

A-9 CPN7

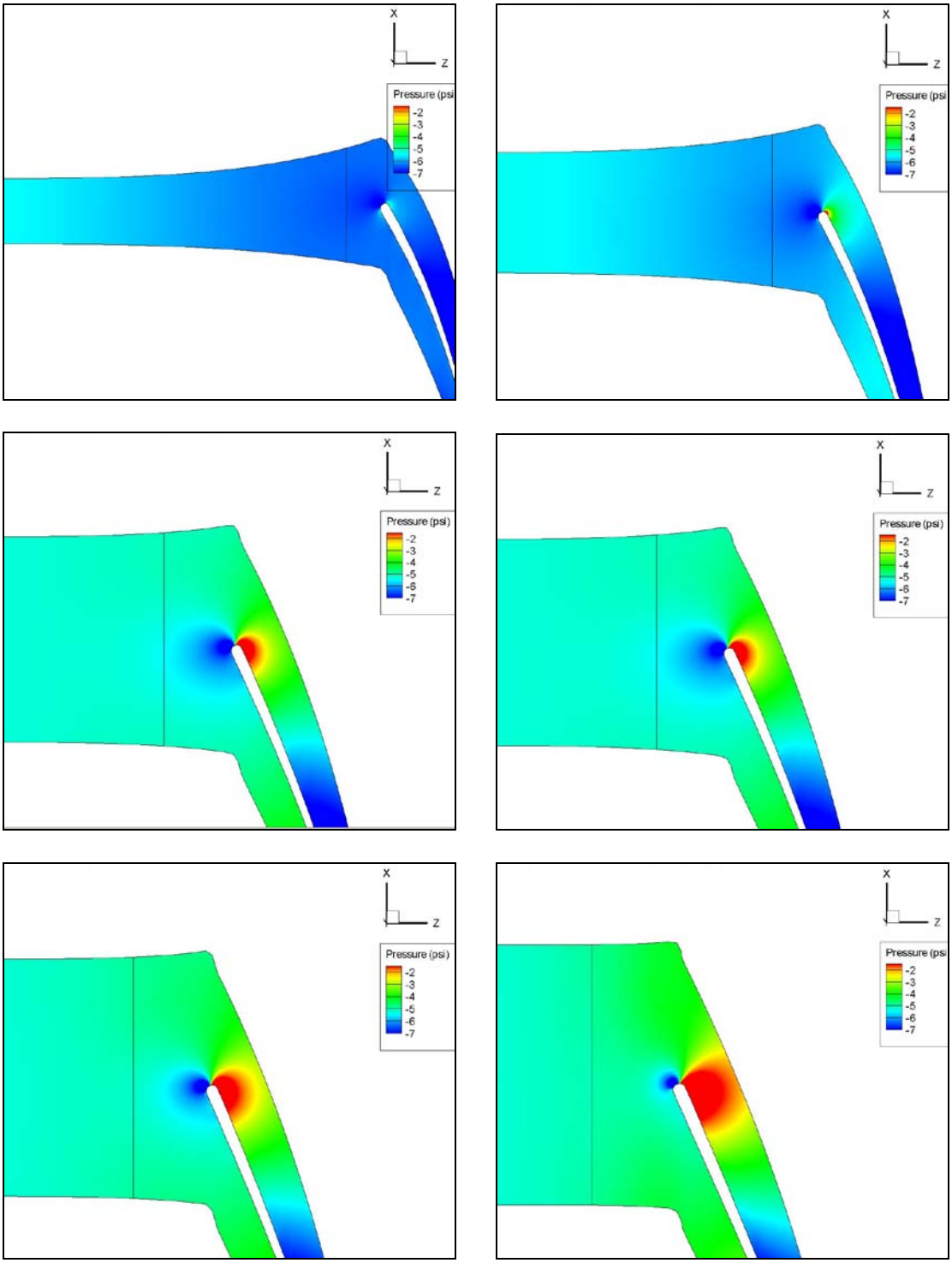

Figure A-33 Static pressure 2-D contour plots for CPN7 at a mass flow rate of 90.26 lbm/s at six spanwise positions progressing from hub-to-shroud. The upper left panel corresponds to the hub with successive panels moving from left to right and top to bottom, in the following order: $\hat{H}$ = 0, $\hat{H}$ = 0.25, $\hat{H}$ = 0.5, $\hat{H}$ = 0.7, $\hat{H}$ = 0.9 and $\hat{H}$ = 1.

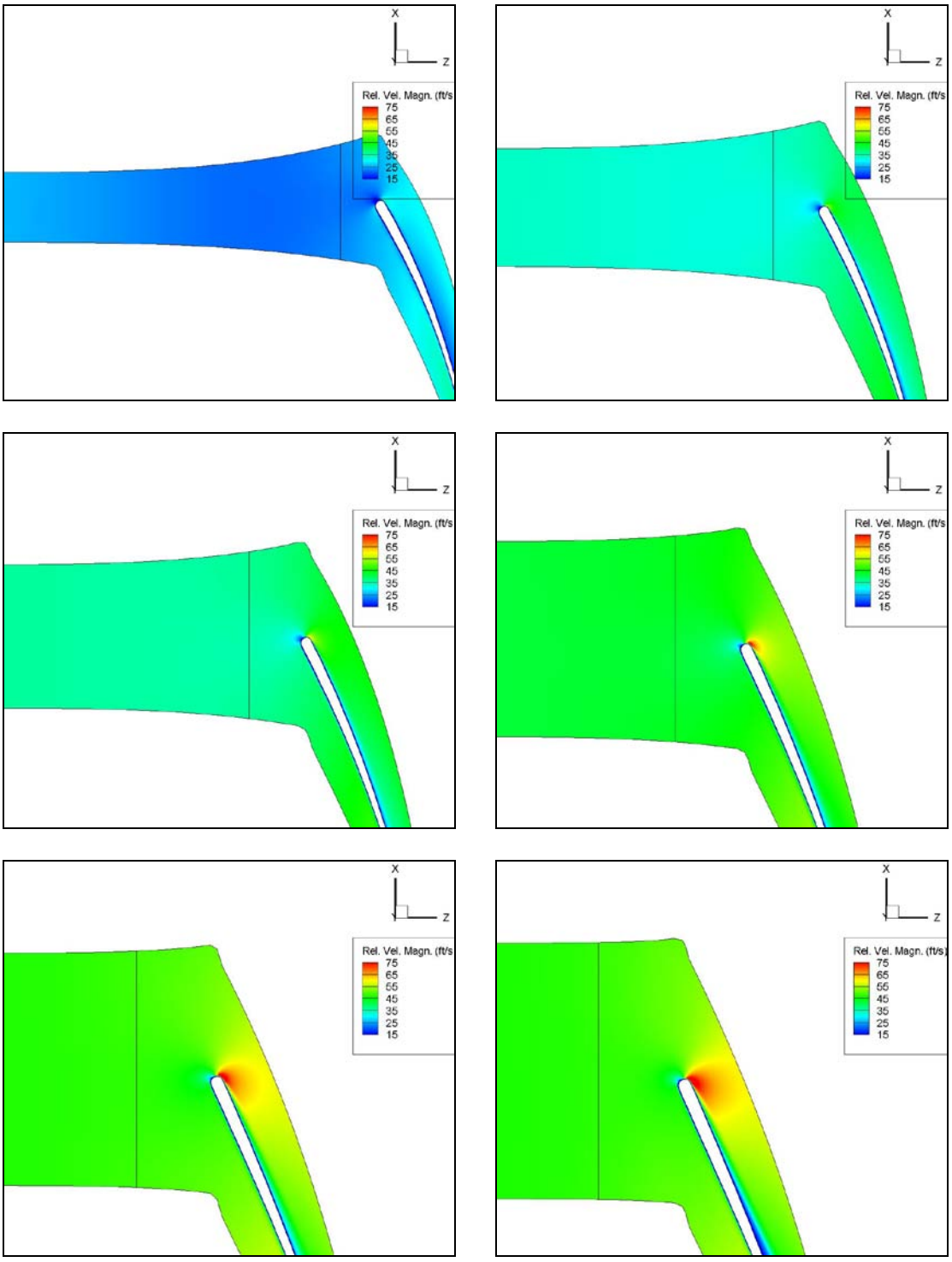

Figure A-34 Velocity magnitude 2-D contour plots for CPN7 at a mass flow rate of 90.26 lbm/s at six spanwise positions progressing from hub-to-shroud. The upper left panel corresponds to the hub with successive panels moving from left to right and top to bottom, in the following order: $\hat{H}$ = 0, $\hat{H}$ = 0.25, $\hat{H}$ = 0.5, $\hat{H}$ = 0.7, $\hat{H}$ = 0.9 and $\hat{H}$ = 1.

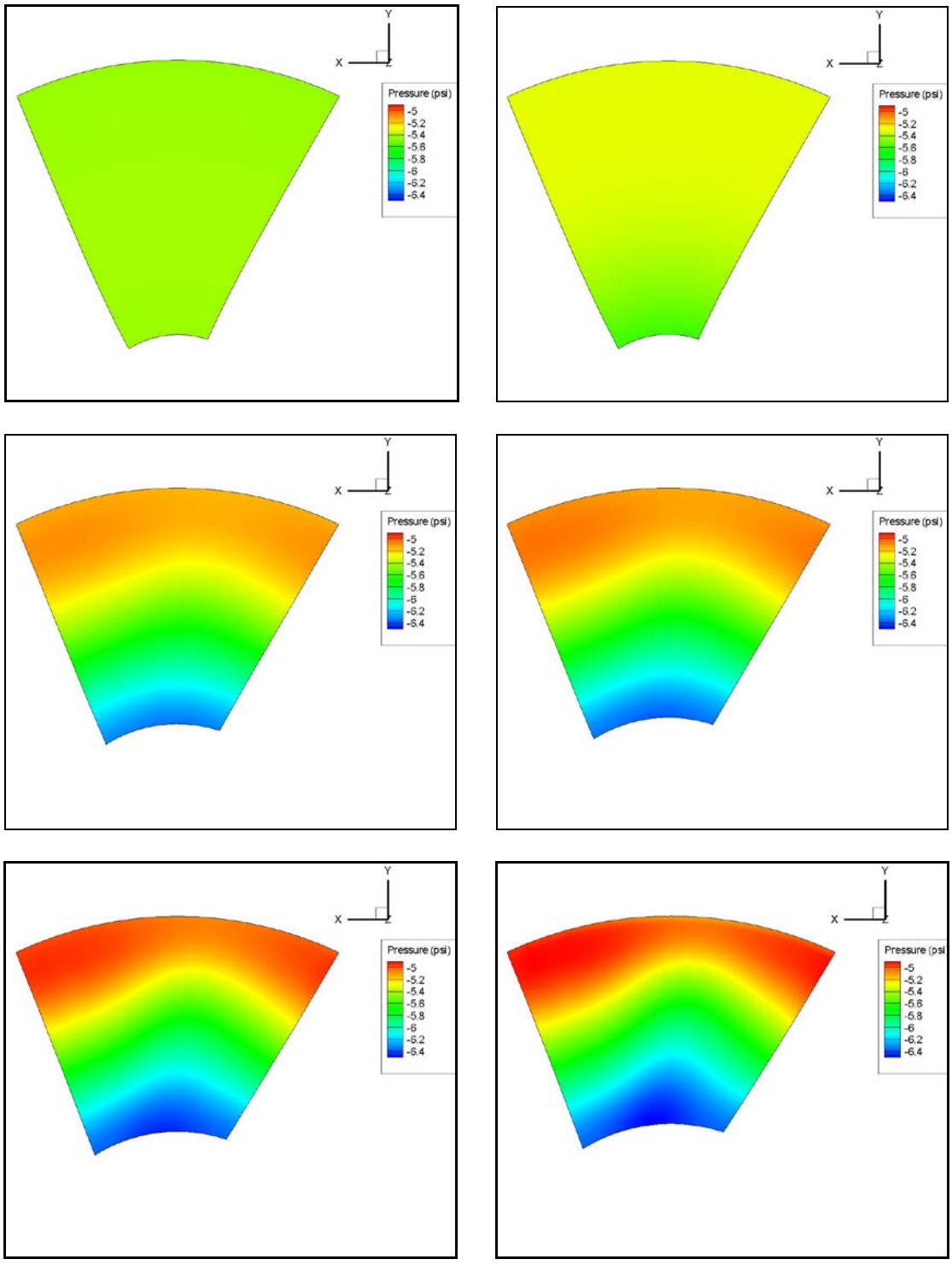

Figure A-35 Static pressure 2-D contour plots at six streamwise locations moving from the beginning of the computational domain to the impeller leading edge. The upper left panel corresponds to $\hat{S}$ = -4.92 with successive panels moving from left to right and top to bottom, in the following order: $\hat{S}$ = -4.92, $\hat{S}$ = -1.15 $\hat{S}$ = -0.47, $\hat{S}$ = -0.42, $\hat{S}$ = -0.33, and $\hat{S}$ = -0.29.

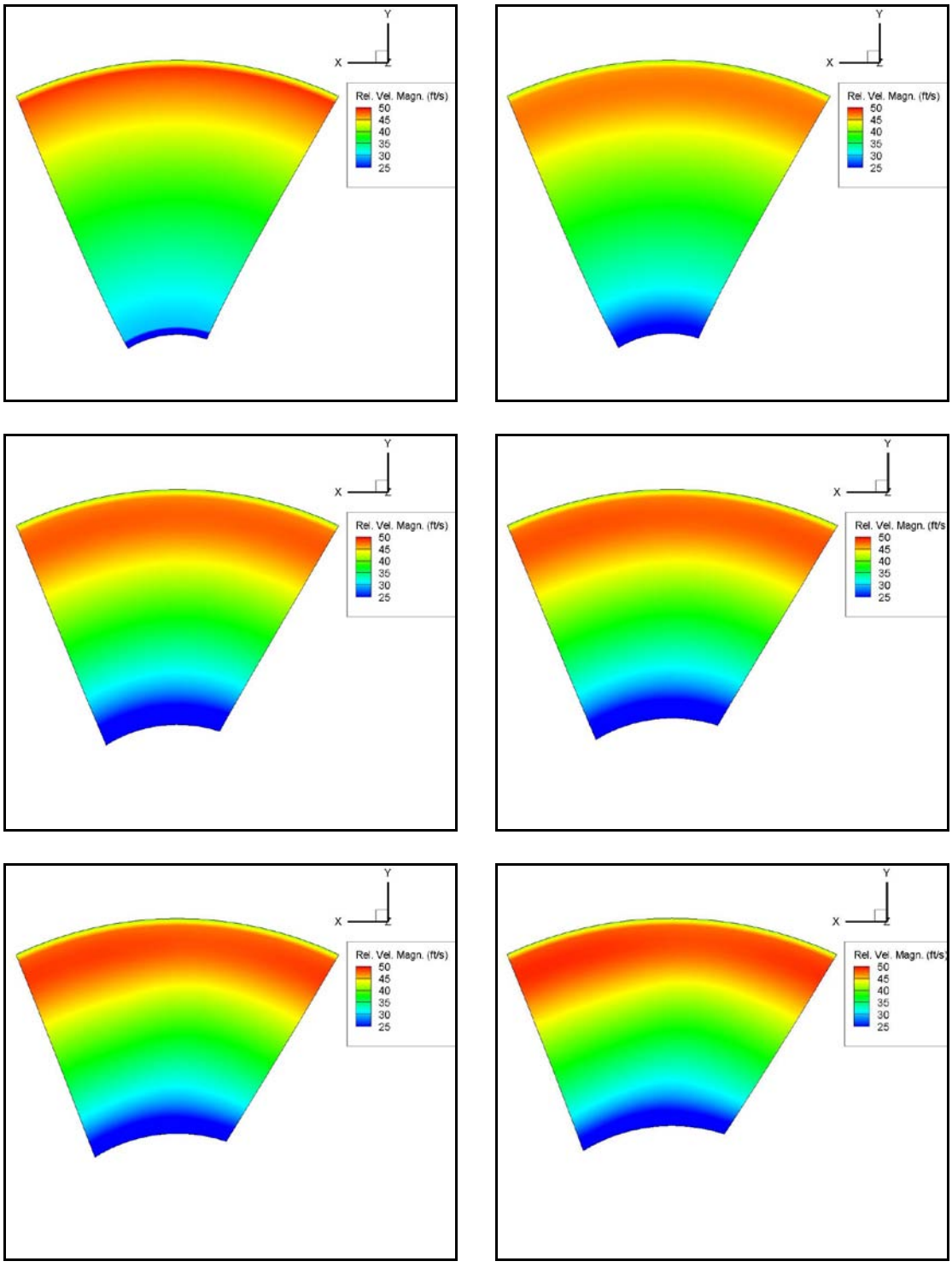

Figure A-36 Velocity magnitude 2-D contour plots at six streamwise locations moving from the beginning of the computational domain to the impeller leading edge. The upper left panel corresponds to $\hat{S}$ = -4.92 with successive panels moving from left to right and top to bottom, in the following order $\hat{S}$ = -4.92, $\hat{S}$ = -1.15 $\hat{S}$ = -0.47, $\hat{S}$ = -0.42, $\hat{S}$ = -0.33, and $\hat{S}$ = -0.29.

A-10 CPN28

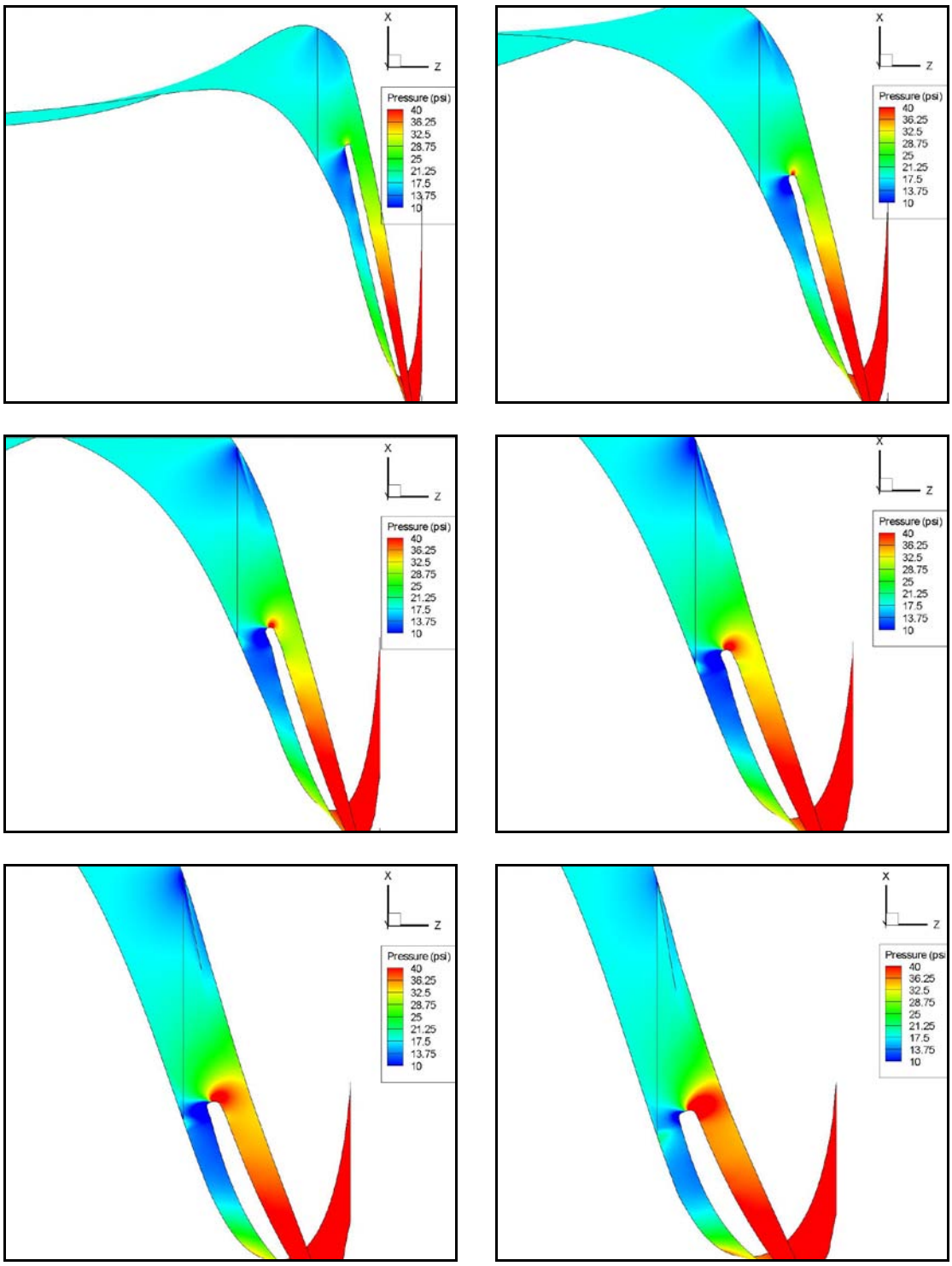

Figure A-37 Static pressure 2-D contour plots for CPN28 at a mass flow rate of 133.39 lbm/s at six spanwise positions progressing from hub-to-shroud. The upper left panel corresponds to the hub with successive panels moving from left to right and top to bottom, in the following order: $\hat{H}$ = 0, $\hat{H}$ = 0.25, $\hat{H}$ = 0.5, $\hat{H}$ = 0.7, $\hat{H}$ = 0.9 and $\hat{H}$ = 1.

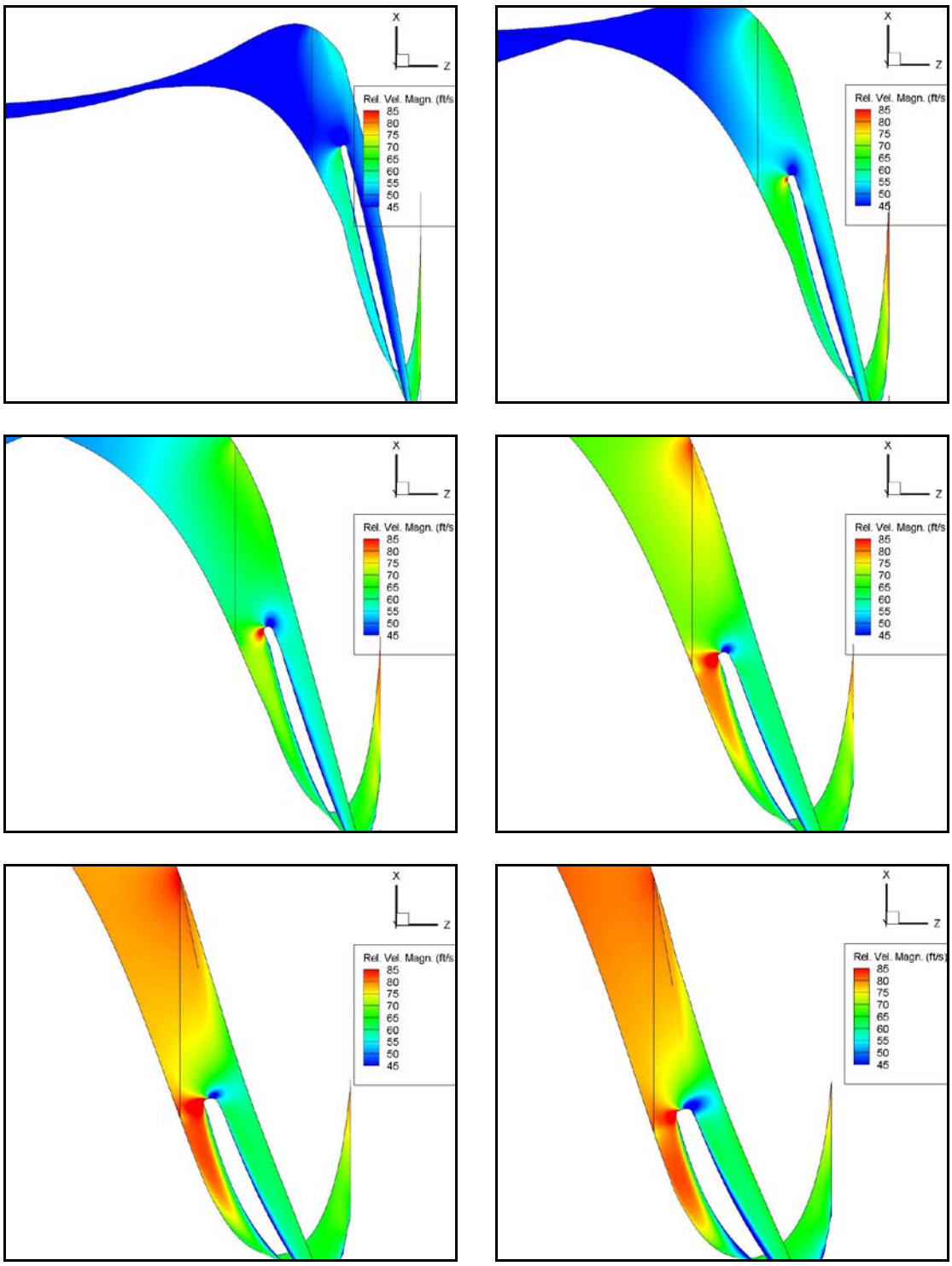

Figure A-38 Velocity magnitude 2-D contour plots for CPN28 at a mass flow rate of 133.39 lbm/s at six spanwise positions progressing from hub-to-shroud. The upper left panel corresponds to the hub with successive panels moving from left to right and top to bottom, in the following order: $\hat{H}$ = 0, $\hat{H}$ = 0.25, $\hat{H}$ = 0.5, $\hat{H}$ = 0.7, $\hat{H}$ = 0.9 and $\hat{H}$ = 1.

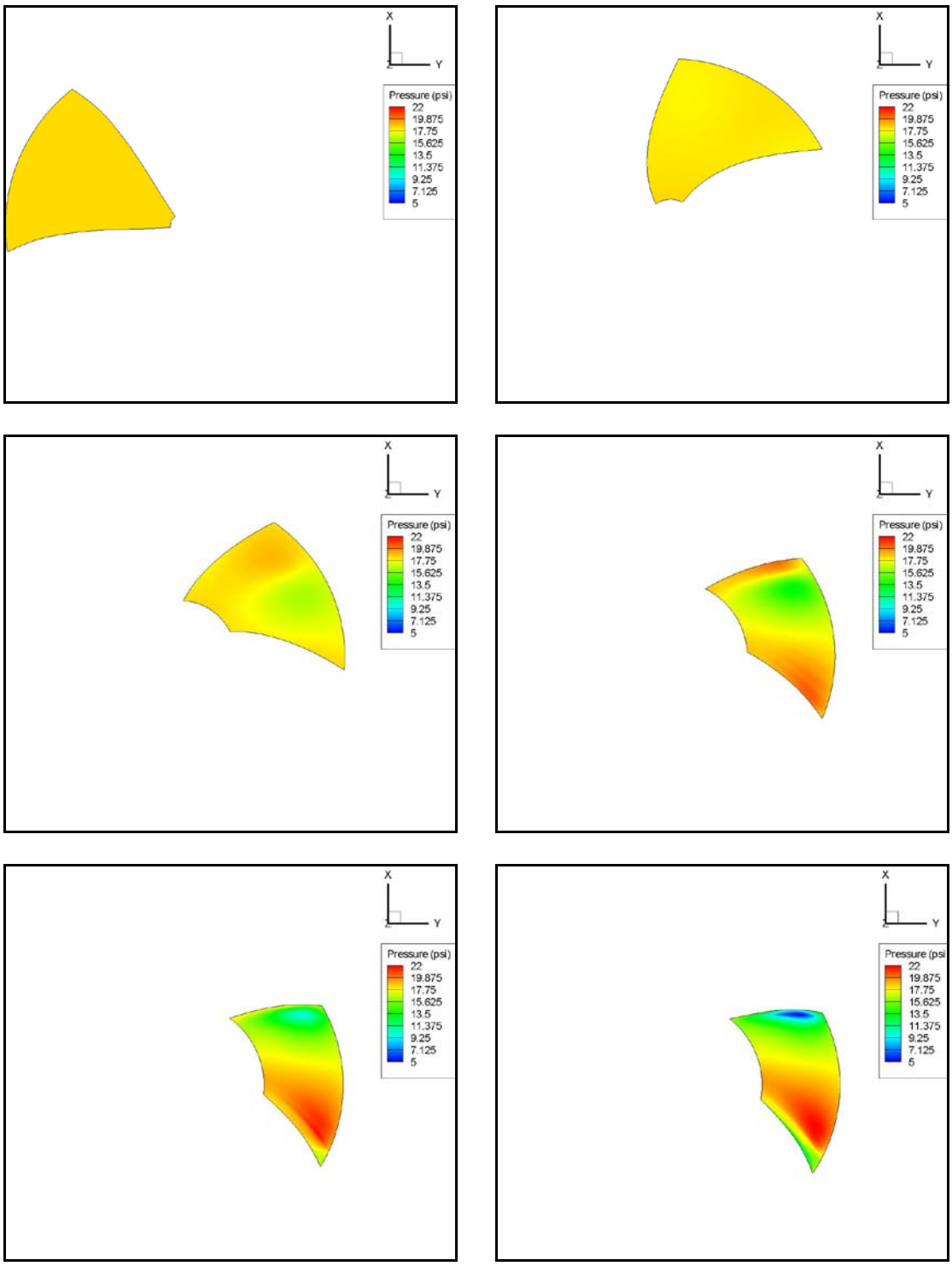

Figure A-39 Static pressure 2-D contour plots at six streamwise locations moving from the beginning of the computational domain to the impeller leading edge. The upper left panel corresponds to $\hat{S}$ = -6.33 with successive panels moving from left to right and top to bottom, in the following order: $\hat{S}$ = -6.33, $\hat{S}$ = -1.14 $\hat{S}$ = -0.60, $\hat{S}$ = -0.36, $\hat{S}$ = -0.26, and $\hat{S}$ = -0.22.

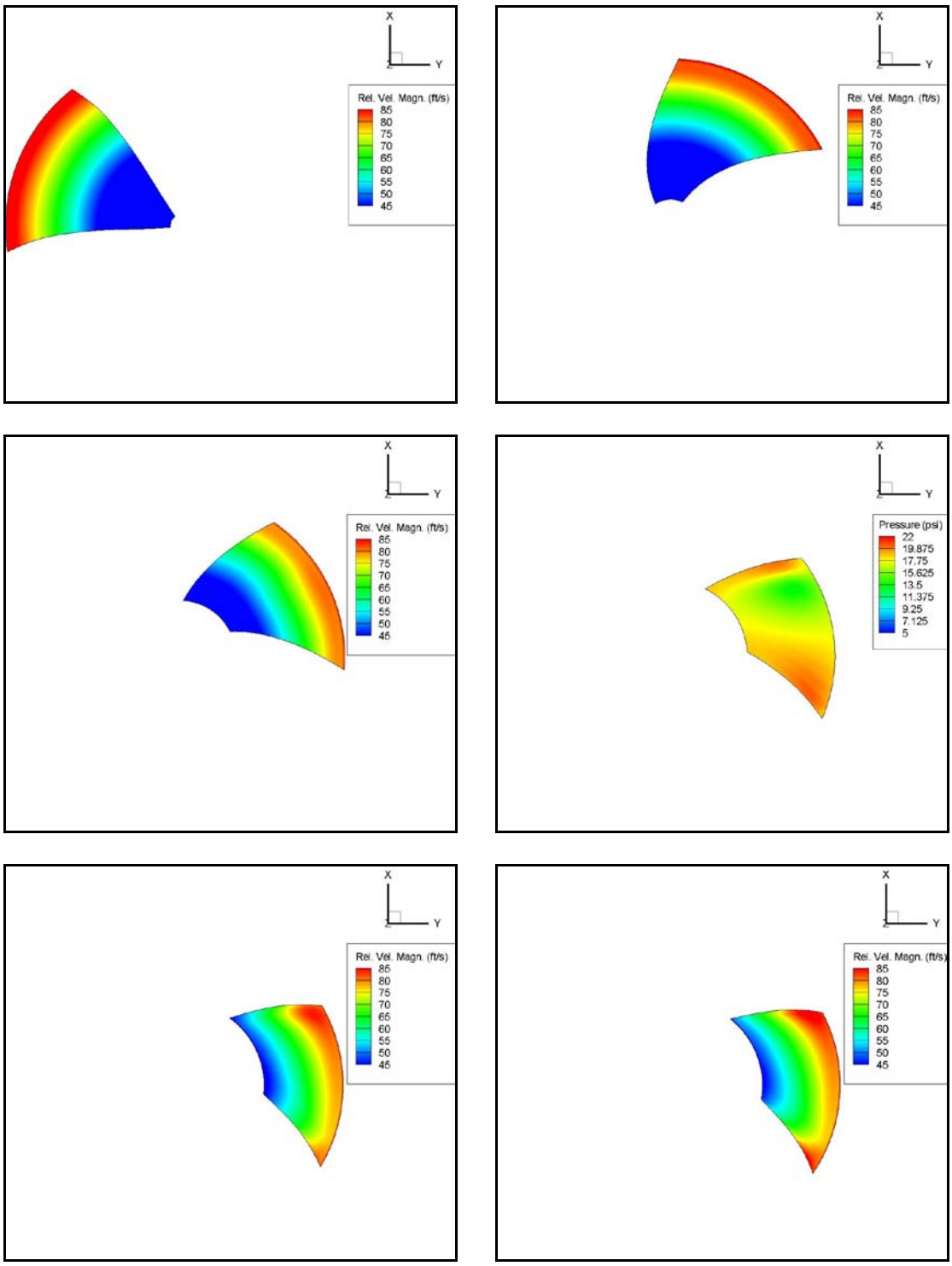

Figure A-40 Velocity magnitude 2-D contour plots at six streamwise locations moving from the beginning of the computational domain to the impeller leading edge. The upper left panel corresponds to $\hat{S}$ = -6.33 with successive panels moving from left to right and top to bottom, in the following order $\hat{S}$ = -1.14, $\hat{S}$ = -0.60 $\hat{S}$ = -0.36, $\hat{S}$ = -0.33, $\hat{S}$ = -0.26, and $\hat{S}$ = -0.22.